Institut für Geowissenschaften
Mathematisch-Naturwissenschaftliche Fakultät
Universität Potsdam

School of Earth, Atmospheric and Life Sciences
Faculty of Science, Medicine and Health
University of Wollongong

Kumulative Dissertationsschrift

Interactions between tectonics, climate, and surface processes in the Kyrgyz Tian Shan

zur Erlangung des akademischen Grades

DOCTOR RERUM NATURALIUM

»DR. RER. NAT.«

Eingereicht durch

Anna Kudriavtseva

im Fachbereich Geowissenschaften

Eingereicht an der

Mathematisch-Naturwissenschaftlichen Fakultät

der Universität Potsdam

Potsdam, März 2023

Advisors

apl Prof. Edward R. Sobel, University of Potsdam, Germany
Dr. Alexandru Codilean, University of Wollongong

Published online on the
Publication Server of the University of Potsdam:
https://doi.org/10.25932/publishup-60372
https://nbn-resolving.org/urn:nbn:de:kobv:517-opus4-603728

Declaration of Authenticity

I declare that I wrote this thesis entitled "Interactions between tectonics, climate, and surface processes in the Kyrgyz Tian Shan" on my own and it does not contain any unmentioned sources.

All sources and materials have been indicated by in-text citations and references. This thesis has not been submitted to any other University.

My contribution to this thesis has been explained in the Introduction. I acknowledge that Chapter 2 “Miocene to Early Pleistocene Depositional History and Tectonic Evolution of the Issyk-Kul basin, Central Tian Shan” constitutes a part of Sophie Roud’s doctoral thesis submitted and defended at the Ludwig-Maximilians-Universität München.

Potsdam, March 21, 2023 ……………………………………

Date Anna Kudriavtseva

Table of contents

List of figures

List of tables

ABSTRACT

During the Cenozoic, global cooling and uplift of the Tian Shan, Pamir, and Tibetan plateau modified atmospheric circulation and reduced moisture supply to Central Asia. These changes led to aridification in the region during the Neogene. Afterwards, Quaternary glaciations led to modification of the landscape and runoff.

In the Issyk-Kul basin of the Kyrgyz Tian Shan, the sedimentary sequences reflect the development of the adjacent ranges and local climatic conditions. In this work, I reconstruct the late Miocene – early Pleistocene depositional environment, climate, and lake development in the Issyk-Kul basin using facies analyses and stable $\delta^{18}O$ and $\delta^{13}C$ isotopic records from sedimentary sections dated by magnetostratigraphy and $^{26}Al/^{10}Be$ isochron burial dating. Also, I present ^{10}Be-derived millennial-scale modern and paleo-denudation rates from across the Kyrgyz Tian Shan and long-term exhumation rates calculated from published thermochronology data. This allows me to examine spatial and temporal changes in surface processes in the Kyrgyz Tian Shan.

In the Issyk-Kul basin, the style of fluvial deposition changed at ca. 7 Ma, and aridification in the basin commenced concurrently, as shown by magnetostratigraphy and the $\delta^{18}O$ and $\delta^{13}C$ data. Lake formation commenced on the southern side of the basin at ca. 5 Ma, followed by a ca. 2 Ma local depositional hiatus. $^{26}Al/^{10}Be$ isochron burial dating and paleocurrent analysis show that the Kungey range to the north of the basin grew eastward, leading to a change from fluvial-alluvial deposits to proximal alluvial fan conglomerates at 5-4 Ma in the easternmost part of the basin. This transition occurred at 2.6-2.8 Ma on the southern side of the basin, synchronously with the intensification of the Northern Hemisphere glaciation. The paleo-denudation rates from 2.7-2.0 Ma are as low as long-term exhumation rates, and only the millennial-scale denudation rates record an acceleration of denudation.

This work concludes that the growth of the ranges to the north of the basin led to creation of the topographic barrier at ca. 7 Ma and a subsequent aridification in the Issyk-Kul basin. Increased subsidence and local tectonically-induced river system reorganization on the southern side of the basin enabled lake formation at ca. 5 Ma, while growth of the Kungey range blocked westward-draining rivers and led to sediment starvation and lake expansion. Denudational response of the Kyrgyz Tian Shan landscape is delayed due to aridity and only substantial cooling during the late Quaternary glacial cycles led to notable acceleration of denudation. Currently, increased glacier reduction and runoff controls a more rapid denudation of the northern slope of the Terskey range compared to other ranges of the Kyrgyz Tian Shan.

PLAIN LANGUAGE SUMMARY

During the past ~66 Myr, global cooling and growth of the Tibetan plateau, Tian Shan, and Pamir mountains modified atmospheric circulation and reduced moisture supply to Central Asia. These changes resulted in a dry and arid climate in the region. Afterwards, glaciations in the past ~2.6 Myr modified the landscape and river runoff.

In the Issyk-Kul basin of the Kyrgyz Tian Shan, sedimentary layers record information about the development of the adjacent mountain ranges and local climatic conditions. In this work I reconstruct the processes that led to climatic changes and lake development. In order to do so, I describe and date sedimentary deposits and extract oxygen and carbon isotopic data, which are a proxy for local climatic conditions. Also, I present denudation rates (modern and from 2.7-2.0 Ma) from across the Kyrgyz Tian Shan and long-term (millions of years) exhumation rates calculated from published data. This allows me to examine spatial and temporal changes in surface processes in the Kyrgyz Tian Shan.

The results show that in the Issyk-Kul basin, the style of the river sediment accumulation changed at ~7 Ma, and aridification in the basin commenced concurrently. Lake formation commenced on the southern side of the basin at ~5 Ma, followed by a ~2 Ma local break in sediment accumulation. Directions of sedimentary deposition indicate that the Kungey range to the north of the basin grew eastward and caused intensification of sediment accumulation at 5-4 Ma in the easternmost part of the basin, which is reflected by an abrupt increase in grain size. Similar intensification of sediment accumulation occurred at 2.6-2.8 Ma on the southern side of the basin synchronously with the intensification of the Northern Hemisphere glaciations. The denudation rates from 2.7-2.0 Ma are as low as long-term exhumation rates, and only modern denudation rates record an acceleration of denudation.

This work concludes that the growth of the ranges to the north of the basin led to creation of the topographic barrier at ~7 Ma, which prevented moisture-bearing winds from penetrating into the Issyk-Kul basin, leading to aridification. Local tectonic activity on the southern side of the basin reorganized the river system and enabled lake formation at ~5 Ma, while eastward growth of the Kungey range blocked the connection of the Issyk-Kul basin with other eastern basins, leading to lake expansion.

Landscape modification of the Kyrgyz Tian Shan is slow due to aridity and only substantial cooling and glaciations during the latest glacial cycles led to notable acceleration of denudation. Currently, increased glacier reduction and river runoff controls a more rapid denudation of the northern slope of the Terskey range compared to other ranges of the Kyrgyz Tian Shan.

ALLGEMEINVERSTÄNDLICHE ZUSAMMENFASSUNG

Während der letzten ca. 66 Millionen Jahre veränderten die globale Abkühlung und das Wachstum der tibetischen Hochebene, des Tian Shan und des Pamirgebirges die atmosphärische Zirkulation und verringerten die Feuchtigkeitszufuhr nach Zentralasien. Diese Veränderungen führten zu einem trockenen und ariden Klima in der Region. Danach veränderten die Vergletscherungen der letzten ca. 2,6 Millionen Jahre die Landschaft und den Flussabfluss.

Im Issyk-Kul-Becken des Kirgisischen Tian Shan geben die Sedimentschichten Aufschluss über die Entwicklung der angrenzenden Gebirgszüge und die lokalen klimatischen Bedingungen. In dieser Arbeit rekonstruiere ich die Prozesse, die zu den klimatischen Veränderungen und der Entstehung der Seen geführt haben. Zu diesem Zweck beschreibe und datiere ich die Sedimentablagerungen und extrahiere Sauerstoff- und Kohlenstoffisotopendaten, die stellvertretend für die lokalen klimatischen Bedingungen stehen. Außerdem präsentiere ich Denudationsraten (heutige und aus der Zeit von vor 2,7 bis 2,0 Millionen Jahren) aus dem gesamten kirgisischen Tian Shan und langfristige (Millionen von Jahren) Exhumierungsraten, die aus veröffentlichten Daten berechnet wurden. Dies ermöglicht es mir, räumliche und zeitliche Veränderungen der Oberflächenprozesse im kirgisischen Tian Shan zu untersuchen.

Die Ergebnisse zeigen, dass sich im Issyk-Kul-Becken der Stil der Flusssedimentakkumulation vor ca. 7 Millionen Jahren veränderte und gleichzeitig eine Aridifizierung des Beckens einsetzte. Die Bildung von Seen begann auf der Südseite des Beckens vor ca. 5 Millionen Jahren, gefolgt von einer lokalen Unterbrechung der Sedimentakkumulation vor ca. 2 Millionen Jahren. Die Richtungen der Sedimentablagerung deuten darauf hin, dass das Kungey-Gebirge im Norden des Beckens nach Osten wuchs und vor 5-4 Millionen Jahren im östlichsten Teil des Beckens eine Intensivierung der Sedimentakkumulation bewirkte, was sich in einer abrupten Zunahme der Korngröße widerspiegelt. Eine ähnliche Intensivierung der Sedimentakkumulation fand vor 2,6-2,8 Millionen Jahren auf der Südseite des Beckens statt, zeitgleich mit der Intensivierung der Vergletscherung der Nordhemisphäre. Die Denudationsraten von vor 2,7-2,0 Millionen Jahren sind so niedrig wie die langfristigen Exhumierungsraten, und nur die modernen Denudationsraten zeigen eine Beschleunigung der Denudation.

Diese Arbeit kommt zu dem Schluss, dass das Wachstum der Gebirgsketten im Norden des Beckens zur Entstehung der topografischen Barriere vor ca. 7 Millionen Jahren geführt hat, die das Eindringen feuchtigkeitsführender Winde in das Issyk-Kul-Becken verhinderte und zur Aridifizierung führte. Lokale tektonische Aktivitäten auf der Südseite des Beckens führten zu einer Neuordnung des Flusssystems und ermöglichten die Bildung von Seen vor ca. 5 Millionen Jahren, während das östliche Wachstum des Kungey-Gebirges die Verbindung des Issyk-Kul-Beckens mit anderen östlichen Becken blockierte, was zur Ausdehnung der Seen führte.

Die Landschaftsveränderung im kirgisischen Tian Shan erfolgt aufgrund der Trockenheit nur langsam, und erst die starke Abkühlung und die Vergletscherung während der letzten Gletscherzyklen führten zu einer bemerkenswerten Beschleunigung der Denudation. Gegenwärtig wird die Denudation des Nordhangs des Terskey-Gebirges im Vergleich zu anderen Gebirgszügen des kirgisischen Tian Shan durch den verstärkten Gletscherschwund und den Flussabfluss beschleunigt.

Acknowledgements

First of all, I would like to thank my supervisors Edward Sobel and Alexandru Codilean for the guidance, support, patience, and encouragement. Every time I had obstacles in the way of my research and life, they helped me to find a solution and get back on track. I am very thankful to them for this fascinating project that expanded my knowledge of our planet enormously and let me achieve a very clear understanding of how closely everything and everyone is linked, even if it seems otherwise at first glance. And of course, I am very thankful for the opportunity they gave me to live and work in a beautiful Potsdam and wonderful Wollongong.

I am also very grateful to all my co-authors and colleagues for their help with field trips, lab work, discussions, and advice that helped me develop an all-round view of my research topic.

I am especially grateful to my family for their endless moral support and to our cats Marius and Olve for their unique stress relief qualities which helped me a lot over the years.

1 INTRODUCTION

1.1 OVERVIEW OF THE RESEARCH

My work is focused on the reconstruction of Cenozoic paleoclimatic changes in the Kyrgyz Tian Shan and the development of the Issyk-Kul basin (Figure 1.1). The main goal of the project is to decipher the relative importance of global and regional climatic changes, surface processes, and tectonic uplift shaping the Central Asian environment.

The most significant stages of the tectonic and climatic development of the Tian Shan and, more broadly, Central Asia occurred during the Miocene and Pliocene. The uplift of the Tibetan Plateau, Pamir, Tian Shan, and Altai mountains (e.g., Molnar & Tapponnier, 1975) occurred simultaneously with westward Parathetys retreat (e.g., Ramstein et al., 1997; Bosboom et al., 2017; Kaya et al., 2019) and global cooling (e.g., Herbert et al., 2016), changing atmospheric circulation and leading to aridification in Central Asia (e.g., Caves Rugenstein & Chamberlain, 2018), which led to changes in flora and fauna across the region (e.g., Barbolini et al., 2020).

Subsequently, the Plio-Pleistocene onset of glaciation and Quaternary glacial-interglacial cycles also affected the Central Asian climate and landscape development. Glacial erosion modifies topography, and associated changes in the hypsometry of the landscape influence the relationships between climate and glacial extent by enabling rapid and nonlinear glacial growth (Pedersen & Egholm, 2013). Ice and snow accumulation affect river runoff, particularly during interglacial periods. Moreover, Pleistocene moisture variability caused by the interplay between high topography in Central Asia and air masses influenced Siberian rivers discharge and their ability to transfer fresh water to the Arctic Ocean (Prud'homme et al., 2021).

At present, Central Asia is the largest arid region in the Northern Hemisphere, accommodating millions of people living in Kazakhstan, Kyrgyzstan, Uzbekistan, Tajikistan, Turkmenistan, Afghanistan, western China, and Mongolia (Figure 1.1A), who depend on the regional climatic conditions and water resources. Aridity controls vegetation and water availability, and glacial retreat due to climatic changes raises concern about the future of the region (Chen et al., 2022a). The Miocene and Pliocene periods are considered the best analogues for future climatic conditions (Burke et al., 2018; Steinthorsdottir et al., 2021). Studying the Cenozoic development of the landscape and climate in Central Asia is, therefore, essential for understanding moisture transfer in Eurasia and estimation of future climatic changes on the continent.

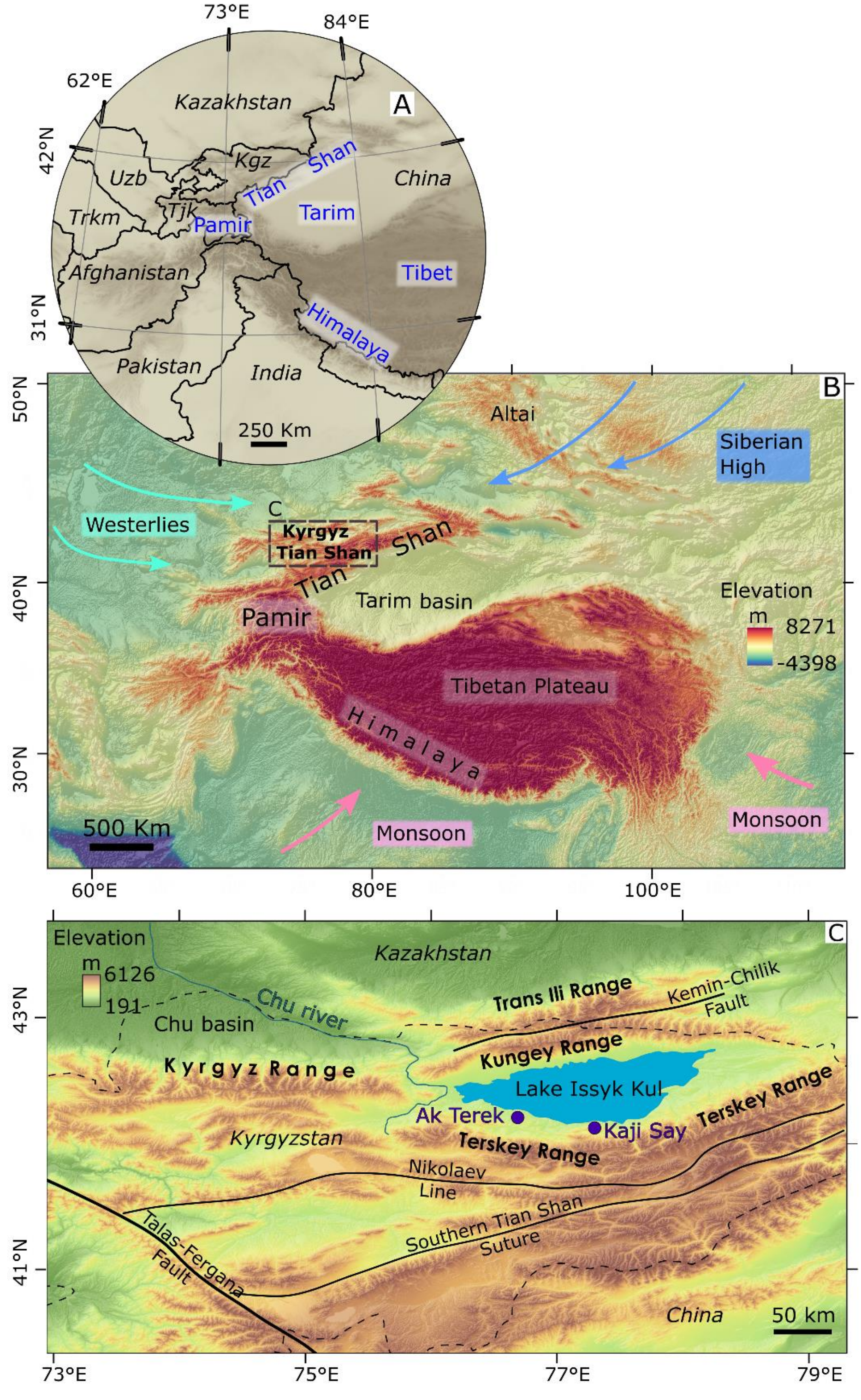

Figure 1.1. Topographic maps of Central Asia and the Kyrgyz Tian Shan based on SRTM90 digital elevation data. (A) Map of Central Asia with countries and major topographic features. Kgz – Kyrgyzstan; Tjk – Tajikistan; Uzb – Uzbekistan; Trkm – Turkmenistan. (B) Map of Central Asia showing major ranges and major atmospheric circulation directions. Light blue arrows – westerly winds; dark blue arrows – Siberian High; pink arrows – monsoons. (C) Topographic map of the Kyrgyz Tian Shan showing the main ranges and faults, the north-flowing Chu river, country borders (dashed line), and locations of the Ak Terek and Kaji Say sedimentary sections.

In this study, I focus on the Kyrgyz part of the Tian Shan range (Figures 1.1B-C). Together with other active mountain ranges in Central Asia, the Tian Shan was created due to reactivation of Palaeozoic structures by the Cenozoic India-Asia collision (Molnar and Tapponnier, 1975). The Kyrgyz Tian Shan is a perfect area for studying tectonic-climatic interactions because this range is situated in the north-western part of Central Asia (Figure 1.1B), creating an immediate topographic barrier in the way of the moisture-bearing westerly winds, enhancing aridification in Central Asia (Baldwin & Vecchi, 2016), and ultimately leading to desertification of the Tarim basin (Heermance et al., 2018; Richter et al., 2022).

This work emphasises the importance of studying the tectonic-climatic interactions within the range and particularly in the Issyk-Kul basin (Figure 1.1C). The internally-drained intermontane Issyk-Kul basin hosts a large lake and is mainly fed by meltwater from snow and glaciers of the Terskey and Kungey ranges (Aizen et al., 1995). The lake formed while the basin and the whole Kyrgyz Tian Shan experienced intensive aridification, creating a unique environment. The basin contains late Mesozoic - Cenozoic sedimentary deposits (Abdrakhmatov et al., 2001), which record information about local climatic conditions, tectonic activity, and lake-level fluctuations. Therefore, by studying these deposits, we are able to obtain information about the development of the basin and the adjacent ranges and interactions with global climatic changes.

Previously, the late Oligocene – late Miocene (ca. 25-8 Ma) Issyk-Kul basin deposits have been dated using magnetostratigraphy (Wack et al., 2014) and the first paleoclimatic record was provided for these deposits using stable $\delta^{18}O$ and $\delta^{13}C$ isotopes (Macaulay et al., 2016). In this study we aim to complete the Cenozoic record of the Issyk-Kul basin by providing the first magnetostratigraphic age models, $^{26}Al/^{10}Be$ isochron burial ages, and paleoclimatic records using stable $\delta^{18}O$ and $\delta^{13}C$ isotopes for the late Miocene – early Pleistocene sedimentary deposits. We also examine the landscape development by discussing spatial and temporal variability of surface processes in the Kyrgyz Tian Shan and particularly in the Terskey range and their interactions with tectonic activity and climatic changes. In order to do this, we provide a dataset of modern ^{10}Be-derived denudation rates from across the Kyrgyz Tian Shan, ^{10}Be-derived paleo-denudation rates from the Issyk-Kul basin, and long-term exhumation rates calculated from published thermochronology data.

We collected samples for magnetostratigraphic dating, $^{26}Al/^{10}Be$ isochron burial dating, and stable isotope analysis during the field seasons in 2016 and 2017. During the 2016 field season, we also collected samples for the study of denudation rates, which constitute a part of the whole dataset. This dataset of modern ^{10}Be-derived denudation rates was kindly provided by Dr. Angela Landgraf and Dr. Alexandru Codilean for interpretation and publication. We aimed to collect samples from as many late Miocene – early Pleistocene sedimentary sections around the lake Issyk-Kul as possible. However, due to poor quality of outcrops and scarce availability of material suitable for sampling and analysis, I was able to provide detailed description and study of only two stratigraphic sequences on the southern side of the basin. These sequences provide valuable information related to the development of the Terskey range, local climatic conditions, and commencement of lake formation.

The study and analysis of the magnetostratigraphic record was primarily conducted by Dr. Sophie Roud, Prof. Stuart Gilder, and Dr. Michael Wack. I prepared the samples for stable isotope analysis; measurements were performed at the Joint Goethe University–Senckenberg BiK-F Stable Isotope Facility at Goethe University Frankfurt, Germany in collaboration with Prof. Andreas Mulch and Prof. Maud Meijers. I prepared samples for ^{26}Al/^{10}Be isochron burial dating in both Potsdam and during my 3-month and 14-month stays in Wollongong; analyses were conducted at the University of Wollongong, Australia, and the Australian Nuclear Science and Technology Organisation (ANSTO). Measurements for the ^{10}Be denudation rates were conducted at ANSTO and the AMS facility DREAMS, Dresden. The results are discussed in the following chapters, two of which are peer-reviewed and published in the journals Geochemistry, Geophysics, Geosystems and Basin Research, and one is submitted to the Journal of Geophysical Research: Earth Surface. In chapters 3-4, I refer to the publications instead of chapters: chapter 2 is referred to as Roud et al. (2021), chapter 3 is referred to as Kudriavtseva et al. (2023).

1.2 Thesis outline

1.2.1 Chapter 2: Miocene to early Pleistocene depositional history and tectonic evolution of the Issyk-Kul basin

In chapter 2, we present a magnetostratigraphic age model for the sedimentary section Ak Terek in the southwestern part of the Issyk-Kul basin, and we propose two magnetostratigraphic age models for the section Kaji Say further east (Figure 1.1C). Previously, lithostratigraphic correlation with deposits in the neighboring Chu basin suggested a late Miocene – early Pliocene age for the Issyk-Kul sediment accumulation, and this work provides the first relatively robust age models based on the Issyk-Kul basin data.

The Ak Terek age model suggests sedimentation between 6.3 and 2.8 Ma. The two Kaji Say models suggest very different ages and depositional environments for the sequence: one suggests continuous sedimentation from 12.7 to 9.5 Ma, while the second one suggests sediment accumulation from 7.0 to 5.1 Ma and from 3.0 to 2.4 Ma with a ca. 2 Myr hiatus. At this point it was impossible to suggest which of the two options was more plausible. However, the advantage of the second option is that it places the transition from fine-grained to coarse-grained deposits in the Kaji Say section to the same time interval as the age model of the Ak Terek section. Additionally, in this chapter we reevaluate magnetostratigraphic age models for older deposits in the eastern part of the basin previously described by Wack et al. (2014). These previously published age models showed inconclusive results because of ambiguous polarity intervals.

This work allowed us to date transitions between sedimentary groups of the Issyk-Kul basin, estimate sedimentation rates, and describe Miocene-Pliocene tectonic development of the Terskey range. Inconclusive results of the magnetostratigraphic dating of the Kaji Say section raise a question of precise timing of sediment accumulation there, which we discuss in the next chapter.

1.2.2 Chapter 3: Neogene aridification and lake development in the Issyk-Kul basin

Chapter 3 further develops the study of the sedimentary sequences in the Issyk-Kul basin. This work is based on detailed descriptions of the Ak Terek and Kaji Say sedimentary sections. We provide $^{26}Al/^{10}Be$ isochron burial ages for the upper parts of both sections. These results support the Ak Terek magnetostratigraphic age model and allow us to choose one of the age models for the Kaji Say section. The chosen Kaji Say age model suggests a ca. 2 Myr depositional hiatus in the middle of the section occurring simultaneously with commencement of lake formation. Therefore, we provide an explanation for existence of the hiatus in a tectonically active region. We also provide the first paleoclimatic record for the late Miocene – early Pleistocene deposits based on stable $\delta^{18}O$ and $\delta^{13}C$ isotope data from the Ak Terek and Kaji Say sections. This record suggests that aridification in the basin started at ca. 7 Ma. As there were no significant global climatic changes at this time, we suggest that local tectonic activity is responsible for this environmental change, which was later amplified by global climatic changes. Furthermore, we discuss how the lake formed in arid climatic conditions.

This chapter provides a comprehensive description of the environmental development of the Issyk-Kul basin and surrounding ranges in the late Miocene – early Pleistocene due to local tectonic activity and global climatic changes. However, we were not able to fully clarify the timing of sediment deposition in the Kaji Say section because the samples for the $^{26}Al/^{10}Be$ isochron burial dating of the basal part of the section did not provide any reliable results. Therefore, the question remains whether the proposed depositional hiatus existed as described.

1.2.3 Chapter 4: Impact of Quaternary glaciations on denudation rates in the Kyrgyz Tian Shan inferred from cosmogenic ^{10}Be and low-temperature thermochronology

In chapter 4 we discuss denudation and exhumation rates at different timescales within the Kyrgyz Tian Shan. These data reflect different surface processes that shaped the landscape during the Cenozoic. A combination of 54 millennial-timescale ^{10}Be-derived denudation rates from across the Kyrgyz Tian Shan with three ^{10}Be-derived denudation rates from 2.7-2 Ma from the southern Issyk-Kul basin, as well as with 421 long-term exhumation rates derived from published thermochronology data provides an insight into spatial and temporal variability of denudation in the Kyrgyz Tian Shan. The data show that the Plio-Pleistocene onset of Northern Hemisphere glaciations did not significantly affect denudation in the Terskey range, but Pleistocene glacial-interglacial cycles led to a widespread increase in denudation after substantial cooling and growth of the glacial cover. We show that tectonic activity notably but temporarily affects exhumation rates in the Kyrgyz range, situated in the northwestern part of the Kyrgyz Tian Shan (Figure 1.1C), due to rapid exhumation of the sediments, which covered the area before surface uplift. Our data also show relatively fast modern denudation of the Terskey range due to intensive glacier melting compared to the rest of the Kyrgyz Tian Shan. We compare our data with published ^{10}Be-derived denudation rates from the parts of the Tian Shan to the west and to the east from our study area. We show a west to east decreasing trend and suggest that enhanced deformation in the Pamir and Western Tian Shan controls denudation there, erasing the glacial signal, while further east, the intensity of deformation decreases and the influence of global climate and local factors increases.

In summary, this chapter shows that in the Kyrgyz Tian Shan surface processes are mainly controlled by local factors, while on a regional scale only substantial environmental changes triggered by global climate affect denudation.

1.2.4 Chapter 5: Discussion and conclusions

Chapter 5 summarizes the conclusions of each chapter and provides an integrated view of environmental development of the Issyk-Kul basin and the entire Kyrgyz Tian Shan in relation to tectonic activity in the range and climatic changes.

1.3 Publication and author contribution

For the study discussed in chapter 2, magnetostratigraphic analysis was done by Dr. Sophie Roud, Prof. Stuart Gilder, and Dr. Michael Wack based on my descriptions and sedimentological analysis of the Kaji Say and Ak Terek sedimentary sequences. I participated in sample collection and data discussion and interpretation by providing information about the depositional environment in the Issyk Kul basin. The text was drafted by Dr. Sophie Roud and refined by all coauthors. This work is published as: Roud, S.C., Wack, M.R., Gilder, S.A., Kudriavtseva, A., & Sobel, E.R. (2021). Miocene to Early Pleistocene Depositional History and Tectonic Evolution of the Issyk-Kul Basin, Central Tian Shan. *Geochemistry, Geophysics, Geosystems*, *22*(4), e2020GC009556. https://doi.org/10.1029/2020GC009556

For the study discussed in chapter 3, I described the sedimentary sequences, participated in sampling, sample preparation, analytical work, and interpretation of the results. I drafted the manuscript, which was then refined by all coauthors. Also, I refined the text according to comments provided by reviewers during the peer-review process. This work is published as: Kudriavtseva, A., Sobel, E.R., Codilean, A.T., Meijers, M.J.M., Mulch, A., Hoke, G.D., Fink, D., Mikolaichuk, A.V., Fülöp, R.-H., Wilcken, K.M., & Enge, T.G. (2023). Neogene aridification and lake development in the Issyk-Kul basin, Kyrgyzstan. *Basin Research*, *00*, 1– 35. https://doi.org/10.1111/bre.12751

For the study discussed in chapter 4, I interpreted the data and participated in sampling, sample preparation, and analytical work for the ^{10}Be-derived paleo-denudation rates analysis. Sampling for modern ^{10}Be-derived denudation rates was conducted mainly by Dr. Angela Landgraf and Dr. Alexandru Codilean. I drafted the manuscript, which was then refined by all coauthors. This manuscript has been submitted to the Journal of Geophysical Research: Earth Surface as: Kudriavtseva, A., Codilean, A.T., Sobel, E.R., Landgraf, A., Fülöp, R.-H., Dzhumabaeva, A., Abdrakhmatov, K., Wilcken, K.M., Schildgen, T., Fink, D., Fujioka, T., Rosenwinkel, S., Merchel, S., Rugel, G. Impact of Quaternary glaciations on denudation rates in the Kyrgyz Tian Shan inferred from cosmogenic ^{10}Be and low-temperature thermochronology.

Potsdam, March 21, 2023 ……………………………………

Date Signature principal advisor

2 Miocene to early Pleistocene depositional history and tectonic evolution of the Issyk-Kul basin, Central Tian Shan

Sophie C. Roud, Michael R. Wack, Stuart A. Gilder, Anna Kudriavtseva, & Edward R. Sobel

Abstract

The Issyk-Kul basin (Kyrgyzstan), situated in the central Tian Shan Mountains, hosts the largest and deepest mountain lake in Central Asia. Erosion of the surrounding Terskey and Kungey ranges led to the accumulation of up to 4 km of sediment in the adjacent depression. Creation of the basin from regional shortening and uplift likely initiated around the Oligocene-Miocene, yet precise age control is sparse. To better understand the timing of these processes, we obtained magnetostratigraphic age constraints on fossil-poor, fluvio-lacustrine sediments exposed south of lake Issyk-Kul, that agree well with previous age constraints of the equivalent strata outside the Issyk-Kul basin. Two 500–650 m thick sections comprised mainly of Chu Group sediments were dated at 6.3–2.8 Ma and 7.0–2.4 Ma (late Miocene to early Pleistocene). Together with reinterpreted magnetostratigraphic constraints from underlying strata, we find that syn-tectonic deposition commenced at ca. 22 Ma with average sedimentation rates <10 cm ka^{-1}. Sedimentation rates increased to 10–30 cm ka^{-1} at 7 Ma, concurrent with accelerated uplift in the Terskey Range to the south. A deformation event in one section (Kaji-Say) between 5 and 3 Ma together with concurrent shifts of depositional centers throughout the basin signal the onset of substantial uplift of the Kungey Range to the north at ca. 5 Ma. This uplift and deformation transformed the Issyk-Kul area into a closed basin that facilitated the formation of a deep lake. Lacustrine facies deposited around 3 Ma mark the existence of lake Issyk-Kul by that time.

2.1 Introduction

2.1.1 Regional geology

The Tian Shan mountains comprise a 2500-km-long orogenic belt in Central Asia. Ongoing uplift of the range is driven by the India-Asia collision. Although located 1500 km north of the India-Asia plate boundary, the Tian Shan currently accommodate about 20 mm yr^{-1} of north-south shortening, which is equivalent to nearly two-thirds of the total convergence between India and Asia (Zubovich et al., 2010). Mountain building in Central Asia initiated along reactivated Paleozoic structures in the late Oligocene, creating vast basins that were subsequently dissected by younger ranges (Sobel & Dumitru, 1997; Buslov et al., 2003; Macaulay et al., 2014).

The Issyk-Kul basin is one of the largest intermountain basins in the Tian Shan realm, bounded by the Kungey range to the north and the Terskey range to the south (Figure 2.1) with maximum peak heights of 4.8 and 5.2 km, respectively. The basin contains up to 4 km of Cenozoic sediments (Turchinskiy, 1970; Buslov et al., 2003) that record the uplift and erosion history of the surrounding mountain ranges. Unroofing of the Terskey range commenced around the Oligocene-Miocene boundary between 26 and 20 Ma based on thermochronologic cooling ages (De Grave et al., 2013; Macaulay et al., 2013, 2014) and on the onset of sediment deposition in the adjacent Issyk-Kul basin (Wack et al., 2014). The initial uplift phase was followed by a second phase of rapid basement cooling after 10 ± 5 Ma when deformation of the Terskey range propagated northward, creating the Issyk-Kul Broken Foreland (Macaulay et al., 2013, 2014). Uplift of the youngest ranges initiated in the Plio-Pleistocene. Unroofing of the Kungey range that led to the closure of the Issyk-Kul basin is loosely estimated to ca. 7–4 Ma based on sediment provenance data (Selander et al., 2012).

To better resolve the uplift history of the Central Tian Shan around the Issyk-Kul basin, we collected Cenozoic sediments at two sections, Ak Terek and Kaji Say (Figure 2.1), in the southern rim of the basin in 2016 and 2017 to constrain the age, sedimentation rate and the depositional environment. Here, we describe the geologic setting, the rock magnetism and magnetostratigraphy of the sections. We then discuss the new and existing magnetostratigraphic age constraints from the Issyk-Kul basin, and place our results in the larger context of the tectonic evolution of the area.

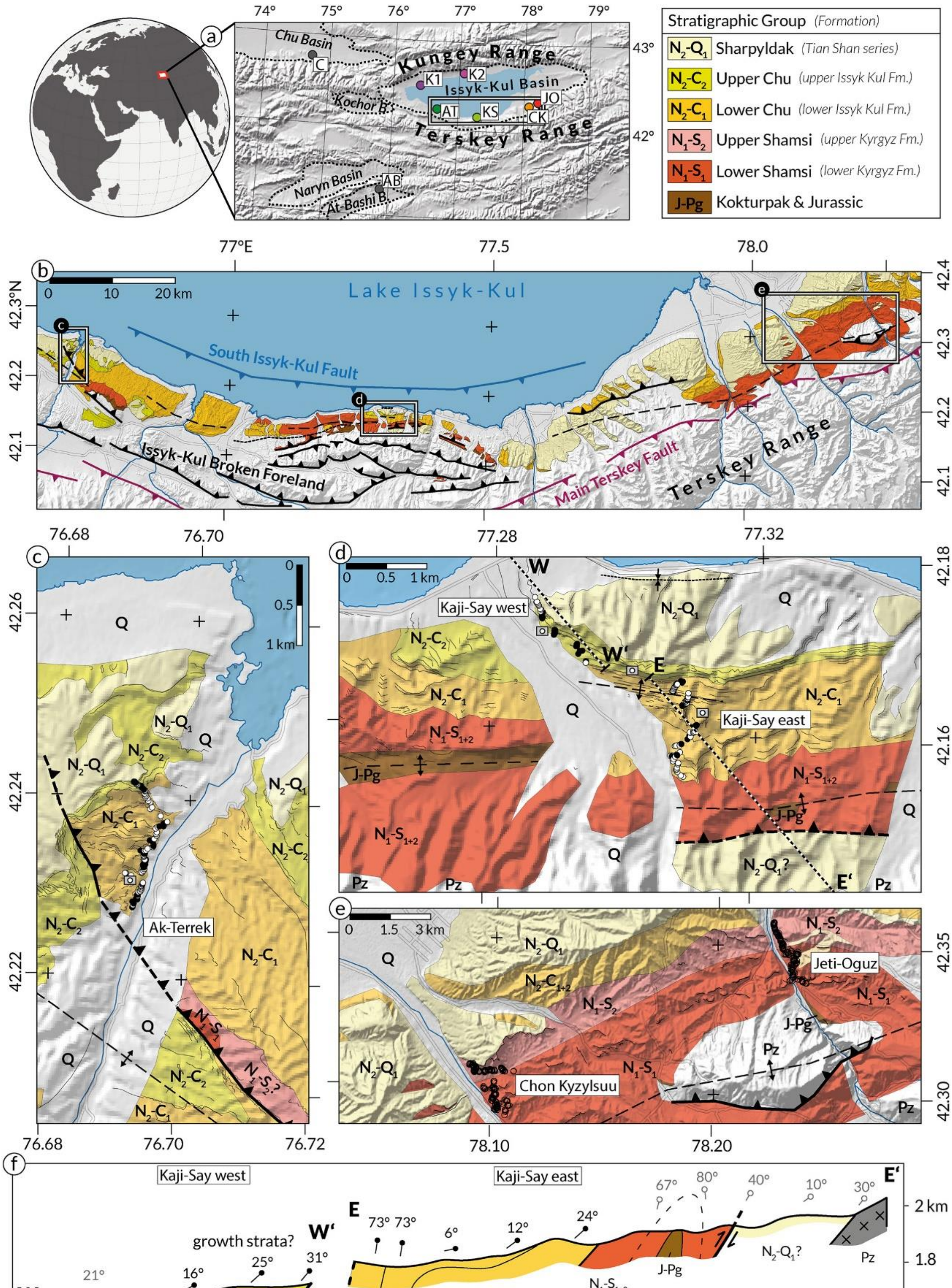

Figure 2.1. Geologic overview of the study area at lake Issyk-Kul (Central Tian Shan, Kyrgyzstan). (a) General location map. Names and abbreviations in white boxes denote locations of new and previously studied stratigraphic sections as follows: (C) Chu, (AB) At Bashi, (K1) Toru Aygir, (K2) Cholpon Ata, (AT) Ak Terek, (KS) Kaji Say, (CK) Chon Kyzylsuu and (JO) Jeti Oguz. (b) Geology of the southern Issyk-Kul basin with mapped sedimentary units (see legend and text for details), major faults (thick lines) and folds (thin lines, anticlines dashed, synclines dotted). Geologic and structural information were mapped from satellite images, a digital elevation model, Burgette (2008), Macaulay et al. (2013; 2014; 2016) and Korzhenkov and Deev (2017). Rectangles show locations of maps (c)–(e); units corresponding to the

legend: Q, Quaternary; N, Neogene; 1, lower, 2, upper; Pg, Paleogene, J, Jurassic; Pz, Paleozoic basement. Filled circles in (c) and (d) indicate paleomagnetic sample locations of this study (black = normal polarity and white = reversed polarity). Circles in (e) show sample locations from Wack et al. (2014). Projection (b)–(e): Pulkovo 1942/Gauss-Kruger zone 14. (f) Cross-section through the western (W-W′) and eastern transect (E-E′) at Kaji Say (2:1 vertical exaggeration); bedding attitudes outside the magnetostrigraphic section from Burgette (2008). Camera symbols show locations where the field photos in Figure 2.2 were taken.

2.1.2 Local geology and stratigraphy

Cenozoic sediments in the Central Tian Shan can be divided into four main lithologic groups. These are, from oldest to youngest, the Kokturpak, Shamsi, Chu, and Sharpyl Dak groups (Abdrakhmatov et al., 2001). All four groups are exposed in the southern Issyk-Kul basin, where we mapped their extent with satellite images (Bing Maps and Sentinel 2, Bands 12-4-2) using QGIS software (Figure 2.1). Outside our study area, we also referred to Soviet geological maps (Turchinskiy, 1970; Pomazkov, 1971) and the PhD thesis of Burgette (2008).

The Kokturpak group represents pre-orogenic sediments. It comprises deeply weathered paleosols, thin lacustrine deposits and reddish sandstones that formed in shallow, low-relief areas above the Paleozoic basement or above locally preserved Jurassic deposits (Fortuna et al., 1994). In the Issyk-Kul basin, the Kokturpak group reaches up to 100 m in thickness (Selander et al., 2012). The age is loosely constrained as late Cretaceous to Eocene (Fortuna et al., 1994; Sobel & Arnaud, 2000). Kokturpak and Jurassic sediments were combined in our geologic maps (Figure 2.1, J-Pg); these are identified as white and yellow layers that cover basement rocks and/or by resistant red horizons that crop out in the cores of anticlines (Figures 2.1D-E).

The Shamsi group represents the basal, syn-orogenic sediments (locally called the Kyrgyz or Dzhety Oguz formation) overlying the Kokturpak group. In the Issyk-Kul basin, these deposits consist of poorly sorted sandstone and conglomerate with a characteristic red pigment near the base that fades toward the top. In the vicinity of the Terskey Range (CK and JO in Figure 2.1A), the ca. 1-km-thick sections were magnetostratigraphically dated between 26 and 11 Ma (Wack et al., 2014). We mapped the Shamsi unit in Figure 2.1 based on its distinctive red color and strong reflectance in the Sentinel bands 12 and 4. In the eastern part of the basin, the Shamsi group can be subdivided into a lower (N_1-S_1, red) and upper (N_1-S_2, light red) unit based on a characteristic decrease in red pigment (Figure 2.1E). The similar appearance of lower Shamsi and upper Kokturpak groups made it sometimes ambiguous to distinguish them on the aerial images.

The Shamsi group grades upward into lighter, more fine-grained strata of the Chu group, which consists of white to tan sandstone and siltstone, intercalated with conglomerate. The Chu group is often described as the main basin-filling unit, with thicknesses up to 2.5 km reported in the Naryn basin (Goode et al., 2011), 1.5 km in the Chu basin (Bullen et al., 2001) and 3 km in the At-Bashi basin (Abdrakhmatov et al., 2001). In the latter two, the Chu group was magnetostratigraphically dated between 7.5 and 3.0 Ma (Abdrakhmatov et al., 2001; Bullen et al., 2001). Selander et al. (2012) reported a maximum thickness of 600 m in the northern Issyk-Kul basin. This unit was mapped based on its tan color at the base that fades toward the top and possesses alternating lighter and darker horizons. Where possible, we differentiated between lower Chu (dominantly darker tones; mapped as N_1C_1) and upper Chu (highly reflective, grayish beds; mapped as N_1C_2; Figures 2.1B-D).

Poorly sorted, coarse conglomerates of the Sharpyl Dak group overlie the Chu group, with the contact being sometimes gradual and sometimes unconformable, indicating that locally, deformation has occurred prior to deposition of the conglomerates. The basal age of the Sharpyl Dak group was dated to ca. 5–3 Ma in adjacent basins (Abdrakhmatov et al., 2001; Bullen et al., 2001). We mapped the Sharpyl Dak deposits (N_2-Q_1) based on their bright gray appearance without visible bedding structures. The Sharpyl Dak conglomerates are locally covered by lacustrine deposits and river terraces that formed in response to lake level variations and glaciation events during the Quaternary (Burgette et al., 2017). We did not map these youngest features (Q in Figures 2.1C-E) in detail. The distinction between Sharpyl Dak conglomerates and Quaternary terraces in Figure 2.1 was primarily based on topography.

The major tectonic structures in Figure 2.1 were adapted from Burgette (2008), Macaulay et al. (2013, 2014, 2016), and Korzhenkov and Deev (2017) and mapped on a 30″ (arcsec) digital surface model (Tadono et al., 2015) that is shown as topographic shading in all maps. The two major thrust faults are the north-vergent South Issyk-Kul Fault and the Main Terskey Fault. The Issyk-Kul Broken Foreland, north of the Main Terskey Fault, is dominated by secondary south-vergent reverse faults that thrust Cenozoic sediments over basement rocks (Burgette, 2008; Macaulay et al., 2014; Korzhenkov & Deev, 2017), thereby producing E-W striking folds in the southern Issyk-Kul basin. Anticlines with gently tilted northern and steep southern limbs are typically thrust up along reverse faults (Buslov et al., 2003; Figure 2.1F).

2.2 Sections and sampling

2.2.1 Ak Terek section

The Ak Terek section was sampled on the west side of the Ak Terek river valley, spanning 500 m in stratigraphic height (Figures 2.1C, 2.2A, and 2.3A). Figure 2.3A includes a stratigraphic column of the section that can be subdivided into three lithologic units (AT-1 to AT-3). The lower part (AT1) contains alternating sand and silt layers intercalated with conglomerate. Above ca. 230 m, fine massive sandstones become dominant (AT2). Above 324 m, the number of conglomerate layers, sporadic calcareous deposits and paleosols increase (AT3). A 30-cm-thick gypsum layer was found at 430 m. Massive conglomerates above ca. 500 m mark the conformable transition from Chu to Sharpyl Dak deposits. Bedding dips gradually flatten from 21° at the base to 5° at the top, reflecting regional scale folding or growth strata. No major discontinuity, unconformity, or fault was observed in the section.

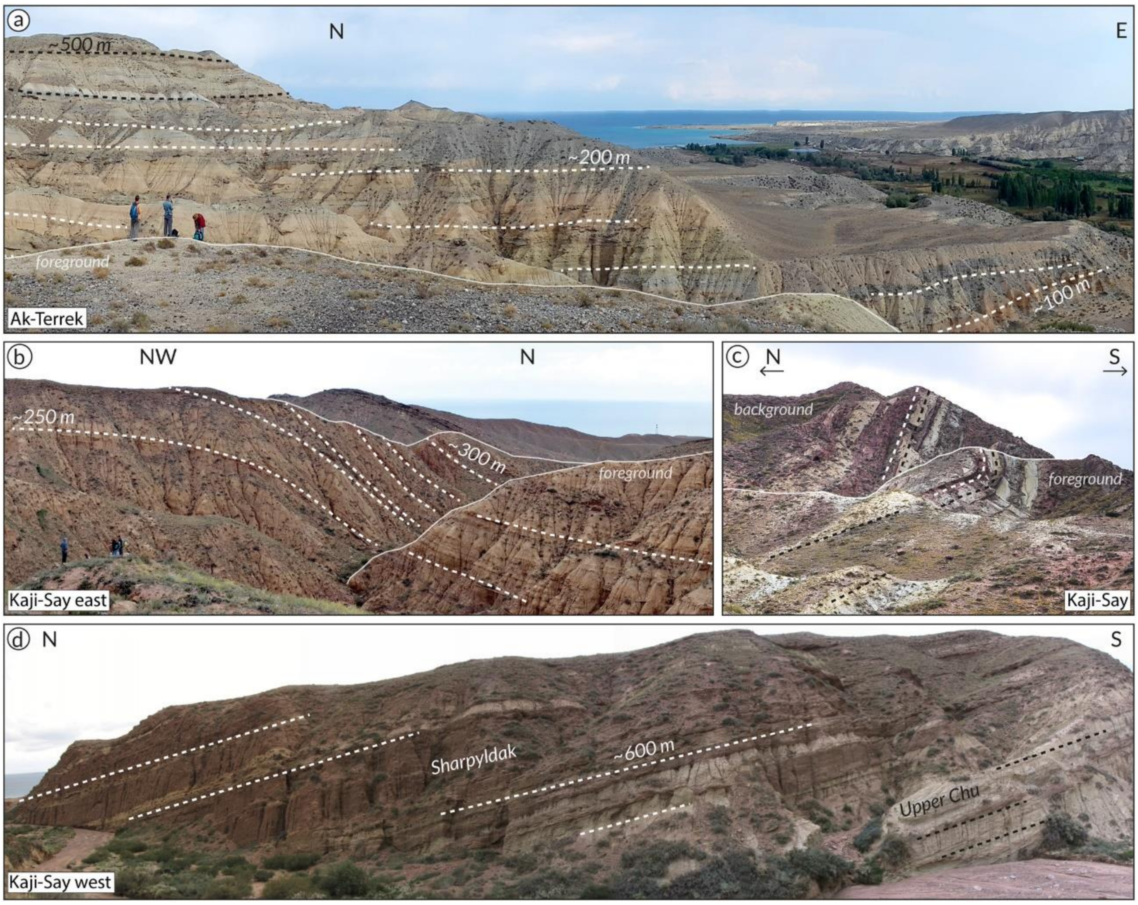

Figure 2.2. Field photos of the Ak Terek (AT) and Kaji Say (KS) sections. (a) Upper ca. 400 m of the AT section; view to the north with lake Issyk-Kul in the background; dashed lines highlight bedding structures and numbers indicate approximate stratigraphic heights. (b) Panorama of the eastern part of the KS section with bedding attitudes steepening from nearly horizontal to >70° above ca. 250 m. (c) Syncline structure between the eastern and western parts of KS (d) Panorama of the Chu-Sharpyl Dak

contact in the western part of the KS section. See Figure 2.1 for the locations where the photos were taken.

We collected two oriented paleomagnetic cores per horizon (302 in total), generally selecting fine-grained mud or silt layers. The lower 200 m of the section were sampled along the Ak Terek river valley in ca. 2 m intervals. The coarser grained upper 300 m of the section were sampled every 7 m on average, following tributaries away from the river valley. Samples were obtained using a battery-powered, water or air-cooled drill; poorly lithified strata were sampled with a handheld push corer that we manufactured for this purpose. The corer injects the extracted, oriented sediment directly into plastic cylinders of the same dimension as standard paleomagnetic specimens (2.5 cm diameter, 2.2 cm height). All samples were oriented with a magnetic and, when possible, with a sun compass using a Pomeroy orientation tool. The average anomaly from 58 sun compass readings was 4.0° ± 2.5°, in good agreement with the International Geomagnetic Reference Field (IGRF) declination anomaly of 4.6°, which we used to correct the declination azimuths of all samples.

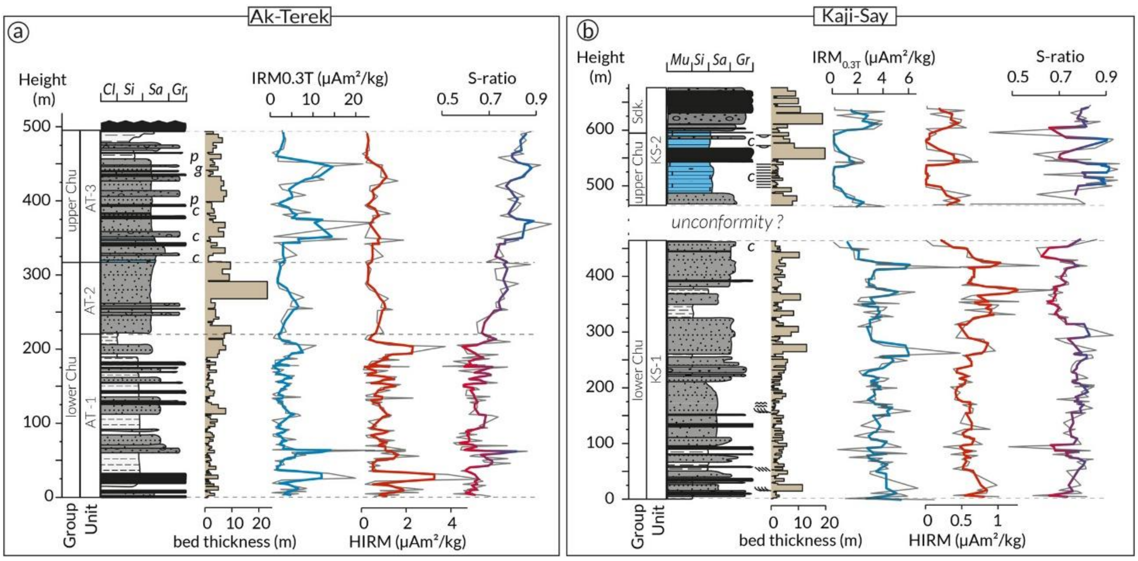

Figure 2.3. Summary of sedimentologic and rock magnetic data of the Ak Terek (a) and Kaji Say (b) sections. Lithologic columns show fluvial beds in gray scale; lacustrine carbonates in blue, with dominant grain size of clay (Cl), mud (Mu), silt (Si), sand (Sa) and gravel (Gr). Letters indicate: p, paleosol; c, carbonate; g, gypsum. Groups correspond to the lower and upper Chu and Sharpyl Dak (Sdk.) groups mapped in Figure 2.1; Units (AT-1 to AT-3 and KS-1 to KS-2) defined based on prominent changes in the lithologic and rock magnetic parameters. Parameters left to right: bed thickness, $IRM_{0.3T}$ reflecting magnetite concentration, HIRM reflecting hematite concentration and S-ratio reflecting relative magnetite to hematite proportions.

2.2.2 Kaji Say section

The Kaji Say section is located 10 km northeast of Kaji Say village and spans 650 m in stratigraphic height. We sampled the section along two transects, west and east

(Figures 2.1D and 2.1F). Bedding dips in the eastern transect are ca. 25° (N) at the base of the section (0 m) and flatten to horizontal at around 225 m height. After 245 m the beds abruptly dip ca. 75° (N), defining an asymmetric anticline with its axis striking E-W (Figure 2.2B). The beds remain steeply dipping (ca. 75°) until the top of the eastern transect at 464 m. Farther north of these sites, the steeply dipping beds disappear under Sharpyl Dak conglomerates. Following 1 km along strike to the west (western transect), the Chu beds dip more gently around 30° (N) (Figure 2.2D) shallowing to ca. 15° (N) toward the top of the section. The beds thicken to the northwest and pinch out to the southeast, which could indicate the presence of growth strata.

We could not follow individual beds between the eastern and western transects. The change in dip from ca. 75° in the eastern section to ca. 30° in the western section could signal an unconformable surface thereby suggesting the section was folded prior to the deposition of the upper unit, with a hiatus between the two. The postulated unconformable surface likely strikes E-W, parallel to the strike of the strata, which would explain why we did not identify it on the ground or in aerial images. An alternate interpretation that we cannot rule out is that a syncline observed between the two transects (Figure 2.2C) connects the steeply dipping (ca. 75°) units in the east to the shallow-dipping (ca. 30°) units in the west.

Fluvial deposits of alternating sand, silt, and mudstone layers intercalated with conglomerates characterize the lower, eastern part of the section (Figure 2.3B, KS-1). At the top of this transect, between 440 and 460 m, we identified two, < 0.5 m thin calcareous interbeds. Along the western transect, the sediments consist mostly of fine-grained calcareous silt, and carbonates that alternate with laminated silt or mudstone, and rippled or cross-bedded sandstone (Figure 2.3B, KS-2). The up to 9 m thick calcareous, partially laminated beds indicate lacustrine deposition. The number and thickness of interbedded coarse conglomerates increases above ca. 550 m, marking the transition between Chu and Sharpyl Dak style deposits (Figure 2.2D); above 600 m the section is dominated by Sharpyl Dak conglomerates.

Paleomagnetic samples were collected in approximately 2 m intervals, taking two oriented cores per horizon (312 in total) and selecting fine grained mud or silt when possible. In contrast to Ak Terek, most strata in this section were poorly lithified. We obtained drill cores from 15 horizons, while 297 horizons were sampled with the push corer. Therefore, samples from Kaji Say were predominantly contained within plastic cylinders. The average anomaly from 156 Sun compass readings was 4.2° ± 2.3°, again in good agreement with the IGRF declination anomaly of 4.5°.

2.3 PALEO AND ROCK MAGNETIC CHARACTERIZATION

2.3.1 LABORATORY METHODS

Because the majority of the samples were contained in plastic cylinders that prevented thermal treatment, we subjected one sample of each horizon to stepwise alternating field (AF) demagnetization. In case of unstable trajectories, or if polarity intervals were defined by a single specimen, a second sample was AF demagnetized. In addition, samples from all 15 drilled horizons from Kaji Say and from 23 of the drilled sites from Ak Terek were thermally demagnetized using 14 heating steps to compare against the AF demagnetization data. AF demagnetization (16 steps up to 90 mT) and magnetic moment measurements were conducted inside a magnetically shielded room (ca. 500 nT) using an automated measurement system (SushiBar) based on a 2G Enterprises, three-axis superconducting magnetometer (Wack & Gilder, 2012). Characteristic remanent magnetizations were determined by principal component analysis (Kirschvink, 1980) and mean directions were calculated with Fisher statistics (Fisher, 1953) using the software PaleoMac (Cogné, 2003).

Rock magnetic parameters were measured on at least one sample per horizon to determine magnetic mineralogy and grain size variations throughout both sections. We measured magnetic susceptibility (χ), anhysteretic remanent magnetization (ARM) with a peak alternating field of 90 mT and a 0.1 mT bias field and calculated the ARM/χ ratio as a proxy for grain size and/or mineralogic changes (King et al., 1982). Subsequently, a 1 T isothermal magnetic remanence (IRM) followed by a back field IRM of -0.3 T were measured in order to calculate the S-ratio (Bloemendal et al., 1992), which is a proxy for the relative hematite to magnetite concentration. We further determined the low coercivity component ($IRM_{0.3T}$) and the high coercivity component (HIRM) representative of the magnetite and hematite concentrations, respectively (e.g., Liu et al., 2012).

2.3.2 ROCK MAGNETIC ANALYSES

Thermal demagnetization experiments indicated that both sections contain two magnetic phases: one that unblocks between 300°C and 580°C, suggestive of magnetite with variable titanium concentrations and another whose magnetic remanence persists to ca. 680°C, indicative of hematite (Figures 2.4A-B, S2.1 and S2.2). At Ak Terek, the magnetic mineralogy changes midsection, as indicated by an increase in the S-ratio from an average of 0.65 below 200 m (AT1) to 0.82 above 300 m (AT3) (Figure 2.3A), signifying a decrease in relative hematite contribution with increasing stratigraphic height. HIRM and $IRM_{0.3T}$ show that this trend is linked to a decrease in hematite concentration above 200 m and an increase in magnetite above 350 m.

At the Kaji Say section, $IRM_{0.3T}$ and HIRM indicate that hematite and magnetite concentrations are significantly lower above the hypothetical unconformity at 464 m (KS-2) compared to below (KS-1) (Figure 2.3B). In unit KS-2, the magnetic properties correlate with lithology, where calcareous lacustrine horizons have an order of magnitude lower $IRM_{0.3T}$ and HIRM than coarser grained, fluvial deposits. Substantially lower magnetite and hematite concentrations in the lacustrine sediments likely reflect the dilution of detrital particles by diamagnetic carbonate. Sharpyl Dak conglomerates are characterized by elevated HIRM and low S-ratios, reflecting higher proportions of hematite. A slightly reddish color of the Sharpyl Dak Group at Kaji Say (Figure 2.2C) further suggests the presence of hematite pigment in these layers.

2.3.3 Paleomagnetic analyses

AF demagnetization removed 70%-80% of the natural remanent magnetization (NRM) on average, suggesting that at least 20%-30% of the NRM is carried by hematite. Most samples had a single magnetization component that decayed toward the origin or close to it, and demagnetization trajectories from thermal and AF treatment of samples from the same horizon yielded compatible demagnetization components (Figures 2.4A-B, and S2.2).

Best-fit directions from AF demagnetized samples were derived using an average of nine steps between 20 and 80 mT, and thermally demagnetized samples were mostly fit between 400°C and 680°C. For Ak Terek, we retained 188 magnetization directions out of 216 demagnetized samples (Figure 2.4C). For Kaji Say, 163 magnetization directions were retained from 235 demagnetized samples (Figure 2.4D). At both sections, the McFadden and McElhinny (1990) reversals test is negative. For Ak Terek, the angle between the two polarity populations is 6.3°, which exceeds the critical angle of 4.3°; for Kaji Say, the angle between the two means is 7.9° with a critical angle of 6.7° (Table 2.1, Figures 2.4C-D). The bootstrap reversals test of Tauxe (2010) shows that the Y and Z components overlap at 95% confidence but not X for Ak Terek and overlap for the X and Z components but not Y for Kaji Say. Incompletely removed recent field components can explain the differences between the two polarities. For Kaji Say, the fold test is positive at 95% confidence limits McFadden (1990) ($Xicrit_{95}$: 14.85, Xi_{1g}: 23.27, Xi_{1s}: 6.39), with the Fisher (1953) precision parameter (k) being maximized at 96 ± 32% unfolding when considering no uncertainty on bedding attitudes or at 90 ± 18% unfolding with 5° uncertainty on bedding attitudes (Watson & Enkin, 1993). Only minor differences in bedding attitudes at Ak Terek lead to an insignificant change in k, hence an inconclusive/indeterminate fold test.

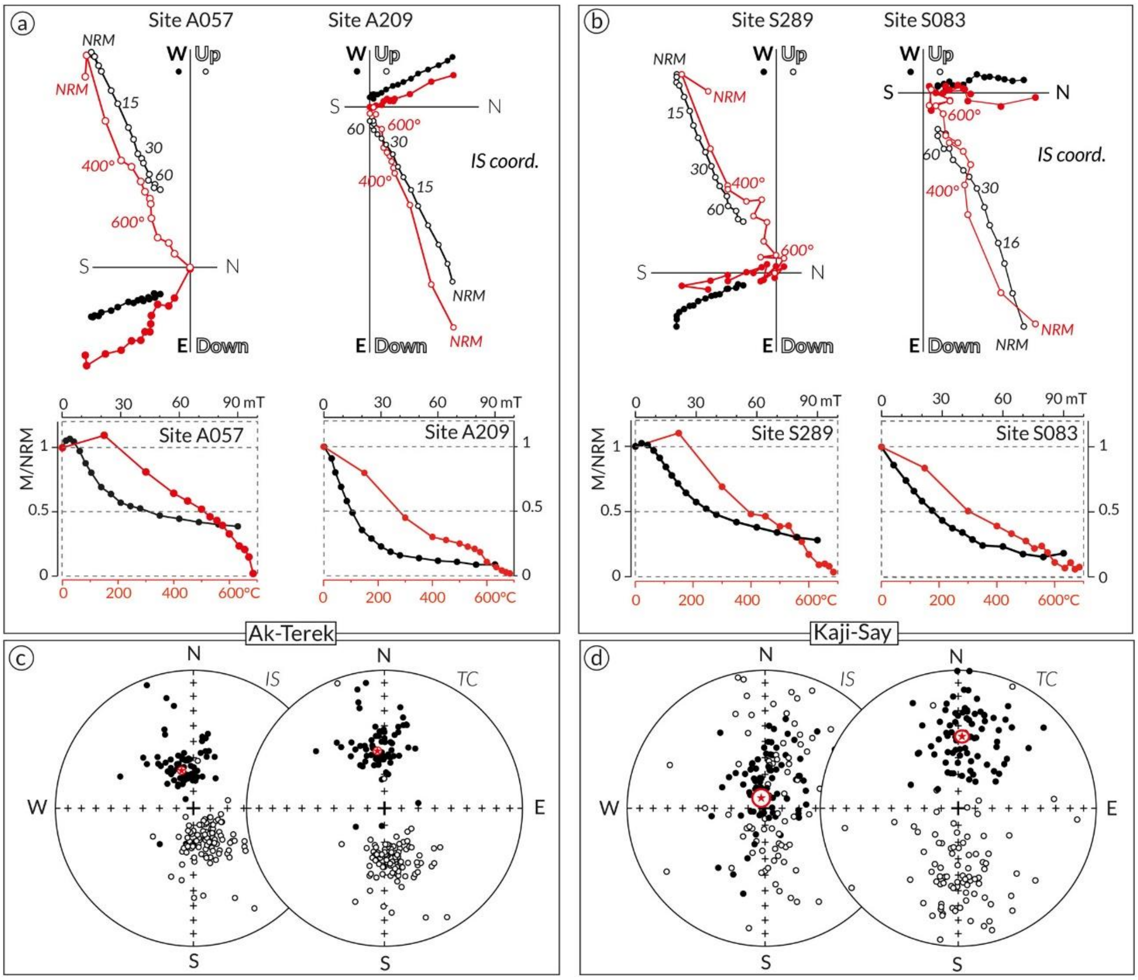

Figure 2.4. Summary of paleomagnetic data. (a)–(b) Comparison of stepwise thermal (red) and AF (black) demagnetization trajectories showing selected demagnetization steps (values in °C and mT, respectively). A normal and reversed polarity sample pair from the same horizons are shown for (a) Ak Terek and (b) Kaji Say. Further examples shown in Supplementary Figures S2.1 and S2.2. (c)–(d) Stereographic projections of the best-fit line components in in-situ (IS) and tilt corrected (TC) coordinates for both sections; mean directions and 95% confidence ellipsoids shown in red.

Table 2.1. Average paleomagnetic directions from this study

	n	Dg	Ig	k	α_{95}	Ds	Is	k	α_{95}
Ak-Terek (42.2°N, 76.7°E)									
All samples	188	341.6	67.0	24.9	2.1	352.4	56.0	24.3	2.1
Reversed-only	110	157.5	−68.8	29.5	2.5	170.3	−58.3	30.8	2.5
Normal-only	78	346.5	64.2	21.5	3.5	355.0	52.6	19.8	3.7
Kaji-Say (42.2°N, 77.3°E)									
All samples	163	335.2	85.7	5.9	5.0	2.9	48.0	11.5	3.4
Reversed-only	83	42.4	−80.5	4.7	8.1	178.0	−50.3	10.5	5.0
Normal-only	80	10.2	76.2	11.0	5.0	7.4	45.5	13.4	4.5

Note. Precise GPS coordinates are given for each sample in the on-line data.
Abbreviations: n, number of samples; D, declination; I, inclination; g, geographic (in-situ) coordinates, s, stratigraphic (tilt-corrected) coordinates; k, best estimate of the precision parameter; α95, radius that the mean direction lies within 95% confidence.

2.4 MAGNETOSTRATIGRAPHY

To establish a magnetic polarity sequence for each section we converted the magnetization component directions into virtual geomagnetic poles (VGPs; Figures 2.5A-B). At least two successive horizons of the same VGP polarity were used to define polarity intervals. The obtained polarity sequence was then correlated to the Neogene geomagnetic polarity time scale (GPTS2012) of Gradstein et al. (2012). Because both sections mostly contain Chu group sediments, our correlations assumed the sections must be younger than the top of the underling Shamsi group, which was previously dated to 11 or 13 Ma (Wack et al., 2014) in the Issyk-Kul basin. We therefore took 13 Ma as the maximum possible age for both sections.

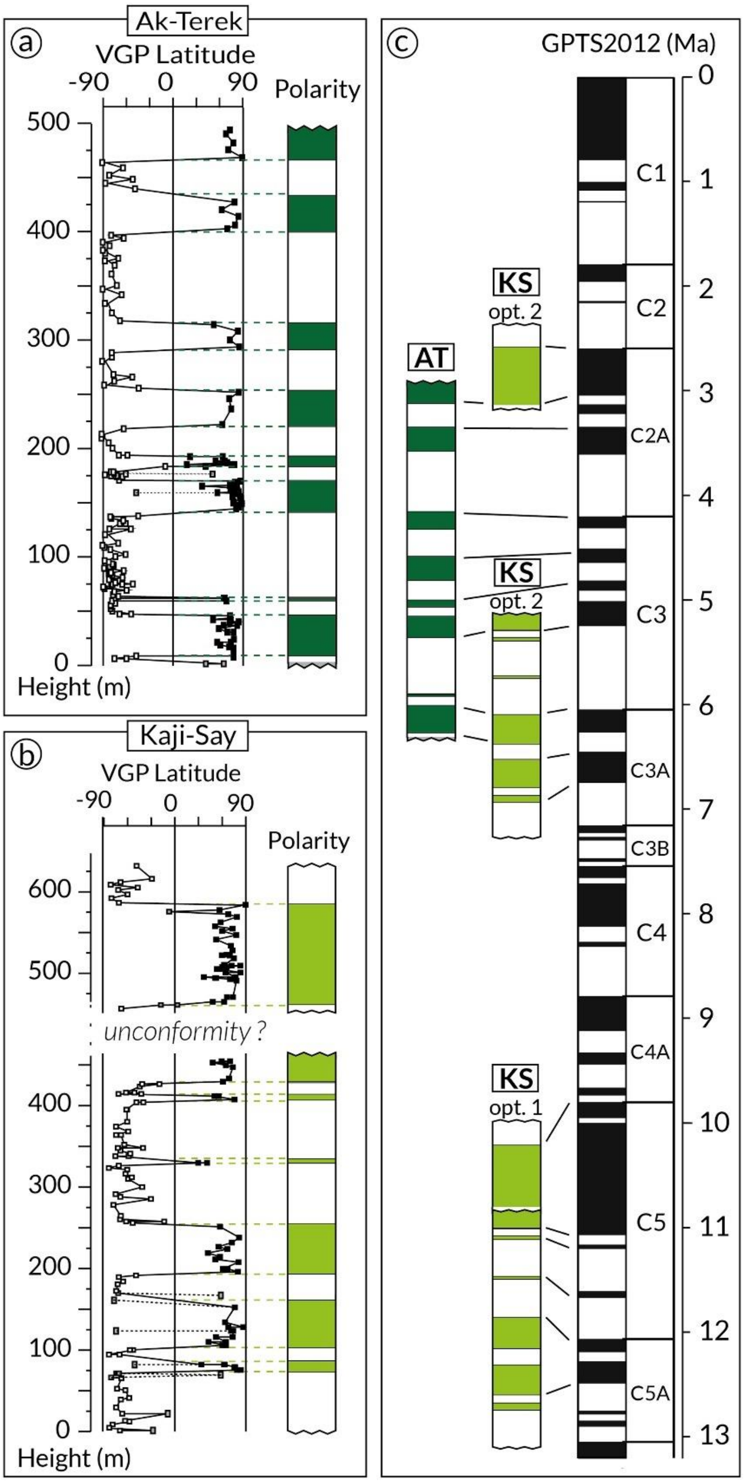

Figure 2.5. Magnetostratigraphy of Ak Terek and Kaji Say. (a)–(b) Virtual geomagnetic pole (VGP) latitude versus stratigraphic height and assigned polarity sequences (green: normal polarity, white: reversed polarity). (c) Magnetostratigraphic correlation of Ak Terek (AT) and Kaji Say (KS) with the geomagnetic polarity time scale (GPTS2012) of Gradstein et al. (2012). Two options are shown for Kaji Say assuming either continuous (Opt. 1) or discontinuous (Opt. 2) deposition between the eastern and western transects. AT, Ak Terek; KS, Kaji Say; VGP, Virtual geomagnetic pole.

2.4.1 Ak Terek

Based on 188 tilt-corrected VGP directions, we established 15 polarity intervals for Ak Terek (Figure 2.5A). Visual correlation of the polarity sequence with the GPTS yields the best match between 6.3 and 2.8 Ma (Figure 2.5C). This correlation includes a missing normal polarity subchron (C2An.2n) at ca. 3.2 Ma (450 m) and a normal polarity interval at 5.9 Ma (60 m) that has no equivalent with the reference scale. The former lasted ca. 90 ka, which corresponds to about 10 m in thickness. With an average sampling interval of 7 m in this part of the section, the subchron could have been missed given fluctuations in the sedimentation process. The normal polarity interval at ca. 60 m is restricted to a 2.5 m thin conglomerate layer of anomalously high IRM values (Figure 2.4A), so it likely represents an isolated aberration in the magnetic recording process.

2.4.2 Kaji Say

The magnetic polarity sequence for Kaji Say was based on 165 tilt-corrected directions (Figure 2.5B), which identified 13 polarity intervals. A normal polarity interval spans ca. 150 m across the potential unconformity between the eastern and western transect. However, the base of the upper section contains a single reversed and two transitional samples, which may indicate that a reversed polarity interval lies below. Two possibilities were considered when correlating the obtained polarity sequence with the global reference scale. Option 1 assumes continuous sedimentation between the eastern and western transects, where a correlation can be found between 12.7 and 9.5 Ma (Figure 2.5C). This solution includes one reversed polarity interval at ca. 100 m that does not exist in the reference scale and misses two short subchrons at the top of the section (580–620 m). Option 2 assumes a hiatus exists between the eastern and western transects at 464 m. The stratigraphically higher, western section spans ca. 200 m in thickness but contains only two polarity intervals. However, assuming the sedimentation rates are similar in the lower unit, restricts the possible correlations with the GPTS. Moreover, the transition between Chu and Sharpyl Dak deposits between 550 and 600 m can serve as a tentative tie point to the equivalent transition at the Ak Terek section. When respecting these criteria, the 160 m normal polarity interval, followed by a 50 m reversed polarity interval of the upper section, best match the reference scale between 3.0 and 2.4 Ma (Figure 2.5C).

Correlating the lower part of the section (eastern transect) individually to the GPTS yields two plausible matches. One possibility is to correlate the lower section in the same way as in Option 1, from 12.7 to 10.9 Ma (Figure 2.5C). However, this correlation results in an 8 Myr hiatus within the section and a ca. 4 Myr age gap between the Chu Group at

Kaji Say and Ak Terek. The other possible correlation to the reference scale lies between 7.0 and 5.1 Ma, which overlaps our age estimate for the base of the Ak Terek section and reduces the hiatus to 2 Myr (Figure 2.5C). This correlation involves two normal polarity zones around 320 and 400 m height that are not matched to the reference scale. Considering their short duration, the unmatched intervals are likely explained by local magnetic recording aberrations in our sections but could also represent true subchrons that were too short to be recognized in the global polarity scale.

2.5 DEPOSITIONAL HISTORY OF THE ISSYK-KUL BASIN

2.5.1 DEPOSITIONAL AGE AT AK TEREK

The magnetostratigraphic correlation of the 500-m-thick Ak Terek section yields a robust correlation to the reference scale, suggesting that the Chu sediments were deposited between 6.3 and 2.8 Ma with an average sedimentation rate of 14 cm ka^{-1}. The conformable transition to conglomerate at the top of the section dates the Chu-Sharpyl Dak transition at 2.8 Ma. We did not observe a lithologic transition at the base of the section; however, along strike to the east, Shamsi deposits are exposed by a reverse fault (Figure 2.1C). Together with the observation of slightly reddish layers at the base of the section (Figure 2.2A) that are rich in hematite (Figure 2.3A), this points to a Shamsi-Chu transition close to 6.3 Ma at Ak Terek.

2.5.2 DEPOSITIONAL AGE AT KAJI SAY

Of the two plausible magnetostratigraphic correlations for Kaji Say, Option 1 assumes quasi-continuous sedimentation between the eastern and western transects, thereby dating the ca. 650 m thick section to between 12.7 and 9.5 Ma, with an average sedimentation rate of 25 cm ka^{-1} and places the Chu-Sharpyl Dak transition at ca. 10 Ma. Based on more reddish strata south of the sampled section, suggestive of Shamsi type deposits (Figure 2.1D), we assume that the base of our section represents approximately the base of the Chu group at Kaji Say. A basal age of ca. 13 Ma for the Chu group is consistent with previous age estimates from the eastern Issyk-Kul basin that dated the top of the Shamsi group to 13–11 Ma (Wack et al., 2014). On the other hand, this age model implies a 4 Myr hiatus between the Chu sediments deposited at Kaji Say and Ak Terek. It also suggests that the stratigraphic boundary between the Chu and Sharpyl Dak groups at Kaji Say predates the equivalent transition at Ak Terek by more than 7 Myr.

Option 2 dates the lower unit to 7.0–5.1 Ma and the upper unit to 3.0–2.4 Ma with average sedimentation rates of 23 and 30 cm ka^{-1}, respectively. This places the Shamsi-Chu transition at around 7 Ma and the Chu-Sharpyl Dak transition at 2.8–2.6 Ma, which agrees well with the stratigraphic boundaries inferred for Ak Terek. Although average sedimentation rates of the two age models are similar, Option 2 involves less variability within the section (20–30 cm ka^{-1}, Figure 2.7A) compared to Option 1 (16–43 cm ka^{-1}). The presence of calcareous lacustrine deposits in the upper part of Kaji Say (Figure 2.3B) yields an additional age constraint that points to the younger age of Option 2, as it implies the existence of a lake (lake Issyk-Kul) at the time of deposition. A precondition for lake formation was the closure of the Issyk-Kul basin, caused by uplift of the Kungey Range, which was estimated to post-date 7 Ma (Selander et al., 2012; Macaulay et al., 2014).

A conformable transition to Sharpyl Dak conglomerates in the upper section also argues for the younger ages implied by Option 2. Deposition of Sharpyl Dak-type conglomerates marks a prominent transition from a low to high energy depositional regime, a widely recognized phenomenon throughout the Tian Shan, with Sharpyl Dak equivalents identified in China as the Xiyu Formation (e.g., Zhou et al., 2020) and the Polizak Formation in Tajikistan (e.g., Dedow et al., 2020). Commonly, these formations are late Plio-Pleistocene in age and have been linked to the onset of northern hemispheric glaciation (e.g., Peizhen et al., 2001; Zhao et al., 2021). However, other authors described the Xiyu conglomerates as a time-transgressive prograding gravel wedge with depositional ages ranging from ca. 15 to 2 Ma (Heermance et al., 2007; Charreau et al., 2009), therefore, regional correlation of the formations should be made with caution.

In the Chu basin (Noruz section, 150 km west of AT, Figure 2.1A), the transition between the Shamsi equivalent (Saryagach Formation) and the 1.5 km thick Chu Formation was dated magnetostratigraphically to ca. 7.5 Ma, while the Chu-Sharpyl Dak transition was dated to ca. 3 Ma (Bullen et al., 2001) and 4.5 Ma (Abdrakhmatov et al., 2001; C1 and C2 in Figure 2.6). Based on similar depositional ages inferred for a ca. 3.5 km thick Chu group in the At-Bashi basin (AB in Figure 2.6) and on further preliminary magnetostratigraphic studies from the Kochor and Naryn basins, Abdrakhmatov et al. (2001) suggested that the transitions between the main stratigraphic groups occurred coevally from basin to basin in the Central Tian Shan. Their proposed Shamsi-Chu and Chu-Sharpyl Dak transition ages around 8 and 4 Ma, respectively, generally agree with the depositional ages we determined for Ak Terek and with the age model of Option 2 at Kaji Say (Figure 2.6).

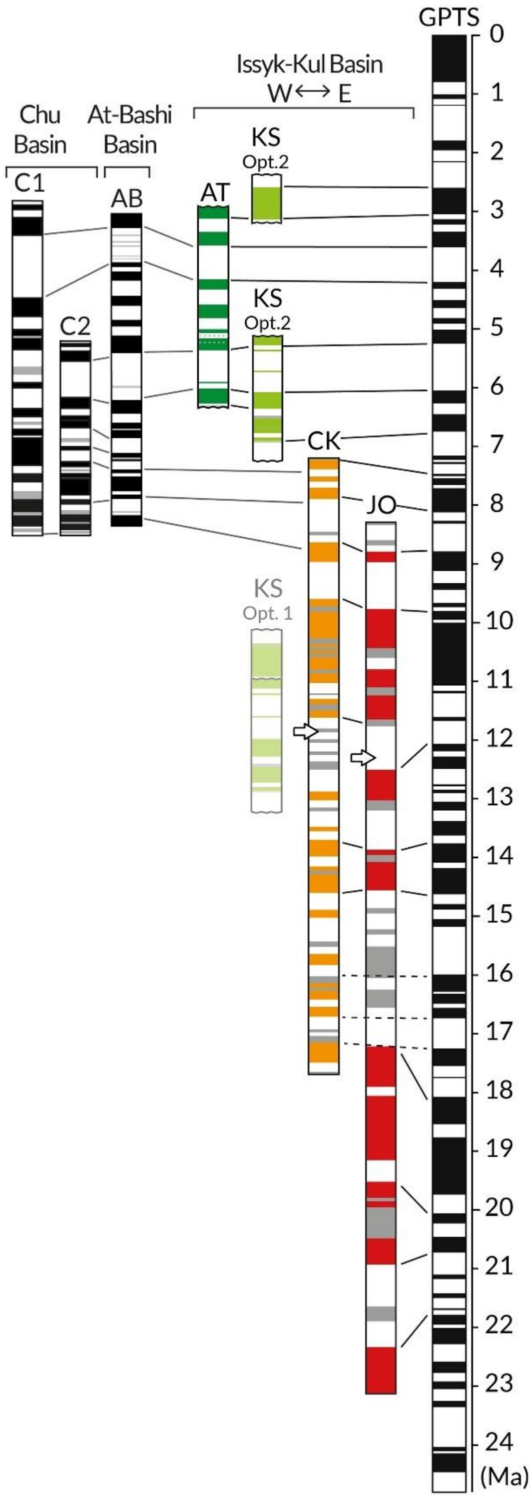

Figure 2.6. Magnetostratigraphic correlations of sections from the central (Kyrgyz) Tian Shan. Abbreviations above the polarity sequences indicate name and location of the sections from Figure 2.1. New and reinterpreted magnetostratigraphies from the Issyk-Kul basin are shown in color (this study). Polarity sequences of CK and JO after Wack et al. (2014); arrows indicate tie points based on a prominent change in magnetic properties (see also Figure 2.8). C1 and C2 represent the Naryn section from the Chu Basin after Bullen et al. (2001) and Abdrakhmatov et al. (2001), respectively; AB is from the At Bashi basin (Abdrakhmatov et al., 2001). CK, Chon Kyzylsuu; JO, Jeti-Oguz.

Taking into account all local and regional age constrains from the Chu and Sharpyl Dak-equivalent formations supports Option 2 at Kaji Say, suggesting a depositional age of ca. 7.0–2.4 Ma, with a hiatus between ca. 5 and 3 Ma.

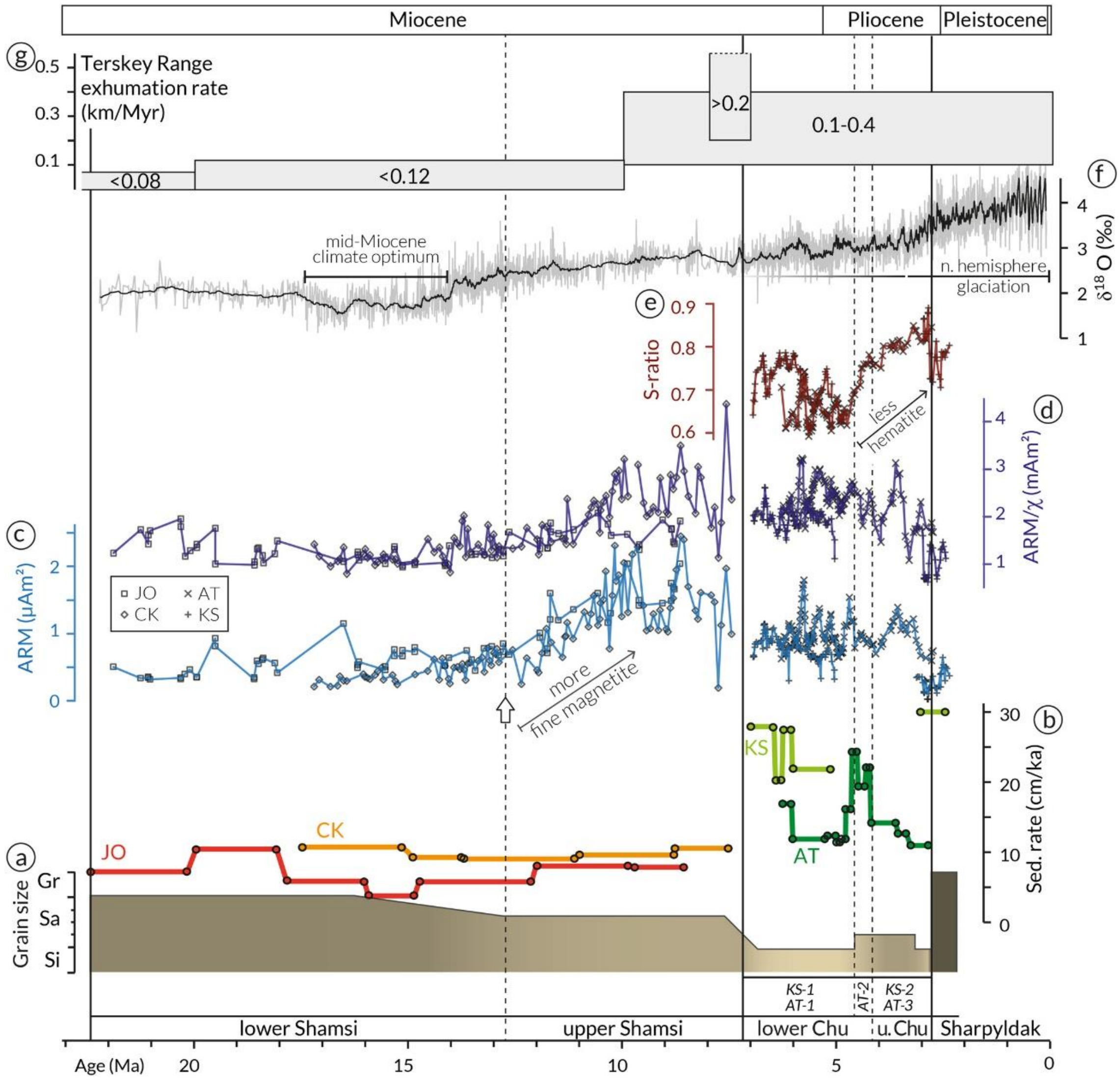

Figure 2.7. Characterization of the Mio- to early Pleistocene sediments from the southern Issyk-Kul basin. From bottom to top: (a) Dominant average grain size; data for the Shamsi group after Macaulay et al. (2016). (b) Sedimentation rates determined from the magnetostratigraphic age models; JO, CK, KS, and AT indicate section name/location from Figure 2.1. Option 2 is shown for KS. (c)–(e) Rock magnetic parameters ARM, ARM/Xχ, and S-ratio; symbols denote the section as shown in (c); arrow indicates tie point between sections; data for the Shamsi group from Wack et al. (2014), data for the Chu group (this study) were smoothed using a 5 point moving average. (f) Global climate trends represented by compiled deep-sea oxygen isotope (δ^{18}O) record from Zachos et al. (2001) using a 90 point moving average. (g) Exhumation rates of the Terskey Range in 10 Ma bins determined from thermochronologic data (Macaulay et al., 2013). Vertical lines indicate transitions between stratigraphic groups and lithologic units (solid and dashed lines, respectively). AT, Ak Terek; CK, Chon Kyzylsuu; JO, Jeti Oguz; K1, Toru Aygir; K2, Cholpon Ata; KS, Kaji Say.

2.5.3 The Shamsi group, eastern Issyk-Kul basin

The new age constraints for the Chu group at Ak Terek and Kaji Say with a tentative Shamsi-Chu transition age close to 7 Ma led us to reevaluate the magnetostratigraphy of the Shamsi group in the eastern Issyk-Kul basin (Figure 2.1E), previously dated between 26 and 11 Ma (Wack et al., 2014). Owing to its lower sedimentation rate and poorer magnetic recording than the Chu group, the magnetizations in the Shamsi group were less stable and their polarity sequence yielded ambiguously defined polarity intervals, leading to inconclusive magnetostratigraphic age estimates (Wack et al., 2014). The polarity sequence of Chon Kyzylsuu (CK) was assigned to two age models (A) and (B), with model A yielding 26–16 Ma and model B yielding 25–11 Ma. Re-correlating this section with the GPTS2012 (Gradstein et al., 2012) to the period from 26 to 7 Ma, by considering all inconclusive horizons as unknown polarities, yields a plausible match between 17.3 and 7.5 Ma (Figure 2.6), with an average sedimentation rate of 9 cm ka^{-1}.

The polarity sequence of Jeti-Oguz (JO) was originally correlated between ca. 23 and 13 Ma or 23 and 11 Ma (Wack et al., 2014). The lower 400 m of the section are robustly defined as 23–18 Ma in both age models they considered. Polarity intervals were more ambiguously defined above 400 m. However, a tie-point exists between the two sections based on a characteristic change in magnetic properties (up-section increase in ARM) observed at around 550 and 700 m stratigraphic height in the CK and JO sections, respectively (arrows in Figures 2.6 and 2.7; Wack et al., 2014). Respecting this tie point, the whole section yields a plausible correlation to the GPTS2012 as well as to the CK polarity sequence between 22.4 and 8.5 Ma with an average sedimentation rate of 8 cm ka^{-1} (Figure 2.6).

Geologic mapping based on satellite images further supports the proposed tie-point between the two sections (Figure 2.1E). In both sections, the levels characterized by increasing ARM values, reflecting an increase in fine grained magnetite (Figures 2.7C-D), mark a prominent color transition from intense dark red beds below (lower Shamsi) to lighter, pale red beds above (upper Shamsi; Figure 2.1E), indicating a decrease in pigmentary hematite. The difference in basal ages (22.4 Ma vs. 17.3 Ma) of the two sections appears reasonable, considering that the Shamsi deposits extend significantly farther below the base of the CK section. In contrast, the base of JO lies above white (lower) Kokturpak or Jurassic strata (observed on satellite images and in the field) that onlap on up-thrusted basement rocks (Figure 2.1E). The transition from Shamsi to Chu type deposits is unconformably overlain by Sharpyl Dak conglomerates at both sections and was therefore not identified in the field. However, our satellite image mapping further supports that the top of both sections lies within the uppermost Shamsi group (Figure 2.1E). Good agreement between the here suggested age of the Shamsi group, the new age constraints for the Chu Group, and geologic mapping between the studied sections, leads us to conclude that the Shamsi group was likely deposited throughout the Miocene, between ca. 22 and 7 Ma in the Issyk-Kul basin.

2.6 Tectonic implications of the syn-orogenic sedimentary record

2.6.1 Uplift of the Terskey range

Taken together, the age constraints from four different sedimentary sections yield a nearly complete record of the Neogene to early Pleistocene depositional history of the southern Issyk-Kul basin. These sediments accumulated in response to the exhumation and successive erosion of the Terskey Range (Macaulay et al., 2016), thus the sedimentation rate and lithologic characteristics of these units hold information concerning the uplift- and climate-history of the area. The Shamsi group, deposited between 22.4 and 7.5 Ma, consists dominantly of coarse-medium sized sandstone (Figure 2.7A) with relatively low sedimentation rates of 4–11 cm ka^{-1} (Figure 2.7B). A prominent increase in fine grained magnetite (higher ARM and ARM/Sus, Figures 2.7C and 2.7E) and a decrease in pigmentary hematite mark the transition from lower to upper Shamsi Group at ca. 12 Ma and coincide with a grain size fining from coarse to medium sand (Figure 2.7A). Assuming that the oldest sediments from the Jeti-Oguz section represent the base of the Shamsi group, implies that syn-tectonic sedimentation in the Issyk-Kul basin, and therefore uplift in the Terskey range, commenced by 22.4 Ma, which is compatible with the estimated onset of deformation in the range at 26-20 Ma (Macaulay et al., 2013, 2014). Relatively constant and low sedimentation rates throughout the Shamsi group imply that erosion rates were comparatively low and did not change significantly until 7.5–7.0 Ma. However, changes in magnetic mineralogy may indicate a change in source material around 12 Ma. The timing of these changes generally coincides with the onset of global cooling after the mid-Miocene climate optimum (Figure 2.7F); consequently, a climatically driven change in erosion cannot be excluded. Exhumation rates inferred from thermochronologic data (Figure 2.7G) point to a slight increase in exhumation during the early to middle Miocene from <0.08 to <0.12 km Myr^{-1} (Macaulay et al., 2013), which is, however, not mirrored by an increase in sedimentation rate.

The transition from Shamsi to Chu-type deposits between 7.5 and 7.0 Ma is linked to a fining in grain size from medium sand to dominantly fine sand and silt deposits and an overall increase in sedimentation rates (Figures 2.7A-B). Up to three-fold higher sedimentation rates of the Chu compared to the Shamsi group indicate an increase in erosion rate after 7 Ma. Thermochronologic data point to accelerated unroofing of the Terskey range after 10 Ma with exhumation rates of 0.1–0.4 km Myr^{-1} and of >0.2 km Myr^{-1} between 8 and 7 Ma (Figure 2.7G and 2.7F) (Macaulay et al., 2013). A good agreement between the increase in exhumation and sedimentation rates suggests that the stratigraphic boundary between the Shamsi and Chu groups at ca. 7 Ma marks the onset of accelerated uplift of the Terskey range.

Based on local and temporal variations in lithology and sedimentation rates, the Chu group can be subdivided into two distinctly different deposition stages. Stage 1, between 7 and 5 Ma, is characterized by comparatively high sedimentation rates (on average 23 cm ka^{-1}) in the central part of the basin (at Kaji Say) and low sedimentation rates (ca. 13 cm ka^{-1}) at Ak Terek further west. It comprises the lithologic units KS-1 and AT-1. Stage 2 between 5 and 3 Ma is characterized by a hiatus at Kaji Say, while sedimentation rates nearly doubled at Ak Terek between 5 and 4 Ma (AT-2, Figure 2.7B) and the lithology changed to more massive and uniform sandstone beds (Figure 2.3A). After ca. 4 Ma sedimentation rates decreased again, and a more frequently changing lithology includes sporadic carbonates and a gypsum layer that indicate still water deposition (AT-3), while laminated limestones deposited after 3 Ma imply lacustrine deposition (KS-2). The hiatus together with strongly folded strata (dip > 70°) of the lower Chu group at Kaji Say likely reflect the onset of deformation and uplift within the foreland basin, which shifted the local depocenter farther north. The concurrent changes in sedimentation rates, lithology and magnetic mineralogy at Ak Terek (Figures 2.7C and 2.7E) may signal a change of source material in the western side of the basin at ca. 4.5 Ma. The transition from Stage 1 to 2, between 4.5 and 5.0 Ma, therefore, marks a prominent change in the deposition dynamics in the Issyk-Kul basin. The associated northward propagation of the locus of deformation at Kaji Say indicates that the formation of the Issyk-Kul Broken Foreland initiated around 5 Ma.

Uplift of the mountain ranges to the north may have influenced the depositional dynamics throughout the basin. Thermochronologic data suggest an onset of exhumation of the northern Tian Shan (Zaili Range) between 29 and 15 Ma (De Grave et al., 2013). However, paleocurrent and provenance data from the Kungey Range in the northern Issyk-Kul basin attest that sediments from the Terskey Range in the south persisted until ca. 7–4 Ma, suggesting that substantial uplift north of the lake commenced only after 7 Ma (Selander et al., 2012).

2.6.2 Uplift of the Kungey range and formation of lake Issyk-Kul

A shift in sediment provenance within the Chu Group exposed north of lake Issyk-Kul, from the lower Terskey member to the upper Kungey member, marks the onset of substantial uplift in the Kungey range (Selander et al., 2012). Although no precise age constraints are available for the sediments in the northern part of the basin, our new age constraints for the Chu group at Ak Terek and Kaji Say (7.0–2.8 Ma) likely apply to the entire Issyk-Kul basin, yielding an average sedimentation rate of 14 cm ka^{-1} for the up to 600 m thick Chu group in the northern basin. Assuming a constant sedimentation rate dates the transition from the Terskey member (up to 200 m thickness) to the Kungey member (up to 400 m thickness) to ca. 5.5 Ma. Consideration of the evidence for major spatio-temporal shifts of depocenters during this time interval in the southern and in the northern part of the Issyk-Kul basin points to a link between the change in deformation style around 5 Ma in the southern basin and the shift from Terskey to Kungey-sourced Chu deposits in the northern basin. We therefore propose that the unconformity at Kaji Say and the doubling of sedimentation rates at Ak Terek at ca. 5 Ma coincide with the initiation of substantial uplift in the Kungey range.

To further test this hypothesis, we dated the available stratigraphic columns of the northern side of the Issyk-Kul basin (K1 and K2 in Figure 2.1A; Selander et al., 2012), based on the depositional record of the southern basin, by assuming synchronous transitions between equivalent stratigraphic groups (Figure 2.8). Based on the stratigraphic thicknesses of ca. 500 m for the Shamsi and Sharpyl Dak groups and ca. 600 m for the Chu group reported by Selander et al. (2012) and assuming Shamsi, Chu, and Sharpyl Dak were deposited between ca. 22–7, 7–3, and <3 Ma, respectively, (Figure 2.7), we infer a progressive increase in average sedimentation rates over time from ≤3 to ≤12 to ≥20 cm ka^{-1}, respectively. Assuming further that the transition from Terskey (10–200 m at K1; 600 m at K2) to Kungey-derived Chu group sediments (400 m at K1, absent at K2) coincides with the transition from Stage 1 to Stage 2 in the southern side of the basin at ca. 5 Ma, yields a sedimentation rate of ca. 25 cm ka^{-1} for the Terskey member at location K1 in the northwest and suggests an increase from <8 to ca. 20 cm ka^{-1} after 5 Ma at K2 in the central Kungey area (Figure 2.8).

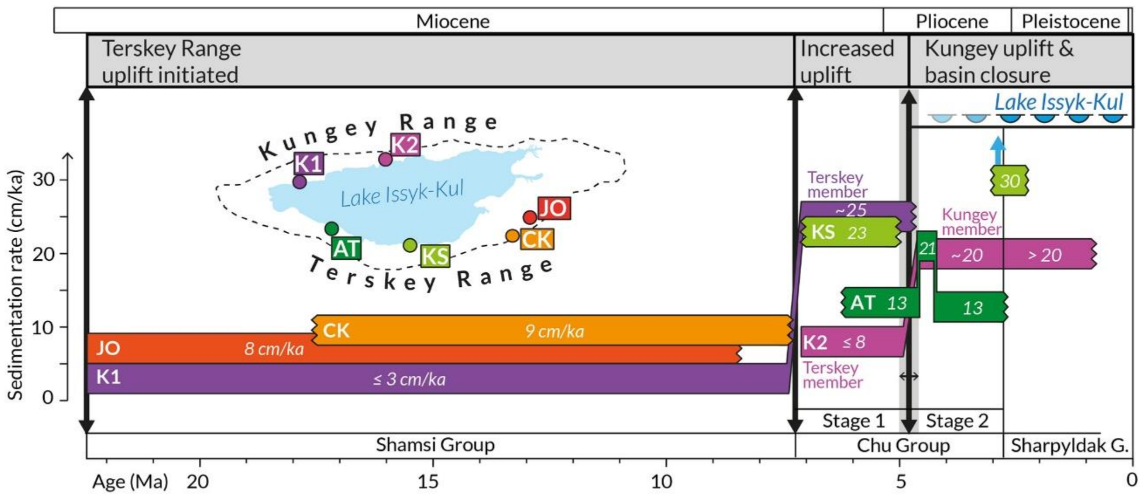

Figure 2.8. Depositional history of the Issyk-Kul basin with implications for mountain building and lake formation. Sedimentation rates and depositional ages of four magnetostratigraphic sections located in the southern side of the Issyk-Kul basin (Terskey area; JO, CK, KS, AT) and two stratigraphic sequences from the northern part of the basin (Kungey areas K1 and K2). Sedimentation rates in the Terskey area were based on the magnetostratigraphic age models of this study and average values were determined for the whole Shamsi group and for the lithologic sub-units (see also Figure 2.3) of the Chu group. The respective average sedimentation rates for the Kungey area were estimated based on stratigraphic thicknesses reported by Selander et al. (2012) and the stratigraphic boundaries dated in the southern part of the basin (black arrows). Site locations in inset (see also Figure 2.1). AT, Ak Terek; CK, Chon Kyzylsuu; JO, Jeti Oguz; K1, Toru Aygir; K2, Cholpon Ata; KS, Kaji Say.

The proposed sedimentation rates compare well with the values determined in the southern part of the basin (Figure 2.8). Comparing Kaji Say and K2 both located in the central basin, more sediment was deposited at Kaji Say (up to 28 cm ka^{-1}), in proximity to the Terskey Range, than at K2 (<8 cm ka^{-1}) between 7 and 5 Ma. However, comparing Ak Terek and K1, in the western side of the basin, indicates that here sedimentation rates were twice as high at the more distal location K1 (ca. 25 cm ka^{-1}) than at Ak Terek (ca. 13 cm ka^{-1}) before 5 Ma. Together, this suggests that between 7 and 5 Ma in the western part of the basin, deposition was located farther north from the Terskey range than in the central part of the basin. This pattern may be applicable for the entire Miocene, as indicated by the westward thickening of the Shamsi group in the northern side of the basin (Selander et al., 2012) and an apparent eastward thickening of the Shamsi group on the southern side (Figure 2.1B). Uplift of the Kungey range would shift the deposition of Terskey sourced sediments southward to more proximal areas, which is consistent with the observed doubling of sedimentation rates around 4.5 Ma at Ak Terek. This uplift event may be associated with a change in the direction of compression from NW-SE to N-S reported for the central Tian Shan around the Miocene-Pliocene transition (Buslov et al., 2003).

Mountain building north of the basin transformed the Issyk-Kul area from a foreland to an intermountain basin, thereby facilitating the formation of a deep lake within it. Two thin limestone layers at the top of the eastern transect at Kaji Say, corresponding to ca. 5 Ma according to Option 2, as well as sporadic calcareous horizons and a gypsum layer deposited between 4 and 3 Ma at Ak Terek, may point to the expansion and retreat of an early lake. Up to 50 m thick sequences of mostly calcareous lacustrine strata in the western section at Kaji Say signify the existence of lake Issyk-Kul at 3 Ma.

2.7 CONCLUSIONS

New and reinterpreted magnetostratigraphic age constraints of continental sediments from the Issyk-Kul basin yield a near-continuous stratigraphic record of the Mio- to early Pleistocene, syn-tectonic depositional history in one of the largest sedimentary basins in the central Tian Shan. From these, we draw the following main conclusions:

- The Shamsi group, which represents the basal syn-tectonic unit, was deposited between 22.4 and 7.5 Ma. This unit is found in the southeastern and northwestern parts of the basin, with maximum thicknesses of ca. 1,000 and 500 m, respectively, implying average sedimentation rates of 8–9 cm ka^{-1} and ca. 3 cm ka^{-1}, respectively. Slight fining in grain size and changes in magnetic mineralogy after the middle Miocene (ca. 13 Ma) may reflect a gradual shift in sediment source or transport conditions

- A major grain size fining between 7.5 and 7 Ma marks the stratigraphic boundary between the Shamsi and Chu groups. Overall higher sedimentation rates after 7 Ma (11–28 cm ka^{-1}) indicate that erosion rates increased, linked to accelerated uplift of the Terskey Range around this time. It is interesting to note the inverse relationship between grain size and sedimentation rate across the Shamsi-Chu transition, which may be related to longer sediment transport or increased subsidence of the basin

- Spatio-temporal shifts in the deposition centers documented north and south of lake Issyk-Kul indicate that the locus of deformation propagated from the Terskey range into the basin around 5 Ma, forming the Issyk-Kul Broken Foreland. This change in deformation style likely coincides with the initiation of uplift in the Kungey range to the north, which led to the closure of the basin, a precondition for the formation of lake Issyk-Kul. Lacustrine deposits dated at ca. 3 Ma demonstrate that a substantial lake must have existed by that time

- Equivalent stratigraphic boundaries around 7 and 3 Ma in nearby basins suggest that the driving mechanisms that controlled sediment accumulation and the lithology of the three main syn-tectonic units were regionally synchronized throughout the central (Kyrgyz) Tian Shan

3 Neogene aridification and lake development in the Issyk-Kul basin, Kyrgyzstan

Anna Kudriavtseva, Edward R. Sobel, Alexandru T. Codilean, Maud J.M. Meijers, Andreas Mulch, Gregory D. Hoke, David Fink, Alexander V. Mikolaichuk, Réka-H. Fülöp, Klaus M. Wilcken, & T. Gabriel Enge

Abstract

Uplift of the Tian Shan range modified regional climate during Cenozoic aridification in Central Asia. This study presents facies analyses and Neogene oxygen and carbon isotopic records from magnetostratigraphically-dated terrestrial sedimentary sections on the southern side of the intermontane Issyk-Kul basin in the Kyrgyz Tian Shan and $^{26}Al/^{10}Be$ isochron burial ages from the southern and eastern sides of the basin. The $\delta^{18}O$ and $\delta^{13}C$ data show a positive ca. 2‰ shift in values between ca. 8 and 7 Ma and a change from a negative to a positive trend. This change is attributed to the upwind growth of the Kyrgyz, Kungey and Trans Ili (Zaili) ranges, which diverted the westerlies, thereby changing the Issyk-Kul basin from a windward to a leeward position, enhancing aridification, and establishing the modern-day spring and summer precipitation regime within the basin. Two 4 to 5 Ma $^{26}Al/^{10}Be$ isochron burial ages constrain the onset of Sharpyl Dak deposition on the eastern side of the basin; southward paleocurrent directions there suggest the eastward growth of the Kungey range in the Pliocene. Increased subsidence on the southern side of the basin and local tectonically-induced river system reorganization led to the commencement of lake formation at ca. 5 Ma, followed by a ca. 2 Ma local depositional hiatus. The transition from sandstones of the Chu sedimentary group to conglomerates of the Sharpyl Dak group, marking a change from fluvial-alluvial deposits to a proximal alluvial fan, is dated at 2.6-2.8 Ma by $^{26}Al/^{10}Be$ isochron burial dating on the southern side of the basin, driven either by tectonics or Northern Hemisphere glaciation. This study concludes that the late Miocene - Pliocene northward growth of Tian Shan significantly altered environmental conditions within the range, preventing the moisture-bearing westerlies from reaching the intermontane Issyk-Kul basin and promoting lake formation and expansion.

3.1 Introduction

Central Asia is the largest arid region in the Northern Hemisphere. Aridity there has increased during the Cenozoic (e.g., Caves et al., 2016; Li et al., 2018; Fang et al., 2020; Wasiljeff et al., 2022). A decrease in the moisture flux delivered by the northern mid-latitude westerlies, which transport moisture eastward across Eurasia, likely played a major role in aridification (e.g., Caves et al., 2015). Decreased westerly moisture transport resulted from Cenozoic global cooling (e.g., Miao et al., 2012; Bosboom et al., 2014a) and Paratethys retreat (e.g., Ramstein et al., 1997, Bosboom et al., 2014b, 2017; Kaya et al., 2019), while surface uplift of the Tibetan Plateau, Tian Shan and other mountain ranges created topographic barriers to moisture input (e.g., Kent-Corson et al., 2009; Caves et al., 2014; Liu et al., 2014; Sun et al., 2015; Chang et al., 2021).

The Issyk-Kul intermontane basin in the Kyrgyz Central Tian Shan (Figure 3.1) contains a Neogene geological record that provides valuable information about the complex interactions between tectonic deformation and Central Asian climate at global and regional scales (e.g., Oberhänsli and Molnar, 2012; Macaulay et al., 2016). Nevertheless, details of how and why this internally-drained basin formed remain unclear. Within the Tian Shan range, changes in the magnitude of precipitation and the vegetation system can reflect either globally- or locally-driven climatic changes or a combination of both. Local and regional climate and landscape can be modified by tectonic surface uplift, which influences the distribution of precipitation, river discharge, and erosion rates, while global climatic changes alter overall moisture delivery to the region, vegetation, and the characteristics of surface processes (e.g., Ramstein et al., 1997; Dupont-Nivet et al., 2007; Rowley and Garzione, 2007; Chamberlain et al., 2012; Herbert et al., 2016). The spatial and temporal distribution of paleoprecipitation proxy data, such as oxygen and carbon isotopes, has been used to distinguish between the influence of tectonic and global climatic factors (e.g., Miao et al., 2012; Caves Rugenstein and Chamberlain, 2018). Here we investigate differences in timing of regional environmental change and corresponding global climate change to identify the impact of changing relief and elevation of the regional mountain belts.

Available paleoclimate records from northern Central Asia are relatively scarce compared to data from the Chinese portion of East Asia; moisture, delivered by the westerlies, was blocked from reaching the latter region as a result of the development of complex topography (e.g., Dettman et al., 2003; Graham et al., 2005; Fan et al., 2007; Kent-Corson et al., 2009; Hough et al., 2011; Zhuang et al., 2011; Li et al., 2016). The >2500-km-long Tian Shan (also called the Tien Shan, i.e. the Heavenly mountains in Chinese) presently forms a significant orographic barrier to the westerlies, which creates a distinctive difference in seasonality of precipitation on its windward and leeward sides, as well as within the range (e.g., Baldwin and Vecchi, 2016). Creation of an orographic barrier occurred during the late Oligocene by growth of the Pamir and western Tian Shan (Wang et al., 2020).

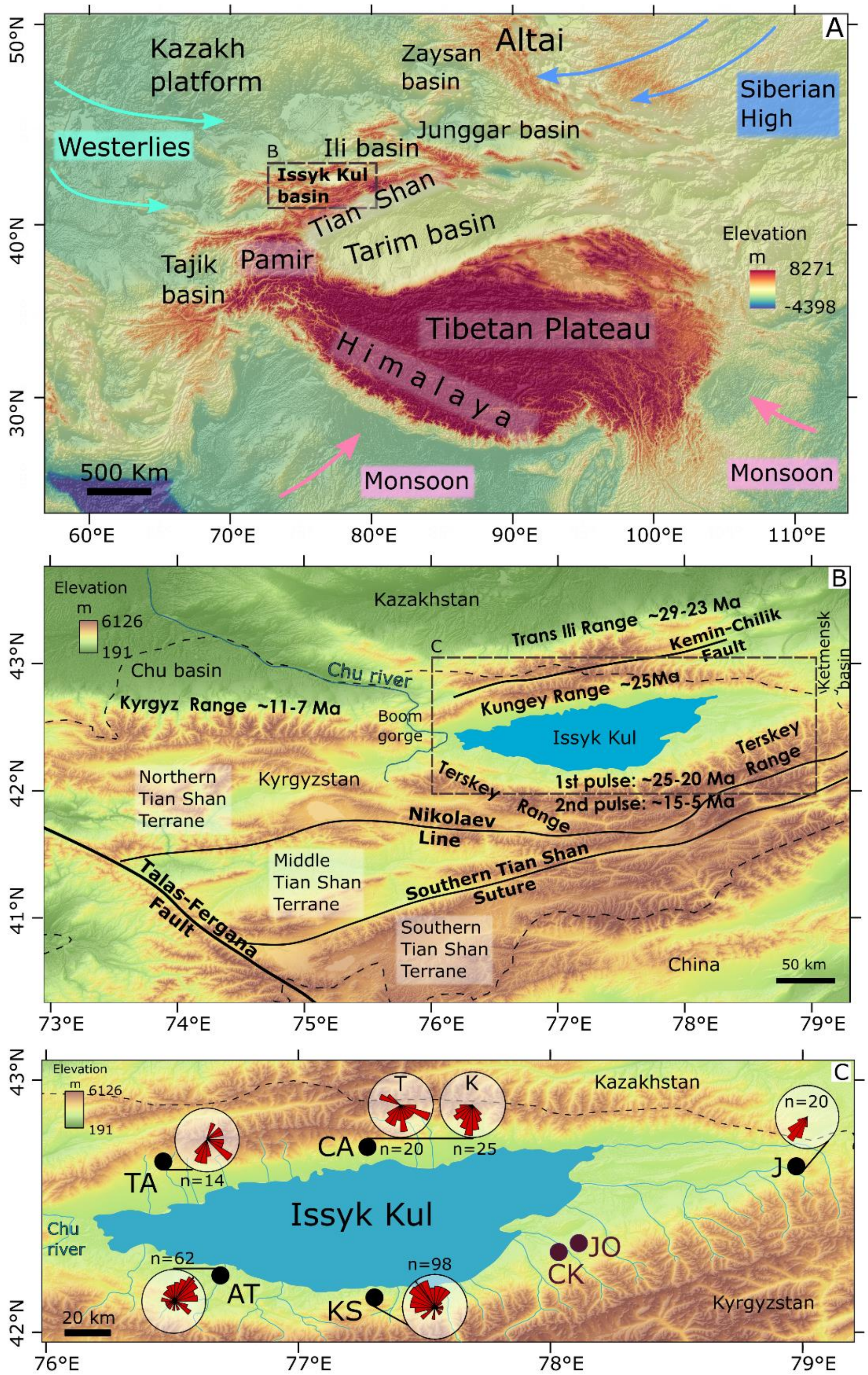

Figure 3.1. (A) Topographic map of Central Asia based on SRTM90 digital elevation data showing major ranges and sedimentary basins. Light blue arrows – westerly winds; dark blue arrows – Siberian High; pink arrows – monsoons. (B) Topographic map of the Kyrgyz Central Tian Shan showing the main faults, positions of the basement terranes, the north-flowing Chu river, country borders (dashed line), and the main ranges with estimated ages for the onset of Cenozoic deformation: Kyrgyz Range (Bullen et al., 2001, 2003; Sobel et al., 2006b); Terskey Range (Macaulay et al., 2013, 2014, 2016); Kungey and Trans Ili Ranges (de Grave et al., 2013; De Pelsmaeker et al., 2015). (C) Topographic map of the study area and paleocurrent directions measured in imbricated clasts and cross-bedded sandstones. Localities of this study: AT – Ak Terek; KS – Kaji Say; J – Jergalan; TA – Toru Aygir; CA – Cholpon Ata. T – Terskey member of the Chu group, K – Kungey member of the Chu group. Localities from Wack et al. (2014) and Macaulay et al. (2016): CK – Chon Kyzylsu; JO – Jeti Oguz. Dashed line shows country borders.

We present a study of the sedimentary record preserved in the Issyk-Kul basin, which is located to the west and/or north of other published Cenozoic climatic records from this region: Tajik basin, Ili basin, Junggar basin, Zaysan basin. (Figure 3.1A; Charreau et al., 2012; Caves et al., 2014, 2017; Hellwig et al., 2018; Frisch et al., 2019a; Wang et al., 2020; Prud'homme et al., 2021). The Issyk-Kul basin is connected to the Ketmensk basin to the east and is situated between the Terskey, Kungey, Trans Ili (also called Zaili) and the Kyrgyz ranges; these ranges are all part of the northern Tian Shan (Figure 3.1B). The Issyk-Kul basin contains up to 4 km of Oligocene to Quaternary strata, which record the sedimentary response to regional climate change and proximal tectonic processes. The first magnetostratigraphic dating of the fossil-poor sedimentary deposits of the Chon Kyzylsu and Jeti Oguz sections in the southeastern part of the Issyk-Kul basin (Wack et al., 2014) shows early to middle Miocene ages of these deposits. Macaulay et al. (2016) presented the first oxygen ($\delta^{18}O$) and carbon ($\delta^{13}C$) stable isotope data for the dated sections. Roud et al. (2021) presented late Miocene to early Pleistocene magnetostratigraphic age models for two new sections (Kaji Say and Ak Terek) from the southern flank of the Issyk-Kul basin and revised age models for Wack et al.'s (2014) stratigraphically-older sections.

Here, we present facies analyses from five stratigraphic sections around lake Issyk-Kul (Kaji Say, Ak Terek, Toru Aygir, Cholpon Ata, Jergalan; Figure 3.1C), $^{26}Al/^{10}Be$ isochron burial ages from three of them (Kaji Say, Ak Terek, Jergalan), and $\delta^{18}O$ and $\delta^{13}C$ records of pedogenic, fluvial, and lacustrine carbonates from the two late Miocene – early Pleistocene sections (Kaji Say, Ak Terek) dated by Roud et al. (2021) using magnetostratigraphy. Our $^{26}Al/^{10}Be$ isochron burial ages refine the age model for these deposits and constrain when lake Issyk-Kul formed. We combine our data with published records from stratigraphically-older nearby sections (Macaulay et al., 2016) to present nearly complete Miocene-Pliocene $\delta^{18}O$ and $\delta^{13}C$ records and to study how the growth of the adjacent mountain ranges influenced the environmental conditions in the Issyk-Kul basin. Comparing our combined stable isotopic record from the Issyk-Kul basin with data from across the region provides new insights into the role of the Tian Shan and its interaction with the westerlies under a globally cooling climate in the late Neogene.

3.2 GEOLOGICAL AND CLIMATIC SETTING

3.2.1 CENOZOIC REACTIVATION OF THE TIAN SHAN

The Cenozoic India – Asia collision led to the creation of the Tibetan Plateau and the Pamir and tectonically reactivated the Tian Shan and Altai ranges to the north during the late Oligocene – Miocene (Figure 3.1A; e.g., Molnar and Tapponnier, 1975; Abdrakhmatov et al., 2002; Sobel et al., 2006a; Glorie et al., 2016). The Tian Shan is a 2500-km-long orogenic belt with present-day shortening rates of up to 20 $mm.yr^{-1}$ (Abdrakhmatov et al., 1996; Zubovich et al., 2010). The Central Kyrgyz Tian Shan and the Chinese Central and Western Tian Shan are bounded by the Tarim basin to the south and the Kazakh platform to the north. The Issyk-Kul basin is situated within the Northern terrane of the Central Kyrgyz Tian Shan (Figure 3.1B).

The Northern, Middle and Southern Tian Shan terranes comprise the three major fault-bounded Paleozoic terranes of the Central Kyrgyz Tian Shan (Figure 3.1B; Bakirov and Maksumova, 2001; Biske and Seltmann, 2010). The Northern terrane is built of late Ordovician to early Silurian granites, along with Precambrian metamorphic rocks and early Paleozoic ophiolites, overlain by Ordovician sedimentary rocks (Bakirov and Maksumova, 2001; Maksumova et al., 2001; Windley et al., 2007). The Middle Tian Shan comprises Paleoproterozoic metamorphic rocks, overlain by Neoproterozoic and Paleozoic clastic and volcanic rocks, as well as middle Devonian to early Permian marine carbonate and clastic rocks (Biske, 1996; Bakirov and Maksumova, 2001; Maksumova et al., 2001; Seltmann et al., 2011). The Southern Tian Shan consists of Silurian – lower Permian ophiolites and sedimentary rocks of a Late Paleozoic collisional system with early Permian granites (Biske, 1996; Maksumova et al., 2001; Seltmann et al., 2011).

Paleozoic deformation of the Tian Shan started in the late Carboniferous and the late Permian - Triassic collision led to development of the Southern Tian Shan Suture and large sinistral strike-slip faults, including the Nikolaev line, which separate the terranes (Figure 3.1B; e.g., Bazhenov et al., 1999; Bazhenov and Mikolaichuk, 2004). Afterwards, parts of the Tian Shan were reactivated during the Mesozoic and early Cenozoic (see Figure 8 in Macaulay et al., 2014 for a detailed depiction).

The most recent deformation started in the late Oligocene after a period of tectonic quiescence. Deformation during the Miocene led to the formation of a vast, east-west trending mountain range (e.g., De Grave et al., 2013; Macaulay et al., 2013). Thermochronological data show that the Terskey range on the south side of the Issyk-Kul basin and the Trans Ili range on the north side of the basin started deforming in the late

Oligocene – early Miocene (De Grave et al., 2013; De Pelsmaeker et al., 2015; Macaulay et al., 2013, 2014, 2016). Deformation within the Terskey range propagated eastward and reached the eastern side of the Issyk-Kul basin by the middle Miocene (Macaulay et al., 2014). The onset of deformation in the Kungey range, separated from the Trans Ili range by the Kemin-Chilik fault, also started in late Oligocene, as defined by thermochronology (de Grave et al., 2013; De Pelsmaeker et al., 2015). However, paleocurrent data suggest that the sediments from the Terskey range were deposited on the southern flank of the Kungey range area until the late Miocene, with a late Miocene – early Pliocene estimated age of initiation of significant deformation there (Selander et al., 2012). Thermochronological data show that deformation of the Kyrgyz range, to the northwest of the Issyk-Kul basin, initiated in the present center of the range during the late Miocene and propagated eastward (Bullen et al., 2001, 2003; Sobel et al., 2006b).

3.2.2 Precipitation in the Tian Shan

Today, the entire Tian Shan range forms a significant topographic barrier to westerly winds and is responsible for the differences in seasonality of precipitation with dominantly winter-spring precipitation on the windward (northwestern) side of the Tian Shan and summer precipitation within the range itself and on its leeward (southeastern) side (Baldwin and Vecchi, 2016). However, during the late Cretaceous, a low-relief and low-elevation erosion surface extended over much of the Tian Shan region; therefore, the orographic barrier postdates this time (e.g., Bullen et al., 2001, 2003; Sobel et al., 2006b; Yang et al., 2014; Macaulay et al., 2014). The moisture supply in Central Asia has been dominated by the westerlies since at least the Eocene (Caves et al., 2015; Licht et al., 2016; Bougeois et al., 2018). The Tian Shan and Pamir have interacted with the westerlies since the late Oligocene (Wang et al., 2020) and caused a reorganization of Central Asian climate during the Neogene (e.g., Bougeois et al., 2018; Caves Rugenstein and Chamberlain, 2018; Hellwig et al., 2018). Growth of the Terskey range formed a topographic barrier during the Miocene, placing the Issyk-Kul basin area in a windward position with respect to the path of the westerlies and local topography (Figure 3.1; Macaulay et al., 2016). Formation of an orographic barrier typically requires relief of ca. 1300 - 2000 m (Bookhagen and Strecker, 2008; Bookhagen and Burbank, 2010).

Precipitation in the Tian Shan is seasonally influenced by interactions between the westerlies and the Siberian High (e.g., Aizen et al., 1997; Zech, 2012; Schwarz et al., 2017; Prud'homme et al., 2021). Moisture, delivered by the monsoon, never consistently reached the Tian Shan and did not influence long-term climate within the range (Caves et al., 2015). The westerlies bring moisture from the North Atlantic, the Mediterranean, and the Black Sea (Aizen et al., 2006; Lauterbach et al., 2014). In winter, the Siberian High reaches the Tian Shan and blocks the midlatitude westerlies, resulting in cold conditions and low precipitation (Aizen et al., 2001; Ricketts et al., 2001).

3.2.3 Development of the Issyk-Kul basin

Today, the semi-arid Issyk-Kul basin is internally drained, hosting a large lake (ca. 180 km x ca. 60 km with a depth of 668 m). Issyk-Kul means warm lake in the Kyrgyz language; however, to prevent confusion in this paper, we refer to the basin as Issyk-Kul and to the lake as lake Issyk-Kul. During past lake highstands, the lake has been periodically externally drained via the northward-flowing Chu river, which flows through the Boom gorge (Figure 3.1B; e.g., Rosenwinkel et al., 2017; Gebhardt et al., 2017). Maximum precipitation is recorded in spring and summer (Aizen et al., 2001). As indicated by palynologic data, during the Cenozoic the basin underwent aridification and forests were gradually replaced by steppe and desert elements (Grigina and Fortuna, 1981). Since the late Pleistocene, the vegetation is similar to modern flora (Grigina and Fortuna, 1981; Fortuna et al., 2017). Subsurface sedimentological data from the eastern side of the basin suggest that a local shallow lake existed in the Miocene and expanded westward in the late Pliocene (Grigina and Fortuna, 1981; Voskresenskaya, 2013; Voskresenskaya and Leflat, 2015). However, to date there are only sparse data with well-established age constraints indicating when or how the lake first formed or when the present climate was established.

The late Mesozoic - Cenozoic sedimentary deposits of the Issyk-Kul basin are divided into four sedimentary groups: the Kokturpak, Shamsi, Chu and Sharpyl Dak groups (Abdrakhmatov et al., 2001). The Kokturpak group is the oldest in the Issyk-Kul basin with a late Cretaceous to Eocene age based on palynology (Fortuna et al., 1994) and comprises paleosols, lacustrine and poorly-sorted low energy fluvial sedimentary rocks. The unconformably overlying Shamsi group contains reddish conglomerates deposited in a high energy regime; the deposits are coarser and better rounded than those in the underlying group. Palynologic data implies an Oligocene – early Miocene age of the group (Fortuna et al., 1994). The first magnetostratigraphic age models of the Shamsi group suggest depositional ages of 22.8 to 13.3 Ma or 22.1 to 11.1 Ma in the Jeti Oguz section and 26.0 to 16.2 Ma or 25.2 to 11.0 Ma in the Chon Kyzylsu section (Figure 3.1C; Wack et al., 2014). More recent paleomagnetic results (Roud et al., 2021) from these two sections allowed for a reevaluation of the age models. The revised magnetostratigraphic age models from Roud et al. (2021) suggest a depositional age of 22.4 to 8.5 Ma in the Jeti Oguz section and 17.3 to 7.5 Ma in the Chon Kyzylsu section. Deposits of the stratigraphically younger Chu group are finer-grained than the older Shamsi group. The Chu group contains beige and yellowish fluvial sandstones and siltstones, as well as conglomerates deposited by high energy river systems. The estimated age of the Chu group in the Chu basin is late Miocene – early Pliocene; lithostratigraphic correlation implies the same age range in the Issyk-Kul basin (Bullen et al., 2001; Omuraliev and Omuralieva, 2004). The Sharpyl Dak group overlies the Chu group gradually or with an unconformity and represents poorly sorted, very coarse conglomerates. Palynologic data implies a late Pliocene – early Pleistocene age of the group (Grigina and Fortuna, 1975; Fortuna et al., 1994). The first magnetostratigraphic age models for the Chu group and Chu – Sharpyl Dak transition were proposed by Roud et al. (2021). In that study, the depositional age of the Chu group in the Ak Terek section is interpreted to be 6.3 to 2.8 Ma. Two possible age models were proposed for the Chu – Sharpyl Dak deposits in the Kaji Say section. The first one is 12.7 to 9.5 Ma. The second option implies a hiatus in the middle of the section, with ages of 7.0 to 5.1 Ma for the lower part and 3.0 to 2.4 Ma for the upper part.

3.3 MATERIALS AND METHODS

3.3.1 SEDIMENTOLOGICAL DESCRIPTIONS

Sedimentary sequences were described at five localities around lake Issyk-Kul during field work in 2016 and 2017: Kaji Say and Ak Terek on the southern side, which were previously dated by Roud et al., (2021) using magnetostratigraphy, Jergalan on the eastern side, and Cholpon Ata and Toru Aygir on the northern side (Figure 3.1C). The work included detailed descriptions of composition, bedding structures, paleocurrent directions, conglomerate clast counts and facies interpretations. Paleocurrent directions were defined by measuring the orientations of imbricated conglomerate clasts and cross-bedding. Conglomerate clast counts were performed by identifying at least 100 clasts within a 1 m^2 space in suitable areas of the sections.

3.3.2 ^{26}AL/^{10}BE ISOCHRON BURIAL DATING

We use the technique of terrestrial cosmogenic nuclide isochron burial dating to determine the age of the sedimentary sequences. Terrestrial cosmogenic nuclides are isotopes produced in silicate minerals by the interactions of secondary cosmic rays with the upper few meters of the Earth's surface (Lal, 1991; Schaefer et al., 2022). Quartz is the main target mineral from which the concentration of cosmogenic radionuclides ^{26}Al and ^{10}Be are most routinely measured. Burial dating is based on the radioactive decay of ^{26}Al and ^{10}Be isotopes in rocks that are completely shielded from new production. The concentrations of ^{26}Al and ^{10}Be in a sample are proportional to the duration of exposure (Granger and Muzikar, 2001). The ^{26}Al is produced faster than the ^{10}Be. Although the exact $^{26}Al/^{10}Be$ production ratio is still debated (see Corbett et al., 2017 and references therein; Halsted et al., 2021), the consensus value, widely used in the literature, is 6.75:1 (Balco et al., 2008). Therefore, for consistency with other work, we use the latter in our calculations here. The two isotopes decay at different rates according to their half-lives: 0.717 Myr for ^{26}Al (Norris et al., 1983) and 1.387 Myr for ^{10}Be (Korschinek et al., 2010; Chmeleff et al., 2010). When sediments are buried and completely shielded from cosmic radiation, there is no new isotope production and the initial $^{26}Al/^{10}Be$ ratio, which is equal to the production ratio, decreases. Assuming that sediments were rapidly buried after deposition and minimally re-exposed to new production prior to collection, the half-lives of the two nuclides and their initial production rate ratio (above) can be used to calculate the time of burial. The lower the ratio and concentrations, the longer the duration of burial. This assumption is the basis for conventional burial dating that requires the measurement of a single $^{26}Al/^{10}Be$ ratio from a clast or an amalgamated sand sample in order to provide a meaningful age (Granger and Muzikar, 2001).

In tectonically active areas like the Tian Shan, ideal burial conditions rarely occur. Sediments may experience post-burial production that can alter the inferred burial age. Post-burial nuclide production occurs if the overlying deposits are not thick enough (approx. <30 m) – and therefore material is not completely shielded from incoming cosmic radiation – or when sediments are brought close to the surface after the initial deposition and burial due to erosion, river incision or other factors. Post-burial nuclide production will increase nuclide concentrations and ratios and result in seemingly younger burial ages. Also, the sediments are affected by a complex combination of exposure and material mixing prior to burial which can lead to obtaining inherited concentrations of nuclides (Codilean and Sadler, 2021). In settings where conventional burial dating assumptions are violated, a relatively new method – isochron burial dating – may be used to obtain a reliable burial age (Balco and Rovey, 2008; Erlanger et al., 2012; Knudsen et al., 2020).

The isochron burial dating method does not require information about depth, exposure, and post-burial nuclide production (Balco and Rovey, 2008). Rather, it requires a set of quartz-bearing clasts from one depositional horizon that was sufficiently shielded such that post-burial production is minimized (but not necessarily eliminated). Each clast in the depositional horizon will record the same post-burial history but different pre-burial exposure histories as the clasts likely originated from different source areas. The ^{26}Al and ^{10}Be concentrations form an isochron on a ^{10}Be-^{26}Al plot and the slope of this isochron will depend only on the burial age. The isochron slope reflects the deviation from the $^{26}Al/^{10}Be$ production rate, and will depend on the half-lives of the nuclide pair and on the duration of decay. Therefore, the burial age (t_b) may be calculated as shown by Balco and Rovey (2008):

$$t_b = -\ln (R_M/R_{init}) / (\lambda_{26} - \lambda_{10})$$

where R_M is the slope of the isochron; R_{init} is the $^{26}Al/^{10}Be$ production ratio; λ_{26} and λ_{10} are the decay constants of ^{26}Al and ^{10}Be, respectively.

To confirm and improve the magnetostratigraphic age models from Roud et al. (2021), we dated the Kaji Say and Ak Terek sections. We also attempted to date the sections on the northern and eastern sides of the basin. We therefore collected a total of ten samples (one sample is one isochron) of individual clasts and amalgamated sand (250 – 500 μm grain size) from four localities – the Kaji Say, Ak Terek, Jergalan and Cholpon Ata sections (Figure 3.1C). Four samples were taken in the Kaji Say section: PET-L and PET-U from the lowermost part of the section, PET-QTS-PIT from the Chu-Sharpyl Dak transition, and PET-QTS-L from the uppermost Sharpyl Dak. Two samples were taken in the Ak Terek section: AKT-U from the uppermost Chu and AKT-Q from the lower Sharpyl Dak. Two samples were taken in the Jergalan section: JGL-2 from the Chu deposits and JGL17 from the Chu-Sharpyl Dak transition. Two samples were taken in the Cholpon Ata section: CA17-6 from the upper Chu part and CA17-1 from the lower Sharpyl Dak.

At each of the ten sampled locations, we collected about ten clasts. Clasts were chosen based on their size, lithology, and inferred amount of quartz present. Our aim was to collect diverse, quartz-rich lithologies, in order to capture different pre-burial histories. All collected clasts were approximately 10-12 cm in diameter. Smaller clasts would not contain enough quartz and larger clasts could have been subject to self-shielding. The clasts were collected from areas where modern production is minimized due to shielding. Due to very low quartz yield in some of the clasts, only three to six clasts were analyzed per isochron. At six of the sampled locations, in addition to the individual clasts, we also collected an amalgamated sand sample as an independent test of the isochron and assumptions about shielding and post-burial production (the ^{26}Al-^{10}Be of the sand sample should plot on the isochron defined by the individual clasts if assumptions are met).

The initial sample preparation (crushing and sieving) was done at the University of Potsdam, Germany. Quartz was isolated and purified at the University of Wollongong, Australia, following procedures described in Kohl and Nishiizumi (1992), using froth flotation to separate feldspars from quartz. Be and Al were separated at the University of Wollongong following procedures described in von Blanckenburg et al. (1996) with the modification that Al was separated from Be and Ti using pH sensitive precipitation before Be cation exchange chromatography (Child et al., 2000). Samples were spiked with ≈300 μg of ^{9}Be from a low-level beryllium carrier solution added prior to complete HF dissolution. ^{10}Be/^{9}Be and ^{26}Al/^{27}Al ratios were measured using the 6MV SIRIUS facility at the Australian Nuclear Science and Technology Organisation (ANSTO; Wilcken et al., 2019; 2022). The native Al concentrations of the samples ranged from 47 to 490 ppm (median = 96 ppm; average = 124 ppm) and were determined via ICP-OES with a precision of 3-4% (Fujioka et al., 2015). ^{10}Be/^{9}Be ratios were normalised to the KN-5-2 and KN-5-3 (Nishiizumi et al., 2007) standards and ^{26}Al/^{27}Al ratios were normalised to the KN-4-2 (Nishiizumi, 2004) standard. Analytical uncertainties for the final ^{10}Be and ^{26}Al concentrations (atoms g^{-1}) include AMS measurement uncertainties (the larger of counting statistics or standard deviation of repeats and blank corrections) in quadrature with 1-2% for ^{10}Be and 2-3% for ^{26}Al standard reproducibility (depending on the individual AMS measurement conditions), 1% uncertainty in the ^{9}Be carrier concentration and 4% uncertainty in the ICP-OES Al measurements.

3.3.3 Thin section petrography

Petrographic analysis was performed using a polarized light microscope on 27 sandstone and lacustrine micrite thin sections from Kaji Say and 16 sandstone thin sections from Ak Terek to evaluate the diagenetic and palustrine alteration of the sediment sequences. Compaction and cementation of fluvial-alluvial samples as well as the amount of recrystallization and pedogenic alteration of lacustrine micrite samples were evaluated.

3.3.4 Stable isotope analysis

To reconstruct paleoenvironmental conditions, a total of 122 carbonate samples were collected for stable isotope analysis: 53 samples from the Kaji Say section and 69 from the Ak Terek section. The Kaji Say samples consist of pedogenic nodules (17 samples), sparitic cement in sandstones (16 samples), micrite in lacustrine mudstone (10 samples), and micrite in lacustrine marl and siltstone (10 samples). The majority of the Ak Terek samples are pedogenic nodules (64 samples), with only 5 samples of sparitic cement in sandstones.

Stable isotope values were measured at the Joint Goethe University– Senckenberg BiK-F Stable Isotope Facility at Goethe University Frankfurt, Germany. The finest parts of the samples were drilled, the powder was digested in orthophosphoric acid and analyzed using a Thermo MAT 253 mass spectrometer interfaced with a Thermo GasBench II. The analytical procedures follow Spötl and Vennemann, (2003). Raw isotopic ratios were calibrated against NBS 18, Merck and Carrara marble standards. All isotope values are relative to the Pee Dee Belemnite (V-PDB). Analytical uncertainties are typically smaller than 0.10 ‰ ($\delta^{18}O$) and 0.07 ‰ ($\delta^{13}C$).

3.4 RESULTS

3.4.1 SEDIMENTARY SEQUENCES

3.4.1.1 Kaji Say section

The 700-m-thick Kaji Say section is located in the Tossor – Kaji Say area and comprises the Chu and Sharpyl Dak groups (Figure 3.1C). Paleocurrent directions indicate predominantly NW flow directions in the section. The Chu group deposits can be divided into two depositional units (Figure 3.2). The lower unit is 450 m thick; it is formed of alternating grey rounded conglomerates with clasts of mainly cobble and boulder size (Figure 3.3A), red angular conglomerates with clasts of mainly gravel and cobble size (Figure 3.3B), grey and red sandstones, and beige siltstones. The upper unit is 190 m thick and comprises alternating red angular conglomerates with clasts of mainly gravel and cobble size, beige pebbly sandstones, blue calcareous mudstones, white marls, calcareous siltstones and marly sandstones (Figures 3.3C-E). The red and grey colors represent different sedimentary lithologies. Red conglomerates are matrix supported and composed of clasts of porphyry with quartz phenocrysts in a fine-grained groundmass. Grey conglomerates are clast supported and consist predominantly of granite clasts. In order to measure well-exposed outcrops, the Kaji Say section was divided into western and eastern transects, situated in different valleys (Figure 3.4). Continuous beds can be followed between the two transects; no more than 10 m of strata was omitted. Bedding dips indicate the presence of a fold: ca. 10-25° (dip direction is ca. 350-355N) at the base of the section (0-245 m), ca. 75° (ca. 0N) at the top of the lower Chu unit (ca. 245-480 m), ca. 25-35° (ca. 5-10N) in the upper Chu unit (ca. 480-640 m), and ca. 15° (ca. 5-10N) at the top of the section (Figure 3.4).

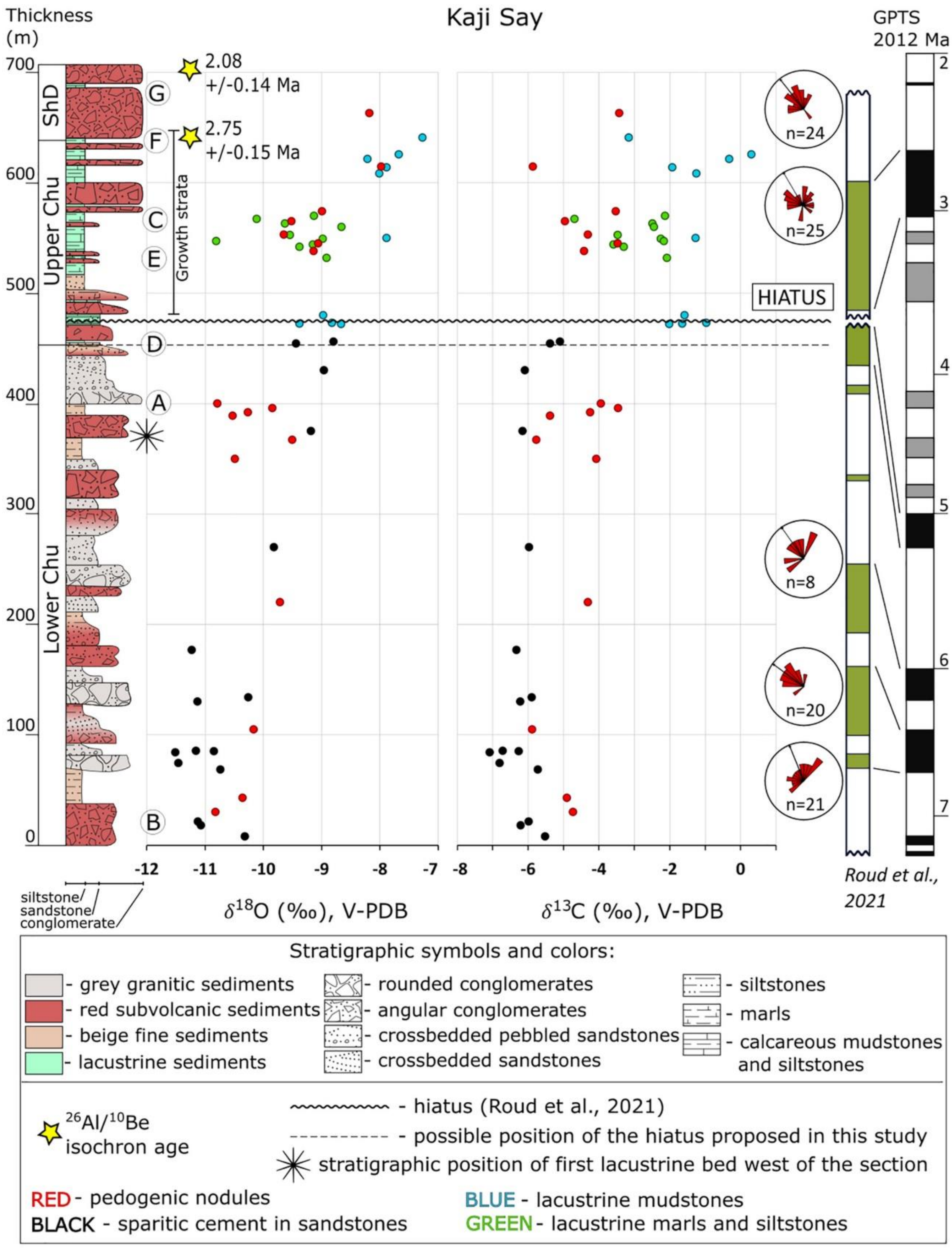

Figure 3.2. The Kaji Say stratigraphic section (location shown in Figure 3.1) with $^{26}Al/^{10}Be$ isochron burial ages, rose diagrams of paleocurrent flow directions (black arrow shows the main vector) and stable isotopic values plotted against the magnetostratigraphic age model of Roud et al. (2021). ShD is Sharpyl Dak. A-G show stratigraphic positions of photos, represented in Figure 3.3.

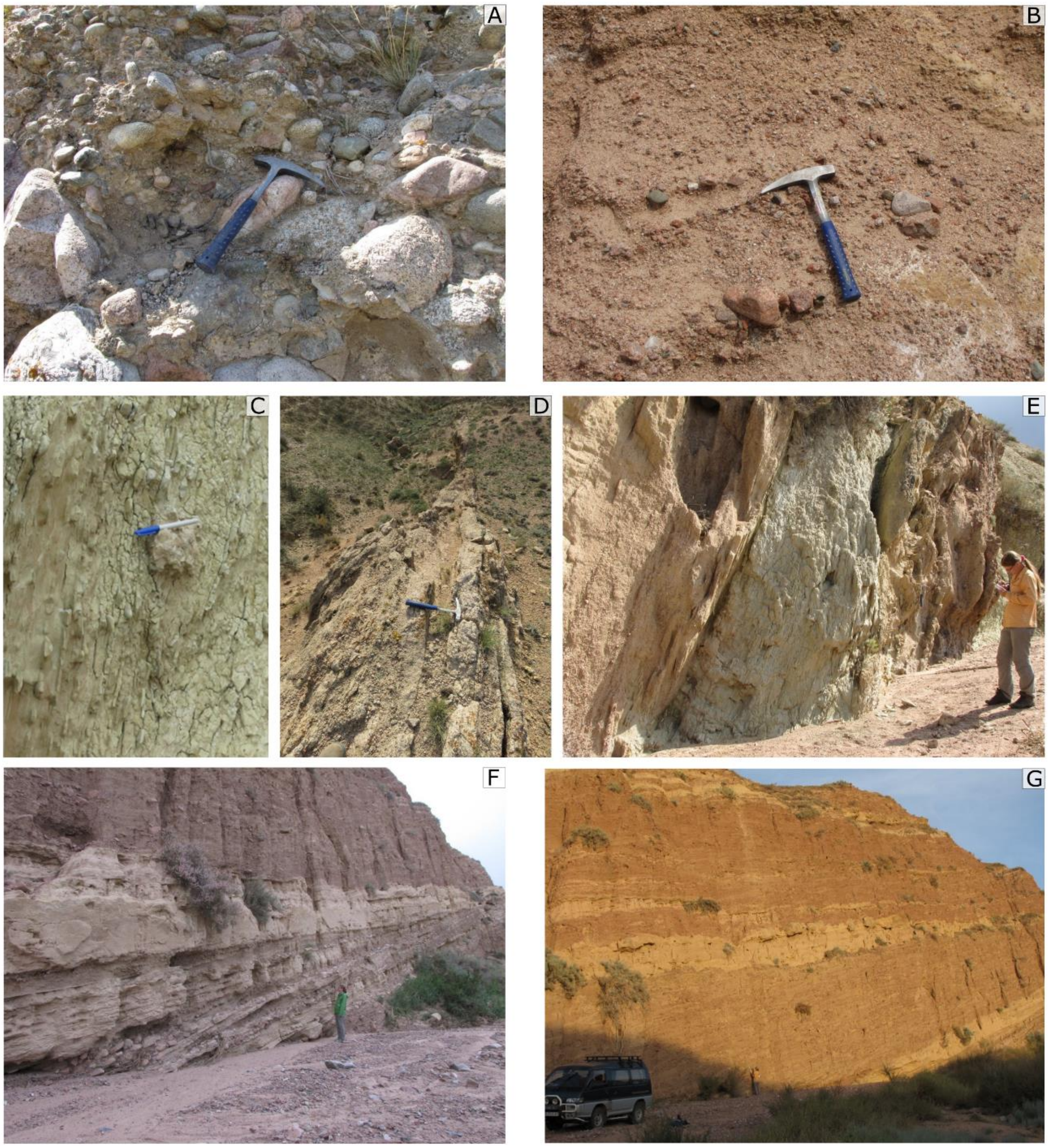

Figure 3.3. Characteristic field photos from the Kaji Say section. Stratigraphic positions are shown in Figure 3.2; locations are shown in Figure 3.4. (A) Grey granitic conglomerates. Hammer for scale. (B) Angular red gravel conglomerates. Hammer for scale. (C) Lacustrine sediments. Pen for scale is 15 cm long. (D) Sandstones of the beach facies, which mark the beginning of lacustrine deposition. Hammer for scale. (E) Interbedding of lacustrine (greenish-white) and alluvial (beige) deposits. Person for scale is 170 cm tall. (F) Growth strata. Person for scale is 170 cm tall. (G) Deposits of the Sharpyl Dak sedimentary group. Car for scale is ca. 2 m high.

In the lower Chu unit, the red and grey conglomerates laterally and stratigraphically change into sandstones and siltstones. Grey and red beds alternate and have sharp boundaries. Mixed coarse grey and greyish-red sandstones with red gravel lenses occur in the middle part of the section. Grey granitic channel lag conglomerates are generally coarser than the red ones, and grey deposits are better sorted and better cemented. Sandstones are crossbedded; siltstones are laminated and contain pedogenic calcrete nodules and lenses of poorly sorted pebbly and sandy gravel. In the upper Chu unit, white marly sandstones are fine, well sorted and well cemented; beige sandstones are coarse and contain lenses of red gravel. Blue calcareous mudstones contain rare ostracode shells (see petrography section, below); calcareous siltstones contain rare pedogenic calcrete nodules and display soft sediment deformation and slump folding directed towards the lake. The beds in the upper Chu unit thicken to the northwest. The Chu – Sharpyl Dak transition is gradational. Sharpyl Dak deposits are 60 m thick in the section; they consist of 10-20-m-thick red conglomerate beds of angular gravel and cobble clasts with poorly sorted matrix, as well as beige sandstones, white marls and white calcareous siltstones.

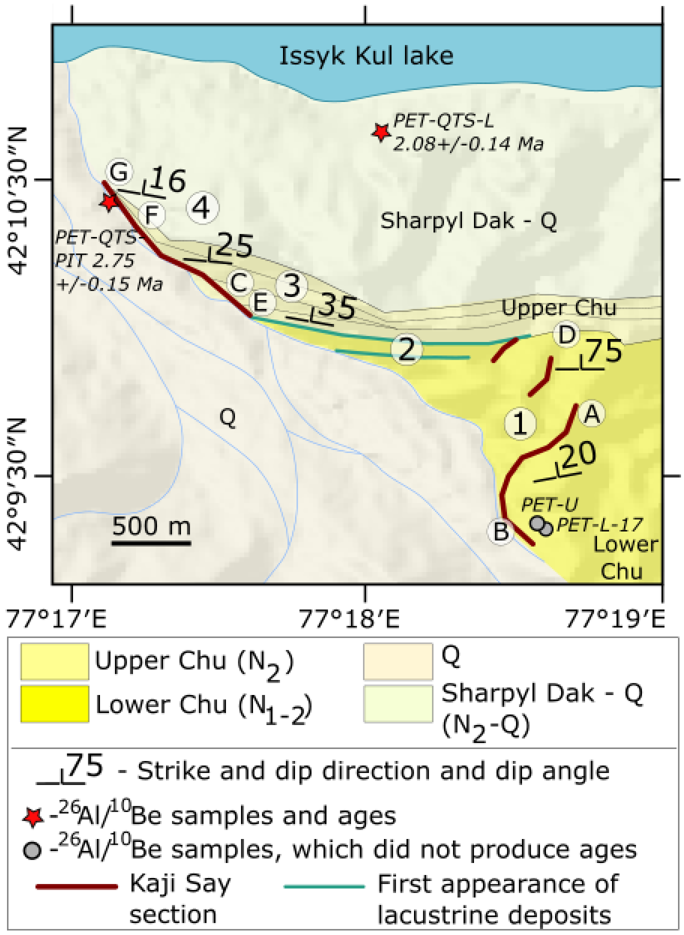

Figure 3.4. Kaji Say section area (location shown in Figure 3.1). Sedimentary units are mapped using Bing Maps satellite imagery and topography based on SRTM30 digital elevation data. A-G show locations of the corresponding photos, represented in Figure 3.3. 1 – Eastern transect of the section showing shallow dips in the stratigraphically older part and vertical dips in the stratigraphically younger part. This dip pattern defines a fold; cross section shown in Roud et al. (2021). 2 – First lacustrine beds in the area. The stratigraphically older lacustrine bed does not reach the measured section and is not included in the description (Figure 3.2). The stratigraphically younger bed represents the first lacustrine beds included in the description. 3 – Growth strata (photo shown in Figure 3.3F). 4 – Western transect of the section with shallow dips. Stratigraphic units in the legend: N_{1-2} – Late Miocene – early Pliocene; N2 – Pliocene; N2-Q – Pliocene – Quaternary; Q – Quaternary.

Clast counting was performed at 4 localities in the lower Chu unit: 85 m, 144 m, 320 m, and 411 m. Grey conglomerates consist predominantly of white and red granite clasts with a minor occurrence of volcanic rocks, shale, quartzite, pegmatitic quartz, metamorphic sandstone, and sandstone clasts. Red angular conglomerates show the prevalence of red porphyry clasts with quartz phenocrysts, and the presence of granite, quartzite, pegmatitic quartz, volcanic, and metamorphic sandstone clasts. Clast compositional data for this and the other four localities are shown in the Supplementary Material.

3.4.1.2 Ak Terek section

The Ak Terek section is a 500-m-thick sequence of the Chu group, located in the southwestern part of the basin (Figure 3.1C; see Supplementary Figure S3.1 for detailed location of the section; detailed geological maps of the Ak Terek section area are available in Roud et al., 2021 and Burgette et al., 2017). The deposits represent a series of depositional cycles with normal gradation: grey conglomerates are interbedded with well sorted sandstones, beige siltstones and mudstones (Figure 3.5). The top of the section represents the uppermost Chu deposits close to the overlying coarse conglomerates of the Sharpyl Dak group. Paleocurrent measurements indicate predominantly northeast flow directions. Well rounded conglomerate clasts are of gravel and cobble size (Figure 3.6A). Granite is the dominant source rock type in the lowermost part of the section. Metamorphic sandstone, volcanic rocks and quartzite clasts are also found.

In the lowermost part of the section, mudstone beds contain layers of poorly developed paleosols and slickensides, with a gradual upsection increase in paleosol nodule abundance (Figure 3.6B). In the uppermost 80 m of the section, the thickness of fine deposits and the amount of pedogenic nodules decrease. Two prominent 30-cm-thick gypsum layers were found at 430-440 m of the section, while older deposits of the section contain only rare thin lenses of gypsum.

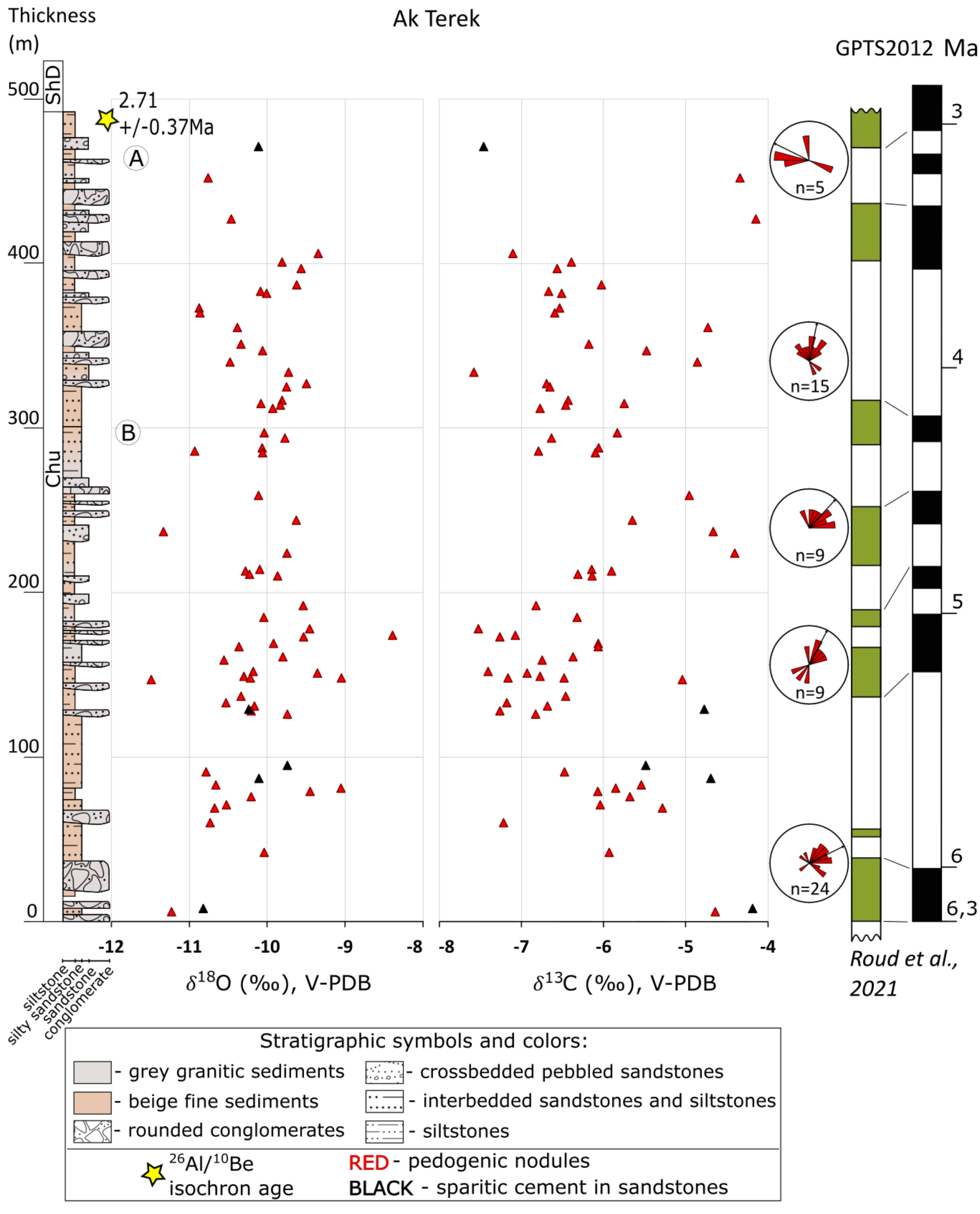

Figure 3.5. The Ak Terek stratigraphic section (location shown in Figure 3.1) with a $^{26}Al/^{10}Be$ isochron burial age, rose diagrams of paleocurrent flow directions (black arrow shows the main vector) and stable isotopic values plotted against the magnetostratigraphic age model of Roud et al. (2021). ShD is Sharpyl Dak. A-B show stratigraphic positions of photos, represented in Figure 3.6.

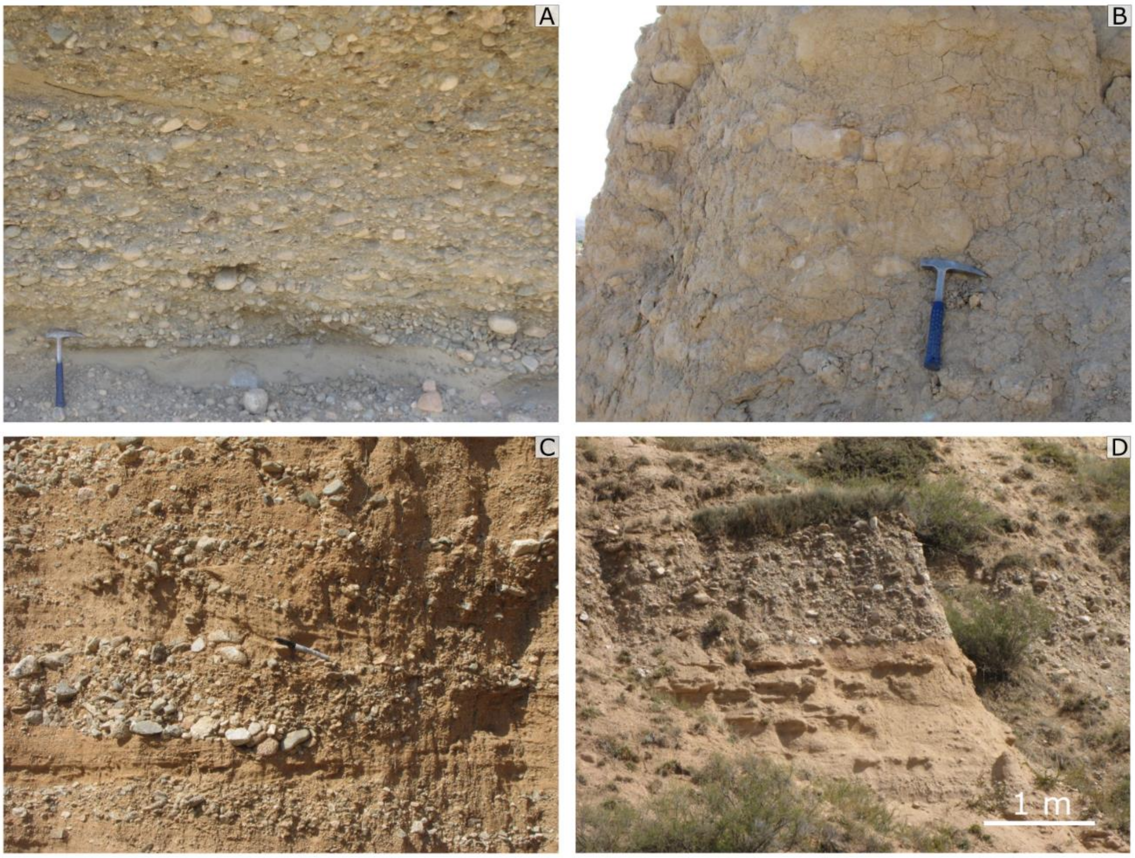

Figure 3.6. Characteristic field photos from the Ak Terek (A-B), Toru Aygir (C) and Cholpon Ata (D) sections. Stratigraphic positions of A-B are shown in Figure 3.5; geographical locations of A-B are shown in Supplementary Figure S3.1. Stratigraphic position of C is shown in Supplementary Figure S3.3. Stratigraphic position of D is shown in Supplementary Figure S3.4. (A) Conglomerates in the Ak Terek section. Hammer for scale. (B) Floodplain deposits with paleosol horizons in the Ak Terek section. Hammer for scale. (C) Conglomerate channels in the Toru Aygir section. Pen for scale is 15 cm long. (D) Conglomerate channels and floodplain deposits in the Cholpon Ata section.

3.4.1.3 Jergalan section

The Jergalan section is located in the eastern part of the Issyk-Kul basin (Figure 3.1C). We could not describe the sedimentary sequence in detail because of the steep relief and poor exposure due to numerous landslides. The sequence crops out in two cliffs (Figure 3.7A). The lower part of the section in cliff 1 represents mostly sandstones and fine-grained material. The amount and thickness of conglomerates gradually increase upsection. The conglomerates are massive, matrix supported, and interbedded with thin sandstone beds. Conglomerates were deposited in channel structures incising into finer beds. The beds dip gently to the west. We estimated the most probable position of the Chu – Sharpyl Dak transition prior to sampling for $^{26}Al/^{10}Be$ isochron burial dating. The contact between lower fine-grained sedimentary rocks and upper conglomerates in cliff 2 is visually similar to the Chu – Sharpyl Dak transition in the Kaji Say section and might also represent the beginning of the Sharpyl Dak conglomerate accumulation (Figure

3.7D). Sharp contacts are exposed in the uppermost parts of both ca. 200 m high cliff walls (Figures 3.7B-C). The gently dipping beds are truncated by almost flat-lying boulder-bearing conglomerates. These conglomerates cut down into the underlying units. Clast count and paleocurrent measurements were performed at the position of sample JGL17 at the base of the gently-dipping conglomerates above the lower part of the section. Conglomerates are mainly composed of clastic sedimentary rocks, as well as clasts of granites, volcanic rocks, quartzite and quartz. Paleocurrent measurements suggest south-directed transport.

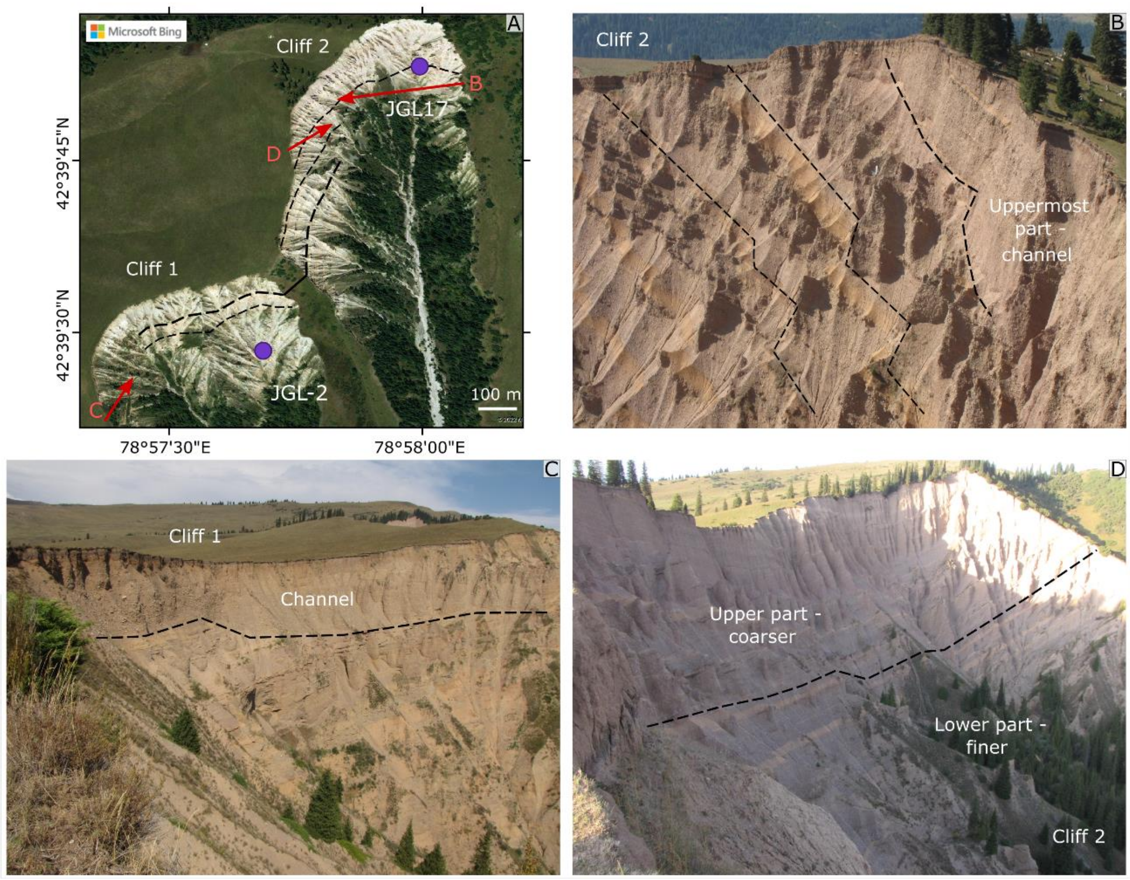

Figure 3.7. Satellite imagery and field photos of the Jergalan section (location shown in Figure 3.1). (A) Bing Maps image of the section showing the two cliffs and positions of the $^{26}Al/^{10}Be$ isochron burial dating samples. Lower (finer) part of the section outcrops in cliff 1; cliff 2 represents the transition between the lower and upper (coarser) parts of the section. Dashed lines show bedding and correlation of beds between the two cliffs. Red arrows show the view directions of the corresponding photos B-D. (B) Uppermost part of the section with angular unconformity and a channel structure on top of the cliff 2. (C) Angular unconformity and a channel structure on top of the cliff 1. (D) Gradational transition between the lower (finer) and upper (coarser) parts. Dashed line shows the estimated beginning of the Sharpyl Dak group deposition.

3.4.1.4 Toru Aygir section

The 24-m-thick Toru Aygir section is situated in the northwestern side of the basin (Figure 3.1C; detailed geological map of the Toru Aygir area is shown in Supplementary

Figure S3.2). The lower part consists of brown fine and coarse sandstones, with interbeds of granitic pebbles and gravel and thin lenses of siltstones. The upper part consists of a series of normally-graded conglomerates deposited in channel structures and well-sorted sandstones (Figure 3.6C; stratigraphic log is shown in Supplementary Figure S3.3). The conglomerates and sandstones gradually change into one another along strike. Paleocurrent measurements show predominantly south-directed transport (Figure 3.1C and Supplementary Figure S3.3). The most abundant rock type among the conglomerate clasts is subvolcanic rocks with plagioclase phenocrysts. Clasts of granites, mafic igneous rocks, and volcanic rocks are also found.

3.4.1.5 Cholpon Ata section

The 20-m-thick Cholpon Ata section is situated on the northern side of the basin (Figure 3.1C; detailed geological map of the Cholpon Ata area is shown in Supplementary Figure S3.2). It consists of rounded conglomerates, siltstones, and beige well-sorted crossbedded fine to coarse sandstones with lenses of granitic pebbles and cobbles (Figure 3.6D; stratigraphic log is shown in Supplementary Figure S3.4). Interbeds of well-cemented and well-sorted sandstones appear every ca. 1.5 meter. Thickness of conglomerate beds varies along the section from 20 cm to 1.5 m. Paleocurrent directions show predominantly southward flow directions (Figure 3.1C and Supplementary Figure S3.4). Granites are dominant among conglomerate clasts besides clasts of phyllite, volcanic rocks and clastic sedimentary rocks.

3.4.2 ^{26}AL/^{10}BE ISOCHRON BURIAL DATING

Five of the ten collected samples yielded usable results (Figure 3.8). The ^{26}Al and ^{10}Be concentrations of the other samples do not form an isochron – either due to the low number of datapoints (e.g., PET-L and PET-U) or due to burial ages exceeding the useful time range of the ^{26}Al - ^{10}Be isotope pair (e.g., CA17-1 and CA17-6) – and so burial ages could not be calculated with confidence for these samples. In the Kaji Say section, the Chu – Sharpyl Dak ^{26}Al/^{10}Be-isochron-inferred transition age is 2.75 ± 0.15 Ma (sample PET-QTS-PIT; Figure 3.8E) and the top of the section in the Sharpyl Dak deposits is 2.08 ± 0.14 Ma (sample PET-QTS-L; Figure 3.8D). In the Ak Terek section, the upper Chu deposits close to the overlying Sharpyl Dak provide an age of 2.71 ± 0.37 Ma (sample AKT-U; Figure 3.8C). In the Jergalan section, sample JGL17 yielded an age of 4.26 ± 0.44 Ma for the presumable Chu – Sharpyl Dak transition (Figure 3.8H). In the case of JGL-2, the obtained ^{26}Al concentrations were statistically indistinguishable from the procedural blank. Given that no ^{27}Al carrier solution was added to the JGL-2 samples during processing, correcting for ^{26}Al blank is not strictly necessary (see Wilcken et al., 2022 for more details). Using the raw (i.e., not blank-corrected) ^{26}Al, JGL-2 produces an age of 4.76 ± 0.82 Ma (Figure 3.8I2).

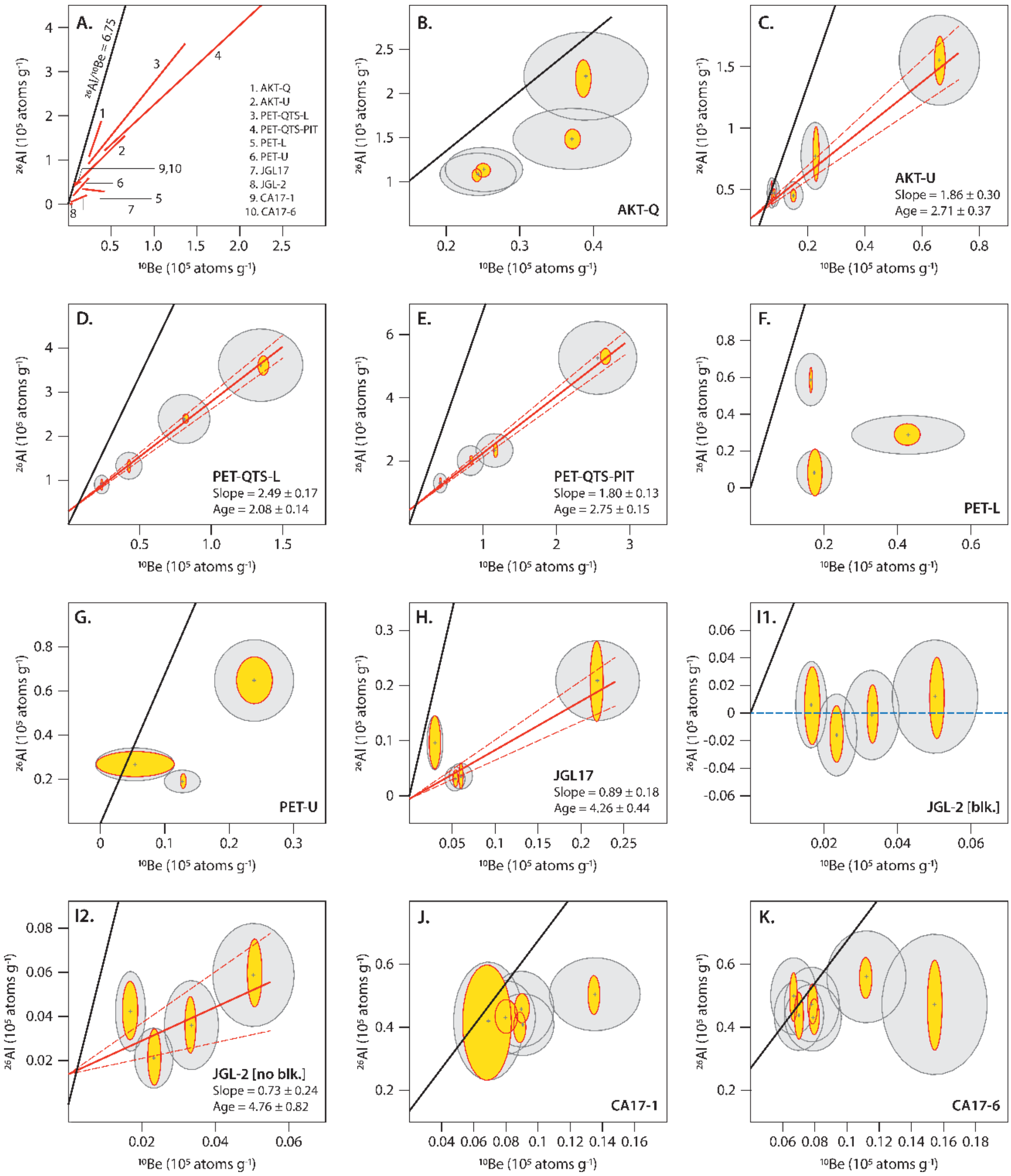

Figure 3.8. Summary of cosmogenic ^{26}Al/^{10}Be isochron burial dating results. (A) Compilation of isochrons (solid red lines) with data points excluded for clarity. Plots (B-C) – Ak Terek; (D-G) – Kaji Say; (H-I2) – Jergalan; (J-K) – Cholpon Ata. (B-K) Raw cosmogenic ^{26}Al and ^{10}Be concentrations are shown as yellow 1-sigma error ellipses and linearised concentrations are shown as grey 1-sigma error ellipses. Solid red lines are the error-weighted best fit to the data, and dashed red lines are 1-sigma error bounds. Ages are in Myr. Solid black lines in all plots represent theoretical isochrons for constant production (i.e., no burial) assuming an ^{26}Al/^{10}Be production rate ratio of 6.75. Amalgamated sand samples are not included in the plots. (I1) shows ^{26}Al concentrations at JGL-2 corrected for procedural blank (blue dashed line) and (I2) shows results without blank correction applied to the ^{26}Al data (see text for more details).

3.4.3 Petrographic study of thin sections

Thin sections of fluvial-alluvial sandstones from the Kaji Say and Ak Terek sections show mechanical compaction of sandstones, which resulted in point to concavo-convex contacts, as well as ductile deformation of detrital mica (Figures 3.9A-B). Detrital feldspar grains are partially corroded by calcite cement. The Ak Terek and Kaji Say sandstone samples are predominantly arkose and cemented by calcite, which consists mostly of sparitic blocky cement (Figure 3.9A). Poikilotopic calcite cement is found in samples of fluvial-alluvial sandstones of the Ak Terek section and the lower Chu unit of the Kaji Say section (Figure 3.9B). Sandstones from the upper Chu unit of the Kaji Say section are not compacted; they contain primary carbonate micrite and microsparite cement, as well as patchy sparitic cement (Figure 3.9C). Lacustrine samples are composed of primary dense micrite and microsparite (Figure 3.9D). Some lacustrine samples contain ostracode shells, desiccation cracks, and pores with alveolar textures filled with sparitic cement (Figures 3.9D-E).

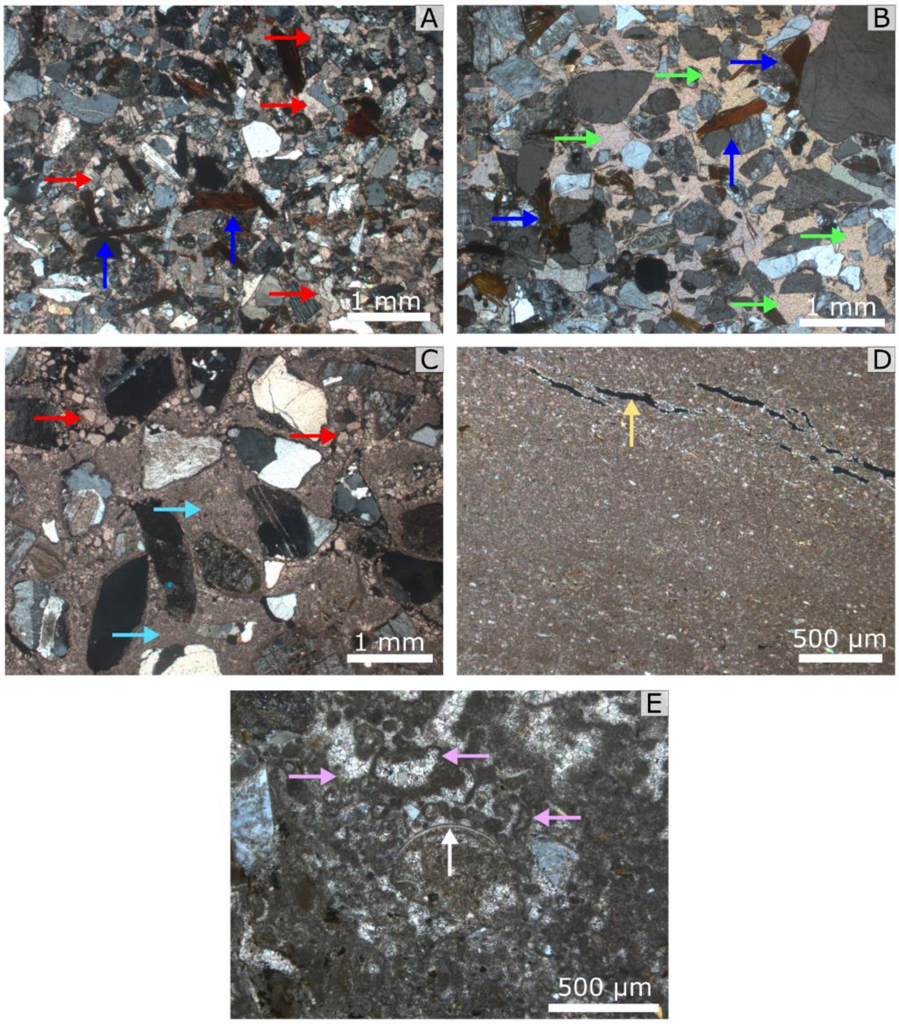

Figure 3.9. Characteristic microphotographs of thin sections from the Kaji Say and Ak Terek sequences under XPL representing early diagenetic and palustrine alteration. (A) Sandstones from the fluvial-alluvial

facies, characteristic of the Kaji Say and Ak Terek sections, with sparitic blocky calcite cement (red arrows) and mechanical compaction (dark blue arrows). (B) Sandstones from the fluvial-alluvial facies, characteristic of the Kaji Say and Ak Terek sections, with poikilotopic calcite cement (green arrows) and mechanical compaction (dark blue arrows). (C) Sandstones from the beach facies (Kaji Say) with primary micrite (light blue arrows) and sparitic calcite cement (red arrows). (D) Lacustrine micrite (Kaji Say) with planar cracks (yellow arrow). (E) Lacustrine micrite (Kaji Say) with an ostracode shell (white arrow) and pores with pedogenic alveolar texture (pink arrows) filled with sparitic calcite cement.

3.4.4 Oxygen and carbon isotope ratios

$\delta^{18}O$ values of Kaji Say samples (Figure 3.2) range from -11.5‰ to -7.3‰ (PDB), with an average value of -9.6 ± 1.1‰ (1σ); $\delta^{13}C$ values range from -7.1‰ to 0.3‰ (PDB), with an average value of -4.1 ± 1.9‰ (1σ). Samples of pedogenic nodules were taken throughout the whole section, with average values of $\delta^{18}O$ = -9.7 ± 0.8‰ and $\delta^{13}C$ = -4.5 ± 0.8‰. Samples of carbonate cement in fluvial sandstones were taken from the lower Chu unit, with average values of $\delta^{18}O$ = -10.4 ± 0.9‰ and $\delta^{13}C$ = -6.1 ± 0.5‰. Samples of lacustrine marl, siltstone, and mudstone were taken from the upper Chu unit, with average values of $\delta^{18}O$ = -8.8 ± 0.9‰ and $\delta^{13}C$ = -2.1 ± 1.2‰.

$\delta^{18}O$ values of Ak Terek samples (Figure 3.5) range from -11.5‰ to -8.4‰ (PDB), with an average value of -10.1 ± 0.6‰ (1σ); $\delta^{13}C$ values range from -7.6‰ to -4.2‰ (PDB), with an average value of -6.1 ± 0.9‰ (1σ).

Both $\delta^{18}O$ and $\delta^{13}C$ values from the Kaji Say gradually increase upsection, whereas Ak Terek values show no trend, but have a higher variability.

The stable isotope data are provided in the Supplementary Material (Table S3.1).

3.5 Discussion

3.5.1 Depositional age and environment

3.5.1.1 Kaji Say

Two magnetostratigraphic age models have been published for the Kaji Say section (Roud et al., 2021). The first option features continuous sedimentation between 12.7 Ma and 9.5 Ma, with an average sedimentation rate of 25 cm ka^{-1} and the Chu − Sharpyl Dak transition at ca. 10 Ma. The second, preferred option assumes a 2 Ma hiatus in the middle of the section with ages of 7.0−5.1 Ma for the lower part and 3.0−2.4 Ma for the upper part, and average sedimentation rates of 23 and 30 cm ka^{-1}, respectively. The Chu − Sharpyl Dak transition for the second option is at 2.8−2.6 Ma. The new $^{26}Al/^{10}Be$ isochron burial ages we obtained from the upper part of the section show that this transition at ca.

640 m in the section is 2.75 ± 0.15 Ma (sample PET-QTS-PIT, Figure 3.8E), and the Sharpyl Dak sample at the top of the section is 2.08 ± 0.14 Ma (sample PET-QTS-L, Figure 3.8D). The two sample localities are shown in Figure 3.2 and Figure 3.4. Although the isochron burial dating did not work in the lowermost part of the section (samples PET-L and PET-U, Figure 3.8F and Figure 3.8G, respectively; see Figure 3.4 for position), our two $^{26}Al/^{10}Be$ isochron burial ages allow for the elimination of the first magnetostratigraphic age model option and stipulate that the age of the Kaji Say section is late Miocene – early Pleistocene (Figure 3.2).

Predominantly northwest paleocurrent flow directions indicate that the sediments were sourced from the Terskey range. The lower Chu unit represents a fluvial-alluvial system with overbank deposits, reflecting a braided river system with different source areas within the Terskey range. Rounded well-sorted grey conglomerate clasts (Figure 3.3A) originated from the widespread granites of the Terskey range. Angular unsorted matrix-supported red gravel conglomerates (Figure 3.3B) were presumably delivered from the Taldysui subvolcanic complex, located at the front of the Terskey range around the Kaji Say area. This interpretation is based on the geological map of Kyrgyzstan (scale 1:500000, VSEGEI, 2008). The Taldysui subvolcanic complex does not crop out upstream of our other studied sedimentary sections and they do not contain such clasts.

The characteristics of the red gravel conglomerates indicate that they are debris flow deposits, which represent an alluvial fan with deposits derived from a proximal source area. The grey granitic conglomerates and sandstones were deposited in channel structures and represent the bedload of a braided river with prolonged flows that allowed sorting and normally-graded deposition. Conglomerates and well-sorted sandstones mark pulses of high-energy flows. Siltstones represent floodplain deposits that accumulated from sheet flows during strong floods. Pedogenic alteration of the fine sediments is weak, represented by immature horizons of small calcrete nodules. Their presence indicates changes in the depositional environment with periods of decreased deposition between pulses of conglomerate accumulation (Alonso-Zarza, 2003; Breecker et al., 2009).

The depositional environment changed significantly in the upper Chu unit, which represents a lacustrine environment with a beach, a distal fan delta, and periodic rapid intense debris flow deposits of predominantly red angular conglomerates. Lacustrine calcareous mudstones, calcareous siltstones and marls (Figure 3.3C) were deposited in a shallow lake with low sedimentation rates and decreased clastic input. These are the oldest reported lacustrine deposits in the Issyk-Kul basin above the modern lake level. The occurrence of pedogenic nodules in the lacustrine carbonates and pedogenetic alteration of the lacustrine mudstone, observed in thin sections (see section 5.2.1), point to repeated lowering of the lake level and exposure of the deposits during dry periods with very slow sedimentation (Alonso-Zarza, 2003; Breecker et al., 2009). The occurrence of thin sandstone lenses within lacustrine marls indicates distal fan delta deposition at the lake margin. The coarse debris flow deposits show that intensified terrigenous input propagated into the lake. Within the measured section, the first beach facies sandstone bed occurs at 450 m, followed by a 5-cm-thick lacustrine calcareous mudstone bed (Figure 3.3D). Our field observations indicate that lacustrine deposits first appear stratigraphically earlier, ca. 200 m to the west of the measured section and laterally change into fluvial-alluvial deposits eastward (Figure 3.4). Overall, there were periodic shifts between slow sedimentation in a lacustrine/palustrine system and rapid sedimentation in an active alluvial system (Figure 3.3E). The gradational Chu - Sharpyl Dak transition marks an increase in frequency and thickness of the conglomerate beds, while lacustrine beds became thinner. The overlying Sharpyl Dak conglomerates represent a large series of debris flow deposits in a proximal alluvial fan that progressively filled the basin and shifted the lake margin northward (Figure 3.3G).

3.5.1.2 Ak Terek

The straightforward correlation of the polarity pattern retrieved from the Chu group deposits with the geomagnetic polarity time scale indicates that the Chu group was deposited between 6.3 and 2.8 Ma with an average sedimentation rate of 13 cm ka^{-1}; there is a short interval with a sedimentation rate of 21 cm ka^{-1} at ca. 5 Ma (Roud et al., 2021). This age model places the Chu – Sharpyl Dak transition at 2.8 Ma (Figure 3.5). Our $^{26}Al/^{10}Be$ isochron burial age for the uppermost Chu is 2.71 ± 0.37 Ma (sample AKT-U, Figure 3.8C; see Figure 3.5 and Supplementary Figure S3.1 for position of the sample), consistent with the magnetostratigraphic age constraints. The sample from the Sharpyl Dak deposits did not yield reliable results (sample AKT-Q, Figure 3.8B). However, these two dating methods provide highly-consistent results; thus, we can conclude that the Ak Terek section was deposited during the late Miocene – Pliocene.

The Ak Terek section is interpreted to represent the deposits of a meandering river system. The rounded and well-sorted conglomerates and sandstones are mostly granitic and originate from the granites of the Terskey range, as indicated by the predominantly northeast paleocurrent flow directions. The conglomerates were deposited in large channels; together with well-sorted grey sandstones, they comprise the river bed load (Figure 3.6A). Sandy siltstones and massive mudstones represent a floodplain with episodical fluvial input during flood stages. Repeated alternations between fluvial and floodplain deposits suggest a distal fluvial system with a migrating channel on a floodplain. Pedogenesis occurred in fine-grained deposits throughout the section with thin, immature, rare horizons of small calcrete nodules in the lower part of the section and a gradual upsection increase in their size and abundance (Figure 3.6B). Calcrete nodule horizons and gypsum layers in the upper part of the section suggest alternation of stronger rainfall and prolonged dry periods (Breecker et al., 2009) with very low sedimentation rates (Alonso-Zarza et al., 1992). The upsection increase in nodule abundance between ca. 6 and ca. 3.5 Ma reflects a Pliocene increase in water availability and seasonality. A decrease in the pedogenic nodule abundance and decreasing thickness of floodplain deposits after ca. 3.5 Ma suggest shortening of periods of slow deposition and soil formation and likely more frequent conglomerate deposition due to an increase in tectonic activity or glaciation in the Terskey range.

3.5.1.3 Jergalan

The sequence records a proximal high energy braided river system gradually transforming into a proximal alluvial fan. Conglomerates in the uppermost parts of the two cliffs represent the fill of a coarse-grained braided river above an angular unconformity (Figures 3.7B-C). Both channel structures probably represent Quaternary deposition. We interpret the Chu – Sharpyl Dak transition to be represented by the gradational contact between finer and coarser gently-dipping deposits; therefore, Sharpyl Dak deposition started when the conglomerates started to prevail. The results from sample JGL17, taken from the bottom of the upper (coarser) part (Figure 3.7A), suggest that the age of the Chu – Sharpyl Dak transition occurs at 4.26 ± 0.44 Ma (Figure 3.8H). The stratigraphically older JGL-2 sample yields an $^{26}Al/^{10}Be$ isochron burial age of 4.76 ± 0.82 Ma when ^{26}Al concentrations are not blank-corrected (Figure 3.8I2). The above results roughly constrain the Chu - Sharpyl Dak transition in Jergalan to be not older than 5 Ma; i.e. early Pliocene. This age is notably older than at Kaji Say and Ak Terek, where the transition occurred at 2.8-2.6 Ma. The paleocurrent analysis suggests that the Chu - Sharpyl Dak transition unit was fed by sediments from the Kungey range. Hence, we suggest that exhumation of the eastern Kungey range began at ca. 5 Ma.

3.5.1.4 Toru Aygir and Cholpon Ata

The Toru Aygir and Cholpon Ata sequences represent deposits from a meandering fluvial system. A series of channels in the Toru Aygir section with subrounded conglomerates and well-sorted sandstones represent deposition in a high energy flow from the bedload of a river (Figure 3.6C). In the Cholpon Ata section, large channels filled with rounded conglomerates and sandstones are interbedded with siltstones and represent the coarse bedload of a migrating channel on a floodplain (Figure 3.6D). A detailed description of both sections and geological maps of the area are presented in Selander et al. (2012). The Toru Aygir area is also described in details in Bowman et al. (2004).

Both sequences belong to the Chu group. Selander et al. (2012) described two members of the Chu group on the southern flank of the Kungey range – the stratigraphically older Terskey member with northward-flowing paleocurrent indicators, sourced from the Terskey range, and the stratigraphically younger Kungey member with southward-flowing indicators, sourced from the Kungey range. The Terskey member is mapped throughout the range front, while the Kungey member is exposed only in the eastern part of the Kungey range (Supplementary Figure S3.2). The initiation of Kungey range growth is estimated to be between 7-4 Ma (Selander et al., 2012). The Toru Aygir section is located in the western Kungey range and the Chu deposits there belong to the Terskey member (Supplementary Figure S3.2), although our measurements of mainly southward paleocurrent directions contradict data from Selander et al. (2012) (Figure 3.1C and Supplementary Figure S3.3). The Cholpon Ata section is situated in the eastern Kungey range and exhibits both members (Supplementary Figure S3.2), although our measurements of mostly southward paleocurrent directions in both the stratigraphically older (Terskey member) and stratigraphically younger (Kungey member) parts of the section also contradict data from Selander et al. (2012) (Figure 3.1C and Supplementary Figure S3.4). This suggests that the Terskey member of the Cholpon Ata and Toru Aygir sections includes deposits sourced mainly from the Kungey range, in contrast with data from Selander et al. (2012), which show a distinctive prevalence of northward-directed paleocurrents in the Terskey member.

3.5.2 Diagenetic characteristics

3.5.2.1 Thin section inspection

Sparitic and poikilotopic calcite cement and mechanical compaction in fluvial-alluvial sandstone samples (Figures 3.9A-B) suggest that the Ak Terek section and the lower Chu unit of Kaji Say underwent early stages of diagenesis (Worden et al., 2018). Higher temperatures associated with diagenesis may lead to crystal growth within the calcite cements (Worden and Burley, 2003). Therefore, the Ak Terek section and the lower Chu unit of Kaji Say might have undergone a higher degree of recrystallization than sandstones from the beach facies, alluvial and lacustrine deposits with microsparitic cement and micrite of the upper Chu unit of the Kaji Say section (Figure 3.9C). Nevertheless, some of the samples with poikilotopic cement only have point contacts between grains, which may mean that cementation occurred at an early stage of alteration without substantial burial and compaction. Lacustrine carbonate of the upper Chu unit of the Kaji Say section consists of primary micrite and microsparite and exhibits evidence of palustrine alteration during dry periods without significant burial, such as desiccation cracks and pores with alveolar textures and pore-filling sparitic calcite cement (Figures 3.9D-E; Alonso-Zarza et al., 2010). Microsparite infills porosity in primary lacustrine micrite and can result from primary cementation in a subaerial environment or during pedogenesis (Freytet and Verrecchia, 2002).

3.5.2.2 Evaluation of the diagenetic overprint in the stable isotopic record

$\delta^{18}O$ values of carbonate depend on the $\delta^{18}O$ values of the fluid from which carbonate precipitated and on the carbonate formation temperature. As such, carbonate formation and recrystallization under elevated temperatures, as well as the presence of basinal fluids during burial diagenesis, can affect the primary $\delta^{18}O$ values of authigenic carbonate minerals. Higher temperature resetting of $\delta^{18}O$ values during burial and diagenesis typically results in low $\delta^{18}O$ values (e.g. Methner et al., 2016; Quade et al., 2020) due to the temperature-dependance of water-calcite fractionation (e.g. Swart et al., 2015 and references therein). The $\delta^{18}O$ values of the Kaji Say and Ak Terek sections do not yield suspiciously low $\delta^{18}O$ values that would be associated with deep (higher temperature) burial diagenesis. One could hypothesize that the increasing $\delta^{18}O$ and $\delta^{13}C$ values with stratigraphy in the Kaji Say section could be burial related, i.e. lower values at the base of the section might reflect a higher level of diagenetic overprint due to higher temperatures. Unlike the Kaji Say samples, those from Ak Terek do not show such a trend; however, the data scatter along the Ak Terek record could reflect alteration in connection with dissolution and reprecipitation of calcite at different temperatures related to different burial depths (Sanyal et al., 2005). Distinctively more positive $\delta^{13}C$ values of lacustrine calcareous mudstone samples suggest that the primary lacustrine isotopic signal was not significantly affected by diagenetic and pedogenetic alteration (Alonso-Zarza, 2003).

We suggest that cementation and pedogenetic alteration happened under similar near-surface meteoric conditions and we argue that the similarity of $\delta^{18}O$ and $\delta^{13}C$ values of sandstone cement, pedogenic and lacustrine carbonates in the Kaji Say section suggests similar post-depositional environments in the stratigraphically older and younger parts of the Kaji Say section. At the same time, as the values in the Kaji Say and Ak Terek sections overlap (Figure 3.10), we conclude that the rocks of the Ak Terek and Kaji Say sections reflect similar post-depositional conditions of early diagenesis. Early diagenesis corresponds to near-surface and shallow burial conditions under the influence of the depositional environment when sediments are buried to less than 2 km and temperatures below 70 °C (Worden and Burley, 2003). Early diagenesis does not alter oxygen isotopic values when occurring at near surface temperatures (Garzione et al., 2004; Sanyal et al., 2005), such as would be expected in the relatively thin stratigraphic sequences that we have studied. Moreover, our stable isotope values overlap with the values from other northern Central Asian sections (Figure 3.11), the rocks of which were reported to be unaffected by burial diagenesis. As the sedimentary sequences in Central Asia have different thicknesses but show similar $\delta^{18}O$ and $\delta^{13}C$ values, burial diagenesis does not appear to have played a major role (Caves Rugenstein and Chamberlain, 2018). We therefore conclude that our sections did not experience late diagenesis and that our isotopic results reflect primary values.

3.5.3 Stable isotope analysis

3.5.3.1 Stable isotope-based paleoenvironmental reconstructions from continental carbonates

$\delta^{18}O$ and $\delta^{13}C$ values of terrestrial carbonates may record information on paleoclimate, paleoaltimetry, vegetation types, lake water characteristics and diagenesis, provided that carbonate precipitation occurs in equilibrium with soil or lake water (e.g., Cerling, 1984; Talbot, 1990; Cerling et al., 1997; Poage and Chamberlain, 2001; Garzione et al., 2004; Levin et al., 2006; Quade et al., 2011).

$\delta^{18}O$ values of pedogenic and lacustrine/palustrine carbonate reflect the temperature of carbonate formation and the $\delta^{18}O$ values of soil water or lake water, respectively. In the absence of reconstructed carbonate formation temperatures, we interpret the pedogenic carbonate $\delta^{18}O$ values in terms of changes in $\delta^{18}O$ values of local precipitation (Cerling and Quade, 1993). We interpret the lacustrine and palustrine carbonate $\delta^{18}O$ values to reflect average precipitation $\delta^{18}O$ values within the catchment area (Talbot, 1990). $\delta^{18}O$ may be modified by the impact of lake level and evaporation dynamics. For example, the preferential release of ^{16}O from lake water during evaporation leads to increased $\delta^{18}O$ values in response to enhanced evaporation.

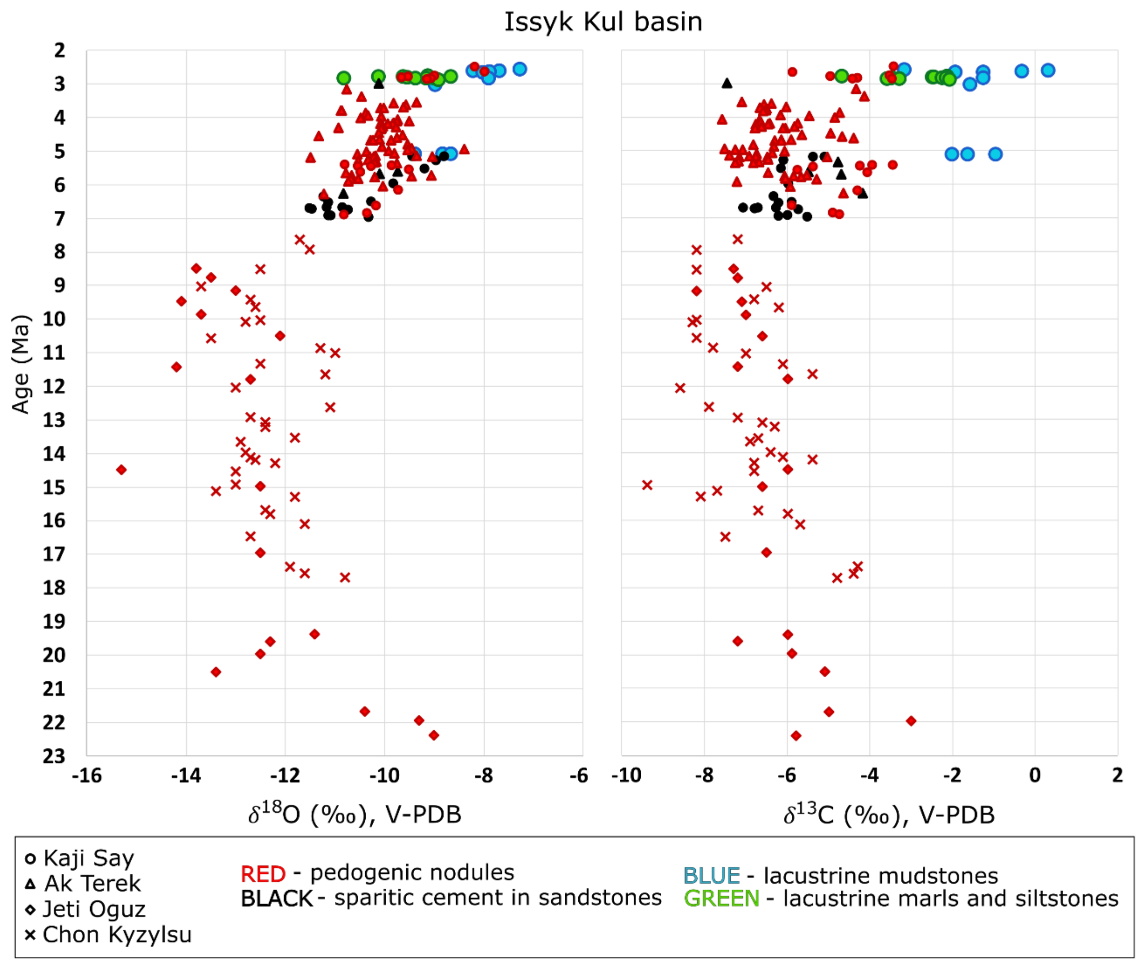

Figure 3.10. $\delta^{18}O$ and $\delta^{13}C$ data from the Issyk-Kul basin plotted against the age model. Kaji Say and Ak Terek data plotted against the original age model of Roud et al. (2021). Using the revised age for the hiatus proposed in this manuscript would shift the lacustrine mudstones plotted at 5 Ma to 3 Ma. Jeti Oguz and Chon Kyzylsu data are from Macaulay et al. (2016), replotted using the age model of Roud et al. (2021).

Mountain growth leads to orographically-induced rainout, which preferentially removes ^{18}O from water vapor and results in a systematic decrease of $\delta^{18}O$ values with elevation on the windward side and low $\delta^{18}O$ values in the lee (e.g., Chamberlain and Poage, 2000; Rowley and Garzione, 2007; Quade et al., 2011; Chamberlain et al., 2012; Mulch, 2016). Therefore, $\delta^{18}O$ values of pedogenic and lacustrine carbonates may provide a proxy for the $\delta^{18}O$ of meteoric water, and thus paleoelevation of carbonate formation.

Moreover, an increase in pedogenic carbonate $\delta^{18}O$ can point to increased evaporation or a shift in seasonality of precipitation to a warmer season. Aridity of Central Asia leads to an increase in soil and lake water evaporation, resulting in moisture recycling and high and relatively steady $\delta^{18}O$ values (Caves Rugenstein and Chamberlain, 2018). Furthermore, topographic growth of the Tian Shan created a seasonality pattern of winter-spring precipitation on the windward (northwestern) side and summer precipitation within the range and on the leeward (southeastern) side (Baldwin and Vecchi, 2016). Dry winter conditions due to weak westerlies and a dominant Siberian High lead to orographic rainout of the westerly moisture on the windward side in winter, but prevalence of cyclonic activity at high elevations in the summer leads to rainfall at high elevations (Bershaw and Lechler, 2019). This effect results in low $\delta^{18}O$ values of winter precipitation on the windward side and high and steady $\delta^{18}O$ values of summer precipitation within the range and in the lee (Wang et al., 2016; Bershaw and Lechler, 2019).

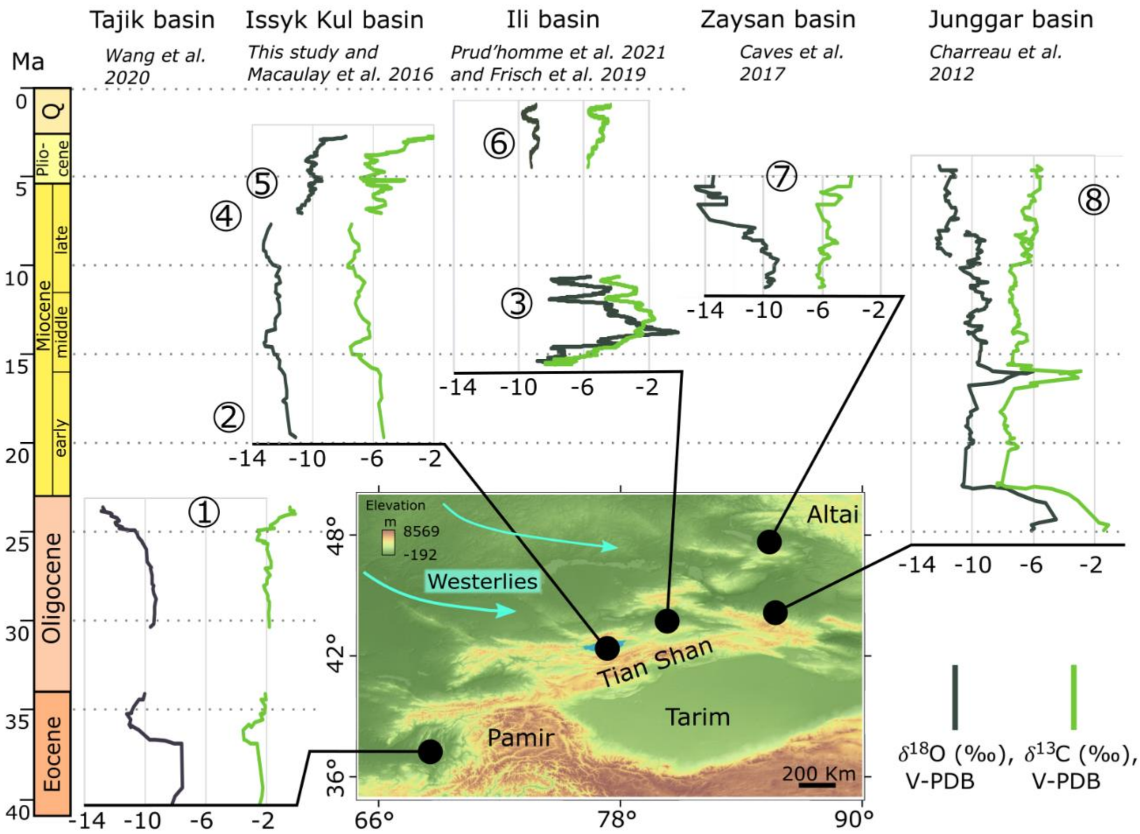

Figure 3.11. New and published $\delta^{18}O$ and $\delta^{13}C$ data from the basins on the northern (windward) side of the Tian Shan, Altai and Pamir, plotted against age. New data from the Issyk-Kul basin plotted against the original age model of Roud et al. (2021). All data except Ili basin are smoothed using a 6-point moving mean, data from the Ili basin are smoothed using a 30-point moving mean. Ili basin data from Hellwig et al. (2018) are not included due to a lack of age constraints. 1-8 show main events, reflected in the stable isotopic records (interpretations are taken from the corresponding articles): (1-2) – windward positions of the Tajik (Wang et al., 2020) and Issyk-Kul (this study and Macaulay et al., 2016) basins due to growing Tian Shan and Pamir; (3) – global climatic changes in the Ili basin caused by orbital forcing (Frisch et al., 2019), which are not reflected in time-equivalent records from other basins; (4) – change from a windward to leeward position of the Issyk-Kul basin due to northward growth of Tian Shan (this study); (5) – aridification in the Issyk-Kul basin after Kyrgyz, Kungey and Trans Ili ranges blocked the westerly moisture from reaching the basin (this study); (6) – aridification in Central Asia, caused by interactions between the westerlies and the Siberian High (Prud'homme et al., 2021); (7) – windward position of the Zaysan basin due to growing Altai (Caves et al., 2017); (8) – two records from the Junggar basin are controlled by hypsometry of the drainage basins and do not reflect climatic or tectonic changes (Charreau et al., 2012).

The $\delta^{13}C$ values of pedogenic carbonates are primarily driven by the carbon isotopic composition of vegetation and ultimately reflect the relative importance of atmospheric and soil-respired CO_2 during their formation (Cerling, 1984; Cerling and Quade; 1993).

Reduced precipitation theoretically leads to lower soil respiration rates and subsequently to a decrease in the soil carbonate formation depth and a higher contribution of atmospheric CO_2. Overall, a decrease in precipitation therefore typically results in more positive $\delta^{13}C$ values of pedogenic carbonates (e.g., Caves et al., 2016). Differences in fractionation of $\delta^{13}C$ in C_3 and C_4 plants during photosynthesis lead to ca. 14 per mil lower $\delta^{13}C$ values in C_3 plants. However, we neglect this effect because of scarce abundance of C_4 vegetation in Central Asia (e.g., Caves Rugenstein and Chamberlain, 2018).

Variations in lake carbonate $\delta^{13}C$ values generally reflect changes in biogenic productivity (e.g., Li and Ku, 1997). Because organic matter preferentially takes up the light carbon isotope (^{12}C), increased biogenic productivity leads to a relative increase of ^{13}C in dissolved CO_2, which is incorporated in carbonate during precipitation. Therefore, increased biogenic productivity in a lake leads to an increase in $\delta^{13}C$ in lacustrine carbonate. Hydrologically closed basins have no surface outlet and hence most water exits the basin through evaporation. $\delta^{13}C$ and $\delta^{18}O$ generally display a covariance in closed basins. This is typically the result of temperature changes during carbonate formation, which governs biogenic productivity as well as evaporation (e.g. Li and Ku, 1997).

3.5.3.2 Published stable isotopic records from the windward basins of the Tian Shan and Altai

By combining new stable isotope data from the Kaji Say and Ak Terek sections and published data from the Jeti Oguz and Chon Kyzylsu sections (Macaulay et al., 2016) with the age models for the four sections (Roud et al., 2021), we have compiled a continuous oxygen and carbon stable isotopic record that covers the time interval from the early Miocene to the early Pleistocene (Figure 3.10).

Other studied windward basins in the Tian Shan and Altai include the Ili basin (Hellwig et al., 2018; Frisch et al., 2019a; Prud'homme et al., 2021), Tajik basin (Wang et al., 2020), Junggar basin (Charreau et al., 2012), and Zaysan basin (Caves et al., 2017) (Figure 3.11). In the sedimentary section in the Tajik basin (1800-m-thick, 41-23.3 Ma), mudstones and carbonate cement in sandstones were analyzed. The $\delta^{18}O$ record shows a change toward wetter conditions after ca. 25 Ma when the basin setting shifted to a windward position due to the establishment of the Pamir and Tian Shan orographic barrier (Wang et al., 2020). The Kendyrlisai Valley section in the Ili basin is ca. 166-m-thick and is of late Oligocene to early Miocene ages. Starting from ca. 23.3 Ma, the sedimentary sequence records the establishment of a fluvial system, while the $\delta^{18}O$ and $\delta^{13}C$ values of pedogenic carbonates increase and reflect increasing aridity and pronounced seasonality

(Hellwig et al., 2018). The Aktau section in the Ili basin (371-m-thick, 15.6-10.6 Ma) provides a sedimentary record with pedogenic and lacustrine carbonates with features of early diagenesis and shows an overall increase in water availability, whereas the $\delta^{18}O$ and $\delta^{13}C$ values reflect changes in the depositional environment due to global climatic changes caused by orbital forcing (Frisch et al., 2019a). The $\delta^{18}O$ and $\delta^{13}C$ values of sampled pedogenic carbonates of the Charyn Canyon section in the Ili basin (ca. 80-m-thick, 4.5-0.5 Ma) reflect long-term aridification in Central Asia, caused by the interplay between the westerlies and the Siberian High (Prud'homme et al., 2021). In the Kuitun He (1800 m, ca. 10-4.5 Ma) and Jingou He (4500 m, ca. 26-8 Ma) sections in the Junggar basin, lacustrine and paleosol carbonates were analyzed, as well as carbonate cement from fluvial deposits. The $\delta^{18}O$ values of the two records are interpreted to be controlled by hypsometry of the drainage basin (Charreau et al., 2012). In the Zaysan basin section (188 m, 11.5-5 Ma), pedogenic carbonates were sampled and the late Miocene decrease in $\delta^{18}O$ values is interpreted to reflect the establishment of the spring and fall precipitation due to the downwind topographic growth of the Altai (Caves et al., 2017).

3.5.3.3 Climatic conditions from 23 to 8 Ma

$\delta^{18}O$ and $\delta^{13}C$ records from the Jeti Oguz and Chon Kyzylsu sections suggest rather stable long-term climatic conditions between 23 and 8 Ma. One may observe a subtle negative trend upsection from ca. -3 to -5‰ to ca. -7 to -8‰ in $\delta^{13}C$ values and from ca. -9 to -11‰ to ca. -12 to -14‰ in $\delta^{18}O$ values (Figure 3.10), which may reflect the establishment of windward conditions at higher elevations within the basin and a progressively higher degree of orographic rainout since the early Miocene due to topographic growth of the Terskey range downwind (Figure 3.12A). The sampled rocks in the Jeti Oguz and Chon Kyzylsu sections are thin overbank deposits with a weak pedogenic overprint; therefore, river run-off water delivered to the river overbank during floodings possibly may have had an impact on stable isotopic values. An increase in catchment area's elevation would cause delivery of water from higher elevations within the Terskey range with lower $\delta^{18}O$ values that would result in lower $\delta^{18}O$ values of the carbonates. Concurrently, wetter conditions would increase soil respiration rates and/or decrease hydraulic stress on the C_3 vegetation and lower $\delta^{13}C$ values (Macaulay et al., 2016). Therefore, this suggests that topographic growth of the Terskey range played the primary role in the decrease of $\delta^{18}O$ and $\delta^{13}C$ values between 23 and 8 Ma.

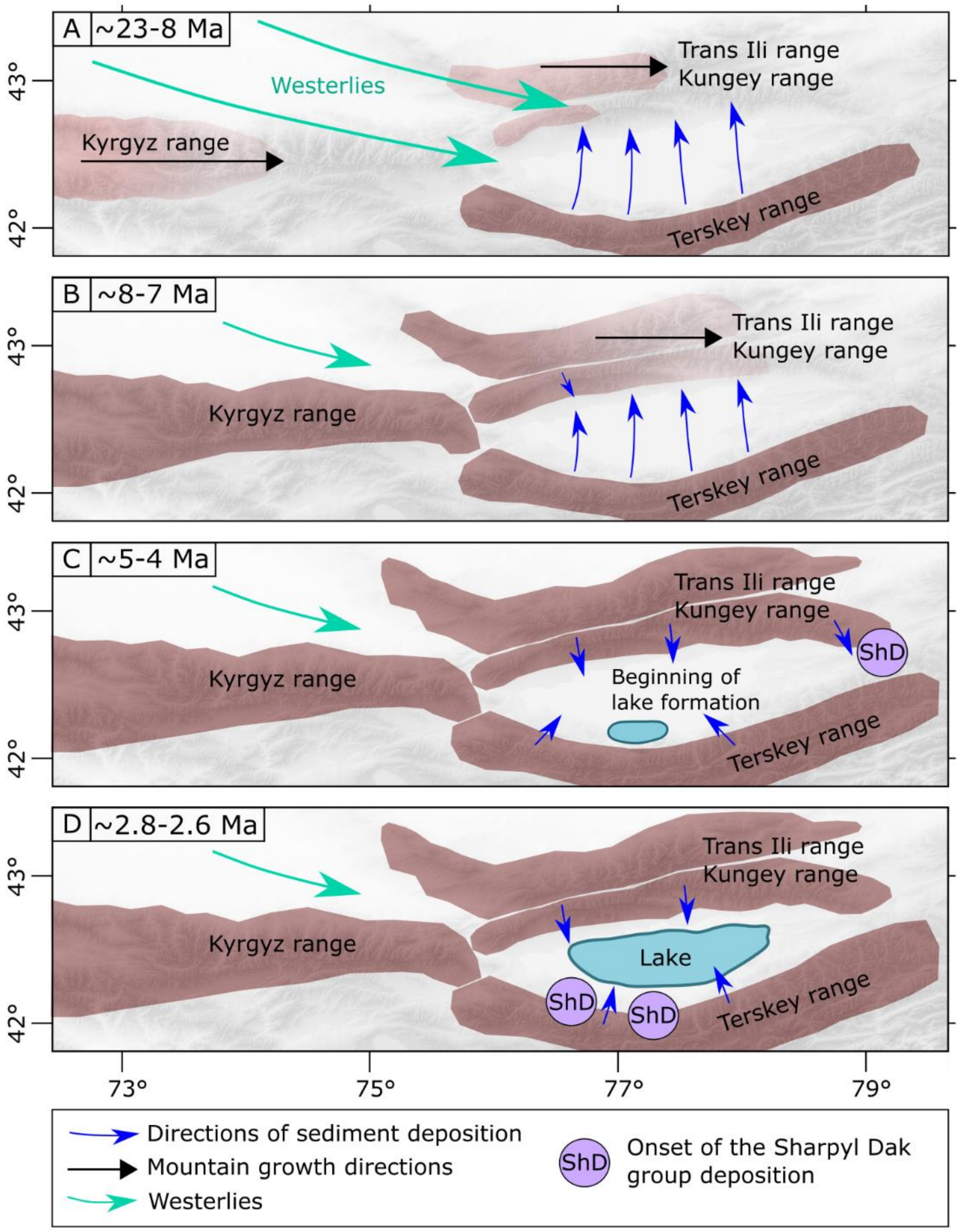

Figure 3.12. A schematic representation depicting the Neogene development of the Issyk-Kul basin. (A) Windward position of the Issyk-Kul basin due to growing Terskey range. Sediments from the Terskey range reach the low-elevated Kungey range area. (B) Sufficient surface uplift of the Kyrgyz, Kungey and Trans Ili ranges prevent the westerlies from reaching the Issyk-Kul basin. Issyk-Kul basin became leeward. (C) Beginning of lake formation in the Kaji Say area and commencement of Sharpyl Dak deposition in Jergalan due to tectonic activity. Sharpyl Dak sediments in Jergalan are sourced from the Kungey range. (D) Lake expansion and commencement of Sharpyl Dak deposition in the Kaji Say and Ak Terek areas.

A similar subtle decreasing trend in $\delta^{18}O$ values from the Tajik basin between ca. 25 and ca. 23.3 Ma, suggests the primary role of the growing topography in both Tajik and Issyk-Kul basins (Figure 3.11). At the same time, the late Oligocene – early Miocene stable isotopic records from the Ili basin show increasing trends of $\delta^{18}O$ from ca. -11 to ca. -7‰ and $\delta^{13}C$ from ca. -9 to ca. -5‰ (Hellwig et al, 2018; these data are not included in Figure 3.10 due to a lack of age constraints). The time-equivalent part of the Junggar basin $\delta^{18}O$

and $\delta^{13}C$ records shows no trend with $\delta^{18}O$ values of ca. -10‰ and $\delta^{13}C$ values of ca. -8‰ (Figure 3.11). Not only the $\delta^{18}O$ values, but also the $\delta^{13}C$ values from the Issyk-Kul and Ili basins show opposing trends. Whereas the Issyk-Kul stable isotopic values reflect the topographic growth of the Terskey range, the results from the Ili basin are interpreted to reflect increased evaporation and aridification in Central Asia (Hellwig et al., 2018), and the Junggar record reflects the hypsometry of the drainage basin (Charreau et al., 2012). Even though higher water availability was detected in the Ili basin by the establishment of a fluvial system at ca. 23 Ma (Hellwig et al., 2018), and in the Junggar basin by the presence of lacustrine deposits in the late Oligocene (Charreau et al., 2012), the stable isotopic records from these two basins do not unequivocally point to locally wetter conditions. The slight negative $\delta^{18}O$ and $\delta^{13}C$ trends in the early Miocene deposits of the Issyk-Kul basin suggest wetter conditions that are mainly controlled by local topographic, rather than regional or global climatic factors.

The middle Miocene Issyk-Kul and Ili stable isotope records show drastically different values and trends (Figure 3.11). This can be explained by the difference in data resolution and the sampled sediment facies. The Ili basin represents lacustrine and distal alluvial facies and has 821 measurements spread over ca. 5 Ma (371 m; Frisch et al., 2019a), whereas the Jeti Oguz and Chon Kyzylsu records include 53 samples, which were taken from overbank pedogenic horizons and spread over ca. 15 Ma. The low-resolution Issyk-Kul record of isotopic values obtained from pedogenic carbonate is therefore mostly driven by long-term climatic conditions. In contrast, the Ili sedimentary succession reflects global climatic and orbital changes (Voigt et al., 2017; Frisch et al., 2019b), and the Ili stable isotopic record is reported to be primarily controlled by the changes in the depositional environment (Frisch et al., 2019a). Therefore, these two records cannot be directly compared. The Issyk-Kul, Zaysan and Junggar stable isotopic records of pedogenic carbonates suggest comparable and relatively unchanged paleoenvironments up to ca. 8 Ma with no significant influence of either climatic changes or mountain growth in the middle Miocene (Figure 3.11).

3.5.3.4 Positive shift in $\delta^{18}O$ and $\delta^{13}C$ values between 8 and 7 Ma

Between 8 and 7 Ma we observe a distinctive ca. 2‰ positive shift of $\delta^{18}O$ and $\delta^{13}C$ values within the Issyk-Kul basin (Figure 3.10). The shift occurs during a ca. 0.6 Ma gap in the combined Issyk-Kul basin record and occurs between the records from the Jeti Oguz and Chon Kyzylsu sections and the records from the Kaji Say and Ak Terek sections.

There are several possible mechanisms that could induce a ca. 2‰ shift in $\delta^{18}O$ and $\delta^{13}C$ values at 8-7 Ma. 1) Given that the ca. 0.6 Ma stratigraphic gap coincides with a change in sampling localities, the decrease in $\delta^{18}O$ values may result from spatial environmental changes within the basin (Figure 3.1C). 2) An orographically-induced change from a windward to a leeward position of the basin by changes in atmospheric circulation and topography to the northwest, blocking of moisture-bearing westerlies, and an increase in evaporation and aridification. 3) Global cooling and retreat of the Parathetys, the proximal moisture source for Central Asia, to the west, which reduced the amount of water vapor in the atmosphere and enhanced aridification during Miocene times (e.g., Ramstein et al., 1997; Zachos et al., 2001; Miao et al., 2012).

Differences in the geographic positions and depositional environments between the sections within the Issyk-Kul basin likely did not play a role in creating the observed change in $\delta^{18}O$ and $\delta^{13}C$ values. The amount of moisture and precipitation, as well as the isotopic composition of rainfall and mean annual temperature were likely the same within the basin. Even though the Kaji Say section is situated ca. 70 km west from the Jeti Oguz and Chon Kyzylsu sections, it is also ca. 50 km east from the Ak Terek section, and the $\delta^{18}O$ and $\delta^{13}C$ values at Kaji Say and Ak Terek overlap. Also, the Jeti Oguz and Chon Kyzylsu sections belong to the Shamsi sedimentary group, which consists of coarser-grained deposits than the Chu group of the Kaji Say and Ak Terek sections. However, there was no isotopic shift or change of trend in the coarse-grained alluvial deposits of the upper Chu and Sharpyl Dak groups compared to the finer-grained lower Chu deposits in the Kaji Say section. The match of the timing of the Shamsi–Chu transition and the shift in stable isotopic values mark a significant tectonic event that could have reorganized local climate and fluvial systems.We consider the intensification of basin-wide evaporation and aridification through changes in topography as the most plausible explanation for this observed shift. Contemporaneous stable isotope data from the Zaysan (Caves et al., 2017) and Junggar (Charreau et al., 2012) basins do not show a similar shift in $\delta^{18}O$ and $\delta^{13}C$ values or changes in the trends in the late Miocene (Figure 3.11). Therefore, we conclude that the positive shift had a local, rather than a regional or global driver, and that global cooling and Paratethys retreat were unlikely to have caused the isotopic shift in the Issyk-Kul record.

Low temperature thermochronological data show that the onset of deformation in the Terskey, Trans Ili, and Kungey ranges occurred during the late Oligocene – early Miocene (Macaulay et al., 2013, 2014, De Grave et al., 2013, De Pelsmaeker et al., 2015), with a second pulse of exhumation during the middle-late Miocene (Macaulay et al., 2014). Paleocurrent data from the Kungey range (Selander et al., 2012) indicate that sediments from the southerly Terskey range were deposited in the Kungey area during the middle Miocene, implying that the Kungey range was relatively low-lying at that time; thus, Selander et al. (2012) proposed that substantial uplift of the Kungey happened during the second pulse of exhumation between 7 and 4 Ma. Thermochronological data from the Kyrgyz range, northwest of the Issyk-Kul basin, indicate that range uplift prograded eastward from 11 to 7 Ma (Bullen et al., 2001, 2003, Sobel et al., 2006b).

We therefore interpret the ca. 2‰ shift in $\delta^{18}O$ and $\delta^{13}C$ values between 8 and 7 Ma to be caused by sufficient surface uplift (ca. 1300 – 2000 m, Bookhagen and Strecker, 2008; Bookhagen and Burbank, 2010) of the Kyrgyz range, as well as the growth of the Trans Ili and Kungey ranges. The isotopic shift therefore reflects a change from a more windward to a more leeward position of the Issyk-Kul basin (Figures 3.12A-B). Prior to surface uplift of the aforementioned ranges, the Issyk-Kul basin received moisture by the westerlies coming mainly from the NW. The formation of a rain shadow would lead to a decrease in $\delta^{18}O$ values in the basin due to orographically-induced rainout on the windward sides of the Kyrgyz, Trans Ili and Kungey ranges. However, the ca. 2‰ shift and the switch of the stable isotopic trend from increasingly negative values between ca. 23 and 8 Ma to increasingly positive $\delta^{18}O$ values and relatively steady $\delta^{13}C$ values rather reflect an increase in aridity and evaporation as a result of surface uplift after ca. 8-7 Ma. Moreover, the change from a windward to a leeward position might have caused a change in the seasonality of precipitation due to interactions of the moisture-bearing air masses with high topography. At present, the Issyk-Kul basin is characterized by a spring and summer precipitation regime with higher $\delta^{18}O$ values of summer precipitation than winter precipitation (Baldwin and Vecchi, 2016; Macaulay et al., 2016; Wang et al., 2016). We suggest that the simultaneous establishment of a rain shadow, which would lower the $\delta^{18}O$ values, and an associated increase in aridity and change in the seasonality of precipitation, which would lead to an increase in the $\delta^{18}O$ values, led to a combined ca. 2‰ positive shift in the $\delta^{18}O$ record.

3.5.3.5 Climatic conditions from 7 to 2.5 Ma

Between 7 and 5 Ma, a subtle upsection trend towards more positive $\delta^{18}O$ and $\delta^{13}C$ values can be observed in Kaji Say. In Ak Terek, $\delta^{18}O$ and $\delta^{13}C$ values are more variable and lack a trend, which can reflect natural scatter of isotopic values and indicate a steady fluvial environment with no noticeable climatic changes. A meandering river, situated farther from the range front, has more diverse water sources and a larger drainage area than a proximal braided river near the range front. This results in the accumulation of runoff water with variable isotopic signals on a floodplain and, subsequently, in higher variability of $\delta^{18}O$ values in the water of a meandering rather than a braided river (Kent-Corson et al., 2009). Sediments in the two studied sections primarily record the isotopic signal of runoff river water, because, as mentioned above, in the Issyk-Kul basin summer rainout occurs at high elevations (Bershaw and Lechler, 2019), which is supported by palynology (Fortuna, 2016). Therefore, between 7 and 5 Ma the difference in Kaji Say and Ak Terek stable isotopic records may reflect a small difference between a more proximal position with respect to the Terskey range front of a braided river in Kaji Say and a more distal position of a meandering river at Ak Terek. The proximal position of the Kaji Say section with a smaller drainage area could result in higher sensitivity of pedogenic carbonates to changes in water isotopic composition and lead to the creation of the observed trend. Nevertheless, between 6.3 and 5 Ma the $\delta^{18}O$ and $\delta^{13}C$ values from the two sections overlap, suggesting a similar fluvial environment across the basin.

In the lower Chu unit of the Kaji Say section (fluvial-alluvial, 0 - 450 m; Figure 3.2), $\delta^{18}O$ and $\delta^{13}C$ values of sandstone cement and pedogenic carbonates are comparable (average values: $\delta^{18}O_{cement}$ = -10.4 ± 0.9‰ and $\delta^{18}O_{pedogenic}$ = -10.2 ± 0.4‰; $\delta^{13}C_{cement}$ = -6.1 ± 0.5‰ and $\delta^{13}C_{pedogenic}$ = -4.7 ± 0.8‰), suggesting that both types of carbonate formed in similar near-surface conditions from meteoric water. In the upper Chu and the Sharpyl Dak units (alluvial and lacustrine, 450 – 700 m; Figure 3.2), lacustrine $\delta^{18}O$ values are comparable to the pedogenic carbonate $\delta^{18}O$ values, and sustain the trend towards more positive values without abrupt changes (average values: $\delta^{18}O_{lacustrine}$ = -8.8 ± 0.9‰ and $\delta^{18}O_{pedogenic}$ = -8.9 ± 0.6‰). This suggests that pedogenic and lacustrine carbonates reflect similar conditions and that the lake did not experience significant evaporation, which would increase the $\delta^{18}O$ and $\delta^{13}C$ values. The lacustrine samples from the Kaji Say section show a relatively weak correlation between the $\delta^{18}O$ and $\delta^{13}C$ values, with $r = 0.49$. Poor correlation with $r < 0.7$ (Talbot, 1990) suggests a hydrologically open lake system with relatively short water residence time and $\delta^{18}O$ values reflecting the isotopic composition of rainfall and inflowing river water (Talbot, 1990; Leng and Marshall, 2004). In contrast, the isotopic composition of lacustrine carbonates in closed lakes is mainly controlled by the hydrological balance and evaporation, so that the $\delta^{18}O$ and $\delta^{13}C$ values of lake water reflect lake level changes, showing variable and high $\delta^{18}O$ values and a strong covariance between $\delta^{18}O$ and $\delta^{13}C$ (Li and Ku, 1997; Leng and Marshall, 2004). The upper Chu and Sharpyl Dak units have more positive lacustrine mudstone $\delta^{13}C$ values (average value: $\delta^{13}C_{lacustrine\ mudstone}$ = -1.4 ± 1.0‰), while lacustrine marls and siltstones samples yield $\delta^{13}C$ values between those from pedogenic carbonates and lacustrine mudstones (average values: $\delta^{13}C_{lacustrine\ marl\ and\ siltstone}$ = -2.9 ± 0.9‰ and $\delta^{13}C_{pedogenic}$ = -4.3 ± 0.9‰). The distinctively more positive lacustrine mudstone $\delta^{13}C$ values likely represent higher biogenic activity within the lake.

Between 7 and 5 Ma, a subtle trend towards positive $\delta^{18}O$ values can be observed in the combined Issyk-Kul record when the data from the Kaji Say and Ak Terek sections are merged (Figure 3.10). This is in agreement with gradual aridification in the basin, which was primarily caused by the growth of the Kyrgyz, Kungey and Trans Ili ranges upwind and was also suggested by the spore and pollen data (Grigina and Fortuna, 1981). Aridification across Central Asia was enhanced since ca. 8-7 Ma (Jia et al., 2020), and global cooling intensified between ca. 7 and ca. 5.4 Ma (Herbert et al., 2016). Therefore, primarily orographically-induced aridification in the Issyk-Kul basin might have been sustained and amplified by global factors. During this period, the $\delta^{18}O$ and $\delta^{13}C$ data are comparable in the Issyk-Kul and Junggar basins and reflect similar climatic conditions (Figure 3.11). The ca. 2‰ difference in $\delta^{18}O$ values of the two records from the Junggar basin is interpreted to be caused by differences in elevation of the catchment area (Charreau et al., 2012), which might also be the case for the ca. 2‰ difference between the Issyk-Kul and Junggar records. The ca. 4‰ lower $\delta^{18}O$ values from the Zaysan basin compared to Issyk-Kul can be explained by the windward position of the Zaysan basin, while the Issyk-Kul basin maintained a leeward position starting from ca. 8 Ma (Figure 3.11). Growth of the Altai, downwind from the Zaysan basin, led to changes in the interactions of the cyclones and topography, and, subsequently, in the seasonality of precipitation, resulting in a decrease in $\delta^{18}O$ values (Caves et al., 2017).

From 4.5 to 2.5 Ma the stable isotopic values from the Issyk-Kul basin are comparable to the values from the nearby Ili basin (Figure 3.11). The Ili basin record is interpreted to be primarily controlled by global climatic changes and to reflect relatively warm and wet conditions between ca. 4.5-3.3 Ma with the dominance of the westerlies and aridification between ca. 3.3-2 Ma due to a southward shift of the westerlies and the prevalence of dry air masses from the Siberian High (Prud'homme et al., 2021). The similarity in records from the two basins indicates that the primarily orographically-induced aridification in the Issyk-Kul basin has been enhanced by these changes in the moisture source at that time.

We conclude that the stable isotopic record from the Issyk-Kul basin reflects a relatively steady environment of a leeward basin with a possible influence of global climatic changes from ca. 7 to ca. 2 Ma. Similarity in records from the northern side of the Tian Shan (Issyk-Kul, Ili, and Junggar basins) may indicate that during this time the character of interactions between the Tian Shan and the westerlies was relatively steady and similar along the range.

3.5.4 Pliocene hiatus and lake formation in the Kaji Say area

3.5.4.1 Three episodes of deformation

Deciphering the relative importance of climate and tectonics on the creation of lake Issyk-Kul requires understanding the stratigraphic, climatic and tectonic records of the formation of the Issyk-Kul basin. The most useful record for this purpose comes from the Kaji Say area, where we see evidence of three deformation episodes.

The first deformation episode recorded in the section occurred at about 5 Ma. The braided river system, which delivered grey granitic conglomerates, was succeeded by lacustrine deposition. The decrease in fluvial clastic input allowed time for lacustrine carbonate mud to precipitate during periods of lake highstands, and for pedogenic carbonate to form during dry periods. We suggest that deformation close to the modern Terskey range front was responsible for a change in drainage pattern; clastic material was apparently delivered either to the east or west along strike. Lacustrine deposition with reduced clastic input in a subsiding basin may reflect slower accumulation rates than in a fluvial system. Lacustrine deposition periodically alternated with short and intensive debris flows, which led to the deposition of poorly-sorted matrix-supported angular rocks from the Taldysui subvolcanic complex, which is the nearest source area. These pulses could have been caused by either an increase in local tectonic activity, by climatically-driven floods, or the combination of the two factors.

Northwestern thickening of the beds in the upper Chu unit indicates the presence of growth strata, which record the second episode of deformation (Figure 3.4). The growth strata can be observed at ca. 480-640 m in the stratigraphic section (Figure 3.3F), i.e. after the 2 Ma hiatus proposed by Roud, et al. (2021). There is no visible unconformity at the base or within the growth strata and the bedding strike does not change; therefore, the orientation of the stress field likely did not change at this time.

The third episode of deformation is represented by folding of the section. This fold is very tight to overturned and only affects the stratigraphy between ca. 245-480 m in the stratigraphic section, which is deeper in the section than the growth strata and located on the eastern flank of this outcrop. The core of the fold is marked by vertically-dipping strata. However, both the overlying growth strata, observed to the northwest, and the base of the section, observed to the south-southeast, have much gentler dips (Figure 3.4). We suggest that this stage of deformation is younger than 2 Ma, because there is no unconformity within the section and because this folding would have prevented northward transportation of the coarse Sharpyl Dak sediments, which outcrop on the north side of this fold.

3.5.4.2 Lake formation in the late Miocene

Lake formation started in the late Miocene in the southern part of the basin in the Kaji Say area (Figure 3.12). There, individual lacustrine and beach beds transition into fluvial sandstone beds eastward or grow thinner and disappear. Growth strata also thicken to the west. This suggests that the deeper part of the basin was located westward along strike. The first lacustrine and beach facies deposits observed in the area are stratigraphically older than those recorded in the described Kaji Say section. They appear ca. 200 m to the west and do not reach the measured section (Figure 3.4). Their stratigraphic position roughly corresponds to 360-380 m in our studied section. Gradual lake progression and northwest thickening of the growth strata suggest enhanced subsidence to the west of the section during the late Miocene-Pliocene. This generally agrees with shallow seismic reflection data from the lake basin that shows that in Holocene time, subsidence was higher in the southern part of the lake basin than in the northern part (Gebhardt et al., 2017). Eastward growth of the Terskey range in the middle − late Miocene (Macaulay et al., 2014) and eastward spreading of the depositional area due to growth of the Kungey range in the late Miocene (Selander et al., 2012) support the idea that higher subsidence occurred in the southwestern part of the basin. However, the steady fluvial environment in the Ak Terek section shows that the lake first formed locally in the Kaji Say area. We conclude that enhanced subsidence in the Kaji Say area (and likely farther north, beneath the modern lake) led to formation of a topographic depression in the late Miocene and enabled formation of the lake on the southern side of the basin. Enhanced subsidence led most likely simultaneously to an internally drained basin, i.e. a closed basin without a surface outlet. Therefore, even though moisture delivery was reduced due to the creation of an orographic barrier, moisture retention in the closed basin resulted in a lake phase. Furthermore, sedimentological evidence of a local shallow lake presence in the early Miocene – Pliocene was observed in the subsurface deposits obtained from the boreholes on the eastern side of the basin (Grigina and Fortuna, 1981; Voskresenskaya, 2013; Voskresenskaya and Leflat, 2015). However, this age constraint is based only on lithostratigraphical correlation of the deposits to the Shamsi and Chu groups and, therefore is imprecise.

3.5.4.3 Position of the hiatus

Roud et al. (2021) proposed a 2 Ma hiatus between ca. 5 and ca. 3 Ma based on the interpretation of the magnetic polarity record (Figure 3.2). The hiatus may be detected by a short interval of one reversed and two transitional polarity samples within a long normal polarity interval. The hiatus was placed at 475 m in the section within an alternation of thin lacustrine mudstones, marls, and sandstones. The end of the hiatus roughly marks the beginning of the growth strata formation. Here, we discuss the hiatus in terms of the sedimentology and the depositional system. The position of the hiatus at 475 m within the interbedded beach and lacustrine deposits might be caused by changes in fluvial input and the disappearance of the braided river system in response to the first stage of deformation in the area. However, deposition of thin, lacustrine and beach sandstone beds implies rapid changes in the depositional environment, which may not be consistent with a depositional hiatus. Moreover, pedogenic alteration in the lacustrine mudstone is weak, indicating that dry periods with no sedimentation were relatively short (Alonso-Zarza, 2003). We suggest that the hiatus actually occurred slightly earlier, during deposition of the first beach facies at 450 m in the section (a shift from lower Chu to upper Chu; Figure 3.2). We assume that the presence of the lake might not be recorded in local stratigraphy if the lake margin and beach position did not change significantly over a period of time. Reworking of material to sustain the beach would prevent rapid soil formation. Together with the disappearance of the braided river system, this would create a gap in the stratigraphic record. This 1.5-m-thick beach sandstone bed at 450 m in the section consists of well reworked and sorted coarse quartz sandstone and is laterally continuous. Such characteristics suggest a long-term and stable beach position without frequent lake transgressions and represent a more plausible stratigraphic location for the hiatus. This interpretation stipulates that the position of the hiatus is within the interval of normal magnetic polarity. Assuming a continuous accumulation rate of ca. 23 cm ka^{-1}, the 25 m downward shift of the stratigraphic position would correspond to an increase of ca. 100 ka in the age of the hiatus, i.e. it would place the hiatus between 5.2 and 3.1 Ma rather than between 5.1 and 3.0 Ma.

As mentioned above, the Kaji Say section consists of the western and eastern transects, situated in different valleys (Figure 3.4). The reversed and transitional polarity samples, which bound the interpreted hiatus, are situated at the base of the western transect. We cannot exclude the possibility that the lacustrine deposits with slow accumulation rates represent a condensed section and some magnetic reversals might have been missed between the two transects. We note that lacustrine micritic carbonates were avoided while collecting paleomagnetic samples as they would likely provide a biased and unreliable magnetic record (Roud et al., 2021). The hiatus may also be misplaced due to general differences in the sedimentation rates of fluvial-alluvial and lacustrine deposits. As we discussed earlier, lacustrine deposits gradually change into fluvial-alluvial sandstones eastward in the Kaji Say area and, therefore, the sedimentation rates also can change laterally. It may be that instead of one long hiatus, the lake experienced a series of shorter hiatuses because of the shifts between the periods of slow lake sediment accumulation, pedogenesis, and rapid debris flow deposition. The studied section may not represent a complete magnetostratigraphic sequence or the polarity intervals may be of different stratigraphic thickness due to increase in sedimentation rates from lacustrine to fluvial environment. However, variations in alternation of lacustrine and fluvial-alluvial deposits in the Kaji Say area can only affect the distribution of possible hiatus positions in the middle of the section. A fluvial system of the lower part of the section represents a steady depositional environment without changes along strike. Moreover, the robust correlation of the magnetostratigraphic age model and $^{26}Al/^{10}Be$ data proves the 2.8-2.6 Ma age of the Chu – Sharpyl Dak transition. Therefore, we consider the overall magnetostratigraphic model to be reliable.

3.5.5 Tectonic and climatic development of the Issyk-Kul basin in the late Miocene - Pliocene

3.5.5.1 Diachronous deposition of the Sharpyl Dak group conglomerates

The hiatus in the Kaji Say section at ca. 5 Ma and disappearance of grey granitic conglomerates possibly reflect tectonically-driven reorganization of the local river system. Intensified tectonic activity in the early Pliocene is also indicated by a short period of increased sedimentation rates in the Ak Terek section at 5 Ma (Roud et al., 2021), and 4-5 Ma onset of Sharpyl Dak deposition at Jergalan. South-directed paleocurrents at Jergalan suggest that Sharpyl Dak deposits were sourced from the Kungey range. Deposition of the Sharpyl Dak group at Jergalan ca. 2 Ma earlier than in the Kaji Say and Ak Terek sections could be driven tectonically because of the eastward progradation of the Kungey range (Figure 3.12). Thermochronological data also show that exhumation increased at 15-5 Ma in the Kyrgyz Tian Shan and that the Terskey range also grew eastward, although lateral propagation was complicated as the deformation in the Terskey range progressed out of sequence (Macaulay et al., 2014). The Xiyu group in the Chinese Tian Shan, which is analogous to the Sharpyl Dak group in the Kyrgyz Tian Shan, is reported to be deposited diachronously with the ages from 15 to 0.7 Ma across Central Asia (e.g., Chen et al., 2002; Heermance et al., 2007). Xiyu deposits have a ca. 3 Ma age difference in the Junggar basin (Charreau et al., 2009). In the Junggar basin, the late Miocene Xiyu-like deposits are related to tectonic activity, while deposition of the younger Pliocene-Pleistocene conglomerates is believed to be induced by the onset of the Northern Hemisphere glaciation (Zhao et al., 2021). Therefore, a ca. 2 Ma age difference for the onset of Sharpyl Dak deposition within the Issyk-Kul basin is plausible. Intensive Pliocene conglomerate deposition in the Jergalan area might have temporarily blocked westward-draining rivers, possibly permanently blocking a paleo-drainage connection with the Ketmensk basin, causing sediment starvation in the Issyk-Kul basin and helping the lake expand. Channels feeding the eastern submerged lake delta are visible now and are associated with the modern rivers that flow westward into the lake (De Batist et al., 2002).

3.5.5.2 Influence of global climatic changes on sedimentation and lake development in the basin

The Pliocene was characterized by the meridional poleward shift of the westerlies, responsible for changes in moisture delivery (Abell et al., 2021). This shift of the westerlies at 5-3.3 Ma caused relatively high rainfall and fluvial activity in Northern Central Asia, as detected in the windward Ili basin (Prud'homme et al., 2021). Although our stable isotopic data does not show intensifying influence of the westerlies, the spore and pollen data from the Issyk-Kul basin suggest wetter conditions in the early Pliocene (Grigina and Fortuna, 1981). We suggest that despite the leeward position of the Issyk-Kul basin, a relatively high level of precipitation and water availability might be marked by expansion of a lake in the Kaji Say area and by the presence of a steady meandering river at Ak Terek with increasing abundance of paleosols from ca. 6 to ca. 3.5 Ma. Increased precipitation might also have enhanced tectonically-driven sedimentation in the Jergalan area.

Late Pliocene expansion of the Northern Hemisphere ice sheets caused a southward shift of the westerlies (Abell et al., 2021). The Siberian High reached the Tian Shan and amplified aridification in Northern Central Asia (Prud'homme et al., 2021). Cooling, aridification, increased aeolian sedimentation in the Ili basin since ca. 3.3 Ma and increased erosion in the Junggar basin since ca. 3 Ma are interpreted to be triggered by prevalence of cold and dry air masses of the strengthened Siberian High and connected to the onset of Northern Hemisphere glaciation (Charreau et al., 2011; Prud'homme et al., 2021). In the Tarim basin, southward-shifted westerlies enhanced aridification since ca. 2.7 Ma (Fang et al., 2020), and a possible Northern Hemisphere glaciation impact was detected in the Qaidam basin since ca. 3.3 Ma (Zhuang et al., 2011). In the Issyk-Kul basin, increased sedimentation and continuing aridification might have been enhanced by the Siberian High and Northern Hemisphere glaciation. Accumulation of the alluvial fan debris flow deposits since ca. 3 Ma at Kaji Say, an increase in the abundance of conglomerates at Ak Terek since ca. 3.5 Ma, as well as deposition of the Sharpyl Dak conglomerates at Ak Terek and Kaji Say since ca. 2.7 Ma may reflect accumulation of sediments derived from upstream glaciation, as well as tectonically-driven deposition. The spore and pollen data suggest intensified aridification in the basin in the late Pliocene

(Grigina and Fortuna, 1981). Increased evaporation due to aridification, as well as vast conglomerate accumulation have affected the lake-level fluctuations and moved the lake shore from the Kaji Say area towards the center of the basin (Figure 3.12D). Lake-level variations of at least 400 m in Issyk-Kul during the Holocene are also connected to changes in precipitation and evaporation due to interactions between the westerlies and the Siberian High rather than tectonic activity (Gebhardt et al., 2017). Today, the Issyk-Kul basin is an underfilled basin, with water depths of up to 668 m. The main sediment input since middle Pleistocene is represented by a westward-propagating delta system at the east end of the lake (De Batist et al., 2002; Gebhardt et al., 2017). We propose that the onset of lacustrine deposition at ca. 5 Ma reflects the commencement of the underfilled basin system. However, proof of this hypothesis will require stratigraphic information taken from deep cores within the lake. A related question is whether basin-wide accumulation rates remained constant but subsidence rates increased or that accumulation rates were drastically reduced.

3.6 CONCLUSIONS

The most notable finding of our study of the Issyk-Kul basin is an environmental change that is expressed by a shift of ca. 2‰ in δ^{18}O and δ^{13}C values at ca. 8-7 Ma and an associated change from a negative to a positive stable isotopic trend. We suggest that the upwind growth of the Kyrgyz, Kungey and Trans Ili (Zaili) ranges created an orographic barrier that diverted westerly moisture sources at ca. 8-7 Ma, which changed the position of the Issyk-Kul basin from windward to leeward, and led to the establishment of the modern-day spring and summer precipitation regime. The associated creation of a rain shadow led to enhanced aridification and evaporation, as expressed in δ^{18}O and δ^{13}C values. During the late Miocene – Pliocene, the primarily orographically-induced aridification in the Issyk-Kul basin has likely been strengthened by the periodic dominance of dry air masses of the Siberian High during Northern Hemisphere glaciations, when the moisture-bearing westerlies shifted southward.

The transition from the Chu sedimentary group, which consist of fluvial-alluvial sandstones and conglomerates, to massive alluvial conglomerates of the Sharpyl Dak group marks the change from a fluvial-alluvial system to a proximal alluvial fan. Our ^{26}Al/^{10}Be isochron burial data suggests a 5-4 Ma age for the transition between the Chu and Sharpyl Dak sedimentary groups in the eastern part of the basin in the Jergalan area; south-directed paleocurrents there suggest the growth of the eastern Kungey range at 5-4 Ma. Also, ^{26}Al/^{10}Be isochron burial dating confirms the previously proposed 2.6-2.8 Ma age of the transition between the Chu and Sharpyl Dak sedimentary groups on the southern side of the Issyk-Kul basin (Roud et al., 2021). Initiation of the Sharpyl Dak conglomerates' deposition at 2.6-2.8 Ma on the southern side of the basin could have been induced tectonically or by the North Hemisphere glaciation, while older late Pliocene Sharpyl Dak deposition in the Jergalan area is related to intensified tectonic activity.

We propose the formation of an internally drained lake Issyk-Kul at ca. 5 Ma on the southern side of the basin due to enhanced subsidence and reorganization of the river systems in the Kaji Say area. Initiation of lake formation coincides with the disappearance of the braided river system and a 2 Ma hiatus in deposition. Changes in the fluvial network and basin subsidence rates were likely induced by deformation of the Terskey range. We suggest that the hiatus occurred because of fluctuations of the water level in a shallow lake with dry periods of very slow sedimentation and a stable lake margin, so that the beach facies deposits were regularly reworked without subsequent sediment accumulation or pedogenesis. Aridification and conglomerate accumulation since the late Pliocene have moved the lake shore towards the center of the basin.

4 Impact of Quaternary glaciations on denudation rates in the Kyrgyz Tian Shan inferred from cosmogenic ^{10}Be and low-temperature thermochronology

Anna Kudriavtseva, Alexandru T. Codilean, Edward R. Sobel, Angela Landgraf, Réka-H. Fülöp, Atyrgul Dzhumabaeva, Kanatbek Abdrakhmatov, Klaus M. Wilcken, Taylor Schildgen, David Fink, Toshiyuki Fujioka, Swenja Rosenwinkel, Silke Merchel, & Georg Rugel

Abstract

We explore the spatial and temporal variations in denudation rates in the Kyrgyz Tian Shan using ^{10}Be-derived denudation rates from modern (n = 54) and buried sediment dated to 2.0–2.7 Ma (n = 3), and long-term exhumation rates derived from published apatite fission track (AFT) and apatite (U-Th-Sm)/He (AHe) thermochronology. Modern ^{10}Be denudation rates are generally higher than the long-term AFT and AHe exhumation rates across the studied area. On average, the highest ^{10}Be denudation rates are recorded in the Terskey range, south of Lake Issyk-Kul. Here, modern denudation rates are higher than ^{10}Be-derived paleo-denudation rates, which are comparable in magnitude with the long-term exhumation rates inferred from AFT and AHe. We propose that denudation in the Kyrgyz Tian Shan, particularly in the Terskey range, remained relatively steady during the Neogene and early Pleistocene. Denudation increased due to glacial-interglacial cycles in the Quaternary, but this occurred after the onset and intensification of the Northern Hemisphere glaciation at 2.7 Ma. Comparison with published data from the wider Pamir–Tian Shan region show a spatial trend of decreasing modern denudation rates from west to east, suggesting that deformation controls denudation in the Pamir and Western Tian Shan, while further east, the denudational response of the landscape to Quaternary glaciations becomes detectable. We find moderate correlations between modern denudation rates and topographic metrics and weak correlation between denudation rate and annual rainfall, highlighting complex linkages between tectonics, climate, and surface processes that vary locally.

4.1 Introduction

The evolution of orogens depends on the balance between rock uplift and denudation, which reflects complex interactions among tectonics, climate, and surface processes (Molnar & England, 1990; Raymo & Ruddiman, 1992; Avouac & Burov, 1996;

Montgomery & Brandon, 2002; Burbank et al., 2003; Whipple, 2009). However, these factors are often interdependent, and their relative importance for denudation is mainly controlled by regional and local conditions (Portenga & Bierman, 2011; Chen et al., 2022b). On a global scale, denudation has been argued to either increase with the late Cenozoic onset of Northern Hemisphere glaciations (Zhang et al., 2001; Molnar, 2004; Herman et al., 2013, 2018; Herman & Champagnac, 2016, Norton & Schlunegger, 2017; Chen et al., 2022b), or remain steady (Willenbring & von Blackenburg, 2010; Willenbring & Jerolmack, 2016). However, other studies argue that denudation rates are too poorly resolved during the late Cenozoic to determine any global patterns (Schildgen et al., 2018), but at least locally, they have been argued to be primarily controlled by enhanced tectonic activity (Koppes & Montgomery, 2009; Hecht & Oguchi, 2017) or by post-orogenic isostatic rebound of foreland basins (Bernard & Sinclair, 2022).

During the Cenozoic, Central Asia experienced extensive tectonic deformation associated with uplift of the Tibetan Plateau, the Pamir mountains, the Tian Shan, and the Altai mountains (Molnar & Tapponnier, 1975), as well as dramatic changes in climate associated with the onset of Quaternary glacial-interglacial cycles (Caves et al., 2016; Batbaatar et al., 2020). Moreover, the Tian Shan creates an important topographic barrier to moisture-bearing westerly winds, playing a crucial role in the Cenozoic aridification of Central Asia (Caves Rugenstein & Chamberlain, 2018).

Studies on the Cenozoic denudation in the Pamir (Fuchs et al., 2015; Grin et al., 2018) and the Eastern (Chinese) Tian Shan (Charreau et al., 2011, 2017, 2023; Liu et al., 2011; Guerit et al., 2016; Puchol et al., 2017; Guan et al., 2022) shed light on spatio-temporal variations in denudation throughout northern Central Asia, yet denudation within the Kyrgyz part of the Tian Shan (Figure 4.1), situated between the Pamir and Chinese Tian Shan, has been poorly studied. Available thermochronology data from the Kyrgyz Tian Shan help to constrain exhumation rates averaging over million-year timescales; however, these data are not suitable for evaluating the variability of late-Cenozoic denudation rates following the Plio-Pleistocene onset of Northern Hemisphere glaciations (e.g.,Reiners & Brandon, 2006).

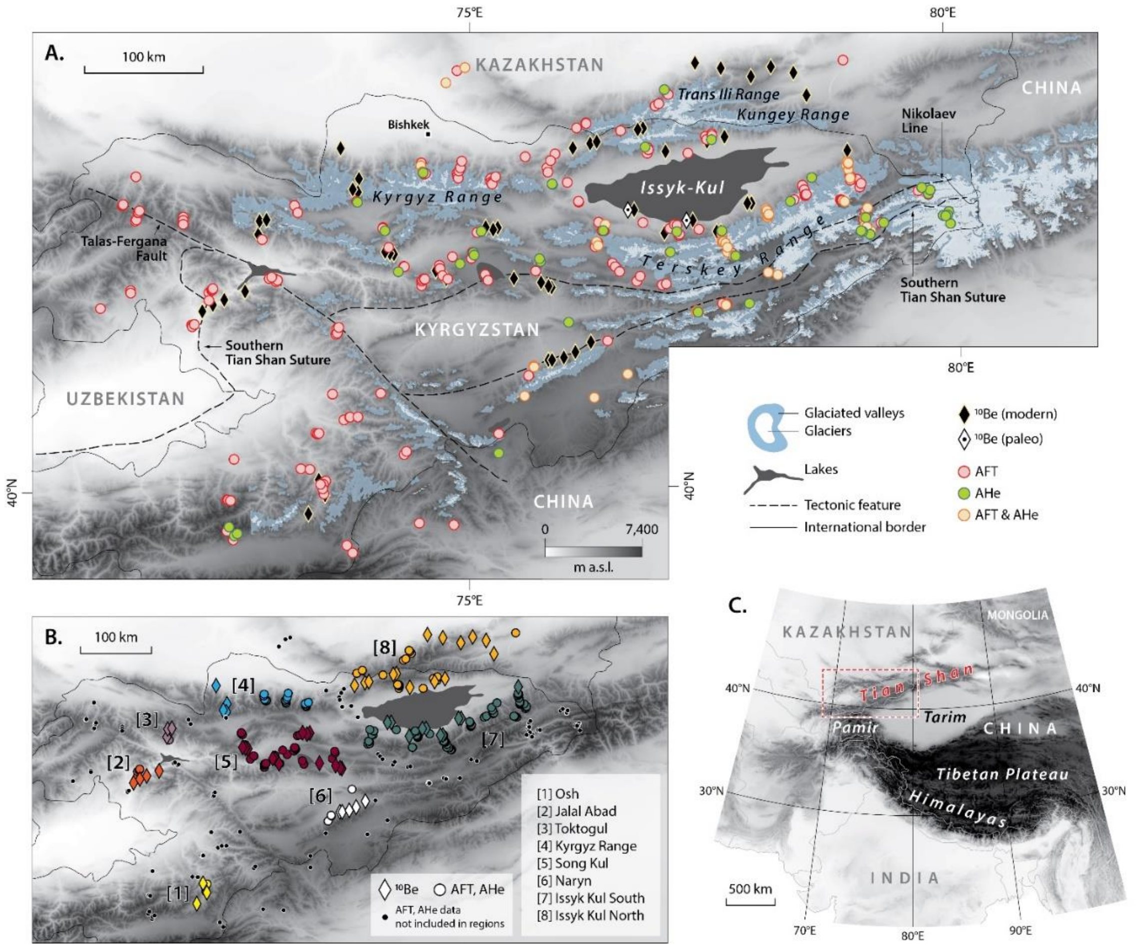

Figure 4.1. Topographic maps of the Tian Shan based on the 90-m SRTM DEM and distribution of samples. (A) Positions of ^{10}Be, AFT, and AHe samples across the Kyrgyz Tian Shan. (B) Distribution of ^{10}Be, AFT, and AHe samples by region within the Kyrgyz Tian Shan. (C) Position of the Kyrgyz Tian Shan in Central Asia. Glacier and glaciated valley extents based on Stroeven et al. (2013).

Here we present ^{10}Be-derived basin-wide denudation rates from modern river sediment (n = 54) from across the Kyrgyz Tian Shan and the Kazakh part of the Trans Ili (Zaili) and Kungey ranges, as well as ^{10}Be-derived paleo-denudation rates from buried river sediment dated to 2.0–2.7 Ma (n = 3) from the southern side of the Issyk-Kul basin (Figure 4.1A). We compare these data to long-term exhumation rates calculated from published apatite fission track (AFT) and apatite (U-Th-Sm)/He (AHe) thermochronology data. We also explore relationships between denudation rates and geomorphic, tectonic, and climatic parameters to identify potential controls on denudation at the regional and local scales. Taken together, these data provide insights into spatial and temporal variations in denudation in the Kyrgyz Tian Shan and allow us to untangle the effects of tectonics and climatic changes on denudation across the range.

4.2 TECTONIC AND CLIMATIC SETTING

The Tian Shan is a 2500-km long intracontinental mountain belt, situated between the Tarim and Tadjik basins to the south and the Kazakh platform to the north, and extending over the territories of north-western China, Kyrgyzstan, southern Kazakhstan, eastern Uzbekistan, and northern Tajikistan (Figure 4.1C).

The Kyrgyz Tian Shan is composed of the Northern, Middle, and Southern terranes, formed by accretion and collision during the Palaeozoic (e.g., Windley et al., 2007; Biske & Seltmann, 2010). The terranes are cross-cut by the dextral strike-slip Talas-Fergana Fault and separated by the sinistral strike-slip Nikolaev Line and the Southern Tian Shan Suture (Figure 4.1A) (Bazhenov & Mikolaichuk, 2004; Glorie et al., 2011; Alexeiev et al., 2017). In the Mesozoic and early Cenozoic, the Tian Shan was periodically reactivated in response to distal collisions (Hendrix et al., 1992; Jolivet et al., 2010; De Grave et al., 2013), followed by a period of tectonic quiescence (Abdrakhmatov et al., 2001; Macaulay et al., 2013).

The present topography of the Tian Shan is a result of crustal shortening triggered by the most recent deformation due to the India-Asia collision (Molnar & Tapponier, 1975). Cenozoic deformation in the Kyrgyz Tian Shan progressed out of sequence and associated rock uplift rates vary along strike (Thompson et al., 2002; Glorie et al., 2011, Goode et al., 2014; Macaulay et al., 2014; Bande et al., 2017b; Glorie & De Grave, 2016). Deformation started in the late Oligocene at ca. 25 Ma, as indicated by thermochronology, and remained tectonically confined to the major fault zones (Sobel et al., 2006a; Glorie & De Grave, 2016). North-south shortening and deformation in the Tian Shan intensified at ca. 15–5 Ma and caused widespread thrusting at ca. 10 Ma (e.g., Bullen et al., 2003; Jolivet et al., 2010; Zubovich et al., 2010; Macaulay et al., 2014; Bande et al., 2017a; Li et al., 2022; Wang et al., 2023). Deformation in the interior ranges possibly intensified at ca. 3–2 Ma (e.g., Glorie et al., 2010, 2011; Goode et al., 2014; Macaulay et al., 2014) mostly in the western and partly in the central parts of the Tian Shan (Wang et al., 2023). Strike slip displacement of the Talas-Fergana Fault commenced at ca. 25 Ma and was relatively rapid until ca. 13.5 Ma (Bande et al., 2017b). The Cenozoic shortening in the Tian Shan decreases from south to north. The present-day shortening rate in the central Tian Shan is ca. 20 mm yr^{-1}, which is approximately half of the present-day India-Asia convergence rate (Abdrakhmatov et al., 1996; Zubovich et al., 2010). Quaternary shortening is distributed across the entire Tian Shan and rates are inferred to be similar to modern shortening rates. However, seismicity seems to be concentrated along the northern margin, including a significant series of five large-magnitudes earthquakes between AD 1885 and 1938 (M6.9 to >8) (e.g., Landgraf et al., 2016). The most rapid Quaternary shortening documented in the Kyrgyz Tian Shan occurred in the Naryn basin (Thompson et al., 2002).

Climate in Central Asia during the Cenozoic has been arid and mainly influenced by the northern mid-latitude westerlies, which transport moisture eastward across Eurasia (e.g., Caves et al., 2015, 2016). Aridification was likely caused by a decrease in the westerlies' moisture flux, which resulted from Cenozoic global cooling and Parathethys retreat (Ramstein et al., 1997; Miao et al., 2012), as well as the creation of an orographic barrier due to surface uplift of the Tibetan Plateau and Tian Shan, and the indentation of the Pamir (Kent-Corson et al., 2009; Caves Rugenstein & Chamberlain, 2018; Wang et al., 2020). The Tian Shan has interacted with the westerlies since the late Oligocene (Wang et al., 2020). In mid-Pliocene and Quaternary interglacial periods, precipitation increased due to the northward migration of the westerlies, while Quaternary glacial periods were drier due to the southward migration of the latter (Botsyun et al., 2022).

Modern precipitation in the Tian Shan is controlled by interactions between the westerlies and the Siberian High (Aizen et al., 1997; Zech, 2012; Schwarz et al., 2017). The westerlies bring moisture from the North Atlantic, the Mediterranean, and the Black Sea (Aizen et al., 2006; Lauterbach et al., 2014). In winter, the Siberian High reaches the Tian Shan and blocks the midlatitude westerlies, resulting in cold conditions and low precipitation (Aizen et al., 2001; Ricketts et al., 2001). The Asian monsoon never consistently reached the Tian Shan and does not influence precipitation and long-term climate within the range (Caves et al., 2015; Wu et al., 2022). Presently, an orographic barrier created by the range is responsible for the seasonality of precipitation, with dominantly winter-spring precipitation on the windward (north-western) side of the Tian Shan and summer precipitation within the range and on its leeward (south-eastern) side (Baldwin & Vecchi, 2016). This seasonality is created because in winter a combination of the prevalent Siberian High and weak westerlies leads to orographic rainout of the westerly moisture on the windward side, while strong cyclonic activity at high elevations in the summer leads to rainfall at high elevations (Bershaw & Lechler, 2019).

Summarizing the above, high topography of the Tian Shan developed during the Neogene due to India-Asia collision, with the most significant intensification at 15-5 Ma. The range prevents the westerly moisture from reaching the Chinese part of Central Asia, playing a part in aridification.

4.3 MATERIALS AND METHODS

4.3.1. COSMOGENIC ^{10}BE ANALYSIS

Cosmogenic ^{10}Be produced in quartz has proven to be the best suited technique for studying the erosion of Earth's continental topography over millennial timescales (Schaefer et al., 2022). Indeed, ^{10}Be-based denudation rates have now been determined in more than 4000 river basins – mostly from mountain landscapes – providing us with a large inventory of denudation rate estimates (Codilean et al., 2018; 2022). The concentration of ^{10}Be nuclides in river sediments is proportional to their exposure age, with the highest ^{10}Be concentrations reflecting longer exposure time and, consequently, slower denudation (Granger & Schaller, 2014; Schaefer et al., 2022).

4.3.1.1. Sampling

We collected 54 modern river sediment samples to calculate ^{10}Be-derived millennial-scale basin-wide denudation rates (Figures 4.1A and Supplementary Figure S4.1, Supplementary Table S4.1). Sampling was performed in locations across Kyrgyzstan accessible by road with the purpose of covering the largest possible area of the Kyrgyz Tian Shan and covering several catchments in individual ranges, if possible. River sediment was sieved in the field to isolate the 250–500 μm fraction for analysis. At two sampling locations we also collected material in the 8–16 mm (samples KYR16-01B and KYR16-02B) and 16–32 mm (sample KYR16-01C) grain size ranges. Sampling of buried sediments for calculation of ^{10}Be-derived paleo-denudation rates and calculation of ages using isochron burial dating (Figure 4.1A, Supplementary Table S4.2) are described in Kudriavtseva et al. (2023). Our sample inventory includes one modern river sediment sample (KYR-DRMS1) previously reported by Landgraf et al (2016).

4.3.1.2. Sample Preparation

Quartz was purified following procedures described in Kohl & Nishiizumi (1992) using froth flotation to separate feldspars from quartz. For all samples except those labelled 'DRMS' in Supplementary Table S4.1, beryllium was separated at the University of Wollongong following procedures described in Codilean et al. (2023). Samples were spiked with ≈300 μg of ^{9}Be from a low-level beryllium carrier solution added prior to complete HF dissolution. ^{10}Be/^{9}Be ratios were measured using the 10 MV ANTARES accelerator (samples with cathode ID's in Supplementary Table S4.1 starting with 'B') and using the 6MV SIRIUS accelerator (samples with cathode ID's in Supplementary Table S4.1 starting with 'Be' and 'XBE') at the Australian Nuclear Science and Technology Organisation (ANSTO) (Fink & Smith, 2007; Wilcken et al., 2017, 2019, 2022), and were normalised to the KN-5-2 and KN-5-3 (Nishiizumi et al., 2007) standards. Analytical uncertainties for the final ^{10}Be concentrations (atoms g^{-1}) include AMS measurement uncertainties (the larger of counting statistics or standard deviation of repeats and blank corrections) in quadrature with 1-2% for ^{10}Be standard reproducibility (depending on the individual AMS measurement conditions) and 1% uncertainty in the ^{9}Be carrier concentration. Samples labelled 'DRMS' were prepared and analysed at the DREAMS facility at Helmholtz-Zentrum Dresden Rossendorf (Rugel et al., 2016).

4.3.1.3. Denudation rates from modern samples

Denudation rates were calculated using the open-source program CAIRN v.1 (Mudd et al., 2016). Basin-averaged nuclide production from neutrons and muons was calculated with the approximation of Braucher et al. (2011) and using a sea-level and high-latitude total production rate of 4.3 atoms g^{-1} yr^{-1} for ^{10}Be (Mudd et al., 2016). Production rates for catchment-wide denudation rates were calculated at every grid cell of a hydrologically enforced 90-m SRTM DEM (Farr et al., 2007), using the time-independent Lal/Stone scaling scheme (Stone, 2000). Atmospheric pressure was calculated via interpolation from the NCEP2 reanalysis data (Compo et al., 2011). Topographic shielding was calculated from the same DEM using the method of Codilean (2006) with $\Delta\theta = 8°$ and $\Delta\phi = 5°$. We also calculated denudation rates with production rates corrected for ice shielding using present day glacier extent data from Stroeven et al. (2013). These along with the uncorrected denudation rates calculated using CAIRN are listed in Supplementary Table S4.1.

4.3.1.4. Paleo-denudation rates from buried samples

Paleo-denudation rates were calculated using three buried amalgamated sand samples (250–500 μm grain size) from south of lake Issyk-Kul (Figure 4.1A), taken from the same stratigraphic layers as the individual clasts collected for isochron burial dating by Kudriavtseva et al. (2023). The ^{26}Al and ^{10}Be concentrations measured in the sand samples plot near (sample AKT) or intersect (samples PET-QTS) the lines defined by the isochron clast samples (Supplementary Figure S4.2) indicating that the sands and clasts have experienced similar exposure and burial histories. We calculate paleo-denudation rates by first correcting the ^{10}Be concentrations measured in the sand samples for radioactive decay using the isochron burial ages calculated for each location (see Supplementary Table S4.2 and Kudriavtseva et al., 2023). To account for uncertainties related to the average elevation of the sediment's source areas and to the possibility of incomplete burial or lengthy exposure to cosmic radiation prior to sampling, we express paleo-denudation rates for each of the three localities as a range of values in addition to a central value obtained by assuming complete and continuous burial (Supplementary Table S4.2).

4.3.2. AFT and AHe thermochronology

Thermochronology is used to reconstruct the timing of rocks cooling through a temperature window during uplift, which allows estimation of the timing and pace of exhumation (e.g., Reiners & Brandon, 2006). The age corresponds to the closure temperature, and different closure temperatures result in different averaging timescales of exhumation. The temperature windows for the AFT and AHe systems are 60–120°C and 40–85°C, respectively, and the typical closure temperatures are 110°C and 70°C, respectively (e.g., Reiners & Brandon, 2006).

To estimate long-term exhumation rates, we compile a set of published apatite fission-track (AFT, n=296, Supplementary Table S4.3) and apatite (U-Th-Sm)/He (AHe, n=125, Supplementary Table S4.4) ages from across Kyrgyzstan (Bullen et al., 2003; De Grave, 2003; Sobel et al., 2006b; Glorie et al., 2010, 2011; De Grave et al., 2011, 2012, 2013; Macaulay et al., 2013, 2014; Bande et al., 2017a, 2017b; DePelsmaeker et al., 2015; Chu et al., 2016; Käßner et al., 2017; Nachtergaele et al., 2018; Rolland et al., 2020). We calculated one-dimensional, steady-state exhumation rates from the published AFT and AHe ages using the *age2exhume* MATLAB code (van der Beek & Schildgen, 2023). The parameters we used for both AFT and AHe systems are as follows: surface temperature = 25°C; temperature lapse rate = 5°C km^{-1}; initial geotherm = 25°C km^{-1}; thermal diffusivity = 30 km^2 Myr^{-1}; model thickness = 30 km. To calculate a smoothed version of the DEM from which Δh values are derived (which enable corrections for local relief and surface temperature), the 90-m resolution SRTM DEM was smoothed over a circular radius equal to 70 pixels (6300 m) for the AHe system, and 105 pixels (9450 m) for the AFT system. These distances are equivalent to assuming a closure depth (z_c) of ca. 2 km for the AHe system, and ca. 3 km for the AFT system, with a smoothing radius equal to $\pi * z_c$ (Willett and Brandon, 2013). The Δh values for each sample (modern elevation minus smoothed DEM) are included in Supplementary Tables S4.3 and S4.4.

4.3.3. Geomorphic, climatic, and tectonic parameters

To explore potential environmental controls on ^{10}Be-derived denudation rates, we calculate the average, median, and standard deviation of various geomorphic, tectonic, and climatic metrics for each drainage basin. For geomorphic metrics we use a hydrologically enforced 90-m SRTM DEM (Farr et al., 2007). We calculate the topographic gradient using the algorithm proposed by Horn (1981), local relief as the elevation range within a moving circular window with radii varying between 1 and 10 km, and we calculate the normalised channel steepness index (k_{sn}) using the Topographic Analysis Kit (TAK) for TopoToolbox MATLAB package (Forte & Whipple, 2019). As metrics for climate, we use the bioclimatic variables available as part of the WorldClim Global Climate database (Fick & Hijmans, 2017), and the global aridity index (AI) map (Zomer et al., 2022), and as a metric for tectonism we use data from the Global Strain Rate Model (Kremer et al., 2014). The extracted metrics are summarised in Supplementary Table S4.5.

We also compare our inferred AFT and AHe exhumation rates to topographic gradient and local relief. To achieve this we calculate the average, median, and standard deviation of the two metrics for 90-m SRTM DEM grid cells falling within 5 km (Figures 4.2 and 4.3) and 10 km (Supplementary Figures S4.3 and S4.4) radii buffers created around each AFT and AHe sample location. The areas defined by these buffers are similar to the areas of the drainage basins for which we have ^{10}Be data, and so the topographic metrics obtained for the different chronometers are comparable.

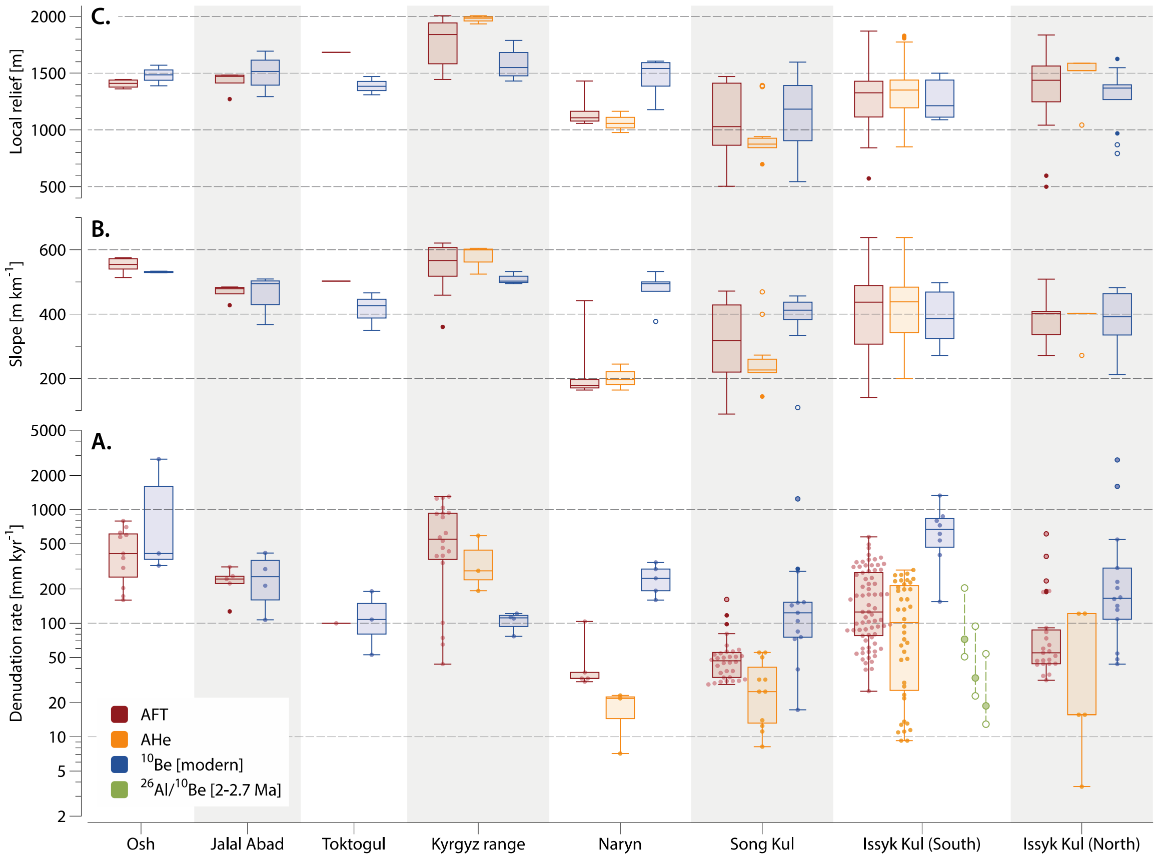

Figure 4.2. ^{10}Be-derived modern and paleo-denudation rates, AFT and AHe exhumation rates, topographic gradient, and local relief data distributed by region. Slope and local relief for ^{10}Be data is calculated as average for drainage basins using 90-m SRTM DEM. Slope and local relief for AFT and AHe data is calculated using 90-m SRTM DEM with 5-km radius buffers created around each AFT and AHe sample location.

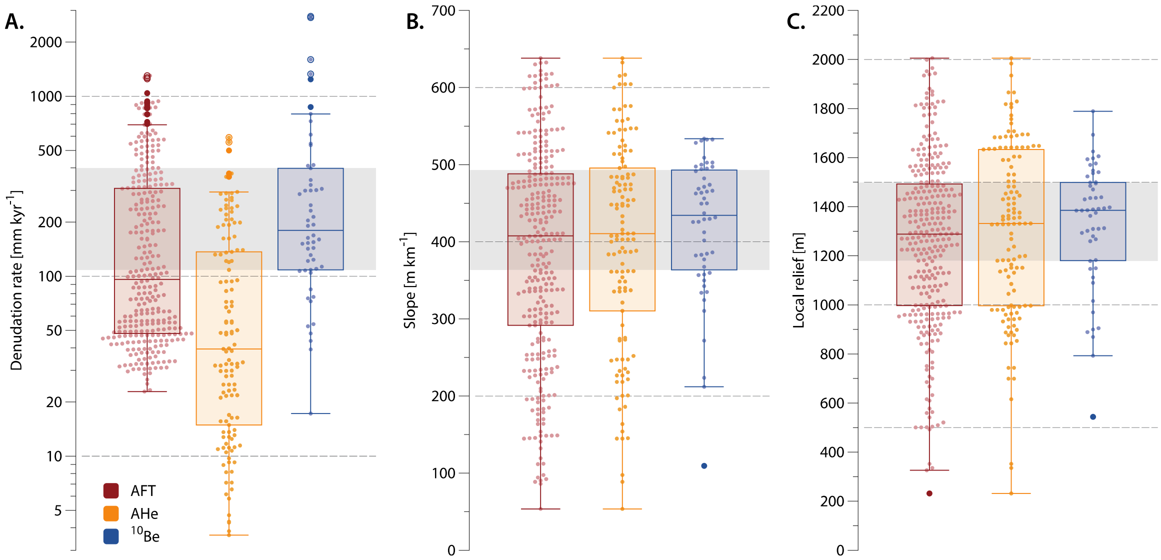

Figure 4.3. Modern ^{10}Be-derived denudation rates, AFT and AHe exhumation rates, topographic gradient, and local relief data from across the Kyrgyz Tian Shan plotted together. See caption of Figure 4.2 for further details.

4.3.4. Data grouping

To facilitate a meaningful comparison between the ^{10}Be-derived denudation rates and the long-term exhumation rates inferred from the published AFT and AHe data, we divide our ^{10}Be dataset into eight regions (Figures 4.1B and Supplementary Figure S4.1, Supplementary Table S4.5): Issyk-Kul North (n = 14), Issyk-Kul South (n = 8), Song Kul (n = 13), Naryn (n = 5), Kyrgyz range (n = 4), Toktogul (n = 3), Jalal Abad (n = 4), and Osh (n = 3). The grouping strategy is focused on the regional distribution of our modern sediment ^{10}Be data. In each region we include AFT and AHe datapoints that are located within or in the proximity of the drainage basins with ^{10}Be data and belong to the same tectonic position (e.g., footwall/hanging wall).

4.4 Results

The ^{10}Be concentrations of modern river sands range between 7.92 ± 0.83 × 10^{3} and 1,460.12 ± 29.24 × 10^{3} atoms g^{-1} (Supplementary Table S4.1). Basin-wide denudation rates calculated from these concentrations range between 17.3 and 2,780.4 mm kyr^{-1}, with the mean value of 393.8 mm kyr^{-1} and median value of 179.6 mm kyr^{-1} (Supplementary Table S4.1). Averaging times range between 34.8 and 0.2 kyr (Supplementary Tables S4.1 and S4.5).

The cosmogenic nuclide concentrations, ages, and paleo-denudation rates of buried samples from the southern part of the Issyk-Kul basin are shown in Supplementary Table S4.2. The ^{10}Be and ^{26}Al concentrations ($\times$ 10^3 atoms g^{-1}) of the buried samples are as follows: 30.80 ± 1.01 and 57.34 ± 6.56 (^{10}Be and ^{26}Al respectively, AKT-U); 92.04 ± 2.53 and 272.15 ± 16.11 (PET-QTS-L); and 114.78 ± 3.16 and 227.15 ± 17.31 (PET-QTS-PIT). Paleo-denudation rates (mm kyr^{-1}) obtained by assuming complete and continuous burial are: 72.2 ± 11.7 (AKT-U), 33.0 ± 3.5 (PET-QTS-L), and 18.7 ± 1.8 (PET-QTS-PIT). Allowing for uncertainties related to the average elevation of the sediment's source areas and to the possibility of incomplete burial or lengthy exposure to cosmic radiation prior to sampling, we obtain the following paleo-denudation rate ranges for the three sites: 50.6 ± 8.2 – 204.0 ± 32.8 for AKT-U; 22.9 ± 2.5 – 94.1 ± 10.0 for QTS-L; and 12.9 ± 1.2 – 53.8 ± 5.1 for QTS-PIT.

The calculated long-term AFT and AHe exhumation rates are summarised in Supplementary Tables S4.3 and S4.4. For each AFT and AHe age we calculate three exhumation rates: high — expressed as the age plus the uncertainty; middle — calculated from the age; and low — expressed as the age minus the uncertainty. Inferred AFT exhumation rates (middle values) range between 22.9 and 1,301.4 mm kyr^{-1}, and inferred AHe exhumation rates (also middle values) range between 3.6 and 590.0 mm kyr^{-1}. The compiled Kyrgyz AFT and AHe data excluded from the eight regions (see above) are still used for calculation of the mean and median values for the entire datasets. Mean and median AFT middle exhumation rates in the Kyrgyz Tian Shan are 212.0 and 96.0 mm kyr^{-1}, respectively. Mean and median middle AHe exhumation rates in the Kyrgyz Tian Shan are 94.1 and 39.4 mm kyr^{-1}, respectively.

We find moderate, but statistically significant, correlations between the log-transformed ^{10}Be-derived modern denudation rates and topographic gradient ($R = 0.430$; p-value < 0.01) and local relief ($R = 0.428$; p-value < 0.01) (Figure 4.4). We also find a weak correlation between the log-transformed denudation rates and mean annual rainfall, albeit this correlation is counterintuitively negative ($R = -0.326$; p-value < 0.05) (Figure 4.4). We find weak correlations between the log-transformed denudation rates and mean basin elevation and normalised channel steepness (k_{sn}), and no correlation between denudation rate and strain rate. When looking at the data grouped into regions, the picture is more complicated: albeit a moderate to strong correlation is observed between denudation rate and topographic gradient in most regions, metrics such as mean annual rainfall, the rainfall of the wettest month, and the aridity index are stronger predictors of ^{10}Be denudation rate in some regions including the Terskey range, south of lake Issyk-Kul (Figure 4.4).

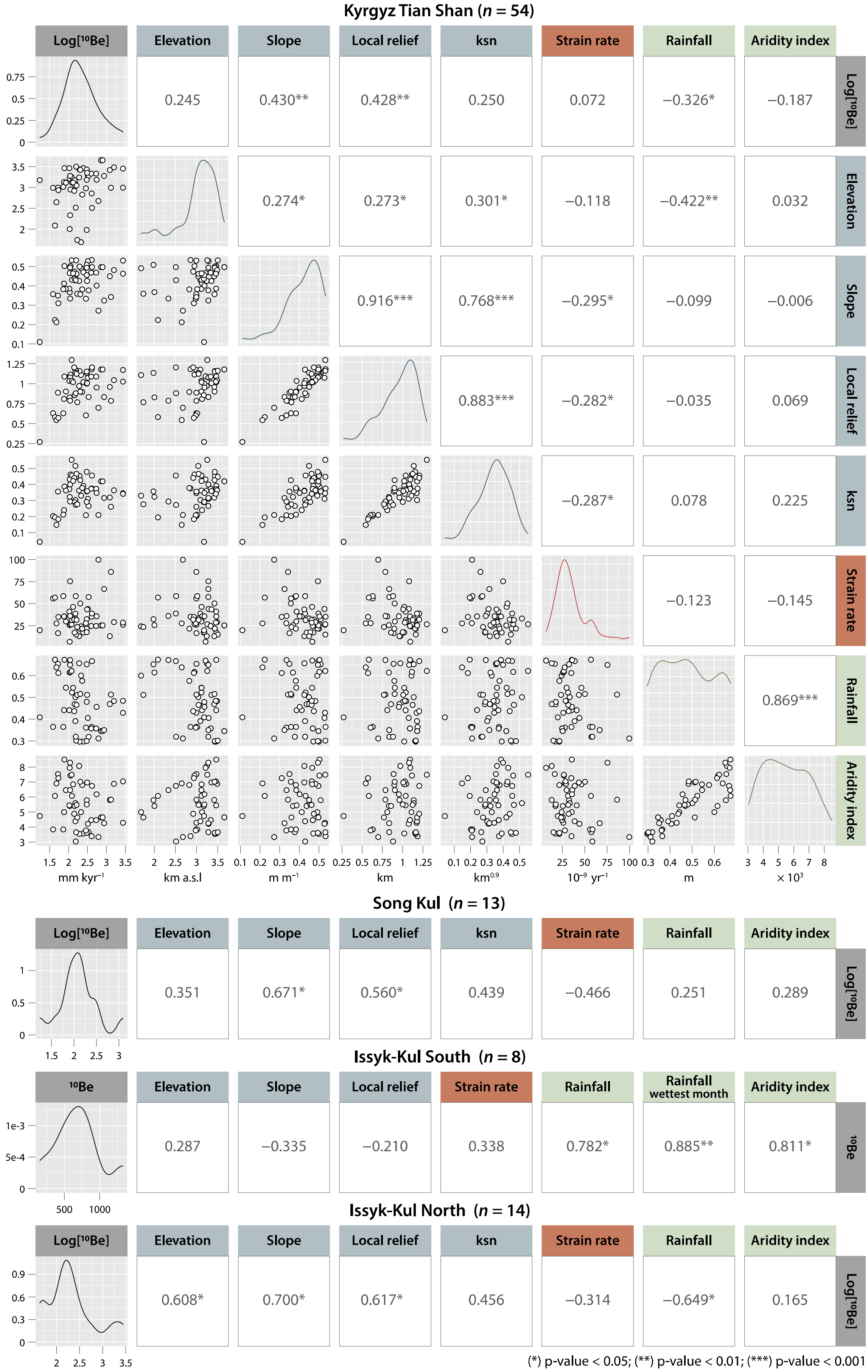

Figure 4.4. Correlation matrix displaying Pearson's correlation coefficients for ^{10}Be-derived denudation rates and different topographic, tectonic, and climatic metrics calculated for the Kyrgyz Tian Shan dataset.

The mean and median values for the ^{10}Be-derived millennial-timescale denudation rates, AFT-, and AHe-derived long-term exhumation rates for each of the eight regions are summarised in Supplementary Table S4.6.

4.5 DISCUSSION

4.5.1. SPATIAL AND TEMPORAL CHANGES IN DENUDATION AND EXHUMATION RATES

The following are some general spatial and temporal trends that we can observe in our data:

- The ^{10}Be-derived paleo-denudation rates obtained from material dated to 2.0–2.7 Ma are lower than the ^{10}Be-derived denudation rates obtained from modern river sediment (Figure 4.2).
- The ^{10}Be-derived denudation rates obtained from modern river sediment are generally higher than the long-term AFT and AHe exhumation rates across the studied area, except for the Kyrgyz range. On average, the highest ^{10}Be-derived denudation rates are recorded in the Issyk-Kul South region (Figure 4.2).
- The ^{10}Be-derived paleo-denudation rates obtained from material dated to 2.0–2.7 Ma are comparable in magnitude with the long-term exhumation rates inferred from AFT and AHe in the Issyk-Kul South region (Figure 4.2).
- Long term exhumation rates inferred from AHe ages are overall lower than those obtained from AFT ages (Figure 4.3).

Sample AKT-U, in the south-western part of the Issyk-Kul basin, dated to 2.71 ± 0.37 Ma (Kudriavtseva et al., 2023), yields a paleo-denudation rate between 50.6 ± 8.2 – 204.0 ± 32.8 mm kyr^{-1}, whereas the nearest modern river sediment sample (KYR16-05) yields a rate of 612.1 ± 112.8 mm kyr^{-1}. Further east, samples PET-QTS-L (2.08 ± 0.14 Ma) and PET-QTS-PIT (2.75 ± 0.15 Ma) (Kudriavtseva et al., 2023) yield paleo-denudation rate ranges between 22.9 ± 2.5 – 94.1 ± 10.0 mm kyr^{-1} and 12.9 ± 1.2 – 53.8 ± 5.1 mm kyr^{-1}, respectively, lower than those obtained from the nearest modern river sediment samples: 154.7 ± 28.6 mm kyr^{-1} (KYR16-03), 871.9 ± 158.8 mm kyr^{-1} (KYR16-55), 727.0 ± 131.3 mm kyr^{-1} (KYR16-01B), and 798.17 ± 144.31 mm kyr^{-1} (KYR16-01C) (Supplementary Tables S4.1 and S4.2). The elevated ^{10}Be-derived modern denudation rates compared to both the 2.0–2.7 Ma ^{10}Be-derived paleo-denudation rates and the long-term AFT and AHe exhumation rates indicate that in the Kyrgyz Tian Shan, denudation remained relatively steady until an increase in the Quaternary, after ca. 2 Ma. Ganti et al. (2016) suggested that in glaciated areas — such as our study area — there is a time-dependent bias of higher denudation rates towards the present with shorter averaging time scales caused by the discrete nature of erosional processes. Their model shows that when using a power law distribution, erosional hiatuses result in a systematic increase in denudation rates towards the present and this mechanism might be invoked to explain the observed increase in ^{10}Be derived modern denudation rates as compared to the long-term AFT and AHe exhumation rates. However, the difference between our modern denudation rates and the ^{10}Be derived paleo-denudation rates — that are also similar in magnitude to the AFT and AHe derived rates — suggests that the observed temporal increase in denudation rates in the Kyrgyz Tian Shan is real rather than being an artefact of differing averaging timescales.

Exhumation of the Kyrgyz range commenced at 11–7 Ma and propagated eastward (Bullen et al., 2001, 2003; Sobel et al., 2006b). Before that time, this area was a basin filled with ca. 2 km of young, relatively poorly consolidated sediments and so the elevated AFT exhumation rates recorded for the Kyrgyz range represent rapid exhumation of these poorly consolidated sediments in the beginning of the range growth (Bullen et al., 2003; Sobel et al., 2006b). ^{10}Be-derived modern denudation rates in the Kyrgyz range are similar to those recorded in other regions (Supplementary Table S4.1; Figure 4.2), suggesting a deceleration of denudation after removal of the poorly consolidated sediments and a subsequent adjustment of denudation rates here to the glacial conditions across the Kyrgyz Tian Shan.

Both AFT and AHe thermochronological systems average exhumation rates over the timescale of millions of years, but the difference in their closure temperatures and closure depths denotes a difference in averaging timescales, with AHe exhumation rates averaging over a shorter timescale than AFT rates (Reiners et al., 2005; Reiners & Brandon, 2006). Our calculated AFT and AHe exhumation rates are comparable, but slightly lower AHe than AFT rates imply slightly decelerating exhumation despite intensification of deformation in the Kyrgyz Tian Shan in the late Miocene (Macaulay et al., 2014; Glorie & De Grave, 2016; Wang et al., 2023). Notwithstanding the above, incorrect AHe ages are more frequently too old rather than too young, as the most prevalent problem with the AHe method is the under detection of U- or Th-rich inclusions (e.g., Farley, 2002). Although every effort is made in the individual studies to remove incorrect aliquot ages, it is possible that some of the reported ages compiled here are too old and hence our calculated AHe exhumation rates may be too low. For this reason, we do not place a strong emphasis on the slight difference between the AFT and AHe exhumation rates reported here.

Northern Hemisphere glaciations initiated in the Pliocene (Westerhold et al., 2020) and intensified after 2.7 Ma (Ruggieri et al., 2009; Hayashi et al., 2020), but our 2.0–2.7 Ma ^{10}Be-derived paleo-denudation rates from the southern side of the Issyk-Kul basin do not seem to reflect these global climatic changes. Furthermore, thermochronological data suggest that the Terskey range (situated on the southern side of the Issyk-Kul basin; Figure 4.1A) formed in the Miocene and did not experience strong deformation and exhumation afterwards (Macaulay et al., 2014). The strongest glacial erosional response is predicted by numerical modelling to occur in regions with large glaciations, moderate rock uplift (0.3–1 mm per year) and wet climate, whereas in arid conditions the response time of glacial erosion is predicted to be long and of small magnitude (Herman et al., 2018). Given the above, we propose that the aridity of the Tian Shan has dampened and delayed the denudational response to climatic forcing, and that the Quaternary glacial-interglacial cycles had a primary role in increasing millennial-scale denudation rates in the Kyrgyz Tian Shan and particularly in the Terskey range. We discuss these trends in more detail next.

4.5.2. Implications of the onset of Plio-Pleistocene glaciation in the Kyrgyz Tian Shan

The similarity in magnitudes between the 2.0–2.7 Ma ^{10}Be-derived paleo-denudation rates and the long-term AFT and AHe exhumation rates implies a relatively steady denudation through the Miocene, Pliocene, and early Pleistocene. The three samples used to determine our ^{10}Be-derived paleo-denudation rates were collected from sandstone lenses in conglomerates from the Sharpyl Dak sedimentary group, which was deposited above finer-grained sediments and is analogous to the Xiyu formation conglomerates in the Chinese Tian Shan (Abdrakhmatov et al., 2001; Chen et al., 2002; Heermance et al., 2007). Deposition of the Sharpyl Dak and Xiyu conglomerates is diachronous across the Tian Shan, varying from mid-Miocene to Pleistocene (Chen et al., 2002; Heermance et al., 2007; Charreau et al., 2009; Kudriavtseva et al., 2023), and is considered to mark either the intensification of tectonic activity or the onset of Plio-Pleistocene glaciation in the region (Zhao et al., 2021). Samples AKT-U (2.71 ± 0.37 Ma) and PET-QTS-PIT (2.75 ± 0.15 Ma) were taken from the basal parts of the conglomerates, whereas sample PET-QTS-L (2.08 ± 0.14 Ma) was collected from the youngest outcropping Sharpyl Dak conglomerates (Kudriavtseva et al., 2023). Therefore, commencement of the deposition of the Sharpyl Dak conglomerates was synchronous with the global intensification of Northern Hemisphere glaciation at 2.7 Ma (Ruggieri et al., 2009; Hayashi et al., 2020). Nevertheless, despite the transition from fine-grained to conglomerate deposition, our data do not indicate an acceleration of denudation at 2.7 Ma.

In the Tian Shan, denudation is generally slow due to arid conditions, despite tectonic activity, high relief, and glaciations (Guerit et al., 2016; Jepson et al., 2021). Absence of a denudational response to the Plio-Pleistocene onset of glaciation inferred from our data may indicate that significant glaciation in the Kyrgyz Tian Shan only initiated after 2 Ma, or that the onset of the Kyrgyz Tian Shan glaciation did occur simultaneously with that of the global Northern Hemisphere glaciations but did not cause a detectable increase in denudation rates. Deciding on which of the two explanations is more likely is confounded by the fact that the onset of glaciation in the Tian Shan is poorly constrained, although there is evidence suggesting that glaciations there occurred asynchronously with those in Europe and North America (Koppes et al., 2008; Sanhueza-Pino et al., 2011). It is also possible that the ^{10}Be-derived paleo-denudation rates reported here are not representative of the entire Kyrgyz Tian Shan and rather reflect local conditions of the Terskey range (Figure 4.1A). For example, Charreau et al. (2011) reported a ^{10}Be-derived erosional pulse from 3.0 to 1.7 Ma in the Eastern (Chinese) Tian Shan, suggesting a transient increase in denudation in response to the onset of glaciation. However, this conclusion is based only on data from a single drainage basin. Conversely, Puchol et al. (2017) report ^{10}Be-derived paleo-denudation rates from four localities in the Eastern (Chinese) Tian Shan that indicate that denudation continuously increased since 9 Ma and remained relatively steady since 4 Ma (i.e., since before the onset of glaciation). Additionally, Puchol et al. (2017) also found an increase in the spatial and short-term (< 1 Myr) temporal variability of denudation rates between 3 and 1 Ma, suggesting a transient response of the landscape to glacial-interglacial cycles. Taken together, the above suggest that the erosional response and adjustment of the landscape to the onset of Plio-Pleistocene glaciation may vary spatially and temporally across the Tian Shan. Furthermore, each studied drainage basin may also be affected by local tectonic processes. However, it is intriguing that the recent sequence of large magnitude earthquakes in the Kyrgyz, Kungey, and Trans Ili ranges (Landgraf et al., 2016) does not seem to be specifically reflected within the modern denudation rates.

4.5.3. The impact of Quaternary glaciation on denudation rates

Glaciers advanced and retreated during the late Pleistocene (Marine Isotope Stages [MIS] 6–2) and extended beyond individual valleys, but the only well-constrained regional glacial expansion occurred during MIS 2 (29–14 ka; Lisiecki & Raymo, 2005), with glaciers restricted to valleys due to aridity (Blomdin et al., 2016 and references therein). The largest glacial cover developed in the eastern part of the Kyrgyz Tian Shan (Blomdin et al., 2016). Alpine glacial cover impacts cosmogenic ^{10}Be abundances via two mechanisms: (1) excavation of material from depth, and (2) shielding of bedrock from cosmic radiation. Both mechanisms result in a decrease in ^{10}Be concentration in the sediment mix exiting a glaciated drainage basin and consequently an overestimation of ^{10}Be-derived denudation rates (Granger & Schaller, 2014; Schaefer et al., 2022). Our ^{10}Be-derived modern denudation rates are consistent with a global compilation of ^{10}Be-derived denudation rates, which shows a detectable increase in denudation in the mid-latitude glaciated regions, driven by Quaternary glaciations (Codilean et al., 2018; 2022; Chen et al., 2022b). Glacial erosion enhances sedimentation, which lasts longer than the period of glaciation, resulting in an increased erosional signal during interglacial periods as well (Ganti et al., 2016). Moreover, extensive glaciation could lead to a change in the locus of deformation in the ranges of the Kyrgyz Tian Shan, which could also result in acceleration of erosion (e.g., Berger et al., 2008).

Relatively high ^{10}Be-derived denudation rates in the Issyk-Kul South region suggest increased denudation of the northern flank of the Terskey range compared to other sampled ranges in the Kyrgyz Tian Shan. The reason for these elevated rates, however, is unclear. This region receives a low amount of precipitation (Supplementary Table S4.5), and exhumation in the Terskey range did not increase after 5 Ma (Macaulay et al., 2014). At the present time, the northern peripheral ranges of the Tian Shan, including the Terskey range, experience severe glacier shrinkage (Kutuzov & Shahgedanova, 2009; Sorg et al., 2012). The Terskey range receives the majority of precipitation in summer, when rainout occurs at high elevations (Bershaw & Lechler, 2019), so that the streams probably bring sediments from previously glaciated areas of the drainage basins. Also, the Tian Shan drainage basins with a higher portion of glaciated area, especially the northern slope of the Terskey range, show a substantial increase in runoff due to glacier reduction (Unger-Shayestech et al., 2013 and references therein). Additionally, correlation between the denudation rates and precipitation (Figure 4.4) indicates that river runoff might be amplified by summer rainout despite the generally low amount of precipitation. Therefore, relatively high ^{10}Be-derived denudation rates in our study area can reflect either an increase in denudation due to higher runoff or admixing of previously shielded sediments with lower ^{10}Be concentration, or a combination of both.

Comparison of our ^{10}Be data with published data from the Western Tian Shan and Northern Pamir (Grin et al., 2018) as well as Eastern (Chinese) Tian Shan (Charreau et al., 2023) illustrates a spatial west to east trend of decreasing average ^{10}Be-derived modern denudation rates (Figure 4.5). In the Northern Pamir and Western Tian Shan, ^{10}Be-derived basin-wide denudation rates (n=20) range from 180.0 to 2700.0 mm kyr^{-1}, with an average of 1400.0 mm kyr^{-1} (Grin et al., 2018), significantly higher than the average of our ^{10}Be-derived denudation rates from across the Kyrgyz Tian Shan (i.e.

393.8 mm kyr^{-1}). Furthermore, our denudation rates are comparable but slightly higher than those in the Eastern (Chinese) Tian Shan, where ^{10}Be-derived basin-wide denudation rates (n=34) range from 20.0 to 530.0 mm kyr^{-1}, averaging at 200.0 mm kyr^{-1} in the north and 110.0 mm kyr^{-1} in the south (Charreau et al., 2023). Denudation rates remained elevated but steady over million-year timescales in the Western Tian Shan and Northern Pamir, as suggested by the similarities in magnitude between short-term (river load), millennial-scale (^{10}Be) and long-term (10^6 years; thermochronology) denudation/exhumation rates (Grin et al., 2018). Conversely, in the Eastern (Chinese) Tian Shan, denudation stayed relatively steady since at least the Pleistocene (Charreau et al., 2011; 2017; 2023). Therefore, high rates of exhumation and denudation in the Pamir and Western Tian Shan are most likely mainly controlled by strong deformation caused by the indentation of the Pamir (Figure 4.5C; Wang et al., 2023), and might also be sustained by higher amount of precipitation because the Pamir acts as a topographic barrier to the westerlies (Figure 4.6; Carrapa et al., 2014; Wang et al., 2020; Richter et al., 2022).

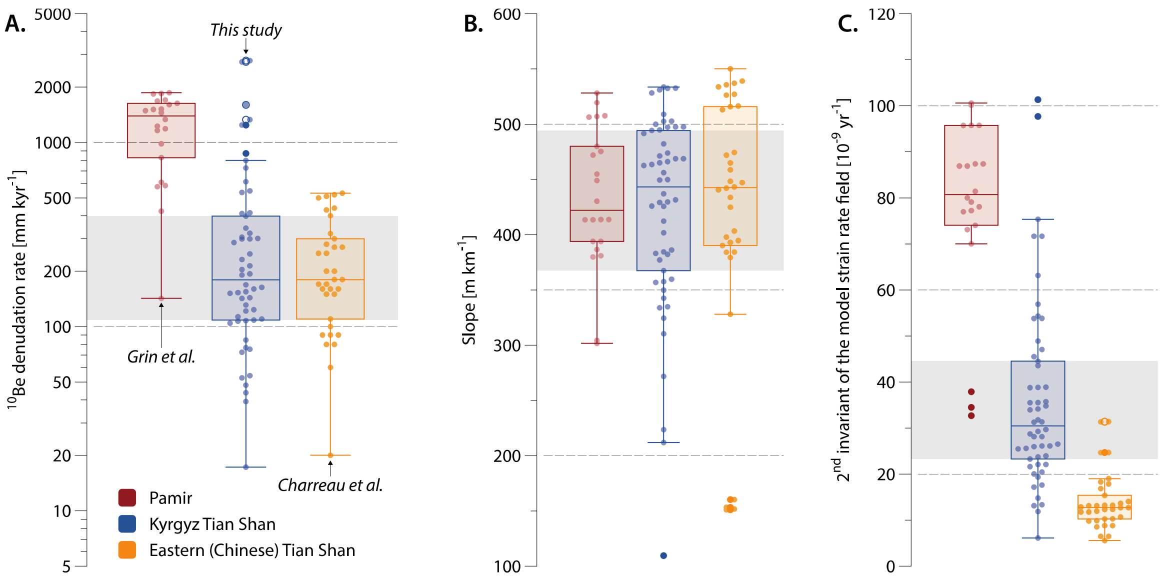

Figure 4.5. Modern ^{10}Be-derived denudation rates, topographic gradient, and strain rate from Pamir (Grin et al., 2018), Kyrgyz Tian Shan (this study), and Eastern (Chinese) Tian Shan (Charreau et al., 2023).

Taken together, the available data suggest that strong tectonic activity and higher precipitation rates exert a pronounced control on denudation in the Western Tian Shan, whereas further east, precipitation and tectonically driven denudation decrease and the denudational response of the landscape to Quaternary glaciations becomes detectable.

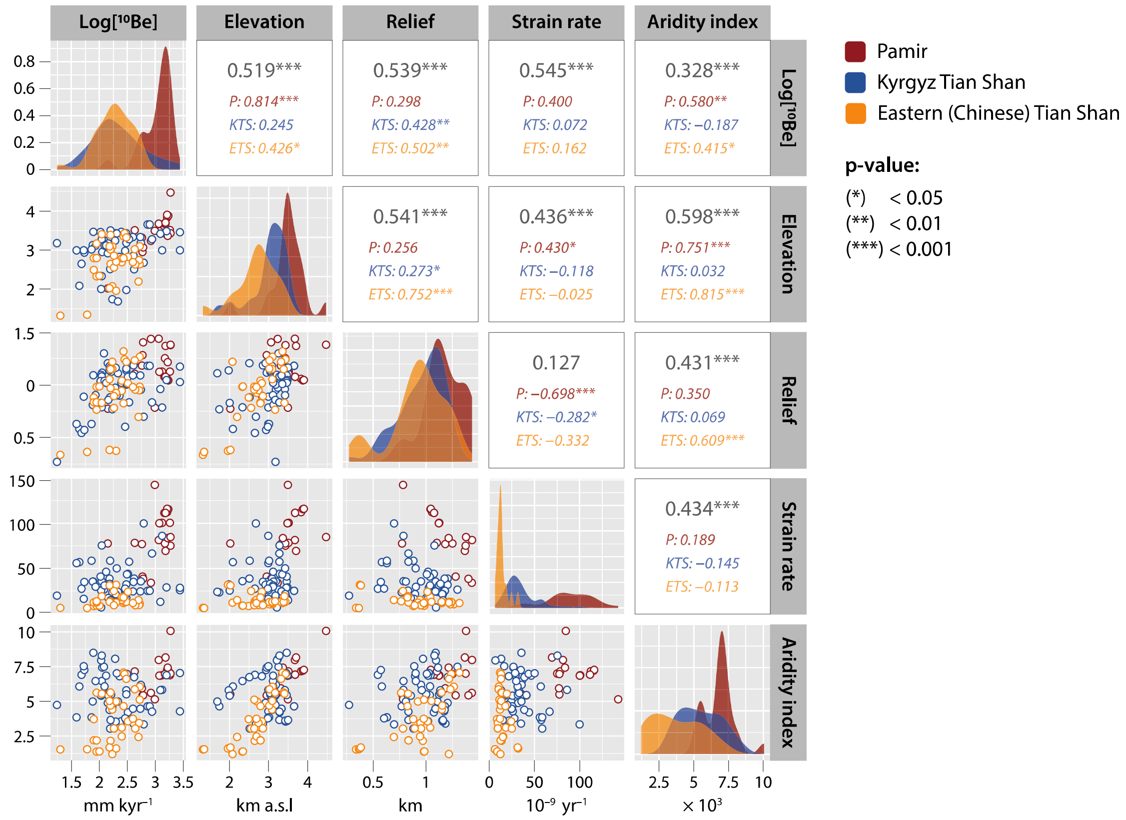

Figure 4.6. Correlation matrix displaying Pearson's correlation coefficients for ^{10}Be-derived denudation rates and different topographic, tectonic, and climatic metrics calculated for data from Pamir (Grin et al., 2018), Kyrgyz Tian Shan (this study), and Eastern (Chinese) Tian Shan (Charreau et al., 2023). The grey values represent the correlation coefficient for the entire dataset when all data are considered together. The coloured values are the correlation coefficients for the three separate datasets.

4.5.4. Correlations between ^{10}Be-derived denudation rates and topographic, tectonic, and climatic metrics

When considering the complete Kyrgyz dataset, our analyses found only moderate correlation between log-transformed ^{10}Be-derived modern denudation rates and topographic metrics such as gradient and local relief (R = 0.430 and R = 0.428, respectively, significant at p-value < 0.01; Figure 4.4). The lack of a strong correlation between denudation rate and topography is not unusual, considering the complex interplay between surface processes and tectonic and climatic controls (Portenga & Bierman, 2011; Dosseto & Schaller, 2016; Chen et al., 2022b), and is consistent with similar findings by Grin et al. (2018) and Charreau et al. (2023) in the Western Tian Shan and Northern Pamir and the Eastern (Chinese) Tian Shan, respectively — both studies reported weak correlations between ^{10}Be denudation rate and topography. Furthermore, our analysis found no correlation between denudation rates in the Kyrgyz Tian Shan and strain rate (expressed as the second invariant of the model strain rate field; Kreemer et al., 2014) and only weak correlations with annual rainfall and the aridity index.

Interestingly, but not surprisingly, however, when considering the entire available dataset (i.e., including the Pamir, the Western Tian Shan, and the Chinese Tian Shan), we find a statistically significant moderate correlation between the log-transformed ^{10}Be denudation rate and strain rate (R = 0.545, p-value < 0.001; Figure 4.6), and we also find a weak but statistically significant correlation between the log-transformed ^{10}Be denudation rate and the aridity index (R = 0.328, p-value < 0.001). The above, again, likely reflects both strong deformation and high precipitation rates in the Pamir.

^{10}Be-derived denudation rates in the Terskey range, south of lake Issyk-Kul (Figures 4.1 and 4.4), show a statistically significant strong correlation with annual rainfall (R = 0.782, p-value < 0.05), the aridity index (R = 0.811, p-value < 0.05), and precipitation of the wettest month (R = 0.885, p-value < 0.01). However, this region, with the exception of the easternmost drainage basin (sample KYR16-04), receives a relatively small amount of precipitation compared to the other regions (Supplementary Table S4.5), and the correlations with annual rainfall and the aridity index break down when this basin is excluded. The exclusion of KYR16-04 is justified by the large number of documented landslides in close vicinity to the sampling point (Pittore et al., 2018). Landslides in Kyrgyzstan are strongly correlated with rainfall and snowmelt (Wang et al., 2021). Unlike other drainage basins in the Terskey range, KYR16-04 has high values of both strain rate and annual precipitation which can cause active landsliding responsible for an over-estimated ^{10}Be denudation rate that may bias the correlation (e.g., Niemi et al., 2005). Correlation with precipitation of the wettest month remains statistically significant when the basin KYR16-04 is excluded. This might indicate that in the Terskey range summer rainout is intense enough to increase river runoff and control denudation, unlike in other parts of the Kyrgyz Tian Shan.

To summarise, the lack of strong correlation at the mountain range scale, and the variability in dominant predictors between regions is not surprising and might be explained by the large spatial spread of our ^{10}Be dataset and the influence of local factors.

4.6 Conclusions

Our study reports ^{10}Be-derived basin-wide denudation rates from modern river sediment from across the Kyrgyz Tian Shan and the Kazakh part of the Trans Ili and Kungey ranges, as well as ^{10}Be-derived paleo-denudation rates from buried river sediment dated to 2.0–2.7 Ma from the southern side of the Issyk-Kul basin. We compare these data to long-term exhumation rates, calculated from published apatite fission track (AFT) and apatite (U-Th-Sm)/He (AHe) thermochronology data, and explore the spatial and temporal variations in denudation rates in the Kyrgyz Tian Shan as well as relationships between denudation rates and geomorphic, tectonic, and climatic metrics to identify potential controls on denudation at the local scale.

Our results show that the ^{10}Be-derived denudation rates obtained from modern river sediment are generally higher than the long-term AFT and AHe exhumation rates across the studied area, except for the Kyrgyz range. Here, ^{10}Be-derived modern denudation rates are lower than long-term exhumation rates likely because of rapid exhumation and removal of soft sediments in the beginning of the range growth. On average, the highest ^{10}Be-derived denudation rates are recorded in the Terskey range, south of lake Issyk-Kul. Here ^{10}Be-derived modern denudation rates are higher than ^{10}Be-derived paleo-denudation rates obtained from material dated to 2.0–2.7 Ma, which are comparable in magnitude with the long-term exhumation rates inferred from AFT and AHe. The high ^{10}Be-derived denudation rates on the southern side of the Issyk-Kul basin compared to other sampled regions in the Kyrgyz Tian Shan suggests a recent increase in denudation rates on the northern slope of the Terskey range due to high glacial meltwater runoff, and/or admixing of previously shielded sediments with low ^{10}Be concentration.

We propose that denudation in the Kyrgyz Tian Shan, particularly in the Terskey range, remained relatively steady during the Neogene and early Pleistocene despite the late Pliocene facies change from fine-grained sediment to conglomerates. Denudation increased due to glacial-interglacial cycles in the Quaternary, but this occurred after the onset and intensification of the Northern Hemisphere glaciation at 2.7 Ma. This delay in the denudational response of the landscape could indicate that glacial erosion in arid regions is detectable using cosmogenic radionuclides only after substantial cooling and extensive growth of glaciers. We acknowledge, however, that our ^{10}Be-derived paleo-denudation rate data is limited in size and areal extent and so might not be representative of the entire Kyrgyz Tian Shan, and that other parts of the range might exhibit different temporal patterns of denudational response to Quaternary climate changes.

Comparison of our ^{10}Be-derived modern denudation rates with published data from the Western Tian Shan, Northern Pamir and Eastern (Chinese) Tian Shan show a spatial trend of decreasing denudation rates from west to east, suggesting that deformation caused by the indentation of the Pamir controls denudation in the Pamir and Western Tian Shan, while further east, precipitation and tectonically driven denudation decrease and the denudational response of the landscape to Quaternary glaciations becomes detectable.

Our analysis found moderate correlations between ^{10}Be-derived modern denudation rates and topographic metrics (i.e., topographic gradient and local relief) and weak correlation between denudation rates and annual rainfall. When considering the entire available dataset (i.e., including the Pamir, the Western Tian Shan, and the Chinese Tian Shan), correlations between ^{10}Be denudation rate and topographic metrics improve slightly, and we also find a statistically significant moderate correlation between the ^{10}Be denudation rate and strain rate, and a weak but statistically significant correlation between ^{10}Be denudation rate and the aridity index. At the local scale the picture is more complicated: albeit a moderate to strong correlation is observed between denudation rate and topographic gradient in most of the eight regions, metrics such as annual rainfall, the rainfall of the wettest month, and the aridity index are stronger predictors of ^{10}Be denudation rate in some regions including the Terskey range, south of lake Issyk-Kul. The above highlights the complex linkages between tectonics, climate, and surface processes, that may lead to the dominant controls on denudation varying locally.

5 Discussion and conclusions

Cenozoic uplift of the Tian Shan, Pamir, and the Tibetan plateau created topographic barriers while upwind, the Paratethys retreated; these occurred simultaneously with global cooling (Ramstein et al., 1997; Miao et al., 2012; Bosboom et al., 2017; Caves Rugenstein & Chamberlain, 2018; Kaya et al., 2019). Together, these changes eventually resulted in a decrease of the westerly moisture supply to Central Asia, subsequent aridification in the region (Miao et al., 2012), and creation of a unique environment within the Tian Shan with a strong difference in precipitation on the windward and leeward sides of the range (Baldwin & Vecchi, 2016; Caves Rugenstein & Chamberlain, 2018; Bershaw and Lechler, 2019). The Issyk-Kul basin lies within the Tian Shan range, surrounded by the Terskey range to the south, the Kungey and Trains Ili (Zaili) ranges to the north, and the Kyrgyz range to the west. Extracting information from the late Cenozoic sedimentary sequences exposed on the south side of the basin allows us to reconstruct the progression of local and regional changes.

5.1 Timing of Cenozoic sedimentary accumulation in the Issyk-Kul basin

The Issyk-Kul basin contains deposits divided into four sedimentary groups: the Kokturpak, Shamsi, Chu and Sharpyl Dak (Abdrakhmatov et al., 2001); our work better constrains the ages of three of these units. The oldest Kokturpak group has a late Cretaceous to Eocene age based on palynology (Fortuna et al., 1994). The overlying coarse deposits of the Shamsi group were first dated using magnetostratigraphy by Wack et al. (2014) in the Chon Kyzylsu and Jeti Oguz sections in the southeastern part of the basin. These authors suggest depositional ages of 22.8 to 13.3 Ma or 22.1 to 11.1 Ma in the Jeti Oguz section and 26.0 to 16.2 Ma or 25.2 to 11.0 Ma in the Chon Kyzylsu section. Poor magnetic recording of the Shamsi group deposits resulted in ambiguously defined polarity intervals and inconclusive age constraints (Wack et al., 2014). We re-evaluated the magnetostratigraphic data from these two sections and discuss the results in chapter 2. For the Chon Kyzylsu section, we re-correlated the polarity sequence considering all inconclusive horizons as unknown polarities and suggest bounding ages of 17.3 and 7.5 Ma. We also re-correlated the polarity sequence from the Jeti Oguz section to 22.4 to 8.5 Ma based on the tie-point between the Jeti Oguz and Chon Kyzylsu sections. This tie-point represents a change in magnetic properties observed in both sections (Wack et al., 2014).

The stratigraphically younger, fine-grained deposits of the Chu group and overlying conglomerates of the Sharpyl Dak group measured in the Ak Terek and Kaji Say sections are the main object of our study. In chapter 2 we propose the first magnetostratigraphic age models for the Chu group and Chu – Sharpyl Dak transition. The depositional age of the Chu group in the Ak Terek section is interpreted to be 6.3 to 2.8 Ma. However, magnetostratigraphy alone was insufficient for providing one robust age model for the Kaji Say section, as shown in chapter 2. Therefore, we propose two possible age models for the Chu – Sharpyl Dak deposits there. The first age model shows continuous sedimentation from 12.7 to 9.5 Ma and suggests that the Chu deposits of the Kaji Say section accumulated synchronously with the Shamsi group deposits from the Jeti Oguz and Chon Kyzylsu sections. The second proposed age model is 7.0 to 5.1 Ma and 3.0 to 2.4 Ma with a depositional hiatus in the middle of the section. $^{26}Al/^{10}Be$ isochron burial dating of the upper part of the Kaji Say section, discussed in chapter 3, resolved the ambiguity in timing of deposition and let us choose the second option (7.0 to 2.4 Ma with a depositional hiatus from 5.1 to 3.0 Ma). Combining our new magnetostratigraphic age models from the Ak Terek and Kaji Say sections with $^{26}Al/^{10}Be$ isochron burial ages from the same sections, we provide a late Miocene – Pliocene age for the Chu group deposits and place the Chu – Sharpyl Dak transition on the southern side of the basin at 2.6-2.8 Ma. However, the $^{26}Al/^{10}Be$ isochron burial age, measured from the Jergalan section, suggests a 5 to 4 Ma age for the Chu – Sharpyl Dak transition in the eastern side of the basin. This shows that the commencement of the Sharpyl Dak conglomerate deposition occurred diachronously in the Issyk-Kul basin, which is consistent with the diachronous deposition of the analogous Xiyu group conglomerates in the Chinese Tian Shan (e.g., Chen et al., 2002; Heermance et al., 2007; Charreau et al., 2009).

5.2 Depositional environment on the southern side of the Issyk-Kul basin in the late Miocene – early Pleistocene

The sedimentary sequence which outcrops at the Ak Terek section in the southwestern part of the basin suggests continuous fluvial deposition in the late Miocene. Rare still water deposition after 4 Ma is indicated by the presence of a gypsum layer. The conglomerates are sourced from the widespread granites of the Terskey range, to the south. Further east, the Kaji Say sedimentary section includes grey rounded granite conglomerates, typical for material sourced from the Terskey range, and red angular gravel conglomerates, sourced from the Taldysui subvolcanic complex, situated locally and proximally to the Kaji Say section.

As shown in chapter 2, a change in depositional environment from the coarse-grained Shamsi group to the fine-grained Chu group at ca. 7 Ma is marked by an increase in sedimentation rates on the southern and on the northwestern sides of the Issyk-Kul basin.

Near the Terskey range, sedimentation rates are faster at Kaji Say than at Ak Terek. At ca. 5 Ma, sedimentation rates increase in the northeastern part of the basin in the Kungey range area, and a short but intensive pulse of increased sedimentation occurred in Ak Terek. These changes in sedimentation rates are consistent with a pulse of exhumation in the Terskey range at 15-5 Ma (Macaulay et al., 2014). Concurrently, a depositional hiatus commenced at Kaji Say due to tectonically-induced river system reorganization.

Tectonically-driven reorganization of the river system recorded in the Kaji Say section at 5 Ma led to the disappearance of grey granitic conglomerates, while enhanced subsidence in the area resulted in commencement of lacustrine deposition and lake formation. We suggest that the hiatus occurred at this time due to changes in fluvial input in response to local deformation in the area. Alternatively, the hiatus might occur during deposition of the stratigraphically older beach facies due to a stable lake margin and reworking of the material. This second option implies that the hiatus is ca. 100 ka older than proposed by our magnetostratigraphic model. After termination of the depositional hiatus at ca. 3 Ma, local deformation in the Kaji Say area intensified. This is shown by higher sedimentation rates in Kaji Say than before the hiatus and formation of growth strata. Northwest thickening of the growth strata supports the idea of enhanced subsidence in the Kaji Say area in the late Miocene – Pliocene, which enabled lake formation. Furthermore, local deformation led to folding in the middle part of the section which is upstream of the youngest outcropping flat-lying Sharpyl Dak conglomerates, dated as 2.08 ± 0.14 Myr old according to the $^{26}Al/^{10}Be$ isochron burial dating. Deformation must postdate conglomerate deposition, as the fold isolated the youngest conglomerates from the source area.

5.3 EASTWARD GROWTH OF THE KUNGEY RANGE IN THE LATE MIOCENE

Our paleocurrent measurements, discussed in chapter 3, show predominantly southward paleocurrent directions of the Chu deposits sourced from the Kungey range. Therefore, our data suggest that the deposits in the northern part of the basin are mainly sourced from the growing Kungey range. If the stratigraphic boundary between the Shamsi and Chu groups adjacent to the Kungey range is 8-7 Ma, as in the Terskey range, then our data show that substantial uplift in the Kungey range commenced by this time. Conversely, Selander et al. (2012) presented mainly northward paleocurrent directions from the Chu deposits from the western Kungey, and both northward (stratigraphically older) and southward (stratigraphically younger) directions from the Chu deposits from the eastern Kungey. This led to a conclusion that in the middle Miocene the Kungey range was flat, sediments were sourced from the Terskey range, and initial uplift of the Kungey range commenced between 7 and 4 Ma (Selander et al., 2012).

However, eastward spreading of the depositional area in the Kungey range (Selander et al., 2012) and eastward increase in sedimentation rates adjacent to the Kungey range, shown in chapter 2, both suggest gradual eastward growth of the Kungey range in the late Miocene. Moreover, our southward paleocurrent directions measured in the Chu – Sharpyl Dak transitional deposits from the Jergalan section, dated to 5-4 Ma by $^{26}Al/^{10}Be$ isochron burial dating, suggest that surface uplift and exhumation of the easternmost Kungey range led to Sharpyl Dak deposition in the easternmost part of the Issyk-Kul basin at ca. 5 Ma, potentially leading to termination of a paleo-drainage connection with eastern basins and causing sediment starvation in the Issyk-Kul basin.

5.4 NEOGENE EVOLUTION OF CLIMATIC CONDITIONS IN THE ISSYK-KUL BASIN

Deformation and surface uplift of the Kyrgyz Tian Shan progressed generally from south to north (e.g., Macaulay et al., 2014; Li et al., 2022). Distribution of precipitation throughout the Kyrgyz Tian Shan shows increased rainout on the windward (northern) side (Baldwin & Vecchi, 2016; Caves Rugenstein & Chamberlain, 2018; Bershaw and Lechler, 2019), and surface uplift of the southern Tian Shan and Pamir resulted in desertification of the Tarin basin at ca. 12 Ma (Richter et al., 2022). Previous study of the Shamsi group deposits from the Jeti Oguz and Chon Kyzylsu sections using stable $\delta^{18}O$ and $\delta^{13}C$ isotopes suggests a windward position of the Issyk-Kul basin and increased rainout in the early and middle Miocene (Macaulay et al., 2016). This interpretation is based on the inconclusive age models from Wack et al. (2014). Our new age models for these sections combined with stable $\delta^{18}O$ and $\delta^{13}C$ isotopic records from Macaulay et al. (2016) support the idea that a growing Terskey range created windward and relatively wet conditions in the basin between 23 and 8 Ma, and prevented the moisture-bearing westerlies from penetrating farther into Central Asia.

Based on the $\delta^{18}O$ and $\delta^{13}C$ data presented in chapter 3, we show that substantial aridification in the Issyk-Kul basin started at 8-7 Ma. This environmental change is represented by a ca. 2‰ shift in $\delta^{18}O$ and $\delta^{13}C$ values and a change in the trend. There were no significant global climatic changes at this time and, furthermore, the $\delta^{18}O$ and $\delta^{13}C$ values from the neighboring Ili basin reflect global climatic changes and do not show similar changes in stable isotopic values (Hellwig et al., 2018; Frisch et al., 2019a; Prud'homme et al., 2021). Therefore, this local environmental change was most likely caused by creation of a local topographic barrier due to tectonic activity. Thermochronology data show that surface uplift of the Kyrgyz range, situated north-west of the Issyk-Kul basin, started at 11-7 Ma and advanced eastward (Bullen et al., 2001, 2003; Sobel et al., 2006b). Additionally, surface uplift of the northern Trans Ili and Kungey ranges commenced in the late Oligocene – early Miocene, as also defined by thermochronology (De Grave et al., 2013; De Pelsmaeker et al., 2015), but paleocurrent data show that the Chu group sediments deposited on the south side of the Kungey range area are sourced from the Tersky range and significant deformation in the Kungey range started in the late Miocene – early Pliocene (Selander et al., 2012). Therefore, surface uplift of the Kyrgyz, Trans Ili, and Kungey ranges created a topographic barrier, changing the position of the Issyk-Kul basin from a windward to a leeward position. During the Pliocene, aridification in the Issyk-Kul basin might have been sustained by global climatic changes when the moisture-bearing westerlies migrated southward and dry air masses of the Siberian High were dominant in Northern Central Asia. This is suggested by similarity of our $\delta^{18}O$ and $\delta^{13}C$ records with data from the contemporaneous Ili basin (Prud'homme et al., 2021).

5.5 Denudational response to Quaternary climatic changes in the Kyrgyz Tian Shan

One might expect that an increase in the rock uplift rate of the Terskey range would cause an increase in the exhumation rate. In turn, this should lead to an increase in the sedimentation rate, such as that observed at ca. 7 Ma. Subsequently, there is a transition from fine-grained fluvial-alluvial deposits of the Chu group to proximal alluvial fan conglomerates of the Sharpyl Dak group. The Chu – Sharpyl Dak transition occurred at 2.6-2.8 Ma on the southern side of the Issyk-Kul basin according to $^{26}Al/^{10}Be$ isochron burial dating, which is synchronous with the intensification of the Northern Hemisphere glaciation (Ruggieri et al., 2009; Hayashi et al., 2020). Additionally, an increase in sedimentation rates in the Kaji Say section occurs at ca. 3 Ma and marks a change in the depositional environment. However, in chapter 4 we show that our ^{10}Be-derived paleo-denudation rates from 2.0-2.7 Ma from the Kaji Say and Ak Terek sections are as low as long-term AFT- and AHe-derived exhumation rates from the adjacent Terskey range and do not reflect the changes recorded in the stratigraphic section. Therefore, our results, presented in chapter 4, suggest that tectonic activity in the late Miocene – Pliocene, river system reorganization, and the Plio-Pleistocene global climatic changes did not cause a detectable increase in denudation rates in the Terskey range.

Across the Kyrgyz Tian Shan, millennial-timescale ^{10}Be-derived denudation rates are higher on average than the long-term AFT- and AHe-derived exhumation rates are, except in the Kyrgyz range. We discuss these data in chapter 4. We suggest that the aridity has dampened and delayed the denudational response in the Kyrgyz Tian Shan (Herman et al., 2018; Jepson et al., 2021), and that only significant glaciation and cooling occurring during the Quaternary glacial-interglacial cycles had a primary role in increasing millennial-timescale denudation rates in the Kyrgyz Tian Shan. Moreover, a global compilation of ^{10}Be-derived denudation rates also shows that Quaternary glaciations caused a detectable increase in denudation in the mid-latitude glaciated regions (Codilean et al., 2018; 2022; Chen et al., 2022).

In the Kyrgyz range, unlike in other regions of the Kyrgyz Tian Shan, long-term thermochronology-derived exhumation rates are higher than millennial-timescale ^{10}Be-derived denudation rates. In chapter 4, we suggest that this is caused by rapid exhumation of young poorly consolidated sediments, which covered this area before commencement of surface uplift at 11-7 Ma (Bullen et al., 2001, 2003; Sobel et al., 2006b). Afterwards, denudation rates adjusted to the glacial conditions and showed similar average values as in other regions of the Kyrgyz Tian Shan.

The millennial-timescale denudation rates are notably higher on the southern side of the Issyk-Kul basin, reflecting more rapid denudation of the northern slope of the Terskey range compared to other areas in the Kyrgyz Tian Shan. We suggest that this is triggered by higher runoff and/or admixing of previously shielded sediments with lower ^{10}Be concentration due to particularly severe glacier shrinkage in the northern side of the Terskey range (Unger-Shayestech et al., 2013 and references therein). This can potentially lead to faster modification of the Terskey range topography and affect lake level.

Our new data presented in chapter 4 allow us elaborate on the spatial distribution of millennial-timescale denudation rates across the Tian Shan when combining with published data from the Western Tian Shan and Northern Pamir (Grin et al., 2018) and Eastern (Chinese) Tian Shan (Charreau et al., 2023). A spatial west to east trend of decreasing average ^{10}Be-derived denudation rates. In the Western Tian Shan and Northern Pamir, millennial-timescale ^{10}Be-derived denudation rates are of a similar magnitude as long-term thermochronology-derived exhumation rates (Grin et al., 2018). We suggest that in this area denudation is mainly controlled by strong deformation caused by the indentation of the Pamir (Wang et al., 2023), while further east in the Kyrgyz Tian Shan the denudational response of the landscape to Quaternary glaciations becomes detectable.

5.6 FACTORS CONTROLLING MODERN ^{10}BE-DERIVED DENUDATION RATES

In chapter 4, we show that in the Kyrgyz Tian Shan, correlations between ^{10}Be-derived modern denudation rates and topographic metrics (i.e., topographic gradient and local relief) are moderate, while correlations between ^{10}Be denudation rates and annual rainfall are weak. However, the correlation between ^{10}Be denudation rates and precipitation during the wettest month is strong in the Terskey range. This area receives the majority of precipitation in summer (Bershaw & Lechler, 2019). Therefore, we suggest that summer rainout in the Terskey range might be strong enough to increase runoff and affect denudation. Moreover, moderate correlation exists between ^{10}Be denudation rates and strain rate in the entire Tian Shan (Northern Pamir and Western Tian Shan, Grin et al., 2018; our study, and the Chinese Tian Shan, Charreau et al., 2023). This illustrates the complex interplay between tectonics, climate, and surface processes at a local and regional scales.

5.7 CONCLUSIONS AND FUTURE RESEARCH

Untangling interactions between climate, tectonics, and surface processes in the Tian Shan during the Cenozoic is the overall goal of my study. This research contributes to our knowledge of such interactions by providing a comprehensive study of the processes which controlled the development of the Issyk-Kul basin and denudation rates in the Kyrgyz Tian Shan. In this thesis, I showed how climatic conditions changed in the Issyk-Kul basin in relation to the uplift of individual mountain ranges of the Kyrgyz Tian Shan and Cenozoic global cooling. These changes within the Kyrgyz Tian Shan contributed to modification of Central Asian climate during the Cenozoic. Also, I described the processes which led to the formation of lake Issyk-Kul and subsequent expansion in the late Miocene – Pliocene, when the general climatic trend was towards aridification. Finally, I showed what controls and affects denudation and exhumation in the Kyrgyz Tian Shan on different timescales and in different climatic conditions and showed how modern Central Asian climate affects surface processes in the individual mountain ranges of the Kyrgyz Tian Shan.

The most significant outcomes of this study are as follows:

- Despite the generally windward position of the Kyrgyz Tian Shan in the northwestern part of Central Asia and immediate interactions with the moisture-bearing westerly wind, climatic conditions within the range, particularly in the Issyk-Kul basin, change drastically at 8-7 Ma with uplift of the northernmost Kyrgyz and Kungey ranges.

- Commencement of lake formation occurred in the Kaji Say area due to local tectonic activity and consequent enhancement of subsidence and reorganization of the river system in the central part of the Terskey range at ca. 5 Ma. Later during the Pliocene, eastward growth of the Kungey range possibly blocked westward-draining rivers, which had formerly connected the Issyk-Kul basin with eastern basins, leading to sediment starvation and lake expansion.

- Denudational response of the landscape to Quaternary glaciations in the Terskey range is delayed due to aridity of the region and becomes detectable only in the late Quaternary when cooling and glaciation was substantial.

- Currently, denudation of the northern slope of the Terskey range is more rapid than denudation of other ranges of the Kyrgyz Tian Shan due to intensive glacier reduction, summer rainout, and consequent increase in runoff. Therefore, the topography of the Terskey range might be modified faster in the future.

In this work, we were not able to unequivocally answer the question of the presence and precise position of the depositional hiatus in the Kaji Say stratigraphical section. Solving this is necessary to better understand the processes and timing of the beginning of lake formation. To answer this, it is necessary to obtain precise ages for the basal and/or middle parts of the section. Our work, described in chapter 3, showed that finding suitable samples for $^{26}Al/^{10}Be$ isochron burial dating at the bottom of the section is problematic. Therefore, more field work in the Kaji Say area is necessary to find suitable deposits which can be reliably correlated to our studied section. Additionally, it will be useful to do more field work to describe stratigraphical and geographical positions of lacustrine deposits in the Kaji Say area but beyond the studied stratigraphical section to see how exactly the initial lake developed.

This study also could not provide ages for the Chu – Sharpyl Dak transition on the south flank of the Kungey range, and our $^{26}Al/^{10}Be$ isochron burial ages for the easternmost Jergalan section are ambiguous. Knowing precise ages of the Chu – Sharpyl Dak transition in these areas will be useful to better reconstruct the eastward growth of the Kungey range and to understand the processes of basin development and lake expansion. Studying and dating the sedimentary deposits in the western and eastern parts of the basin might also help answer the question of when exactly the basin was isolated from the neighboring basins and became internally drained. Obtaining this information is necessary to understand how sediment accumulation in the basin controls the existence of this lake. However, these tasks will require extensive field work and a careful selection of outcrops and samples for dating.

Apart from that, a question remains whether the Plio-Pleistocene onset of glaciation enhanced denudation in other parts of the Kyrgyz Tian Shan besides the sampled Terskey range. This information will broaden our understanding of whether individual ranges respond to global climatic changes or if these processes are relatively uniform across the Tian Shan. This task, however, will require extensive work selecting and dating existing Chu – Sharpyl Dak transitional deposits in other Tian Shan basins.

References

Abdrakhmatov, K., Aldazhanov, S., Hager, B. et al. (1996). Relatively recent construction of the Tien Shan inferred from GPS measurements of present-day crustal deformation rates. *Nature*, *384*(6608), 450-453. https://doi.org/10.1038/384450a0

Abdrakhmatov, K., Djanuzakov, K.D., & Delvaux, D. (2002). Active Tectonics and Seismic Hazard of the Issyk-Kul Basin in the Kyrgyz Tian-Shan. In: Klerkx, J., Imanackunov, B. (editors) *Lake Issyk-Kul: Its Natural Environment.* NATO Science Series, 13. Springer, Dordrecht. https://doi.org/10.1007/978-94-010-0491-6_11

Abdrakhmatov, K., Weldon, R., Thompson, S.C., Burbank, D.W., Rubin, C., Miller, M., & Molnar, P. (2001). Onset, style and current rate of shortening in the central Tien Shan, Kyrgyz Republic. *Russian Geology and Geophysics*, *42*(10), 1585-1609.

Abell, J.T., Winckler, G., Anderson, R.F., & Herbert, T.D. (2021). Poleward and weakened westerlies during Pliocene warmth. *Nature*, *589*(7840), 70-75. https://doi.org/10.1038/s41586-020-03062-1

Aizen, E.M., Aizen, V.B., Melack, J.M., Nakamura, T., & Ohta, T. (2001). Precipitation and atmospheric circulation patterns at mid-latitudes of Asia. *International Journal of Climatology: A Journal of the Royal Meteorological Society*, *21*(5), 535-556. https://doi.org/10.1002/joc.626

Aizen, V.B., Aizen, E.M., Joswiak, D.R., Fujita, K., Takeuchi, N., & Nikitin, S.A. (2006). Climatic and atmospheric circulation pattern variability from ice-core isotope/geochemistry records (Altai, Tien Shan and Tibet). *Annals of Glaciology*, *43*, 49-60. https://doi.org/10.3189/172756406781812078

Aizen, V.B., Aizen, E.M., & Melack, J.M. (1995). Climate, snow cover, glaciers, and runoff in the Tien Shan, Central Asia 1. JAWRA Journal of the American Water Resources Association, 31(6), 1113-1129. https://doi.org/10.1111/j.1752-1688.1995.tb03426.x

Aizen, V.B., Aizen, E.M., Melack, J.M., & Dozier, J. (1997). Climatic and hydrologic changes in the Tien Shan, Central Asia. *Journal of Climate*, *10*(6), 1393-1404. https://doi.org/10.1175/1520-0442(1997)010<1393:CAHCIT>2.0.CO;2

Alexeiev, D.V., Bykadorov, V.A., Volozh, Y.A., & Sapozhnikov, R.B. (2017). Kinematic analysis of Jurassic grabens of soulthern Turgai and the role of the Mesozoic stage in the evolution of the Karatau–Talas–Ferghana strike-slip fault, Southern Kazakhstan and Tian Shan. *Geotectonics*, *51*, 105-120. https://doi.org/10.1134/S0016852117020029

Alonso-Zarza, A.M. (2003). Palaeoenvironmental significance of palustrine carbonates and calcretes in the geological record. *Earth-Science Reviews*, *60*(3-4), 261-298. https://doi.org/10.1016/S0012-8252(02)00106-X

Alonso-Zarza, A.M., & Wright, V.P. (2010). Palustrine carbonates. *Developments in Sedimentology*, *61*, 103-131. https://doi.org/10.1016/S0070-4571(09)06102-0

Alonso-Zarza, A.M., Wright, V.P., Calvo, J.P., & Del Cura, M.G. (1992). Soil-landscape and climatic relationships in the middle Miocene of the Madrid Basin. *Sedimentology*, *39*(1), 17-35. https://doi.org/10.1111/j.1365-3091.1992.tb01021.x

Avouac, J.P., & Burov, E.B. (1996). Erosion as a driving mechanism of intracontinental mountain growth. *Journal of Geophysical Research: Solid Earth*, *101*(B8), 17747-17769. https://doi.org/10.1029/96JB01344

Bakirov, A.B., & Maksumova, R.A. (2001). Geology and evolution of the Tien Shan lithosphere (in Russian). *Russian Geology and Geophysics, 42,* 1359–1366.

Balco, G., & Rovey, C.W. (2008). An isochron method for cosmogenic-nuclide dating of buried soils and sediments. *American Journal of Science*, *308*(10), 1083-1114. https://doi.org/10.2475/10.2008.02

Balco, G., Stone, J.O., Lifton, N.A., & Dunai, T.J. (2008) A complete and easily accessible means of calculating surface exposure ages or erosion rates from 10Be and 26Al measurements. Quaternary Geochronology, 3, 174–195. https://doi.org/10.1016/j.quageo.2007.12.001

Baldwin, J., & Vecchi, G. (2016). Influence of the Tian Shan on arid extratropical Asia. *Journal of Climate*, *29*(16), 5741-5762. https://doi.org/10.1175/JCLI-D-15-0490.1

Bande, A., Sobel, E.R., Mikolaichuk, A., Schmidt, A., & Stockli, D.F. (2017a). Exhumation history of the western Kyrgyz Tien Shan: Implications for intramontane basin formation. *Tectonics*, *36*(1), 163-180. https://doi.org/10.1002/2016TC004284

Bande, A., Sobel, E.R., Mikolaichuk, A., & Torres Acosta, V. (2017b). Talas–Fergana Fault Cenozoic timing of deformation and its relation to Pamir indentation. *Geological Society, London, Special Publications*, *427*(1), 295-311. https://doi.org/10.1144/SP427.1

Barbolini, N., Woutersen, A., Dupont-Nivet, G., Silvestro, D., Tardif, D., Coster, P.M.C., Meijer, N., Chang, C., Zhang, H.X., Licht, A., & Rydin, C. (2020). Cenozoic evolution of the steppe-desert biome in Central Asia. *Science Advances*, *6*(41), p.eabb8227. https://doi.org/10.1126/sciadv.abb8227

Batbaatar, J., Gillespie, A.R., Koppes, M., Clark, D.H., Chadwick, O.A., Fink, D., Matmon, A., & Rupper, S. (2021). Glacier development in continental climate regions of central Asia. In: Waitt, R.B., Thackray, G.D., Gillespie, A.R., (Eds), Untangling the Quaternary Period—A Legacy of Stephen C. Porter. *Geological Society of America, Special Paper, 548*, 119–149. https://doi.org/10.1130/2020.2548(07)

Bazhenov, M.L., Burtman, V.S., & Dvorova, A. V. (1999). Permian paleomagnetism of the Tien Shan fold belt, Central Asia: post-collisional rotations and deformation. *Tectonophysics*, *312*(2-4), 303-329. https://doi.org/10.1016/S0040-1951(99)00181-X

Bazhenov, M.L., & Mikolaichuk, A.V. (2004). Structural evolution of Central Asia to the North of Tibet: a synthesis of paleomagnetic and geological data. *Geotectonics*, *38*(5), 379-393.

Berger, A.L., Gulick, S.P., Spotila, J.A., Upton, P., Jaeger, J.M., Chapman, J.B., Worthington, L.A., Pavlis, T.L., Ridgway, K.D., Willems, B.A., & McAleer, R.J. (2008). Quaternary tectonic response to intensified glacial erosion in an orogenic wedge. *Nature Geoscience*, *1*(11), 793-799. https://doi.org/10.1038/ngeo334

Bernard, T., & Sinclair, H.D. (2022). Accelerated sediment delivery to continental margins during post-orogenic rebound of mountain ranges. *Basin Research, 00, 1-20*. https://doi.org/10.1111/bre.12727

Bershaw, J., & Lechler, A.R. (2019). The isotopic composition of meteoric water along altitudinal transects in the Tian Shan of Central Asia. *Chemical Geology*, *516*, 68-78. https://doi.org/10.1016/j.chemgeo.2019.03.032

Biske, Y. S. (1996). Paleozoic Structure and History of Southern Tien Shan. *Saint Petersburg State University*, p.187 (in Russian)

Biske, Y.S., & Seltmann, R. (2010). Paleozoic Tian-Shan as a transitional region between the Rheic and Urals-Turkestan oceans. *Gondwana Research*, *17*(2-3), 602-613. https://doi.org/10.1016/j.gr.2009.11.014

Bloemendal, J., King, J. W., Hall, F. R., & Doh, S.-J. (1992). Rock magnetism of Late Neogene and Pleistocene deep-sea sediments: Relationship to sediment source, diagenetic processes, and sediment lithology. *Journal of Geophysical Research*, *97*(B4), 4361–4375. https://doi.org/10.1029/91jb03068

Blomdin, R., Stroeven, A.P., Harbor, J.M., Lifton, N.A., Heyman, J., Gribenski, N., Petrakov, D.A., Caffee, M.W., Ivanov, M.N., Hättestrand, C., & Rogozhina, I. (2016). Evaluating the timing of former glacier expansions in the Tian Shan: a key step towards robust spatial correlations. *Quaternary Science Reviews*, *153*, 78-96. https://doi.org/10.1016/j.quascirev.2016.07.029

Bookhagen, B., & Burbank, D.W. (2010). Toward a complete Himalayan hydrological budget: Spatiotemporal distribution of snowmelt and rainfall and their impact on river discharge. *Journal of Geophysical Research: Earth Surface*, *115*(F3). https://doi.org/10.1029/2009JF001426

Bookhagen, B., & Strecker, M.R. (2008). Orographic barriers, high-resolution TRMM rainfall, and relief variations along the eastern Andes. *Geophysical Research Letters*, *35*(6). https://doi.org/10.1029/2007GL032011

Bosboom, R.E., Abels, H.A., Hoorn, C., van den Berg, B.C., Guo, Z., & Dupont-Nivet, G. (2014a). Aridification in continental Asia after the middle Eocene climatic optimum (MECO). *Earth and Planetary Science Letters*, *389*, 34-42. https://doi.org/10.1016/j.epsl.2013.12.014

Bosboom, R.E., Dupont-Nivet, G., Grothe, A., Brinkhuis, H., Villa, G., Mandic, O., Stoica, M., Huang, W., Yang, W., Guo, Z., & Krijgsman, W. (2014b). Linking Tarim Basin sea retreat (west China) and Asian aridification in the late Eocene. *Basin Research*, *26*(5), 621-640. https://doi.org/10.1111/bre.12054

Bosboom, R., Mandic, O., Dupont-Nivet, G., Proust, J.N., Ormukov, C., & Aminov, J. (2017). Late Eocene palaeogeography of the proto-Paratethys sea in Central Asia (NW China, southern Kyrgyzstan and SW Tajikistan). *Geological Society, London, Special Publications*, *427*(1), 565-588. https://doi.org/10.1144/SP427.11

Botsyun, S., Mutz, S.G., Ehlers, T.A., Koptev, A., Wang, X., Schmidt, B., Appel, E., & Scherer, D.E. (2022). Influence of Large-Scale Atmospheric Dynamics on Precipitation Seasonality of the Tibetan Plateau and Central Asia in Cold and Warm Climates During the Late Cenozoic. *Journal of Geophysical Research: Atmospheres*, *127*(12), e2021JD035810. https://doi.org/10.1029/2021JD035810

Bougeois, L., Dupont-Nivet, G., de Rafélis, M., Tindall, J.C., Proust, J.N., Reichart, G.J., de Nooijer, L.J., Guo, Z., & Ormukov, C. (2018). Asian monsoons and aridification response to Paleogene sea retreat and Neogene westerly shielding indicated by seasonality in Paratethys oysters. Earth and Planetary Science Letters, 485, 99-110. https://doi.org/10.1016/j.epsl.2017.12.036

Bowman, D., Korjenkov, A., Porat, N., & Czassny, B. (2004). Morphological response to Quaternary deformation at an intermontane basin piedmont, the northern Tien Shan, Kyrghyzstan. *Geomorphology*, *63*(1-2), 1-24. https://doi.org/10.1016/j.geomorph.2004.03.007

Braucher R., Merchel S., Borgomano J., & Bourlès D. (2011). Production of cosmogenic radionuclides at great depth: a multi element approach. *Earth and Planetary Science Letters*, *309*, 1-9. https://doi.org/10.1016/j.epsl.2011.06.036

Breecker, D.O., Sharp, Z.D., & McFadden, L.D. (2009). Seasonal bias in the formation and stable isotopic composition of pedogenic carbonate in modern soils from central New Mexico, USA. *Geological Society of America Bulletin*, *121*(3-4), 630-640. https://doi.org/10.1130/B26413.1

Bullen, M.E., Burbank, D.W., & Garver, J.I. (2003). Building the northern Tien Shan: Integrated thermal, structural, and topographic constraints. *The Journal of Geology*, *111*(2), 149-165. https://doi.org/10.1086/345840

Bullen, M.E., Burbank, D.W., Garver, J.I., & Abdrakhmatov, K.Y. (2001). Late Cenozoic tectonic evolution of the northwestern Tien Shan: New age estimates for the initiation of mountain building. *Geological Society of America Bulletin*, *113*(12), 1544-1559. https://doi.org/10.1130/0016-7606(2001)113<1544:LCTEOT>2.0.CO;2

Burbank, D.W., Blythe, A.E., Putkonen, J., Pratt-Sitaula, B., Gabet, E., Oskin, M., Barros, A., & Ojha, T. P. (2003). Decoupling of erosion and precipitation in the Himalayas. *Nature*, *426*(6967), 652-655. https://doi.org/10.1038/nature02187

Burgette, R. J. (2008). Uplift in response to tectonic convergence: The Kyrgyz tien Shan and Cascadia subduction zone. PhD Thesis, Oregon. 242 pp.

Burgette, R.J., Weldon II, R.J., Abdrakhmatov, K.Y., Ormukov, C., Owen, L.A., & Thompson, S.C. (2017). Timing and process of river and lake terrace formation in the Kyrgyz Tien Shan. *Quaternary Science Reviews*, *159*, 15-34. https://doi.org/10.1016/j.quascirev.2017.01.003

Burke, K. D., Williams, J. W., Chandler, M. A., Haywood, A. M., Lunt, D. J., & Otto-Bliesner, B. L. (2018). Pliocene and Eocene provide best analogs for near-future climates. *Proceedings of the National Academy of Sciences*, *115*(52), 13288-13293. https://doi.org/10.1073/pnas.1809600115

Buslov, M. M., Klerkx, J., Abdrakhmatov, K., Delvaux, D., Batalev, V. Y., Kuchai, O. A., et al. (2003). Recent strike-slip deformation of the northern Tien Shan. Geological Society, London, Special Publications, 210(1), 53–64. https://doi.org/10.1144/gsl.sp.2003.210.01.04

Carrapa, B., Mustapha, F.S., Cosca, M., Gehrels, G., Schoenbohm, L.M., Sobel, E.R., DeCelles, P.G., Russell, J., & Goodman, P. (2014). Multisystem dating of modern river detritus from Tajikistan and China: Implications for crustal evolution and exhumation of the Pamir. *Lithosphere*, *6*(6), 443-455. https://doi.org/10.1130/L360.1

Caves, J.K., Bayshashov, B.U., Zhamangara, A., Ritch, A.J., Ibarra, D.E., Sjostrom, D.J., Mix, H.T., Winnick, M.J., & Chamberlain, C.P. (2017). Late Miocene uplift of the Tian Shan and Altai and reorganization of Central Asia climate. *GSA Today 27(2), 19–26*. https://doi.org/10.1130/GSATG305A.1

Caves, J.K., Moragne, D.Y., Ibarra, D.E., Bayshashov, B.U., Gao, Y., Jones, M.M., Zhamangara, A., Arzhannikova, A.V., Arzhannikov, S.G., & Chamberlain, C.P. (2016). The Neogene de-greening of central Asia. *Geology*, *44*(11), 887-890. https://doi.org/10.1130/G38267.1

Caves, J.K., Sjostrom, D.J., Mix, H.T., Winnick, M.J., & Chamberlain, C.P. (2014). Aridification of Central Asia and uplift of the Altai and Hangay Mountains, Mongolia: Stable isotope evidence. *American Journal of Science*, *314*(8), 1171-1201. https://doi.org/10.2475/08.2014.01

Caves, J.K., Winnick, M.J., Graham, S.A., Sjostrom, D.J., Mulch, A., & Chamberlain, C.P. (2015). Role of the westerlies in Central Asia climate over the Cenozoic. *Earth and Planetary Science Letters*, *428*, 33-43. https://doi.org/10.1016/j.epsl.2015.07.023

Caves Rugenstein, J.K., & Chamberlain, C.P. (2018). The evolution of hydroclimate in Asia over the Cenozoic: A stable-isotope perspective. *Earth-Science Reviews*, *185*, 1129-1156. https://doi.org/10.1016/j.earscirev.2018.09.003

Cerling, T.E. (1984). The stable isotopic composition of modern soil carbonate and its relationship to climate. *Earth and Planetary science letters*, *71*(2), 229-240. https://doi.org/10.1016/0012-821X(84)90089-X

Cerling, T.E., Harris, J.M., MacFadden, B.J., Leakey, M.G., Quade, J., Eisenmann, V., & Ehleringer, J.R. (1997). Global vegetation change through the Miocene/Pliocene boundary. *Nature*, *389*(6647), 153-158. https://doi.org/10.1038/38229

Cerling, T.E., & Quade, J. (1993). Stable carbon and oxygen isotopes in soil carbonates. *Climate change in continental isotopic records. Geophysical Monograph*, *78*, 217-231. https://doi.org/10.1029/GM078p0217

Chamberlain, C.P., Mix, H.T., Mulch, A., Hren, M.T., Kent-Corson, M.L., Davis, S.J., Horton, T.W., & Graham, S.A. (2012). The Cenozoic climatic and topographic evolution of the western North American Cordillera. *American Journal of Science*, *312*(2), 213-262. https://doi.org/10.2475/02.2012.05

Chamberlain, C.P., & Poage, M.A. (2000). Reconstructing the paleotopography of mountain belts from the isotopic composition of authigenic minerals. *Geology*, *28*(2), 115-118. https://doi.org/10.1130/0091-7613(2000)28<115:RTPOMB>2.0.CO;2

Chang, J., Glorie, S., Qiu, N., Min, K., Xiao, Y., & Xu, W. (2021). Late Miocene (10.0~ 6.0 Ma) rapid exhumation of the Chinese South Tianshan: Implications for the timing of aridification in the Tarim Basin. *Geophysical Research Letters*, *48*(3), e2020GL090623. https://doi.org/10.1029/2020GL090623

Charreau, J., Blard, P.H., Lavé, J., Dominguez, S., & Li, W.S. (2023). Unsteady topography in the eastern Tianshan due to imbalance between denudation and crustal thickening. *Tectonophysics*, *848*, 1-16. https://doi.org/10.1016/j.tecto.2022.229702

Charreau, J., Blard, P.H., Puchol, N., Avouac, J.P., Lallier-Vergès, E., Bourlès, D., Braucher, R., Gallaud, A., Finkel, R., Jolivet, M., & Chen, Y. (2011). Paleo-erosion rates in Central Asia since 9 Ma: A transient increase at the onset of Quaternary glaciations? *Earth and Planetary Science Letters*, *304*(1-2), 85-92. https://doi.org/10.1016/j.epsl.2011.01.018

Charreau, J., Gumiaux, C., Avouac, J.P., Augier, R., Chen, Y., Barrier, L., Gilder, S., Dominguez, S., Charles, N., & Wang, Q. (2009). The Neogene Xiyu Formation, a diachronous prograding gravel wedge at front of the Tianshan: Climatic and tectonic implications. *Earth and Planetary Science Letters*, *287*(3-4), 298-310. https://doi.org/10.1016/j.epsl.2009.07.035

Charreau, J., Kent-Corson, M.L., Barrier, L., Augier, R., Ritts, B.D., Chen, Y., France-Lannord, C., & Guilmette, C. (2012). A high-resolution stable isotopic record from the Junggar Basin (NW China): Implications for the paleotopographic evolution of the Tianshan Mountains. *Earth and Planetary Science Letters*, *341*, 158-169. https://doi.org/10.1016/j.epsl.2012.05.033

Charreau, J., Saint-Carlier, D., Dominguez, S., Lavé, J., Blard, P.H., Avouac, J.P., Jolivet, M., Chen, Y., Wang, S., Brown, N.D., Malatesta, L.C., Rhodes, E., & Aster Team. (2017). Denudation outpaced by crustal thickening in the eastern Tianshan. *Earth and Planetary Science Letters*, *479*, 179-191. https://doi.org/10.1016/j.epsl.2017.09.025

Chen, J., Burbank, D.W., Scharer, K.M., Sobel, E., Yin, J., Rubin, C., & Zhao, R. (2002). Magnetochronology of the Upper Cenozoic strata in the Southwestern Chinese Tian Shan: rates of Pleistocene folding and thrusting. *Earth and Planetary Science Letters*, *195*(1-2), 113-130. https://doi.org/10.1016/S0012-821X(01)00579-9

Chen, F., Yuan, Y., Trouet, V., Büntgen, U., Esper, J., Chen, F., Yu, S., Shen, M., Zhang, R., Shang, H., & Chen, Y. (2022a). Ecological and societal effects of Central Asian streamflow variation over the past eight centuries. *npj Climate and Atmospheric Science*, *5*(1), p.27. https://doi.org/10.1038/s41612-022-00239-5

Chen, S.A., Michaelides, K., Richards, D.A., & Singer, M.B. (2022b). Exploring exogenous controls on short-versus long-term erosion rates globally. *Earth Surface Dynamics*, *10*(6), 1055-1078. https://doi.org/10.5194/esurf-10-1055-2022

Child, D., Elliott, G., Mifsud, C., Smith, A.M., & Fink, D. (2000). Sample processing for earth science studies at ANTARES. *Nuclear Instruments and Methods in Physics Research Section B: Beam Interactions with Materials and Atoms*, *172*(1-4), 856-860. https://doi.org/10.1016/S0168-583X(00)00198-1

Chmeleff, J., von Blanckenburg, F., Kossert, K., & Jakob, D. (2010). Determination of the ^{10}Be half-life by multicollector ICP-MS and liquid scintillation counting. *Nuclear Instruments and Methods in Physics Research Section B: Beam Interactions with Materials and Atoms*, *268*(2), 192-199. https://doi.org/10.1016/j.nimb.2009.09.012

Codilean A.T. (2006). Calculation of the cosmogenic nuclide production topographic shielding scaling factor for large areas using DEMs. *Earth Surface Processes and Landforms, 31*, 785-794. https://doi.org/10.1002/esp.1336

Codilean A.T., Fülöp R.-H., Wilcken K.M., Koutamanis D.S., Fink D., Fifield L.K., Wong H., Enge T.G., Vardanega C., & Rowling B. (2023). Cosmogenic Be-10 and Al-26 sample preparation at the University of Wollongong. *Nuclear Instruments and Methods in Physics Research Section B: Beam Interactions with Materials and Atoms*, *535*, 61-73. https://doi.org/10.1016/j.nimb.2022.12.003

Codilean, A.T., Munack, H., Cohen, T.J., Saktura, W.M., Gray, A., & Mudd, S.M. (2018). OCTOPUS: An open cosmogenic isotope and luminescence database. *Earth System Science Data*, *10*(4), 2123-2139. https://doi.org/10.5194/essd-10-2123-2018

Codilean, A.T., Munack, H., Saktura, W.M., Cohen, T.J., Jacobs, Z., Ulm, S., Hesse, P.P., Heyman, J., Peters, K.J., Williams, A.N., Saktura, R.B.K., Rui, X., Chishiro-Dennelly, K., & Panta, A. (2022). OCTOPUS database (v.2). *Earth System Science Data, 14*(8), 3695–3713. https://doi.org/10.5194/essd-14-3695-2022

Codilean, A.T., & Sadler, P.M. (2021). Tectonic Controls on Himalayan Denudation? *AGU Advances*, *2*(3), e2021AV000539. https://doi.org/10.1029/2021AV000539

Cogné, J. P. (2003). PaleoMac: A Macintosh™ application for treating paleomagnetic data and making plate reconstructions. Geochemistry, Geophysics, Geosystems, 4(1), 1007. https://doi.org/10.1029/2001gc000227

Compo G.P., Whitaker J.S., Sardeshmukh P.D., Matsui N., Allan R.J., Yin X., Gleason B.E., Vose R.S., Rutledge G., Bessemoulin P., Brönnimann S., Brunet M., Crouthamel R.I., Grant A.N., Groisman P.Y., Jones P.D., Kruk M.C., Kruger A.C., Marshall G.J., Maugeri M., Mok H.Y., Nordli O., Ross T.F., Trigo R.M., Wang X.L., Woodruff S.D., & Worley S.J. (2011). The Twentieth Century Reanalysis Project. *Quarterly Journal of the Royal Meteorological Society, 137*, 1-28. https://doi.org/10.1002/qj.776

Corbett, L.B., Bierman, P.R., Rood, D.H., Caffee, M.W., Lifton, N.A., & Woodruff, T.E. (2017). Cosmogenic ^{26}Al/^{10}Be surface production ratio in Greenland. *Geophysical Research Letters*, *44*(3), 1350-1359. https://doi.org/10.1002/2016GL071276

De Batist, M., Imbo, Y., Vermeesch, P., Klerkx, J., Giralt, S., Delvaux, D., Lignier, V., Beck, C., Kalugin, I., & Abdrakhmatov, K.E. (2002). Bathymetry and sedimentary environments of Lake Issyk-Kul, Kyrgyz Republic (Central Asia): a large, high-altitude, tectonic lake. In *Lake Issyk-Kul: its natural environment* (pp. 101-123). Springer, Dordrecht. https://doi.org/10.1007/978-94-010-0491-6_9

Dedow, R., Franz, M., Szulc, A., Schneider, J. W., Brückner, J., Ratschbacher, L., et al. (2020). Tajik Basin and Southwestern Tian Shan, Northwestern India-Asia collision zone: 3. Preorogenic to synorogenic retro-foreland basin evolution in the eastern Tajik depression and linkage to the Pamir hinterland. Tectonics, 39(5). e2019TC005874. https://doi.org/10.1029/2019tc005874

De Grave, J. (2003). *Apatite fission-track thermochronology of the Altai Mountains (South Siberia, Russia) and the Tien Shan Mountains (Kyrgyzstan): relevance to Meso-Cenozoic tectonics and denudation in Central Asia* (Doctoral dissertation, Ghent University).

De Grave, J., Glorie, S., Buslov, M.M., Izmer, A., Fournier-Carrie, A., Batalev, V.Y., Vanhaecke, F., & Elburg, M. (2011). The thermo-tectonic history of the Song-Kul plateau, Kyrgyz Tien Shan: Constraints by apatite and titanite thermochronometry and zircon U/Pb dating. *Gondwana Research*, *20*(4), 745-763. https://doi.org/10.1016/j.gr.2011.03.011

De Grave, J., Glorie, S., Buslov, M.M., Stockli, D.F., McWilliams, M.O., & Batalev, V.Y. (2013). Thermo-tectonic history of the Issyk-Kul basement (Kyrgyz northern Tien Shan, central Asia). *Gondwana Research*, *23*(3), 998-1020. https://doi.org/10.1016/j.gr.2012.06.014

De Grave, J., Glorie, S., Ryabinin, A., Zhimulev, F., Buslov, M.M., Izmer, A., Elburg, M., & Vanhaecke, F. (2012). Late Palaeozoic and Meso-Cenozoic tectonic evolution of the southern Kyrgyz Tien Shan: Constraints from multi-method thermochronology in the Trans-Alai, Turkestan-Alai segment and the southeastern Ferghana Basin. *Journal of Asian Earth Sciences*, *44*, 149-168. https://doi.org/10.1016/j.jseaes.2011.04.019

De Pelsmaeker, E., Glorie, S., Buslov, M.M., Zhimulev, F.I., Poujol, M., Korobkin, V.V., Vanhaecke, F., Vetrov, E.V. & De Grave, J. (2015). Late-Paleozoic emplacement and Meso-Cenozoic reactivation of the southern Kazakhstan granitoid basement. *Tectonophysics*, *662*, 416-433. https://doi.org/10.1016/j.tecto.2015.06.014

Dettman, D.L., Fang, X., Garzione, C.N., & Li, J. (2003). Uplift-driven climate change at 12 Ma: a long $\delta^{18}O$ record from the NE margin of the Tibetan plateau. *Earth and Planetary Science Letters*, *214*(1-2), 267-277. https://doi.org/10.1016/S0012-821X(03)00383-2

Dosseto, A., & Schaller, M. (2016). The erosion response to Quaternary climate change quantified using uranium isotopes and in situ-produced cosmogenic nuclides. *Earth-Science Reviews*, *155*, 60-81. https://doi.org/10.1016/j.earscirev.2016.01.015

Dupont-Nivet, G., Krijgsman, W., Langereis, C.G., Abels, H.A., Dai, S., & Fang, X. (2007). Tibetan plateau aridification linked to global cooling at the Eocene–Oligocene transition. *Nature*, *445*(7128), 635-638. https://doi.org/10.1038/nature05516

Erlanger, E.D., Granger, D.E., & Gibbon, R.J. (2012). Rock uplift rates in South Africa from isochron burial dating of fluvial and marine terraces. *Geology*, *40*(11), 1019-1022. https://doi.org/10.1130/G33172.1

Fan, M., Dettman, D.L., Song, C., Fang, X., & Garzione, C.N. (2007). Climatic variation in the Linxia basin, NE Tibetan Plateau, from 13.1 to 4.3 Ma: The stable isotope record. *Palaeogeography, Palaeoclimatology, Palaeoecology*, *247*(3-4), 313-328. https://doi.org/10.1016/j.palaeo.2006.11.001

Fang, X., An, Z., Clemens, S.C., Zan, J., Shi, Z., Yang, S., & Han, W. (2020). The 3.6-Ma aridity and westerlies history over midlatitude Asia linked with global climatic cooling. *Proceedings of the National Academy of Sciences*, *117*(40), 24729-24734. https://doi.org/10.1073/pnas.1922710117

Farley, K.A. (2002). (U-Th)/He dating: Techniques, calibrations, and applications. *Reviews in Mineralogy and Geochemistry*, *47*(1), 819-844. https://doi.org/10.2138/rmg.2002.47.18

Farr T.G., Rosen P.A., Caro E., Crippen R., Duren R., Hensley S., Kobrick M., Paller M., Rodriguez E., Roth L., Seal D., Shaffer S., Shimada J., Umland J., Werner M., Oskin M., Burbank D., & Alsdorf D. (2007). The Shuttle Radar Topography Mission. *Reviews of Geophysics*, *45*, RG2004. https://doi.org/10.1029/2005RG000183

Fick, S.E., & Hijmans, R.J. (2017). WorldClim 2: new 1-km spatial resolution climate surfaces for global land areas. *International Journal of Climatology*, *37*(12), 4302-4315. https://doi.org/10.1002/joc.5086

Fink, D., Smith, A. (2007). An inter-comparison of ^{10}Be and ^{26}Al AMS reference standards and the 10Be half-life. *Nuclear Instruments and Methods in Physics Research Section B: Beam Interactions with Materials and Atoms, 259*, 600-609. https://doi.org/10.1016/j.nimb.2007.01.299

Fisher, R. (1953). Dispersion on a sphere. Proceedings of the Royal Society A: Mathematical, Physical & Engineering Sciences, 217(1130), 295–305. https://doi.org/10.1098/rspa.1953.0064

Forte, A.M., & Whipple, K.X. (2019). The topographic analysis kit (TAK) for TopoToolbox. *Earth Surface Dynamics*, *7*(1), 87-95. https://doi.org/10.5194/esurf-7-87-2019

Fortuna, A.B. (2016). Paleogene and Neogene paleoclimate in the Northern Tian Shan (in Russian). *Vestnik IS NAN KR*, 1(7), 102-111.

Fortuna, A.B., Abdieva, S.V., & Korzhenkov, A.M. (2017). The history of flora and vegetation development in the Issyk-Kul basin during the Cenozoic (in Russian). *Vestnik KRSU*, *17*(8), 201-205.

Fortuna, A.B., Kerimbekov, C.K., Kuzikov, S.I., & Mikolaichuk, A.V. (1994). Lithostratigraphic and palynologic data of Cenozoic deposits of Tessik-Sarybulak depression (in Russian). In: *Geology of Cenozoic and Seismotectonics of the Tien Shan* (Edited by O.K. Chediya), 26–39. Frunse: Ilim, Bishkek, Kyrgyzstan.

Freytet, P., & Verrecchia, E.P. (2002). Lacustrine and palustrine carbonate petrography: an overview. *Journal of Paleolimnology*, *27*(2), 221-237. https://doi.org/10.1023/A:1014263722766

Frisch, K., Voigt, S., Verestek, V., Appel, E., Albert, R., Gerdes, A., Arndt, I., Raddatz, J., Voigt, T., Weber, Y., & Batenburg, S.J. (2019a). Long‐period astronomical forcing of westerlies' strength in Central Asia during Miocene climate cooling. *Paleoceanography and Paleoclimatology*, *34*(11), 1784-1806. https://doi.org/10.1029/2019PA003642

Frisch, K., Voigt, S., Voigt, T., Hellwig, A., Verestek, V., & Weber, Y. (2019b). Extreme aridity prior to lake expansion deciphered from facies evolution in the Miocene Ili Basin, south‐east Kazakhstan. *Sedimentology*, *66*(5), 1716-1745.

Fuchs, M.C., Gloaguen, R., Merchel, S., Pohl, E., Sulaymonova, V.A., Andermann, C., & Rugel, G. (2015). Denudation rates across the Pamir based on ^{10}Be concentrations in fluvial sediments: dominance of topographic over climatic factors. *Earth Surface Dynamics*, *3*(3), 423-439. https://doi.org/10.5194/esurf-3-423-2015

Fujioka, T., Fink, D., & Mifsud, C. (2015). Towards improvement of aluminium assay in quartz for in situ cosmogenic ^{26}Al analysis at ANSTO. *Nuclear Instruments and Methods in Physics Research Section B: Beam Interactions with Materials and Atoms*, *361*, 346-353. https://doi.org/10.1016/j.nimb.2015.07.120

Ganti, V., Von Hagke, C., Scherler, D., Lamb, M.P., Fischer, W.W., & Avouac, J. P. (2016). Time scale bias in erosion rates of glaciated landscapes. *Science Advances*, *2*(10), e1600204. https://doi.org/10.1126/sciadv.1600204

Garzione, C.N., Dettman, D.L., & Horton, B.K. (2004). Carbonate oxygen isotope paleoaltimetry: evaluating the effect of diagenesis on paleoelevation estimates for the Tibetan plateau. *Palaeogeography, Palaeoclimatology, Palaeoecology*, *212*(1-2), 119-140. https://doi.org/10.1016/j.palaeo.2004.05.020

Gebhardt, A.C., Naudts, L., De Mol, L., Klerkx, J., Abdrakhmatov, K., Sobel, E.R., & De Batist, M. (2017). High-amplitude lake-level changes in tectonically active Lake Issyk-Kul (Kyrgyzstan) revealed by high-resolution seismic reflection data. *Climate of the Past*, *13*(1), 73-92. https://doi.org/10.5194/cp-13-73-2017

Glorie, S., & De Grave, J. (2016). Exhuming the Meso–Cenozoic Kyrgyz Tianshan and Siberian Altai-Sayan: a review based on low-temperature thermochronology. *Geoscience Frontiers*, *7*(2), 155-170. https://doi.org/10.1016/j.gsf.2015.04.003

Glorie, S., De Grave, J., Buslov, M.M., Elburg, M.A., Stockli, D.F., & Gerdes, A. (2010). Multi-method chronometric constraints on the evolution of the Northern Kyrgyz Tien Shan granitoids (Central Asian Orogenic Belt): from emplacement to exhumation. *Journal of Asian Earth Sciences*, *38*(3-4), 131-146. https://doi.org/10.1016/j.jseaes.2009.12.009

Glorie, S., De Grave, J., Buslov, M.M., Zhimulev, F.I., Stockli, D.F., Batalev, V.Y., Izmer, A., Van den Haute, P., Vanhaecke, F., & Elburg, M.A. (2011). Tectonic history of the Kyrgyz South Tien Shan (Atbashi‐Inylchek) suture zone: The role of inherited structures during deformation‐propagation. *Tectonics*, *30*(6). https://doi.org/10.1029/2011TC002949

Goode, J. K., Burbank, D. W., & Bookhagen, B. (2011). Basin width control of faulting in the Naryn Basin, south-central Kyrgyzstan. Tectonics, 30(6). TC6009. https://doi.org/10.1029/2011tc002910

Goode, J.K., Burbank, D.W., & Ormukov, C. (2014). Pliocene‐Pleistocene initiation, style, and sequencing of deformation in the central Tien Shan. *Tectonics*, *33*(4), 464-484. https://doi.org/10.1002/2013TC003394

Gradstein, F. M., Ogg, J. G., Schmitz, M. D., & Ogg, G. M. (Eds.), (2012). The geologic time scale 2012. Elsevier.

Graham, S.A., Chamberlain, C.P., Yue, Y., Ritts, B.D., Hanson, A.D., Horton, T.W., Waldbauer, J.R., Poage, M.A., & Feng, X. (2005). Stable isotope records of Cenozoic climate and topography, Tibetan plateau and Tarim basin. *American Journal of Science*, *305*(2), 101-118. https://doi.org/10.2475/ajs.305.2.101

Granger, D.E., & Muzikar, P.F. (2001). Dating sediment burial with in situ-produced cosmogenic nuclides: theory, techniques, and limitations. *Earth and Planetary Science Letters*, *188*(1-2), 269-281. https://doi.org/10.1016/S0012-821X(01)00309-0

Granger, D.E., & Schaller, M. (2014). Cosmogenic nuclides and erosion at the watershed scale. *Elements*, *10*(5), 369-373. https://doi.org/10.2113/gselements.10.5.369

Grigina, O.M., & Fortuna, A.B. (1975). Main stages of the vegetation development in the Issyk-Kul basin in the Cenozoic (in Russian). In: *History of lakes and inland seas in arid zone: Thesis*, 79–85. Leningrad, 4.

Grigina, O.M., & Fortuna, A.B. (1981). *Paleogeography of the Northern Tian Shan in the Cenozoic* (in Russian). Frunse: Ilim, Bishkek, Kyrgyzstan.

Grin, E., Schaller, M., & Ehlers, T.A. (2018). Spatial distribution of cosmogenic ^{10}Be derived denudation rates between the Western Tian Shan and Northern Pamir, Tajikistan. *Geomorphology*, *321*, 1-15. https://doi.org/10.1016/j.geomorph.2018.08.007

Guan, X., Ma, Y., Lu, H., Jiang, Y., Pang, L., Zheng, X., & Li, Y. (2022). Topographic and climatic controls on decadal-scale catchment-basin erosion rates in the northern Chinese Tian Shan. *Catena*, *210*, 105862. https://doi.org/10.1016/j.catena.2021.105862

Guerit, L., Barrier, L., Jolivet, M., Fu, B., & Métivier, F. (2016). Denudation intensity and control in the Chinese Tian Shan: new constraints from mass balance on catchment-alluvial fan systems. *Earth Surface Processes and Landforms*, *41*(8), 1088-1106. https://doi.org/10.1002/esp.3890.

Halsted, C.T., Bierman, P.R., & Balco, G. (2021). Empirical Evidence for Latitude and Altitude Variation of the In Situ Cosmogenic ^{26}Al/^{10}Be Production Ratio. *Geosciences*, *11*(10), 402. https://doi.org/10.3390/geosciences11100402

Hayashi, T., Yamanaka, T., Hikasa, Y., Sato, M., Kuwahara, Y., & Ohno, M. (2020). Latest Pliocene Northern Hemisphere glaciation amplified by intensified Atlantic meridional overturning circulation. *Communications Earth & Environment*, *1*(1), 25. https://doi.org/10.1038/s43247-020-00023-4

Hecht, H., & Oguchi, T. (2017). Global evaluation of erosion rates in relation to tectonics. *Progress in Earth and Planetary Science*, *4*(1), 1-9. https://doi.org/10.1186/s40645-017-0156-3

Heermance, R.V., Chen, J., Burbank, D.W., & Wang, C. (2007). Chronology and tectonic controls of Late Tertiary deposition in the southwestern Tian Shan foreland, NW China. *Basin Research*, *19*(4), 599-632. https://doi.org/10.1111/j.1365-2117.2007.00339.x

Heermance, R.V., Pearson, J., Moe, A., Langtao, L., Jianhong, X., Jie, C., Richter, F., Garzione, C.N., Junsheng, N., & Bogue, S. (2018). Erg deposition and development of the ancestral Taklimakan Desert (western China) between 12.2 and 7.0 Ma. *Geology*, *46*(10), pp.919-922. https://doi.org/10.1130/G45085.1

Hellwig, A., Voigt, S., Mulch, A., Frisch, K., Bartenstein, A., Pross, J., Gerdes, A., & Voigt, T. (2018). Late Oligocene to early Miocene humidity change recorded in terrestrial sequences in the Ili Basin (south-eastern Kazakhstan, Central Asia). *Sedimentology*, *65*(2), 517-539. https://doi.org/10.1111/sed.12390

Hendrix, M.S., Graham, S.A., Carroll, A.R., Sobel, E.R., McKnight, C.L., Schulein, B.J., & Wang, Z. (1992). Sedimentary record and climatic implications of recurrent deformation in the Tian Shan: Evidence from Mesozoic strata of the north Tarim, south Junggar, and Turpan basins, northwest China. *Geological Society of America Bulletin*, *104*(1), 53-79. https://doi.org/10.1130/0016-7606(1992)104<0053:SRACIO>2.3.CO;2

Herbert, T.D., Lawrence, K.T., Tzanova, A., Peterson, L.C., Caballero-Gill, R., & Kelly, C.S. (2016). Late Miocene global cooling and the rise of modern ecosystems. *Nature Geoscience*, *9*(11), 843-847. https://doi.org/10.1038/ngeo2813

Herman, F., Braun, J., Deal, E., & Prasicek, G. (2018). The response time of glacial erosion. *Journal of Geophysical Research: Earth Surface*, *123*(4), 801-817. https://doi.org/10.1002/2017JF004586

Herman, F., & Champagnac, J.D. (2016). Plio-Pleistocene increase of erosion rates in mountain belts in response to climate change. *Terra Nova*, *28*(1), 2-10. https://doi.org/10.1111/ter.12186

Herman, F., Seward, D., Valla, P.G., Carter, A., Kohn, B., Willett, S.D., & Ehlers, T.A. (2013). Worldwide acceleration of mountain erosion under a cooling climate. *Nature*, *504*(7480), 423-426. https://doi.org/10.1038/nature12877

Horn, B.K.P. (1981). Hill shading and the reflectance map. *Proceedings of the IEEE, 69*(1), 14–47. https://doi.org/10.1109/PROC.1981.11918.

Hough, B.G., Garzione, C.N., Wang, Z., Lease, R.O., Burbank, D.W., & Yuan, D. (2011). Stable isotope evidence for topographic growth and basin segmentation: Implications for the evolution of the NE Tibetan Plateau. *Bulletin*, *123*(1-2), 168-185. https://doi.org/10.1130/B30090.1

Jepson, G., Carrapa, B., Gillespie, J., Feng, R., DeCelles, P.G., Kapp, P., Tabor, C.R., & Zhu, J. (2021). Climate as the Great Equalizer of Continental-Scale Erosion. *Geophysical Research Letters*, *48*(20), e2021GL095008. https://doi.org/10.1029/2021GL095008

Jia, Y., Wu, H., Zhu, S., Li, Q., Zhang, C., Yu, Y., & Sun, A. (2020). Cenozoic aridification in Northwest China evidenced by paleovegetation evolution. *Palaeogeography, Palaeoclimatology, Palaeoecology*, *557*, 109907. https://doi.org/10.1016/j.palaeo.2020.109907

Jolivet, M., Dominguez, S., Charreau, J., Chen, Y., Li, Y., & Wang, Q. (2010). Mesozoic and Cenozoic tectonic history of the central Chinese Tian Shan: Reactivated tectonic structures and active deformation. *Tectonics*, *29*(6). https://doi.org/10.1029/2010TC002712

Kaya, M.Y., Dupont-Nivet, G., Proust, J.N., Roperch, P., Bougeois, L., Meijer, N., Frieling, J., Fioroni, C., Altiner, S.Ö., Vardar, E., & Barbolini, N. (2019). Paleogene evolution and demise of the proto-Paratethys Sea in Central Asia (Tarim and Tajik basins): Role of intensified tectonic activity at ca. 41 Ma. *Basin Research*, *31*(3), 461-486. https://doi.org/10.1111/bre.12330

Käßner, A., Ratschbacher, L., Pfänder, J.A., Hacker, B.R., Zack, G., Sonntag, B.L., Khan, J., Stanek, K.P., Gadoev, M., & Oimahmadov, I. (2017). Proterozoic–Mesozoic history of the Central Asian orogenic belt in the Tajik and southwestern Kyrgyz Tian Shan: U-Pb, 40Ar/39Ar, and fission-track geochronology and geochemistry of granitoids. *GSA Bulletin*, *129*(3-4), 281-303. https://doi.org/10.1130/B31466.1

Kent-Corson, M.L., Ritts, B.D., Zhuang, G., Bovet, P.M., Graham, S.A., & Chamberlain, C.P. (2009). Stable isotopic constraints on the tectonic, topographic, and climatic evolution of the northern margin of the Tibetan Plateau. *Earth and Planetary Science Letters*, *282*(1-4), 158-166. https://doi.org/10.1016/j.epsl.2009.03.011

King, J., Banerjee, S. K., Marvin, J., & Özdemir, Ö. (1982). A comparison of different magnetic methods for determining the relative grain size of magnetite in natural materials: Some results from lake sediments. Earth and Planetary Science Letters, 59(2), 404–419. https://doi.org/10.1016/0012-821x(82)90142-x

Kirschvink, J. L. (1980). The least-squares line and plane and the analysis of paleomagnetic data. Geophysical Journal International, 62(3), 699–718. https://doi.org/10.1111/j.1365-246x.1980.tb02601.x

Knudsen, M.F., Nørgaard, J., Grischott, R., Kober, F., Egholm, D.L., Hansen, T.M., & Jansen, J.D. (2020). New cosmogenic nuclide burial-dating model indicates onset of major glaciations in the Alps during Middle Pleistocene Transition. *Earth and Planetary Science Letters*, *549*, 116491. https://doi.org/10.1016/j.epsl.2020.116491

Kohl, C.P., & Nishiizumi, K. (1992). Chemical isolation of quartz for measurement of in-situ-produced cosmogenic nuclides. *Geochimica et Cosmochimica Acta*, *56*(9), 3583-3587. https://doi.org/10.1016/0016-7037(92)90401-4

Koppes, M., Gillespie, A.R., Burke, R.M., Thompson, S.C., & Stone, J. (2008). Late quaternary glaciation in the Kyrgyz Tien Shan. *Quaternary Science Reviews*, *27*(7-8), 846-866. https://doi.org/10.1016/j.quascirev.2008.01.009

Koppes, M.N., & Montgomery, D.R. (2009). The relative efficacy of fluvial and glacial erosion over modern to orogenic timescales. *Nature Geoscience*, *2*(9), 644-647. https://doi.org/10.1038/ngeo616

Korschinek, G., Bergmaier, A., Faestermann, T., Gerstmann, U.C., Knie, K., Rugel, G., Wallner, A., Dillmann, I., Dollinger, G., Von Gosstomski, C.L., Kossert, K., Maiti, M., Poutivtsev, M., Remmert, A. (2010). A new value for the half-life of ^{10}Be by heavy-ion elastic recoil detection and liquid scintillation counting. *Nuclear Instruments and Methods in Physics Research Section B: Beam Interactions with Materials and Atoms*, *268*(2), 187-191. https://doi.org/10.1016/j.nimb.2009.09.020

Korzhenkov, A. M., & Deev, E. V. (2017). Underestimated seismic hazard in the south of the Issyk-Kul Lake region (northern Tian Shan). Geodesy and Geodynamics, 8(3), 169–180. https://doi.org/10.1016/j.geog.2017.03.012

Kreemer, C., Blewitt, G., & Klein, E.C. (2014). A geodetic plate motion and Global Strain Rate Model. *Geochemistry, Geophysics, Geosystems*, *15*, 3849–3889. https://doi.org/10.1002/2014gc005407

Kudriavtseva, A., Sobel, E.R., Codilean, A.T., Meijers, M.J.M., Mulch, A., Hoke, G.D., Fink, D., Mikolaichuk, A.V., Fülöp, R.-H., Wilcken, K.M., & Enge, T.G. (2023). Neogene aridification and lake development in the Issyk-Kul basin, Kyrgyzstan. *Basin Research*, *00*, 1– 35. https://doi.org/10.1111/bre.12751

Kutuzov, S., & Shahgedanova, M. (2009). Glacier retreat and climatic variability in the eastern Terskey–Alatoo, inner Tien Shan between the middle of the 19th century and beginning of the 21st century. *Global and Planetary Change*, *69*(1-2), 59-70. https://doi.org/10.1016/j.gloplacha.2009.07.001

Lal, D. (1991). Cosmic ray labeling of erosion surfaces: in situ nuclide production rates and erosion models. *Earth and Planetary Science Letters*, *104*(2-4), 424-439. https://doi.org/10.1016/0012-821X(91)90220-C

Landgraf, A., Dzhumabaeva, A., Abdrakhmatov, K.E., Strecker, M.R., Macaulay, E.A., Arrowsmith, J.R., Sudhaus, H., Preusser, F., Rugel, G., & Merchel, S. (2016). Repeated large-magnitude earthquakes in a tectonically active, low-strain continental interior: The northern Tien Shan, Kyrgyzstan. *Journal of Geophysical Research: Solid Earth*, *121*(5), 3888-3910. https://doi.org/10.1002/2015JB012714

Lauterbach, S., Witt, R., Plessen, B., Dulski, P., Prasad, S., Mingram, J., Gleixner, G., Hettler-Riedel, S., Stebich, M., Schnetger, B., Schwalb, A., & Schwarz, A. (2014). Climatic imprint of the mid-latitude Westerlies in the Central Tian Shan of Kyrgyzstan and teleconnections to North Atlantic climate variability during the last 6000 years. *The Holocene*, *24*(8), 970-984. https://doi.org/10.1177/0959683614534741

Leng, M.J., & Marshall, J.D. (2004). Palaeoclimate interpretation of stable isotope data from lake sediment archives. *Quaternary Science Reviews*, *23*(7-8), 811-831. https://doi.org/10.1016/j.quascirev.2003.06.012

Levin, N.E., Cerling, T.E., Passey, B.H., Harris, J.M., & Ehleringer, J.R. (2006). A stable isotope aridity index for terrestrial environments. *Proceedings of the National Academy of Sciences*, *103*(30), 11201-11205. https://doi.org/10.1073/pnas.0604719103

Li, B., Sun, D., Wang, X., Zhang, Y., Hu, W., Wang, F., Li, Z., Ma, Z., & Liang, B. (2016). $\delta^{18}O$ and $\delta^{13}C$ records from a Cenozoic sedimentary sequence in the Lanzhou Basin, Northwestern China: implications for palaeoenvironmental and palaeoecological changes. *Journal of Asian Earth Sciences*, *125*, 22-36. https://doi.org/10.1016/j.jseaes.2016.05.010

Li, H.C., & Ku, T.L. (1997). $\delta^{13}C$–$\delta^{18}O$ covariance as a paleohydrological indicator for closed-basin lakes. *Palaeogeography, Palaeoclimatology, Palaeoecology*, *133*(1-2), 69-80. https://doi.org/10.1016/S0031-0182(96)00153-8

Li, J.X., Yue, L.P., Roberts, A.P., Hirt, A.M., Pan, F., Guo, L., Xu, Y., Xi, R.G., Guo, L., Qiang, X.K., Gai, C.C., Jiang, Z.X., Sun, Z.M., & Liu, Q.S. (2018). Global cooling and enhanced Eocene Asian mid-latitude interior aridity. *Nature Communications*, *9*(1), 1-8. https://doi.org/10.1038/s41467-018-05415-x

Li, W., Chen, Y., Yuan, X., Xiao, W., & Windley, B.F. (2022). Intracontinental deformation of the Tianshan Orogen in response to India-Asia collision. *Nature Communications*, *13*(1), 3738. https://doi.org/10.1038/s41467-022-30795-6

Licht, A., Dupont-Nivet, G., Pullen, A., Kapp, P., Abels, H.A., Lai, Z., Guo, Z., Abell, J., & Giesler, D. (2016). Resilience of the Asian atmospheric circulation shown by Paleogene dust provenance. *Nature communications*, *7*(1), 1-6. https://doi.org/10.1038/ncomms12390

Lisiecki, L.E., & Raymo, M.E. (2005). A Pliocene-Pleistocene stack of 57 globally distributed benthic δ18O records. *Paleoceanography*, *20*(1). https://doi.org/10.1029/2004PA001071

Liu, Q., Roberts, A. P., Larrasoaña, J. C., Banerjee, S. K., Guyodo, Y., Tauxe, L., & Oldfield, F. (2012). Environmental magnetism: Principles and applications. Reviews of Geophysics, 50(4), RG4002. https://doi.org/10.1029/2012rg000393

Liu, W., Liu, Z., An, Z., Sun, J., Chang, H., Wang, N., Dong, J., & Wang, H. (2014). Late Miocene episodic lakes in the arid Tarim Basin, western China. *Proceedings of the National Academy of Sciences*, *111*(46), 16292-16296. https://doi.org/10.1073/pnas.1410890111

Liu, Y., Métivier, F., Gaillardet, J., Ye, B., Meunier, P., Narteau, C., Lajeunesse, E., Han, T., & Malverti, L. (2011). Erosion rates deduced from seasonal mass balance along the upper Urumqi River in Tianshan. *Solid Earth*, *2*(2), 283-301. https://doi.org/10.5194/se-2-283-2011

Macaulay, E.A., Sobel, E.R., Mikolaichuk, A., Kohn, B., & Stuart, F.M. (2014). Cenozoic deformation and exhumation history of the Central Kyrgyz Tien Shan. *Tectonics*, *33*(2), 135-165. https://doi.org/10.1002/2013TC003376

Macaulay, E.A., Sobel, E.R., Mikolaichuk, A., Landgraf, A., Kohn, B., & Stuart, F. (2013). Thermochronologic insight into late Cenozoic deformation in the basement-cored Terskey Range, Kyrgyz Tien Shan. *Tectonics*, *32*(3), 487-500. https://doi.org/10.1002/tect.20040

Macaulay, E.A., Sobel, E.R., Mikolaichuk, A.V., Wack, M., Gilder, S.A., Mulch, A., Fortuna, A.B., Hynek, S., & Apayarov, F. (2016). The sedimentary record of the Issyk-Kul basin, Kyrgyzstan: climatic and tectonic inferences. *Basin Research*, *28*(1), 57-80. https://doi.org/10.1111/bre.12098

Maksumova, R.A., Djenchuraeva, A.V., & Berezanskii, A.V. (2001). Structure and evolution of the Tien Shan nappe-folded orogen. *Russian Geology and Geophysics, 42*, 1367–1374.

McFadden, P. L. (1990). A new fold test for palaeomagnetic studies. Geophysical Journal International, 103(1), 163–169. https://doi.org/10.1111/j.1365-246X.1990.tb01761.x

McFadden, P. L., & McElhinny, M. W. (1990). Classification of the reversal test in palaeomagnetism. Geophysical Journal International, 103(3), 725–729. https://doi.org/10.1111/j.1365-246x.1990.tb05683.x

Methner, K., Fiebig, J., Wacker, U., Umhoefer, P., Chamberlain, C.P., & Mulch, A. (2016). Eocene-Oligocene proto-Cascades topography revealed by clumped (Δ47) and oxygen isotope ($\delta^{18}O$) geochemistry (Chumstick Basin, WA, USA). *Tectonics*, *35*(3), 546-564. https://doi.org/10.1002/2015TC003984

Miao, Y., Herrmann, M., Wu, F., Yan, X., & Yang, S. (2012). What controlled Mid–Late Miocene long-term aridification in Central Asia? – Global cooling or Tibetan Plateau uplift: A review. *Earth-Science Reviews*, *112*(3-4), 155-172. https://doi.org/10.1016/j.earscirev.2012.02.003

Molnar, P. (2004). Late Cenozoic increase in accumulation rates of terrestrial sediment: How might climate change have affected erosion rates? *Annu. Rev. Earth Planet. Sci.*, *32*, 67-89. https://doi.org/10.1146/annurev.earth.32.091003.143456

Molnar, P., & England, P. (1990). Late Cenozoic uplift of mountain ranges and global climate change: chicken or egg? *Nature*, *346*(6279), 29-34. https://doi.org/10.1038/346029a0

Molnar, P., & Tapponnier, P. (1975). Cenozoic Tectonics of Asia: Effects of a Continental Collision: Features of recent continental tectonics in Asia can be interpreted as results of the India-Eurasia collision. *Science, 189*(4201), 419-426. https://doi.org/10.1126/science.189.4201.419

Montgomery, D.R., & Brandon, M.T. (2002). Topographic controls on erosion rates in tectonically active mountain ranges. *Earth and Planetary Science Letters*, *201*(3-4), 481-489. https://doi.org/10.1016/S0012-821X(02)00725-2

Mudd S.M., Harel M.A., Hurst M.D., Grieve S.W., & Marrero S.M. (2016). The CAIRN method: automated, reproducible calculation of catchment-averaged denudation rates from cosmogenic nuclide concentrations. *Earth Surface Dynamics, 4*, 655-674. https://doi.org/10.5194/esurf-4-655-2016

Mulch, A. (2016). Stable isotope paleoaltimetry and the evolution of landscapes and life. *Earth and Planetary Science Letters*, *433*, 180-191. https://doi.org/10.1016/j.epsl.2015.10.034

Nachtergaele, S., De Pelsmaeker, E., Glorie, S., Zhimulev, F., Jolivet, M., Danišík, M., Buslov, M.M., & De Grave, J. (2018). Meso-Cenozoic tectonic evolution of the Talas-Fergana region of the Kyrgyz Tien Shan revealed by low-temperature basement and detrital thermochronology. *Geoscience Frontiers*, *9*(5), 1495-1514. https://doi.org/10.1016/j.gsf.2017.11.007

Niemi, N.A., Oskin, M., Burbank, D.W., Heimsath, A.M., & Gabet, E.J. (2005). Effects of bedrock landslides on cosmogenically determined erosion rates. *Earth and Planetary Science Letters*, *237*(3-4), 480-498. https://doi.org/10.1016/j.epsl.2005.07.009

Nishiizumi, K. (2004). Preparation of ^{26}Al AMS standards. *Nuclear Instruments and Methods in Physics Research Section B: Beam Interactions with Materials and Atoms*, *223*, 388-392. https://doi.org/10.1016/j.nimb.2004.04.075

Nishiizumi, K., Imamura, M., Caffee, M.W., Southon, J.R., Finkel, R.C., & McAninch, J. (2007). Absolute calibration of ^{10}Be AMS standards. *Nuclear Instruments and Methods in Physics Research Section B: Beam Interactions with Materials and Atoms*, *258*(2), 403-413. https://doi.org/10.1016/j.nimb.2007.01.297

Norris, T.L., Gancarz, A.J., Rokop, D.J., & Thomas, K.W. (1983). Half-life of ^{26}Al. *Journal of Geophysical Research: Solid Earth*, *88*(S01), B331-B333. https://doi.org/10.1029/JB088iS01p0B331

Norton, K.P., & Schlunegger, F. (2017). Lack of a weathering signal with increased Cenozoic erosion? *Terra Nova*, *29*(5), 265-272. https://doi.org/10.1111/ter.12278

Oberhänsli, H., & Molnar, P. (2012). Climate Evolution in Central Asia during the Past Few Million Years: A Case Study from Issyk-Kul. *Scientific Drilling*, *13*, 51-57. https://doi.org/10.2204/iodp.sd.13.09.2011

Omuraliev, M., & Omuralieva, A. (2004). *Late Cenozoic Tectonics of the Tien Shan.* Institute of Seizmology, National Academy of Sciences Kyrgyz Republic, Bishkek.

Pedersen, V. K., & Egholm, D. L. (2013). Glaciations in response to climate variations preconditioned by evolving topography. *Nature*, *493*(7431), 206-210. https://doi.org/10.1038/nature11786

Pittore, M., Ozturk, U., Moldobekov, B., & Saponaro, A. (2018). EMCA Landslide catalog Central Asia. V. 1.0. GFZ Data Services. https://doi.org/10.5880/GFZ.2.6.2018.004

Poage, M.A., & Chamberlain, C.P. (2001). Empirical relationships between elevation and the stable isotope composition of precipitation and surface waters: considerations for studies of paleoelevation change. *American Journal of Science*, *301*(1), 1-15. https://doi.org/10.2475/ajs.301.1.1

Pomazkov, K. D. (1971). Geological map of the USSR of 1:200,000 scales: Northern Tien-Shan series. Sheet K-43-XVII. Russian Geological Research Institute. (VSEGEI).

Portenga, E.W., & Bierman, P.R. (2011). Understanding Earth's eroding surface with 10Be, *GSA Today*, *21*, 4–10, https://doi.org/10.1130/G111A.1, 2011.

Prud'homme, C., Scardia, G., Vonhof, H., Guinoiseau, D., Nigmatova, S., Fiebig, J., Gerdes, A., Janssen, R., & Fitzsimmons, K.E. (2021). Central Asian modulation of Northern Hemisphere moisture transfer over the Late Cenozoic. *Communications Earth & Environment*, *2*(1), 1-8. https://doi.org/10.1038/s43247-021-00173-z

Puchol, N., Charreau, J., Blard, P.H., Lavé, J., Dominguez, S., Pik, R., Saint-Carlier, D., & ASTER Team. (2017). Limited impact of Quaternary glaciations on denudation rates in Central Asia. *GSA Bulletin*, *129*(3-4), 479-499. https://doi.org/10.1130/B31475.1

Quade, J., Breecker, D.O., Daëron, M., & Eiler, J. (2011). The paleoaltimetry of Tibet: An isotopic perspective. *American Journal of Science*, *311*(2), 77-115. https://doi.org/10.2475/02.2011.01

Quade, J., Leary, R., Dettinger, M.P., Orme, D., Krupa, A., DeCelles, P.G., Kano, A., Kato, H., Waldrip, R., Huang, W., & Kapp, P. (2020). Resetting Southern Tibet: The serious challenge of obtaining primary records of Paleoaltimetry. *Global and Planetary Change*, *191*, 103194. https://doi.org/10.1016/j.gloplacha.2020.103194

Ramstein, G., Fluteau, F., Besse, J., & Joussaume, S. (1997). Effect of orogeny, plate motion and land–sea distribution on Eurasian climate change over the past 30 million years. *Nature*, *386*(6627), 788-795. https://doi.org/10.1038/386788a0

Raymo, M.E., & Ruddiman, W.F. (1992). Tectonic forcing of late Cenozoic climate. *Nature*, *359*(6391), 117-122. https://doi.org/10.1038/359117a0

Reiners, P.W., & Brandon, M.T. (2006). Using thermochronology to understand orogenic erosion. *Annu. Rev. Earth Planet. Sci.*, *34*, 419-466. https://doi.org/10.1146/annurev.earth.34.031405.125202

Reiners, P.W., Ehlers, T.A., & Zeitler, P.K. (2005). Past, Present, and Future of Thermochronology. *Rev Mineralogy Geochem*, *58*, 1–18. https://doi.org/10.2138/rmg.2005.58.1

Richter, F., Pearson, J., Vilkas, M., Heermance, R.V., Garzione, C.N., Cecil, M.R., Jepson, G., Moe, A., Xu, J., Liu, L., & Chen, J. (2022). Growth of the southern Tian Shan-Pamir and its impact on central Asian climate. *GSA Bulletin*. https://doi.org/10.1130/B36471.1

Ricketts, R.D., Johnson, T.C., Brown, E.T., Rasmussen, K.A., & Romanovsky, V.V. (2001). The Holocene paleolimnology of Lake Issyk-Kul, Kyrgyzstan: trace element and stable isotope composition of ostracodes. *Palaeogeography, Palaeoclimatology, Palaeoecology*, *176*(1-4), 207-227. https://doi.org/10.1016/S0031-0182(01)00339-X

Rolland, Y., Jourdon, A., Petit, C., Bellahsen, N., Loury, C., Sobel, E. R., & Glodny, J. (2020). Thermochronology of the highest central Asian massifs (Khan Tengri-Pobedi, SE Kyrgyztan): Evidence for Late Miocene (ca. 8 Ma) reactivation of Permian faults and insights into building the Tian Shan. *Journal of Asian Earth Sciences*, *200*, 104466. https://doi.org/10.1016/j.jseaes.2020.104466

Rosenwinkel, S., Landgraf, A., Schwanghart, W., Volkmer, F., Dzhumabaeva, A., Merchel, S., Rugel, G., Preusser, F., & Korup, O. (2017). Late Pleistocene outburst floods from Issyk-Kul, Kyrgyzstan? *Earth Surface Processes and Landforms, 42*(10), 1535-1548. https://doi.org/10.1002/esp.4109

Roud, S.C., Wack, M.R., Gilder, S.A., Kudriavtseva, A., & Sobel, E.R. (2021). Miocene to Early Pleistocene Depositional History and Tectonic Evolution of the Issyk-Kul Basin, Central Tian Shan. *Geochemistry, Geophysics, Geosystems*, *22*(4), e2020GC009556. https://doi.org/10.1029/2020GC009556

Rowley, D.B., & Garzione, C.N. (2007). Stable isotope-based paleoaltimetry. *Annu. Rev. Earth Planet. Sci.*, *35,* 463-508. https://doi.org/10.1146/annurev.earth.35.031306.140155

Rugel, G., Pavetich, S., Akhmadaliev, S., Baez, S.M.E., Scharf, A., Ziegenrücker, R., & Merchel, S. (2016). The first four years of the AMS-facility DREAMS: Status and developments for more accurate radionuclide data. *Nuclear Instruments and Methods in Physics Research Section B: Beam Interactions with Materials and Atoms, 370,* 94–100. https://doi.org/10.1016/j.nimb.2016.01.012

Ruggieri, E., Herbert, T., Lawrence, K.T., & Lawrence, C.E. (2009). Change point method for detecting regime shifts in paleoclimatic time series: application to δ18O time series of the Plio-Pleistocene. *Paleoceanography*, *24*(1). https://doi.org/10.1029/2007PA001568

Sanhueza-Pino, K., Korup, O., Hetzel, R., Munack, H., Weidinger, J.T., Dunning, S., Ormukov, C., & Kubik, P.W. (2011). Glacial advances constrained by ^{10}Be exposure dating of bedrock landslides, Kyrgyz Tien Shan. *Quaternary research*, *76*(3), 295-304. https://doi.org/10.1016/j.yqres.2011.06.013

Sanyal, P., Bhattacharya, S.K., & Prasad, M. (2005). Chemical diagenesis of Siwalik sandstone: isotopic and mineralogical proxies from Surai Khola section, Nepal. *Sedimentary Geology, 180*(1-2), 57-74. https://doi.org/10.1016/j.sedgeo.2005.06.005

Schaefer, J.M., Codilean, A.T., Willenbring, J.K., Lu, Z.-T., Keisling, B., Fülöp, R.-H. & Val, P. (2022). Cosmogenic nuclide techniques. *Nature Reviews Methods Primers 2***,** 18. https://doi.org/10.1038/s43586-022-00096-9

Schildgen, T. F., van der Beek, P. A., Sinclair, H. D., & Thiede, R. C. (2018). Spatial correlation bias in late-Cenozoic erosion histories derived from thermochronology. Nature, 559(7712), 89-93.

Schwarz, A., Turner, F., Lauterbach, S., Plessen, B., Krahn, K.J., Glodniok, S., Mischke, S., Stebich, M., Witt, R., Mingram, J., & Schwalb, A. (2017). Mid-to late Holocene climate-driven regime shifts inferred from diatom, ostracod and stable isotope records from Lake Son Kol (Central Tian Shan, Kyrgyzstan). *Quaternary Science Reviews*, *177*, 340-356. https://doi.org/10.1016/j.quascirev.2017.10.009

Selander, J., Oskin, M., Ormukov, C., & Abdrakhmatov, K. (2012). Inherited strike‐slip faults as an origin for basement‐cored uplifts: Example of the Kungey and Zailiskey ranges, northern Tian Shan. *Tectonics*, *31*(4). https://doi.org/10.1029/2011TC003002

Seltmann, R., Konopelko, D., Biske, G., Divaev, F., & Sergeev, S. (2011). Hercynian post-collisional magmatism in the context of Paleozoic magmatic evolution of the Tien Shan orogenic belt. *Journal of Asian Earth Sciences, 42,* 821–838, https://doi.org/10.1016/j.jseaes.2010.08.016

Sobel, E. R., & Arnaud, N. (2000). Cretaceous–Paleogene basaltic rocks of the Tuyon basin, NW China and the Kyrgyz Tian Shan: The trace of a small plume. Lithos, 50(1–3), 191–215. https://doi.org/10.1016/s0024-4937(99)00046-8

Sobel, E. R., & Dumitru, T. A. (1997). Thrusting and exhumation around the margins of the western Tarim basin during the India-Asia collision. Journal of Geophysical Research, 102(B3), 5043–5063. https://doi.org/10.1029/96jb03267

Sobel, E.R., Chen, J., & Heermance, R.V. (2006a). Late Oligocene–Early Miocene initiation of shortening in the Southwestern Chinese Tian Shan: implications for Neogene shortening rate variations. *Earth and Planetary Science Letters*, *247*(1-2), 70-81. https://doi.org/10.1016/j.epsl.2006.03.048

Sobel, E.R., Oskin, M., Burbank, D., & Mikolaichuk, A. (2006b). Exhumation of basement‐cored uplifts: Example of the Kyrgyz Range quantified with apatite fission track thermochronology. *Tectonics*, *25*(2). https://doi.org/10.1029/2005TC001809

Sorg, A., Bolch, T., Stoffel, M., Solomina, O., & Beniston, M. (2012). Climate change impacts on glaciers and runoff in Tien Shan (Central Asia). *Nature Climate Change*, *2*(10), 725-731. https://doi.org/10.1038/nclimate1592

Spötl, C., & Vennemann, T.W. (2003). Continuous-flow isotope ratio mass spectrometric analysis of carbonate minerals. *Rapid communications in mass spectrometry*, *17*(9), 1004-1006. https://doi.org/https://doi.org/10.1002/rcm.1010

Steinthorsdottir, M., Coxall, H.K., De Boer, A.M., Huber, M., Barbolini, N., Bradshaw, C.D., Burls, N.J., Feakins, S.J., Gasson, E., Henderiks, J., & Holbourn, A.E. (2021). The Miocene: the future of the past. *Paleoceanography and Paleoclimatology*, *36*(4), p.e2020PA004037. https://doi.org/10.1029/2020PA004037

Stone J.O. (2000). Air pressure and cosmogenic isotope production. *Journal of Geophysical Research: Solid Earth, 105*, 23753-23759. https://doi.org/10.1029/2000JB900181

Stroeven, A.P., Hättestrand, C., Heyman, J., Kleman, J., & Morén, B.M. (2013). Glacial geomorphology of the Tian Shan. *Journal of Maps, 9*, 505–512. https://doi.org/10.1080/17445647.2013.820879

Sun, J., Gong, Z., Tian, Z., Jia, Y., & Windley, B. (2015). Late Miocene stepwise aridification in the Asian interior and the interplay between tectonics and climate. *Palaeogeography, Palaeoclimatology, Palaeoecology*, *421*, 48-59. https://doi.org/10.1016/j.palaeo.2015.01.001

Swart, P.K. (2015). The geochemistry of carbonate diagenesis: The past, present and future. *Sedimentology*, *62*(5), 1233-1304. https://doi.org/10.1111/sed.12205

Tadono, T., Takaku, J., Tsutsui, K., Oda, F., & Nagai, H. (2015). Status of "ALOS World 3D (AW3D)" global DSM generation. In 2015 IEEE international geoscience and remote sensing symposium (IGARSS) (pp. 3822–3825).

Talbot, M.R. (1990). A review of the palaeohydrological interpretation of carbon and oxygen isotopic ratios in primary lacustrine carbonates. *Chemical Geology: Isotope Geoscience Section*, *80*(4), 261-279. https://doi.org/10.1016/0168-9622(90)90009-2

Tauxe, L. (2010). Essentials of paleomagnetism. University of California Press. 489 pp.

Thompson, S.C., Weldon, R.J., Rubin, C.M., Abdrakhmatov, K., Molnar, P., & Berger, G.W. (2002). Late Quaternary slip rates across the central Tien Shan, Kyrgyzstan, central Asia. *Journal of Geophysical Research: Solid Earth*, *107*(B9), ETG-7. https://doi.org/10.1029/2001JB000596

Turchinskiy, V. P. (1970). Geological map of the USSR of 1:200 000 scales: Northern Tien Shan series. Sheet K-43-XVIII. Moscow, Russia: Russian Geological Research Institute (VSEGEI), Nedra.

Tursungasiev, B.T., & Petrov, O.V. (editors) (2008). Geological map of Kyrgyzstan of 1:500000 scales. Russian Geological Research Institute (VSEGEI), Saint Petersburg.

Unger-Shayesteh, K., Vorogushyn, S., Farinotti, D., Gafurov, A., Duethmann, D., Mandychev, A., & Merz, B. (2013). What do we know about past changes in the water cycle of Central Asian headwaters? A review. *Global and Planetary Change, 110*, 4-25. https://doi.org/10.1016/j.gloplacha.2013.02.004

Van der Beek, P., & Schildgen, T.F. (2023). *age2exhume*–a MATLAB/Python script to calculate steady-state vertical exhumation rates from thermochronometric ages and application to the Himalaya. *Geochronology*, *5*(1), 35-49. https://doi.org/10.5194/gchron-5-35-2023

Voigt, S., Weber, Y., Frisch, K., Bartenstein, A., Hellwig, A., Petschick, R., Bahr, A., Pross, J., Koutsodendris, A., Voigt, T., Verestek, V., & Appel, E. (2017). Climatically forced moisture supply, sediment flux and pedogenesis in Miocene mudflat deposits of south-east Kazakhstan, Central Asia. *The Depositional Record*, *3*(2), 209-232. https://doi.org/10.1002/dep2.34

von Blanckenburg, F., Belshaw, N.S., & O'Nions, R.K. (1996). Separation of ^{9}Be and cosmogenic ^{10}Be from environmental materials and SIMS isotope dilution analysis. *Chemical Geology*, *129*(1-2), 93-99. https://doi.org/10.1016/0009-2541(95)00157-3

Voskresenskaya, T.N. (2013). Lacustrine sediments and paleogeography in the Issyk-Kul basin in the Cenozoic (in Russian). In: *Sedimentary basins, sedimentary and postsedimentary processes in the geological history, 1*, 180-183. Novosibirsk: INGG SO RAN.

Voskresenskaya, T.N., & Leflat, O.N. (2015). Paleogeographic evolution of the Issyk-Kul basin during the Pleistocene (in Russian). *Vestnik Moskovskogo Universiteta. Seriya 5, Geografiya*, 71-77.

Wack, M. R., & Gilder, S. A. (2012). The SushiBar: An automated system for paleomagnetic investigations. Geochemistry, Geophysics, Geosystems, 13(3), a. https://doi.org/10.1029/2011gc003985

Wack, M.R., Gilder, S.A., Macaulay, E.A., Sobel, E.R., Charreau, J., & Mikolaichuk, A. (2014). Cenozoic magnetostratigraphy and magnetic properties of the southern Issyk-Kul basin, Kyrgyzstan. *Tectonophysics*, *629*, 14-26. https://doi.org/10.1016/j.tecto.2014.03.030

Wang, X., Carrapa, B., Sun, Y., Dettman, D.L., Chapman, J.B., Caves Rugenstein, J.K., Clementz, M.T., DeCelles, P.G., Wang, M., Chen, J., Quade, J., Wang, F., Li, Z., Oimuhammadzoda, I., Gadoev, M., Lohmann, G., Zhang, X., & Chen, F. (2020). The role of the westerlies and orography in Asian hydroclimate since the late Oligocene. *Geology*, *48*(7), 728-732. https://doi.org/10.1130/G47400.1

Wang, X., Otto, M., & Scherer, D. (2021). Atmospheric triggering conditions and climatic disposition of landslides in Kyrgyzstan and Tajikistan at the beginning of the 21st century. *Natural Hazards and Earth System Sciences*, *21*(7), 2125-2144. https://doi.org/10.5194/nhess-21-2125-2021

Wang, S., Zhang, M., Hughes, C.E., Zhu, X., Dong, L., Ren, Z., & Chen, F. (2016). Factors controlling stable isotope composition of precipitation in arid conditions: An observation network in the Tianshan Mountains, central Asia. *Tellus B: Chemical and Physical Meteorology*, *68*(1), 26206. https://doi.org/10.3402/tellusb.v68.26206

Wang, Y., Zhang, J., Huang, X., & Wang, Z. (2023). Cenozoic exhumation of the Tianshan as constrained by regional low-temperature thermochronology. *Earth-Science Reviews*, 104325. https://doi.org/10.1016/j.earscirev.2023.104325

Wasiljeff, J., Salminen, J.M., Stenman, J., Zhang, Z., & Kaakinen, A. (2022). Oligocene moisture variations as evidenced by an aeolian dust sequence in Inner Mongolia, China. *Scientific reports*, *12*(1), 1-14. https://doi.org/10.1038/s41598-022-09362-y

Westerhold, T., Marwan, N., Drury, A.J., et al. (2020). An astronomically dated record of Earth's climate and its predictability over the last 66 million years. *Science*, *369*(6509), 1383-1387. https://doi.org/10.1126/science.aba6853

Watson, G. S., & Enkin, R. J. (1993). The fold test in paleomagnetism as a parameter estimation problem. Geophysical Research Letters, 20(19), 2135–2137. https://doi.org/10.1029/93gl01901

Whipple, K.X. (2009). The influence of climate on the tectonic evolution of mountain belts. *Nature geoscience*, *2*(2), 97-104. https://doi.org/10.1038/ngeo413

Wilcken K.M., Codilean A.T., Fülöp R.-H., Kotevski S., Rood A.H., Rood D.H., Seal A.J., & Simon K. (2022). Accelerator mass spectrometry of Be-10 and Al-26 at low nuclide concentrations. *Geochronology, 4*, 339-352. https://doi.org/10.5194/gchron-4-339-2022

Wilcken, K.M., Fink, D., Hotchkis, M., Garton, D., Button, D., Mann, M., Kitchen, R., Hauser, T., & O'Connor, A. (2017). Accelerator mass spectrometry on SIRIUS: New 6 MV spectrometer at ANSTO. *Nuclear Instruments and Methods in Physics Research Section B: Beam Interactions with Materials and Atoms, 406*, 278-282. https://doi.org/10.1016/j.nimb.2017.01.003

Wilcken K.M., Fujioka T., Fink D., Fülöp R.-H., Codilean A.T., Simon K., Mifsud C., & Kotevski S. (2019). SIRIUS Performance: Be-10, Al-26 and Cl-36 measurements at ANSTO. *Nuclear Instruments and Methods in Physics Research Section B: Beam Interactions with Materials and Atoms, 455*, 300-304. https://doi.org/10.1016/j.nimb.2019.02.009

Willenbring, J.K., & Jerolmack, D.J. (2016). The null hypothesis: Globally steady rates of erosion, weathering fluxes and shelf sediment accumulation during Late Cenozoic mountain uplift and glaciation. *Terra Nova*, *28*(1), 11-18. https://doi.org/10.1111/ter.12185

Willenbring, J.K., & Von Blanckenburg, F. (2010). Long-term stability of global erosion rates and weathering during late-Cenozoic cooling. *Nature*, *465*(7295), 211-214. https://doi.org/10.1038/nature09044

Willett, S.D., & Brandon, M.T. (2013). Some analytical methods for converting thermochronometric age to erosion rate, *Geochem. Geophy. Geosy.*, *14*, 209–222, https://doi.org/10.1029/2012gc004279.

Windley, B.F., Alexeiev, D.V., Xiao, W., Kröner, A., & Badarch, G. (2007). Tectonic models for accretion of the Central Asian Orogenic Belt. *Journal of the Geological Society, London, 164*, 31–47, https://doi.org/10.1144/0016-76492006-022

Worden, R.H., Armitage, P.J., Butcher, A.R., Churchill, J.M., Csoma, A.E., Hollis, C., Lander, H., & Omma, J.E. (2018). Petroleum reservoir quality prediction: overview and contrasting approaches from sandstone and carbonate communities. *Geological Society, London, Special Publications*, *435*(1), 1-31. https://doi.org/10.1144/SP435.21

Worden, R.H., & Burley, S.D. (2003). Sandstone diagenesis: the evolution of sand to stone. *Sandstone diagenesis: Recent and ancient*, *4*, 3-44. https://doi.org/10.1002/9781444304459.ch

Wu, F., Fang, X., Yang, Y., Dupont-Nivet, G., Nie, J., Fluteau, F., Zhang, T., & Han, W. (2022). Reorganization of Asian climate in relation to Tibetan Plateau uplift. *Nature Reviews Earth & Environment*, *3*(10), 684-700. https://doi.org/10.1038/s43017-022-00331-7

Yang, W., Jolivet, M., Dupont-Nivet, G., & Guo, Z. (2014). Mesozoic–Cenozoic tectonic evolution of southwestern Tian Shan: Evidence from detrital zircon U/Pb and apatite fission track ages of the Ulugqat area, Northwest China. *Gondwana Research*, *26*(3-4), 986-1008. https://doi.org/10.1016/j.gr.2013.07.020

Zachos, J., Pagani, M., Sloan, L., Thomas, E., & Billups, K. (2001). Trends, rhythms, and aberrations in global climate 65 Ma to present. *science*, *292*(5517), 686-693. https://doi.org/10.1126/science.1059412

Zech, R. (2012). A late Pleistocene glacial chronology from the Kitschi-Kurumdu Valley, Tien Shan (Kyrgyzstan), based on ^{10}Be surface exposure dating. *Quaternary Research*, *77*(2), 281-288. https://doi.org/10.1016/j.yqres.2011.11.008

Zhang, P., Molnar, P., & Downs, W.R. (2001). Increased sedimentation rates and grain sizes 2–4 Myr ago due to the influence of climate change on erosion rates. *Nature*, *410*(6831), 891-897. https://doi.org/10.1038/35073504

Zhao, X., Zhang, H., Lv, H., Lü, Y., Li, X., Liu, K., Zhang, J., & Xiong, J. (2021). Signatures of tectonic-climatic interaction during the Late Cenozoic orogenesis along the northern Chinese Tian Shan. *Basin Research*, *33*(1), 291-311. https://doi.org/10.1111/bre.12466

Zhou, Y., Wu, C., Yuan, B., Wang, J., Zhou, T., Wang, Y., & Tang, X. (2020). Cenozoic tectonic patterns and their controls on growth strata in the northern Tianshan fold and thrust belt, northwest China. Journal of Asian Earth Sciences, 198. https://doi.org/10.1016/j.jseaes.2020.104237

Zhuang, G., Hourigan, J.K., Koch, P.L., Ritts, B.D., & Kent-Corson, M.L. (2011). Isotopic constraints on intensified aridity in Central Asia around 12 Ma. *Earth and Planetary Science Letters*, *312*(1-2), 152-163. https://doi.org/10.1016/j.epsl.2011.10.005

Zomer, R.J., Xu, J., & Trabuco, A. (2022). Version 3 of the Global Aridity Index and Potential Evapotranspiration Database. *Scientific Data, 9*, 409. https://doi.org/10.1038/s41597-022-01493-1

Zubovich, A.V., Wang, X.Q., Scherba, Y.G. et al. (2010). GPS velocity field for the Tien Shan and surrounding regions. *Tectonics*, *29*(6). https://doi.org/10.1029/2010TC002772

SUPPLEMENTARY MATERIAL FOR CHAPTER 2

Supplementary figures S2.1 and S2.2 show additional examples of the natural remanent magnetization (NRM) demagnetization behavior from representative samples, complementing Figure 2.4. Dataset S2.1 lists all interpreted paleomagnetic directions shown in Figure 2.5. Data produced during this study are available in the open-access online database Zenodo (https://doi.org/10.5281/zenodo.4548968).

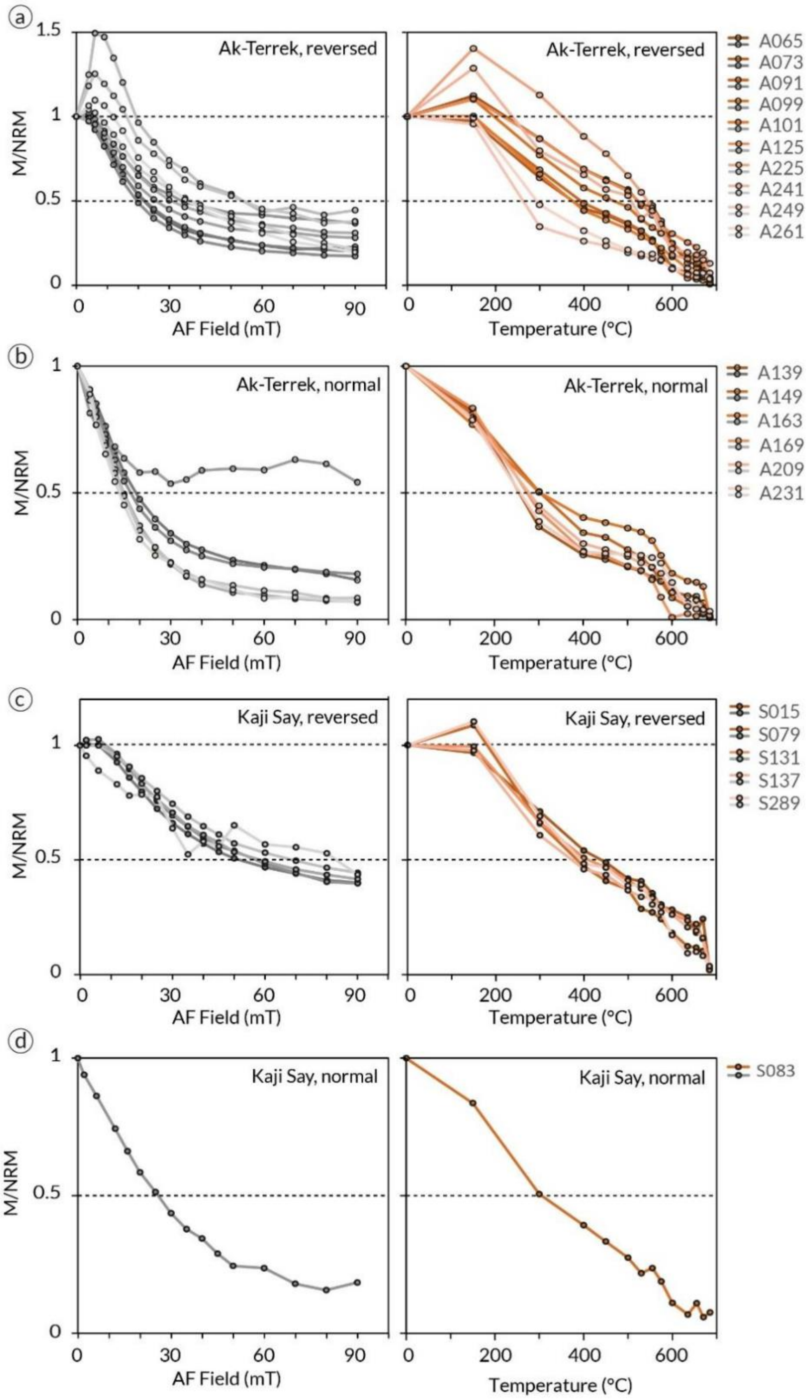

Figure S2.1 Comparison of normalized magnetization decay curves of thermally and AF demagnetized sample pairs of the same sites (horizons) from the Ak Terek and Kaji Say (c and d) sections

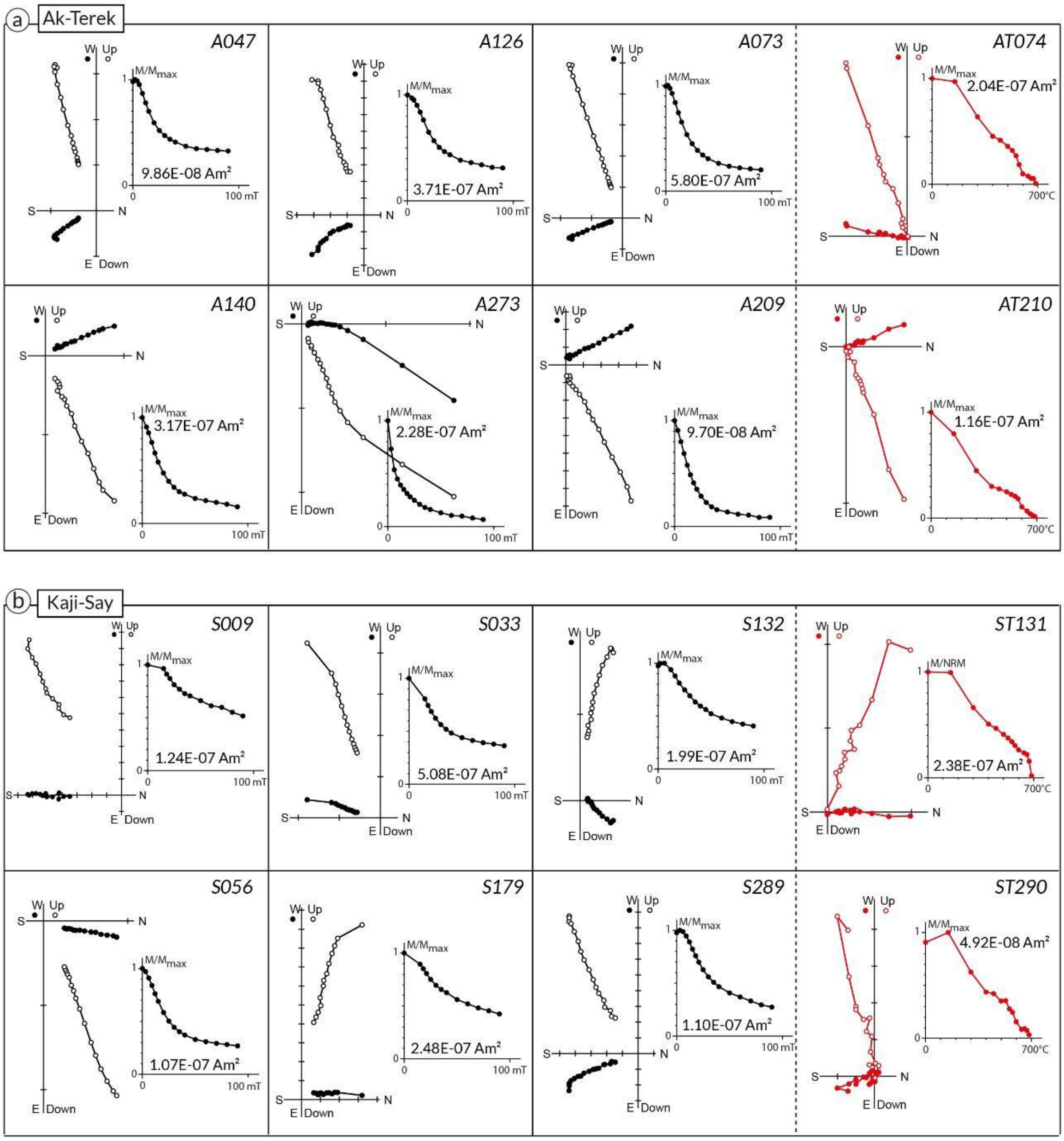

Figure S2.2 Representative Zijderveld plots with normalized magnetization decay curves (M/M_{max}) from a) the Ak Terek and b) the Kaji Say sections. Alternating field and thermal demagnetization experiments are shown in black and red, respectively. Italic names in the upper right corners indicate sample ID; numbers inside the decay plots indicate the maximum magnetic moments of the samples. The four sample pairs on the right, separated by a dashed line, stem from the same horizons.

Dataset S2.1 Interpreted paleomagnetic directions used for the magnetostratigraphy. Given are the section name, sample ID, demagnetization method, number of interpreted demagnetization steps, declination and inclination in geographic and stratigraphic coordinates, stratigraphic height and VGP latitude.

Section: AT, Ak-Terek (42.2°N, 76.7°E), KS, Kaji-Say (42.2°N, 77.3°E)
Method: Demagnetization method
n: number of interpreted demagnetization steps
Dg: Declination (deg) in geographic coordinates (in-situ)
Ig: Inclination (deg) in geographic coordinates (in-situ)
Ds: Declination (deg) in stratigraphic coordinates (tilt-corrected)
Is: Inclination (deg) in stratigraphic coordinates (tilt-corrected)
Height: Stratigraphic height (m)
VGP.Lat: Virtual geomagnetic pole latitude (deg)

Section	Sample_Id	Method	n	Dg	Ig	Ds	Is	Strike	Dip	Height	VGP.Lat
AT	A001	AF	12	293.4	41.8	309.8	35.6	285	21	1.5	42.3
AT	A002	AF	12	14.5	58.4	14.7	37.4	285	21	1.5	65.4
AT	A007.4	AF	5	143	-63	163.3	-47.1	285	21	5.9	-70.6
AT	A007	AF	10	179.5	-68.7	186.6	-48.1	285	21	6.2	-75.9
AT	A007.9	AF	5	155.1	-29.1	160	-12.4	285	21	8.9	-49.9
AT	A009.5	AF	8	325.4	70	349.4	52.9	285	21	10.15	77.9
AT	A012	AF	13	356.8	69.7	5.2	50.2	285	20	15.8	78
AT	A013	AF	12	350.7	61.3	359.5	42.4	285	20	17.1	72.3
AT	A015	AF	11	7.1	46.7	8.9	26.8	285	20	18.8	60.9
AT	A017	AF	9	339.8	39.1	346.2	22.1	285	20	21.3	57
AT	A018	AF	10	331.8	65.1	349.3	48.4	285	20	21.3	74.5
AT	A020	AF	9	344.6	67.6	357.5	50.1	285	19	24	78.5
AT	A021	AF	11	359.9	69.5	6.7	50.8	285	19	30.5	78.1
AT	A022	AF	12	344	57.4	353.7	40.3	285	19	30.5	70
AT	A023	AF	8	339	42.3	346	26.2	285	19	33.9	59.1
AT	A027	AF	11	324.9	74.2	351.4	58.5	285	19	36.8	82.8
AT	A028	AF	9	36.5	68	27.3	49.7	285	19	36.8	65.3
AT	A029	AF	8	340.2	73.1	357.4	56.7	285	18	40.1	84.7
AT	A031	AF	10	347.3	60.2	356.4	43.6	285	18	40.6	73
AT	A033	AF	9	341.6	62.3	353.3	46.2	285	18	42.2	74.4
AT	A034	AF	8	349.3	25.5	351.6	9.1	285	18	42.2	51.6
AT	A035	AF	8	350.9	60.7	358.9	43.8	285	18	43.7	73.4
AT	A037	AF	8	352.3	61.1	360	44	285	18	45.6	73.6
AT	A039	AF	4	156.4	-56.5	167.7	-41.2	285	18	47.3	-68.8
AT	A040	AF	4	77	-69	127.2	-70.1	285	18	47.3	-53.8
AT	A041	AF	8	118.4	-78.9	166.6	-66.9	285	18	50	-78.2
AT	A044	AF	10	141	-72.9	167.6	-58.8	285	18	52.3	-80.3
AT	A045	AF	4	132.3	-75.5	166.4	-62.3	285	18	54.45	-80
AT	A047	AF	11	145.3	-71.8	168.2	-58.2	285	17	55.65	-80.4
AT	A049	AF	10	120.3	-74.8	159	-64.5	285	17	57.25	-74.4
AT	A051	AF	9	146.4	-69.4	167	-55.8	285	17	59.45	-78.4
AT	A051.9	AF	11	7.5	56.8	9.6	39.9	285	17	59.45	68.9
AT	A053	AF	8	15.1	54.6	15.1	37.6	285	17	61.95	65.4
AT	A054	AF	8	12.1	55.2	12.9	38.2	285	17	61.95	66.6
AT	A053.2	AF	3	190.9	-65.5	192.4	-48.5	285	17	61.97	-73.8
AT	A055	AF	10	148	-60.5	163	-47.2	285	17	63.75	-70.5
AT	A057	AF	9	163.2	-64.7	174.8	-49.3	285	17	65.05	-77.3
AT	A059	AF	9	155	-64.2	169.3	-49.8	285	17	68	-75.6
AT	A061	AF	4	198	-46.7	197.3	-29.7	285	17	69.25	-59.8
AT	A064	AF	10	143.3	-78.3	173.6	-64.1	285	17	70.75	-84.1
AT	A065	AF	10	160.4	-73.2	177.1	-57.8	285	17	72.35	-85.6
AT	AT066a	thermal	11	148	-67.1	166.5	-53.5	285	17	72.35	-76.6
AT	A067	AF	11	138.7	-73.9	165.8	-61.8	285	16	73.15	-79.5

AT	A069	AF	10	151.1	-67.3	167.9	-54.1	285	16	74.65	-77.9
AT	A071	AF	10	155.4	-62.2	168.3	-48.7	285	16	76.15	-74.3
AT	A073	AF	11	159.2	-69.9	174.1	-55.7	285	16	79.15	-82.5
AT	AT074a	thermal	10	184.9	-70	189.1	-54.1	285	16	79.15	-79.7
AT	A075	AF	9	139.9	-57.2	155	-46.3	285	16	80.95	-65
AT	A078	AF	10	136.4	-73.2	163.9	-61.5	285	16	83.05	-78.1
AT	A079	AF	9	182.9	-74.8	188.9	-59	285	16	84.55	-82.9
AT	A080	AF	6	138	-78.6	171	-65.8	285	16	84.55	-81.4
AT	A081	AF	8	134	-80.7	172.8	-68	285	16	85.5	-79.9
AT	A084	AF	10	130.7	-59.9	149.7	-50.5	285	16	87.25	-63.5
AT	A085	AF	10	150.4	-73.3	171.3	-59.8	285	16	89.35	-83.3
AT	A088	AF	10	151.8	-74.2	172.8	-60.5	285	16	89.55	-84.6
AT	A089	AF	9	141.1	-80.5	174.9	-67.1	285	16	91.15	-81.6
AT	A092	AF	9	145.6	-67.5	163.8	-55.9	285	15	92.45	-76.3
AT	AT091a	thermal	10	125.9	-78.3	164.7	-68	285	15	92.45	-76.3
AT	A093	AF	9	141.9	-71.4	164.3	-60	285	15	93.45	-78.2
AT	A096	AF	9	155.2	-70.8	171.7	-57.9	285	15	95.25	-82.7
AT	A097	AF	12	172.5	-70.2	181.7	-55.9	285	15	96.55	-84.1
AT	A099	AF	11	146.8	-64.7	162.9	-53.1	285	15	100.25	-74.1
AT	AT100a	thermal	10	151.1	-67.9	167.5	-55.6	285	15	100.25	-78.6
AT	A102	AF	10	128.3	-58.7	146.4	-50.6	285	15	102.25	-61.2
AT	A104	AF	10	146	-72.3	167.4	-60.3	285	15	106.85	-80.5
AT	AT103a	thermal	10	134.3	-76.5	165.6	-65.4	285	15	106.85	-78.5
AT	A106	AF	7	179.7	-76.7	187.6	-62	285	15	108.85	-84.3
AT	A107	AF	5	157	-75.4	175.6	-62	285	15	110.55	-86.6
AT	A110	AF	12	221.7	-83.2	203.9	-69.7	285	14	112.75	-70.6
AT	A111	AF	12	171.9	-68.2	180.3	-54.9	285	14	120.65	-83.3
AT	A113	AF	10	127	-51.7	140.8	-44.9	285	14	125.65	-54.5
AT	A114	AF	6	187.2	-75.7	191	-61.8	285	14	125.65	-81.9
AT	A117	AF	10	114.8	-73.9	150.5	-67.1	285	14	130.75	-68.3
AT	A118	AF	3	123.2	-61.7	143.3	-54.9	285	14	130.75	-60.9
AT	A122	AF	8	133.3	-60	149	-52.3	285	13	133.55	-63.9
AT	A123	AF	10	193.3	-76.4	194.1	-63.4	285	13	135.75	-79.4
AT	A126	AF	7	159.6	-66.7	171.3	-55.4	285	13	136.85	-80.8
AT	AT125a	thermal	10	145	-59.6	157.8	-50.1	285	13	136.85	-69
AT	A127	AF	9	109.4	-52	125	-49.2	285	13	137.65	-44.8
AT	A130	AF	10	2.7	67.9	7	55.1	285	13	144.4	81.5
AT	A131	AF	10	344	70.2	355.5	58.3	285	13	146.15	85.4
AT	A134	AF	10	6.8	71.4	10	58.5	285	13	147.75	81.8
AT	A135	AF	10	349.7	72.1	359.8	59.9	285	13	149.25	88.5
AT	A138	AF	10	15.9	70.6	15.6	57.6	285	13	149.65	77.5
AT	A140	AF	10	337.7	64.6	349.2	53.5	285	13	150.75	78.2
AT	AT139a	thermal	10	354.6	64.9	0.9	52.5	285	13	150.75	80.8
AT	A143	AF	12	352.7	71.7	1.5	59.2	285	13	153.25	87.6
AT	A145	AF	10	344.1	72.5	356.6	60.6	285	13	154.25	87.4
AT	A147	AF	9	356.8	71.6	3.9	59	285	13	155.75	86.1
AT	A150	AF	10	354.5	60.4	0	48	285	13	155.75	76.8
AT	AT149a	thermal	10	343.9	65.7	353.8	53.9	285	13	155.75	80.9
AT	A151	AF	10	335.9	74.4	352.2	64	285	12	158.65	83.4
AT	A154	AF	10	313.5	51.7	324.7	44.9	285	12	159.25	57.2
AT	A156	AF	10	1.6	71.4	6.6	59.6	285	12	159.95	84.8
AT	A157	AF	9	330.9	62.6	342.7	53.1	285	12	162.35	74
AT	A158	AF	10	339.7	62.1	349.1	51.8	285	12	162.35	76.9
AT	A159	AF	10	336.2	70.6	350.2	60.3	285	12	163.65	82.6
AT	A162	AF	10	115.5	71.2	81.2	69.8	285	12	165.35	37.5
AT	A164	AF	9	319.7	82.9	354.8	73	285	12	166.15	73.4
AT	AT163a	thermal	10	12.3	72	13.3	60	285	12	166.15	79.9
AT	A166	AF	8	353.3	61.4	359	50.1	285	12	167.35	78.6
AT	A168	AF	8	327.4	73.4	346.5	63.8	285	12	168.85	79.7
AT	A169	AF	10	349	69.8	358.1	58.6	285	12	169.95	86.8
AT	AT170a	thermal	10	8.1	76.3	11.2	64.4	285	12	169.95	81
AT	A171	AF	4	117.8	-78.6	157.1	-71.8	285	12	170.65	-69.4

AT	A173	AF	10	163	-55.8	170	-45.3	285	12	174.15	-72.6
AT	A174	AF	8	116.5	-71.7	145.1	-66.3	285	12	174.15	-64.9
AT	A175	AF	10	129.7	-74.9	157.4	-67.1	285	12	175	-72.6
AT	A176	AF	10	153.6	-79.1	175	-68.6	285	12	175	-79.7
AT	A175.2	AF	11	194.2	-79.5	194.6	-67.5	285	12	175.2	-77
AT	A175.8	AF	11	180.8	-68.4	185.6	-56.6	285	12	175.8	-83.4
AT	A177.2	AF	8	173.5	-36.4	176	-25.1	285	12	176.5	-60.8
AT	A177.8	AF	11	148.8	-66.1	162.8	-56.7	285	12	176.8	-75.9
AT	A179	AF	10	147.6	-72.2	165.6	-62.7	285	12	178.25	-79.4
AT	A180	AF	9	142.7	-71.6	162.1	-62.6	285	12	178.25	-76.9
AT	A179.1	AF	5	159.8	-79.6	178.4	-68.7	285	12	178.35	-80.1
AT	A181	AF	4	5.2	-61.7	359.5	-72.5	285	11	183.45	-10
AT	A182	AF	7	339.3	5.2	339.4	-3.7	285	11	183.45	42.2
AT	A183.1	AF	10	355.7	60.9	0.4	50.3	285	11	185.25	78.9
AT	A183.2	AF	10	350.4	56.6	355.6	46.4	285	11	185.25	75.1
AT	A184	AF	10	223.2	60.8	237	69.9	285	11	185.25	17.7
AT	A185	AF	10	313.3	68.9	332.4	62	285	11	186.85	69.8
AT	A186	AF	10	328.7	58.3	338.8	49.9	285	11	186.85	69.5
AT	A187	AF	9	315.2	47.2	324	40.9	285	11	188.45	54.8
AT	A188	AF	7	322.4	58.3	333.7	50.7	285	11	188.45	66.5
AT	A189	AF	9	11	44.3	11.6	33.3	285	11	192.55	64
AT	A190	AF	5	191.9	68.5	188.7	79.5	285	11	192.55	22
AT	A191	AF	4	102	-73.4	135.5	-70.6	285	11	193.75	-58.6
AT	A192	AF	10	132.4	-69.2	152.1	-62.5	285	11	193.75	-69.6
AT	A193	AF	5	165.8	-60.9	172.9	-51	285	11	200.15	-78.1
AT	A197	AF	11	156.5	-73.1	170.9	-63.6	285	11	205.25	-82.8
AT	A199	AF	10	168.6	-71	177.2	-61.7	285	10	209.55	-87.8
AT	A201	AF	10	169.7	-72.1	178.3	-62.7	285	10	213.25	-87.7
AT	A204	AF	10	143.7	-53.5	152.5	-46.7	285	10	218.25	-63.5
AT	A205	AF	7	325.1	52.7	333.4	45.7	285	10	222.15	63.6
AT	A207	AF	11	329.8	64.8	341.2	57.1	285	10	236.55	75
AT	A209	AF	11	335.1	58	342.5	50.8	285	9	246.05	72.4
AT	AT210a	thermal	10	343	67.6	351.4	59.6	285	9	246.05	83.3
AT	A211	AF	11	343.7	70.2	352.9	62.2	285	9	251.95	84.6
AT	A213	AF	5	148.6	-16.1	150.1	-9.8	285	9	255.65	-44.3
AT	A215	AF	11	171.2	-74.1	179.5	-65.6	285	9	258.45	-84.4
AT	A217	AF	8	160.8	-59.1	167.5	-51.4	285	9	262.15	-75.8
AT	A219	AF	10	129.2	-49.6	137.8	-45.3	285	9	265.95	-52.5
AT	A222	AF	10	194.3	-63.5	194.5	-54.5	285	9	268.15	-76.6
AT	A223	AF	11	172.3	-66.8	177.7	-59.3	285	8	280.55	-87.2
AT	A225	AF	8	155	-67.9	164.7	-61.4	285	8	284.55	-78.7
AT	AT226a	thermal	10	143.2	-66.5	154.9	-60.9	285	8	284.55	-71.5
AT	A227	AF	6	178.8	-58.2	181.7	-50.5	285	8	288.35	-79
AT	A229	AF	10	0.6	65.8	3.9	58	285	8	293.65	85.3
AT	A231	AF	9	327.1	65.9	337.7	60	285	8	300.15	73.3
AT	AT232a	thermal	10	349.6	58	354	50.7	285	8	300.15	78.2
AT	A233	AF	7	347	65	353.2	57.8	285	8	308.25	83.6
AT	A236	AF	9	346.2	18.9	347.2	12.8	285	7	314.25	52.5
AT	A238	AF	4	189.3	-46.1	189.9	-39.2	285	7	317.75	-68.3
AT	A239	AF	6	165.2	-59.6	170.1	-53.3	285	7	325.05	-78.6
AT	A242	AF	11	186.2	-70.3	188.4	-63.3	285	7	333.85	-83.3
AT	AT241a	thermal	10	153.8	-68.1	162.9	-62.4	285	7	333.85	-77.4
AT	A243	AF	5	135	-67	147.2	-62.9	285	7	341.85	-66.1
AT	A245	AF	10	174.6	-70.6	179.7	-63.9	285	7	347.05	-86.5
AT	A247	AF	8	207.2	-71.1	204	-64.2	285	7	350.35	-72.4
AT	A249	AF	9	191.2	-72.3	192.1	-66.3	285	6	360.85	-79.3
AT	AT250a	thermal	10	177.5	-70	181.3	-64.2	285	6	360.85	-86.1
AT	A251	AF	9	191.3	-55.8	191.7	-49.8	285	6	369.05	-75.1
AT	A254	AF	6	170.1	-62.4	174.1	-56.9	285	6	373.05	-83.5
AT	A255	AF	9	150.6	-59	156.6	-54.5	285	6	375.45	-70.5
AT	A257	AF	9	179.1	-60.7	181.5	-54.9	285	6	380.05	-83.1
AT	A260	AF	8	182.5	-66.4	184.9	-60.5	285	6	383	-86.3

AT	A261	AF	8	190.4	-67.7	191.3	-61.7	285	6	387.05	-81.6
AT	AT262a	thermal	10	176.2	-65.9	179.6	-60.2	285	6	387.05	-88.9
AT	A263	AF	10	181.7	-68.2	184.4	-62.3	285	6	390.35	-86.5
AT	A265	AF	5	179.5	-35.3	180.5	-29.5	285	6	394.05	-63.6
AT	A268	AF	10	193.4	-65.8	193.7	-59.8	285	6	396.65	-79.6
AT	A270	AF	6	22.5	56.9	21.5	50.9	285	6	402.75	69.9
AT	A272	AF	10	358.9	73.6	2.5	68.8	285	5	406.25	79.9
AT	A273	AF	8	5.9	67.7	7.4	62.8	285	5	414.25	84.2
AT	A276	AF	6	321.7	56.2	327.1	53	285	5	420.25	62.9
AT	A278	AF	8	347.2	58.5	350.5	54.1	285	5	427.25	79.3
AT	A281	AF	9	122.8	-53.7	129	-51.9	285	5	439.55	-48.9
AT	A283	AF	12	188.3	-67.2	189.4	-62.3	285	5	444.65	-83
AT	A285	AF	6	235.1	-60.7	230	-56.7	285	5	448.45	-51.8
AT	A287	AF	8	188.9	-63.5	189.8	-58.6	285	5	452.05	-82
AT	A290	AF	9	137.3	-64.7	145.3	-61.8	285	5	458.95	-64.6
AT	A291	AF	9	180.9	-67.5	183.3	-62.6	285	5	463.7	-87
AT	A294	AF	10	356.6	64.9	358.9	61.1	285	4	468.45	89.2
AT	A295	AF	10	10	47.3	10.3	43.3	285	4	475.65	71
AT	A298	AF	11	4.3	73.7	6.3	69.8	285	4	481.9	77.8
AT	A299	AF	9	325.2	63.4	330.7	60.7	285	4	490.15	68.3
AT	A302	AF	11	7.4	49.4	7.9	45.4	285	4	493.75	73.4
KS	S001	AF	9	123.5	-76.1	162	-56.1	274	25	1.3	-75
KS	S002	AF	9	237.2	-16.3	234.3	-0.6	274	25	1.3	-25.9
KS	S004	AF	9	281.9	-88.1	188.5	-65.2	274	25	3.5	-82.1
KS	S005	AF	5	180.3	-78.7	182.8	-53.8	274	25	7.8	-81.8
KS	S007	AF	9	209.3	-48.9	202.2	-25.6	274	25	11.35	-55.5
KS	S009	AF	9	179.9	-52.6	181.1	-28.6	274	24	12.75	-63.1
KS	S011	AF	6	88.7	-16.7	96.1	-17.4	274	24	21.8	-10.5
KS	S012	AF	9	164.6	-60.7	172.2	-37.5	274	24	21.8	-67.8
KS	S013	AF	9	219.8	-74.6	198.7	-52.5	274	24	29.6	-72.7
KS	S015	AF	9	151.9	-64	165.7	-42	274	24	39.3	-68.6
KS	ST016	thermal	8	164.2	-73.6	175.4	-50.2	274	24	39.3	-78.2
KS	S017	AF	10	153.5	-48.3	161.6	-27.6	274	23	41.2	-58.3
KS	S020	AF	9	183.2	-51.4	183.5	-28.4	274	23	47.8	-62.8
KS	S021	AF	8	158.5	-67.7	170.4	-45.8	274	23	51.6	-73.1
KS	S025	AF	9	218	-68.9	201.5	-47.9	274	23	64.2	-68.2
KS	S027	AF	9	224.8	-87.3	188.1	-64.9	274	23	65.45	-82.5
KS	S033	AF	9	194.7	-69.9	189.5	-48.1	274	22	71.45	-74.9
KS	S033.1	AF	9	183.7	-64.8	183.8	-42.8	274	22	71.8	-72.4
KS	S034	AF	9	222.4	-74	201	-54.1	274	22	71.45	-72
KS	S035	AF	9	333.1	77.4	352.2	56.6	274	22	75.45	82.2
KS	S036	AF	9	36.7	82.4	12.6	61.3	274	22	75.45	80.7
KS	S037	AF	8	85.1	85.8	14.5	67	274	22	77.3	77.4
KS	S038	AF	9	195.4	87.2	2.3	70.7	274	22	77.3	77
KS	S040	AF	9	348.3	-3.7	346.6	-24.8	274	22	82.15	33.5
KS	S039.1	AF	8	19.8	55.9	14.6	34.5	274	22	82.3	63.7
KS	S039.8	AF	9	10.6	53.2	8.6	31.3	274	22	84	63.7
KS	S045	AF	10	146.1	-64	161.7	-44.7	274	22	94	-68.2
KS	S046	AF	9	181.4	-83.9	183.4	-61.9	274	22	94	-87.3
KS	S047	AF	9	164	-32.9	166.9	-12	274	22	95.65	-52.1
KS	S048	AF	9	170.2	-38.9	172.8	-17.4	274	22	95.65	-56.2
KS	S049	AF	9	47.2	65	29.3	47.4	274	21	105.75	62.7
KS	S050	AF	9	66.4	75.9	29.4	59.9	274	21	105.75	68
KS	S051	AF	10	261.6	57.8	294.7	56.2	274	21	109.65	40.5
KS	S052	AF	9	128.3	82.2	25.6	72.2	274	21	109.65	67.8
KS	S053	AF	8	66.8	63.7	41.6	49.9	274	21	115.75	55
KS	S054	AF	10	9.4	68.3	6.9	47.4	274	21	115.75	75.2
KS	S056	AF	9	7.4	70.5	5.7	49.5	274	21	122.85	77.3
KS	S055.1	AF	9	4.1	73	4.1	52	274	21	122.85	79.9
KS	S057	AF	10	7.8	58.1	6.6	38.1	274	20	127.55	68.5
KS	S058	AF	9	346.2	77.8	356.9	58.2	274	20	127.55	86
KS	S060	AF	10	2.8	50.2	3.1	30.2	274	20	134.15	63.9

KS	S062	AF	10	347	65.9	353.9	47.4	274	19	152.3	75.5
KS	S064	AF	9	166.1	-65.3	172.5	-49.8	274	16	160.3	-77
KS	S069	AF	9	197	-61.7	193.2	-48	274	14	171.4	-73.1
KS	S071	AF	9	170.6	-60.9	174.5	-47.1	274	14	172.5	-75.4
KS	S075	AF	9	177.2	-54.3	178.7	-42.3	274	12	180.7	-72.3
KS	S077	AF	9	172.7	-43.3	174.4	-31.5	274	12	183.2	-64.4
KS	S080	AF	9	212.2	-75.9	200.9	-66.6	274	10	189.5	-73.9
KS	ST079	thermal	9	192.4	-79.4	188.4	-69.4	274	10	189.5	-77.7
KS	S081	AF	8	187.7	-13.4	187.6	-3.4	274	10	190.6	-49
KS	S084	AF	10	344.2	62.3	348.6	53.7	274	9	196.1	78
KS	ST083	thermal	9	355.6	59.9	357.3	51	274	9	196.1	79.3
KS	S086	AF	10	10.1	49.3	9.2	40.3	274	9	199.2	69.4
KS	S087	AF	9	9.4	36	9	28	274	8	201.7	61.7
KS	S091	AF	8	5.7	57.8	5.4	50.9	274	7	207.85	78.5
KS	S093	AF	9	35.2	41.5	32.8	36.4	274	6	211.35	54.7
KS	S095	AF	9	34.7	68.5	28.5	63.2	274	6	214.45	69.3
KS	S097	AF	9	57.1	44.4	53.5	41.3	274	5	218.8	42.3
KS	S105	AF	8	1.2	57.5	2.2	32.5	274	25	222.85	65.5
KS	S103	AF	8	2.8	40	3	15	274	25	225.25	55.3
KS	S101	AF	9	10.2	75.2	6.5	50.2	274	25	231.85	77.7
KS	S099	AF	9	359.2	81.6	2.7	56.6	274	25	237.65	84.6
KS	S109	AF	9	123.2	72.3	23.2	24.3	276	73	251.05	54.3
KS	S111	AF	8	97.8	-63.6	158.7	-14.4	276	73	256.05	-50.4
KS	S113	AF	8	52.8	-75.8	174.5	-26.4	276	73	256.2	-61.4
KS	S115	AF	9	294.5	-25.3	255.2	-23.5	276	73	257.8	-19.1
KS	S117	AF	8	9.7	-63.1	183.7	-43.8	276	73	259.85	-73.2
KS	S119	AF	8	4.2	-61.9	187.2	-45.1	276	73	264.4	-73.4
KS	S121	AF	8	19.2	-35.3	155.8	-68.2	276	73	278.2	-71.1
KS	S123	AF	8	21.8	-9.1	70.8	-72.7	276	73	285.3	-26.2
KS	S125	AF	8	12.8	-30.2	162	-75.4	276	73	287.9	-67
KS	S127	AF	8	11.6	-57.6	181.4	-49.2	276	73	291.4	-77.8
KS	S130	AF	9	342.6	-29.2	242.3	-65.3	276	73	300	-46.7
KS	S132	AF	9	17.4	-82.2	184.3	-24.6	276	73	310	-60.5
KS	ST131	thermal	9	359.6	-67.4	189.2	-39.5	276	73	310	-68.8
KS	S134	AF	9	329.1	-59.4	209.4	-39.9	276	73	311.8	-58.7
KS	S135	AF	8	6.8	-75.8	185.8	-31.2	276	73	314.05	-64.2
KS	S138	AF	9	347.2	-43.5	213	-59.1	276	73	321.4	-65.1
KS	ST137	thermal	9	6	-37.1	186	-69.9	276	73	321.4	-77.7
KS	S139	AF	8	15.6	-49.5	174.6	-56.6	276	73	323.7	-83.5
KS	S141	AF	8	4.7	-61.9	186.9	-45.1	276	73	326.2	-73.5
KS	S143	AF	4	68.2	67.8	25.6	5.9	276	73	329.8	44.6
KS	S144	AF	5	11.9	50.6	10	-22.2	276	73	329.8	35.5
KS	S145	AF	8	25	-56.9	170.6	-47.6	276	73	338	-74.6
KS	S146	AF	9	4.8	-83.4	186.1	-23.6	276	73	338	-59.7
KS	S147	AF	8	17.2	-80.5	183.9	-26.3	276	73	341	-61.5
KS	S149	AF	8	34.4	-55.6	163.4	-45.7	276	73	344.7	-69.8
KS	S153	AF	9	25.2	-59.1	172	-45.6	276	73	348.1	-73.6
KS	S154	AF	9	12.6	-15.4	82.9	-83.5	276	73	348.1	-39.3
KS	S155	AF	8	30.1	-40.1	148.9	-58.9	276	73	352.1	-66.5
KS	S156	AF	4	46.7	-49.2	149.6	-44	276	73	352.1	-60.2
KS	S161	AF	9	26.8	-42	154.8	-59.4	276	73	364	-71
KS	S162	AF	9	22.9	-38.7	155.1	-63.8	276	73	364	-71.8
KS	S163	AF	8	345.5	-48.8	209.1	-54.1	276	73	368.2	-66.1
KS	S165	AF	8	12.7	-66.2	182.4	-40.6	276	73	374.2	-70.9
KS	S172	AF	8	351.7	-32.2	223.6	-70	276	73	380.2	-59.1
KS	S174	AF	8	11.9	-34.6	170.4	-71.6	276	73	382.9	-74.5
KS	S179	AF	8	357	-77.5	188.2	-29.3	276	73	395	-62.6
KS	S180	AF	9	353.3	-73	190.4	-33.5	276	73	395	-64.6
KS	S183	AF	8	59	-44	139.1	-38.1	276	73	403.5	-50.1
KS	S184	AF	8	43.5	-49.7	151.8	-45.5	276	73	403.5	-62.5
KS	S185	AF	8	194.4	36.3	346.6	69.4	276	73	407.5	75.9
KS	S187	AF	8	105.5	69.3	27.7	19.2	276	73	411.6	49.6

KS	S188	AF	8	243.9	76.9	353.9	23.6	276	73	411.6	59.7
KS	S189	AF	8	5.9	-64.3	186.1	-42.7	276	73	414.3	-71.9
KS	S190	AF	8	40.1	-25.2	116.4	-57.2	276	73	414.3	-42.2
KS	S191	AF	8	70.4	-55.3	150.3	-28.4	276	73	416.1	-52.8
KS	S192	AF	8	48.5	-55.3	155.9	-40	276	73	416.1	-62.1
KS	S196	AF	9	16.3	-18.2	104.2	-80.1	276	73	423.3	-43.9
KS	S197	AF	8	8.1	-32.4	179.2	-74.5	276	73	426.5	-71.2
KS	S198	AF	8	350.8	-18.6	267.4	-75.4	276	73	426.5	-37.7
KS	S199	AF	8	150.2	71.7	18.4	31.4	276	73	429.4	60.3
KS	S201	AF	8	196.3	67.9	1	38.7	276	73	433.3	69.6
KS	S203	AF	8	196.3	57.3	357.5	49	276	73	448.8	77.6
KS	S205	AF	8	199.3	73.6	1.6	32.9	276	73	451	65.7
KS	S207	AF	8	349.4	74.1	1.5	1.7	276	73	454.2	48.7
KS	S209	AF	8	205.7	45.8	340.5	56.9	276	73	463.7	74.4
KS	S209.1	AF	8	218.2	44.3	328.2	51.6	276	73	463.7	63
KS	S211	AF	6	29.1	-46	153.3	-53.1	277	31	465.2	-67.4
KS	S215	AF	5	2.5	59.7	4.4	28.8	277	31	482.4	62.9
KS	S216	AF	9	6.9	78.8	7	47.8	277	31	482.4	75.5
KS	S217	AF	8	20.7	62.6	14.4	32.1	277	31	497.6	62.3
KS	S218	AF	8	39.8	78.9	16.2	49.3	277	31	497.6	72.3
KS	S230	AF	5	112.2	66.7	51.9	57.2	277	31	516.2	50.6
KS	S231	AF	6	55.8	85.3	13.3	55.8	277	31	518	78.2
KS	S232	AF	9	158.1	83.9	13.8	64.2	277	31	518	79.4
KS	S233	AF	9	93.2	70.3	40.8	52.7	277	31	519.7	56.9
KS	S235	AF	5	49.4	36.6	40.6	11.8	277	31	521.6	39
KS	S236	AF	9	257.3	81.5	350.4	60.9	277	31	521.6	82.8
KS	S237	AF	9	25.7	65.5	16.4	35.3	277	31	527.5	63.4
KS	S238	AF	8	336.6	76.7	357.2	47.1	277	31	527.5	75.9
KS	S239	AF	8	54.3	61.9	32.4	36.3	277	31	531.9	54.9
KS	S240	AF	8	351.5	60.7	358.3	30.3	277	31	531.9	64.1
KS	S241	AF	8	343.5	62.6	354.4	33	277	31	534.3	65.3
KS	S242	AF	9	347.9	71.3	359	41	277	31	534.3	71.3
KS	S243	AF	8	208.2	86.9	4.6	61.9	277	31	536.3	86.5
KS	S244	AF	8	312	78.3	351.6	51.2	277	31	536.3	77.7
KS	S245	AF	8	339.5	65.5	353.3	36.2	277	31	537.3	67.2
KS	S246	AF	8	6.9	67.4	7	36.4	277	31	537.3	67.3
KS	S249	AF	8	354.1	79.6	3.5	48.8	277	31	545.3	77.3
KS	S251	AF	8	339.5	71.3	355.6	41.7	277	31	548.6	71.5
KS	S254	AF	8	310.8	61.7	334.2	43.4	277	25	545.3	62.9
KS	S255	AF	8	328.6	65.7	346.3	43.6	277	25	548.6	69.9
KS	S257	AF	8	338.9	72.9	354.8	49.2	277	25	555	77.2
KS	S259	AF	8	318.8	71.3	345.1	50.2	277	25	560.6	73.6
KS	S261	AF	6	85.5	65	49	51.8	277	25	565.6	50.4
KS	S263	AF	9	350.3	71.9	359.4	47.4	277	25	573.8	76.3
KS	S265	AF	7	49.1	58.3	33.3	37.3	277	25	578.8	54.9
KS	S267	AF	8	4.5	65.3	5.7	40.3	277	25	581.6	70.2
KS	S269	AF	8	99.1	70	48.5	59	277	25	584.4	53.8
KS	S271	AF	11	4.5	73.2	5.7	57.3	277	16	589.6	83.9
KS	S274	AF	11	24.8	72.2	16.8	56.6	277	16	593.7	76.2
KS	S275	AF	8	320.2	62.8	335.6	50.3	277	16	596.5	67.6
KS	S279	AF	9	293.5	75.1	330.8	65.4	277	16	604.5	68.8
KS	S281	AF	11	339	76.5	353.8	61.3	277	16	607.5	85.4
KS	S284	AF	9	114.9	-81.8	163.6	-69.9	277	16	613.4	-74.1
KS	S285	AF	9	151.2	-73.2	167.9	-58.8	277	16	619.1	-80.5
KS	S287	AF	8	106.2	-72.3	142.9	-64.5	277	16	623.6	-63.3
KS	S289	AF	9	158	-62.1	167.4	-47.4	277	16	629.1	-73
KS	ST290	thermal	9	178.4	-75.7	182.8	-59.8	277	16	629.1	-87.4
KS	S291	AF	6	253	-69.7	225.8	-59.6	277	16	632.1	-56
KS	S294	AF	8	182.7	-77.7	185.1	-61.7	277	16	635.6	-86.2
KS	S296	AF	9	187	-79	187	-63	277	16	638.7	-84.4
KS	S299	AF	7	147.8	-22.7	150.7	-10	277	16	658.1	-44.6

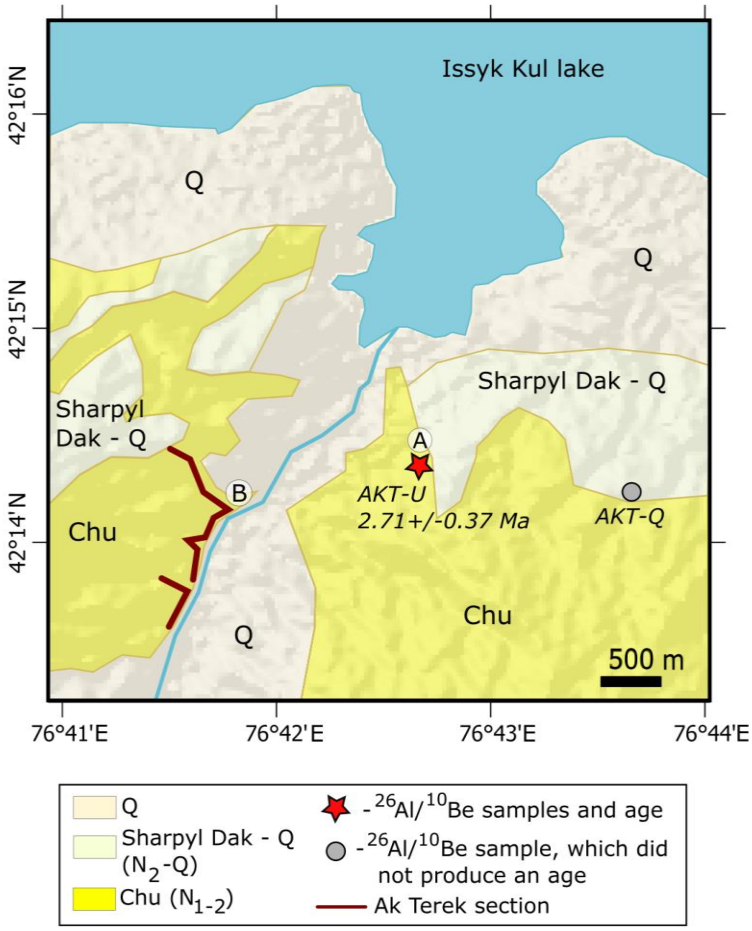

Figure S3.1. Ak Terek section area (location shown in Figure 3.1 in the main text of Chapter 3). Sedimentary units are mapped after Roud et al. (2021) and Burgette et al. (2017) on topography based on SRTM30 digital elevation data. A-B show locations of the corresponding section photos, represented in Fig. 6 in the main text. Stratigraphic units in the legend: N_{1-2} – Late Miocene – Pliocene; N2-Q – Pliocene – Quaternary; Q – Quaternary.

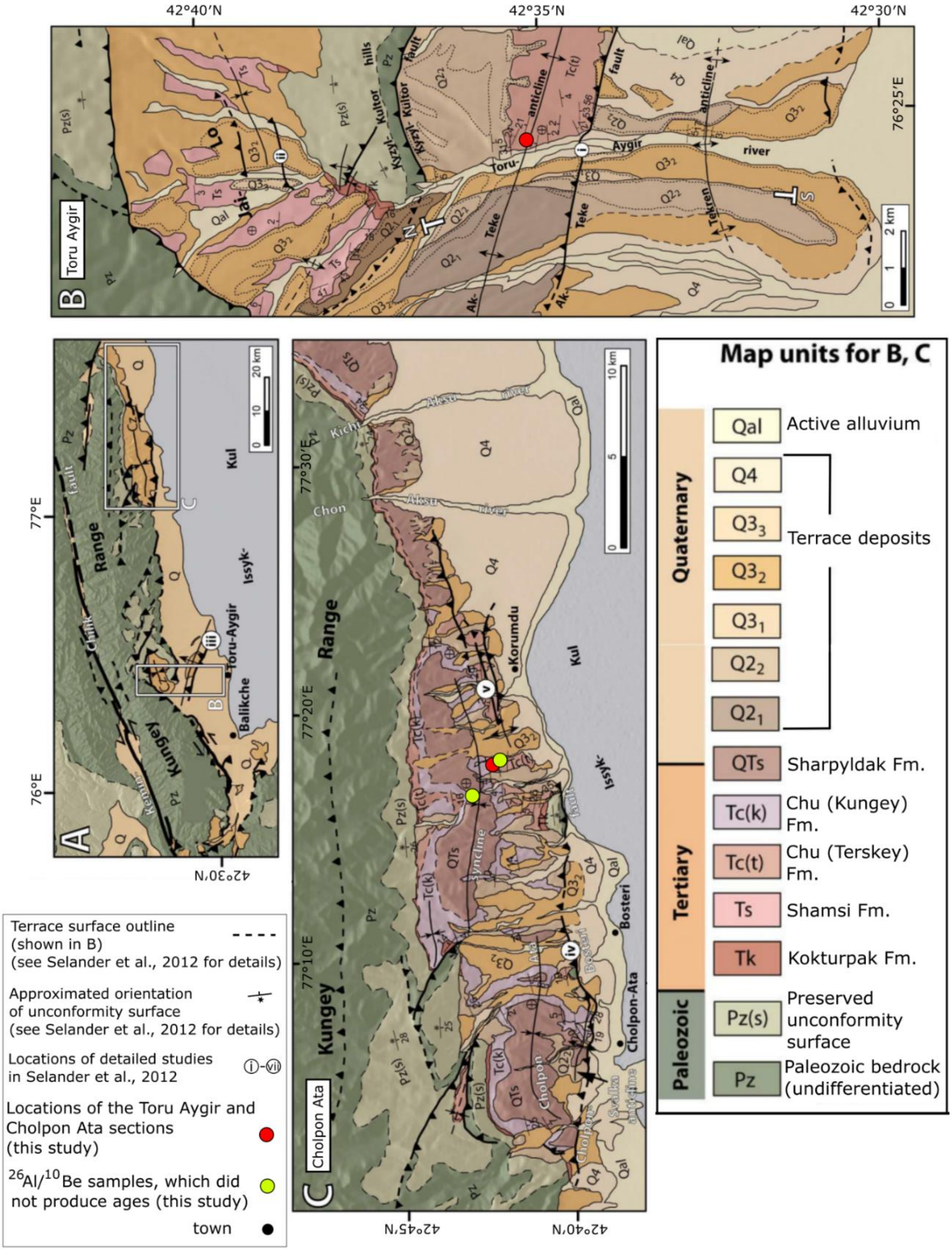

Figure S3.2. Kungey range area (modified from Selander et al., 2012). (A) Geological map of the Kungey range area and positions of the Toru Aygir (B) and Cholpon Ata (C) sections areas.

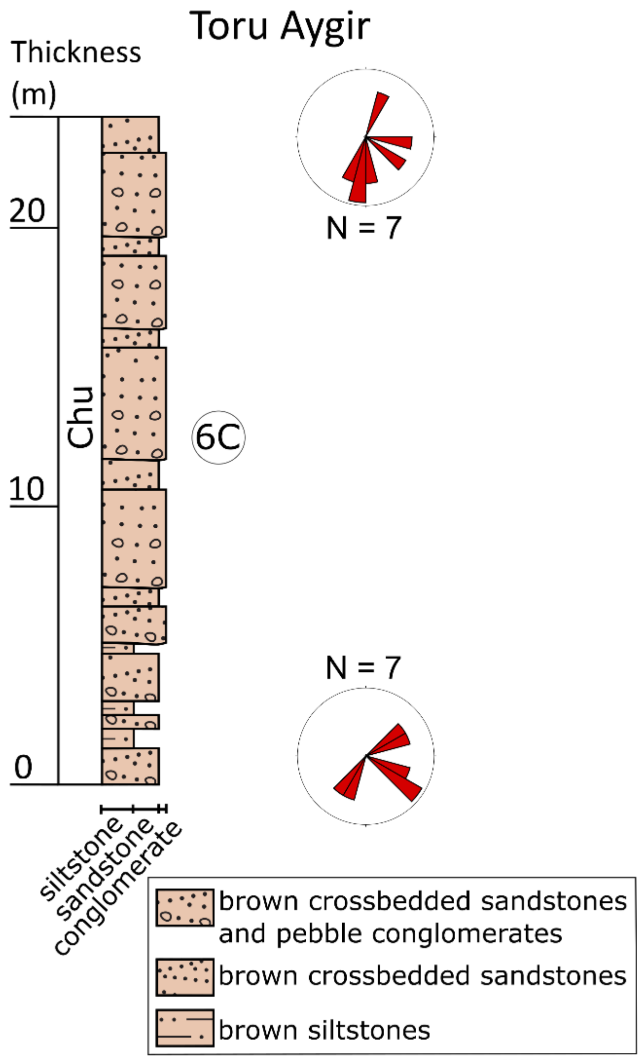

Figure S3.3. The Toru Aygir stratigraphic section (location shown in Supplementary Figure 3.2 and in Figure 3.1 in the main text of Chapter 3) with rose diagrams of paleocurrent flow directions. (6C) shows stratigraphic position of the section photo 3.6C, represented in Figure 3.6 in the main text of Chapter 3.

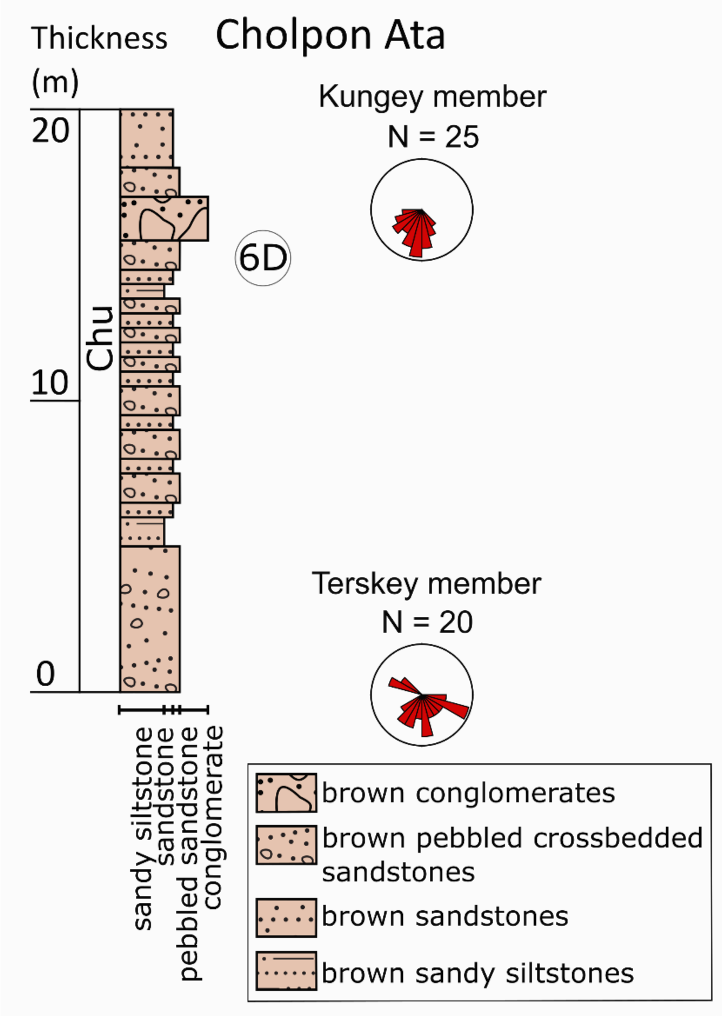

Figure S3.4. The Cholpon Ata stratigraphic section (location shown in Supplementary Figure 3.2 and in Figure 3.1 in the main text of Chapter 3) with rose diagrams of paleocurrent flow directions of the Terskey and Kungey members (see section 3.5.1.4 in Chapter 3 for detailed description). 6D shows stratigraphic position of the section photo 3.6D, represented in Figure 3.6 in the main text of Chapter 3.

Table S3.1 Stable isotope data

Sample ID	Stratigraphic position (m)	Age (Ma)	δ18O, ‰ (PDB)	δ13C, ‰ (PDB)	Material	Group/Unit	Carbonate content (%)
Kaji Say section (42°09'50"N, 77°18'30"E)							
S108	663	2,501	-8,18	-3,42	pedogenic nodule	Sharpyl Dak	23,3
S109	641	2,581	-7,27	-3,16	lacustrine mudstone	Sharpyl Dak	102,4
S106	625,5	2,625	-7,68	0,31	lacustrine mudstone	Upper Chu	43,8
S105	621,5	2,636	-8,21	-0,31	lacustrine mudstone	Upper Chu	37,3
S102	614,5	2,656	-7,98	-5,86	pedogenic nodule	Upper Chu	76,4
269	614	2,658	-7,88	-1,93	lacustrine mudstone	Upper Chu	1,6
S101	608,5	2,673	-8,01	-1,25	lacustrine mudstone	Upper Chu	57,1
S100	574	2,769	-8,99	-3,52	pedogenic nodule	Upper Chu	37,3
245	570	2,780	-9,13	-2,13	lacustrine marl and siltstone	Upper Chu	5,6
243	567	2,788	-10,11	-4,69	lacustrine marl and siltstone	Upper Chu	0,9
16S43	565	2,794	-9,52	-4,96	pedogenic nodule	Upper Chu	57,3
241	563	2,800	-9,63	-2,49	lacustrine marl and siltstone	Upper Chu	7,5
237	560	2,808	-8,66	-2,44	lacustrine marl and siltstone	Upper Chu	40,0
16S41	553	2,828	-9,65	-4,31	pedogenic nodule	Upper Chu	54,6
235	552,5	2,829	-9,54	-3,46	lacustrine marl and siltstone	Upper Chu	19,8
233	550	2,836	-7,89	-1,26	lacustrine mudstone	Upper Chu	8,4
231	549	2,839	-8,98	-2,24	lacustrine marl and siltstone	Upper Chu	12,3
229	547	2,845	-10,81	-2,16	lacustrine marl and siltstone	Upper Chu	5,1
16S40	545	2,850	-9,06	-3,46	pedogenic nodule	Upper Chu	41,7
227	544	2,853	-9,15	-3,58	lacustrine marl and siltstone	Upper Chu	26,6
16S39	542	2,858	-9,38	-3,29	lacustrine marl and siltstone	Upper Chu	51,5
221	538	2,869	-9,14	-4,42	pedogenic nodule	Upper Chu	19,7
219	532	2,886	-8,91	-2,07	lacustrine marl and siltstone	Upper Chu	5,2
16S36	480	3,032	-8,97	-1,58	lacustrine mudstone	Upper Chu	37,1
16S34	473	5,100	-8,82	-0,96	lacustrine mudstone	Upper Chu	61,2
209	472,5	5,102	-9,38	-1,64	lacustrine mudstone	Upper Chu	3,6
16S33	472	5,104	-8,66	-2,00	lacustrine mudstone	Upper Chu	74,7
16S32	456	5,176	-8,79	-5,09	sandstone cement	Upper Chu	72,4
16S30	454,5	5,183	-9,44	-5,37	sandstone cement	Upper Chu	73,8
16S29	430	5,292	-8,96	-6,09	sandstone cement	Lower Chu	29,9
16S27	400	5,423	-10,79	-3,94	pedogenic nodule	Lower Chu	39,2
16S25	396	5,440	-9,85	-3,45	pedogenic nodule	Lower Chu	32,4
16S24	392	5,457	-10,26	-4,25	pedogenic nodule	Lower Chu	31,4
16S23	389	5,470	-10,53	-5,38	pedogenic nodule	Lower Chu	28,7
16S26	375	5,531	-9,18	-6,15	sandstone cement	Lower Chu	28,9
16S22	367	5,566	-9,50	-5,76	pedogenic nodule	Lower Chu	41,3
16S21	350	5,640	-10,48	-4,07	pedogenic nodule	Lower Chu	39,3
16S18	270	5,989	-9,82	-5,97	sandstone cement	Lower Chu	42,9
16S16	220	6,187	-9,71	-4,30	pedogenic nodule	Lower Chu	41,8
16S15	177	6,366	-11,23	-6,32	sandstone cement	Lower Chu	35,3
16S14	134	6,529	-10,26	-5,89	sandstone cement	Lower Chu	87,5
16S13	130	6,543	-11,13	-6,22	sandstone cement	Lower Chu	92,0
16S12	105	6,630	-10,16	-5,88	pedogenic nodule	Lower Chu	36,2
16S10	85,5	6,698	-11,16	-6,71	sandstone cement	Lower Chu	92,6
16S09	85	6,700	-10,84	-6,26	sandstone cement	Lower Chu	104,4
16S08	84	6,703	-11,51	-7,07	sandstone cement	Lower Chu	91,6
S110	74,5	6,736	-11,46	-6,79	sandstone cement	Lower Chu	95,7
16S07	68,5	6,758	-10,73	-5,72	sandstone cement	Lower Chu	37,2
16S06	43	6,851	-10,35	-4,90	pedogenic nodule	Lower Chu	37,2
16S04	30	6,898	-10,82	-4,73	pedogenic nodule	Lower Chu	42,2
16S02	21,5	6,929	-11,12	-5,98	sandstone cement	Lower Chu	51,5
16S03	18	6,942	-11,07	-6,20	sandstone cement	Lower Chu	51,8
16S01	8	6,978	-10,32	-5,52	sandstone cement	Lower Chu	41,5

Ak Terek section (42°14'N, 76°41'40"E)							
A144	471	2,992	-10,11	-7,46	sandstone cement	Chu	54,5
A143	452	3,16	-10,76	-4,34	pedogenic nodule	Chu	41,9
A139	427	3,379	-10,46	-4,15	pedogenic nodule	Chu	37,2
A138	406	3,548	-9,34	-7,10	pedogenic nodule	Chu	48,2
A137	401	3,588	-9,81	-6,39	pedogenic nodule	Chu	36,1
A136	397	3,623	-9,56	-6,57	pedogenic nodule	Chu	35,6
A135	387	3,693	-9,62	-6,03	pedogenic nodule	Chu	58,9
A134	383	3,721	-10,09	-6,67	pedogenic nodule	Chu	43,2
A133	382	3,728	-10,01	-6,51	pedogenic nodule	Chu	45,6
A131	373	3,791	-10,87	-6,53	pedogenic nodule	Chu	40,2
A130	370	3,812	-10,86	-6,59	pedogenic nodule	Chu	38,8
A129	361	3,872	-10,38	-4,73	pedogenic nodule	Chu	37,2
A128	351	3,942	-10,33	-6,18	pedogenic nodule	Chu	44,6
A127	347	3,97	-10,06	-5,48	pedogenic nodule	Chu	32,2
A126	340	4,019	-10,48	-4,86	pedogenic nodule	Chu	21,1
A125	334	4,061	-9,73	-7,58	pedogenic nodule	Chu	43,8
A123	327	4,11	-9,50	-6,69	pedogenic nodule	Chu	48,4
A122	325	4,124	-9,75	-6,65	pedogenic nodule	Chu	36,0
A121	317	4,18	-9,81	-6,43	pedogenic nodule	Chu	55,7
A120	315	4,1915	-10,08	-5,75	pedogenic nodule	Chu	42,9
A119	314	4,196	-9,83	-6,46	pedogenic nodule	Chu	55,2
A118	312	4,205	-9,93	-6,77	pedogenic nodule	Chu	47,3
A117	297	4,2728	-10,04	-5,83	pedogenic nodule	Chu	33,0
A116	294	4,2864	-9,77	-6,64	pedogenic nodule	Chu	47,8
A115	288	4,316	-10,06	-6,06	pedogenic nodule	Chu	25,7
A114	286	4,326	-10,93	-6,79	pedogenic nodule	Chu	37,9
A113	285	4,331	-10,06	-6,10	pedogenic nodule	Chu	35,6
A111	259	4,467	-10,11	-4,96	pedogenic nodule	Chu	23,5
A109	244	4,534	-9,63	-5,65	pedogenic nodule	Chu	45,5
A108	237	4,562	-11,33	-4,67	pedogenic nodule	Chu	17,6
A107	224	4,615	-9,75	-4,40	pedogenic nodule	Chu	36,8
A106	214	4,669	-10,10	-6,15	pedogenic nodule	Chu	56,2
A104	213	4,675	-10,28	-5,90	pedogenic nodule	Chu	42,3
A103	211	4,687	-10,23	-6,31	pedogenic nodule	Chu	50,9
A102	210	4,693	-9,86	-6,14	pedogenic nodule	Chu	39,3
A150	192	4,81	-9,54	-6,82	pedogenic nodule	Chu	52,7
A151	185	4,87	-10,04	-6,32	pedogenic nodule	Chu	53,8
A152	178	4,93	-9,45	-7,52	pedogenic nodule	Chu	52,0
A154	174	4,964	-8,39	-7,07	pedogenic nodule	Chu	54,7
A153	173	4,972	-9,53	-7,26	pedogenic nodule	Chu	40,0
A155	169	5,007	-9,92	-6,07	pedogenic nodule	Chu	65,2
A156	167	5,023	-10,36	-6,07	pedogenic nodule	Chu	31,0
A157	161	5,072	-9,80	-6,37	pedogenic nodule	Chu	62,4
A158	159	5,088	-10,55	-6,75	pedogenic nodule	Chu	50,6
A159	152	5,145	-10,18	-7,41	pedogenic nodule	Chu	48,0
A160	151	5,153	-9,36	-6,93	pedogenic nodule	Chu	46,2
A163	149	5,169	-10,30	-6,77	pedogenic nodule	Chu	18,5
A161	148	5,177	-9,05	-7,16	pedogenic nodule	Chu	46,0
A164	148	5,177	-10,22	-6,48	pedogenic nodule	Chu	42,5
A165	147	5,185	-11,49	-5,04	pedogenic nodule	Chu	28,7
A166	137	5,269	-10,34	-6,46	pedogenic nodule	Chu	48,1
A168	133	5,303	-10,53	-7,18	pedogenic nodule	Chu	43,6
A167	131	5,32	-10,17	-6,68	pedogenic nodule	Chu	41,1
16A10	129	5,337	-10,24	-4,78	sandstone cement	Chu	39,5
A169	128	5,345	-10,20	-7,26	pedogenic nodule	Chu	50,0
A170	126	5,362	-9,74	-6,83	pedogenic nodule	Chu	50,6
16A09	95	5,622	-9,74	-5,48	sandstone cement	Chu	35,6
A171	91	5,656	-10,79	-6,48	pedogenic nodule	Chu	47,2
16A08	87	5,69	-10,10	-4,70	sandstone cement	Chu	23,2
A172	83	5,724	-10,66	-5,54	pedogenic nodule	Chu	62,5
A173	81	5,741	-9,05	-5,85	pedogenic nodule	Chu	29,3
A174	79	5,758	-9,45	-6,07	pedogenic nodule	Chu	38,7
A175	76	5,783	-10,21	-5,68	pedogenic nodule	Chu	36,3
A176	71	5,825	-10,53	-6,04	pedogenic nodule	Chu	31,6
A177	69	5,842	-10,68	-5,28	pedogenic nodule	Chu	26,6
A178	60	5,918	-10,73	-7,22	pedogenic nodule	Chu	45,8
A179	42	6,06	-10,04	-5,93	pedogenic nodule	Chu	33,8
16A01	8	6,262	-10,82	-4,19	sandstone cement	Chu	33,1
A181	6	6,272	-11,23	-4,64	pedogenic nodule	Chu	26,9

Jeti Oguz section (Data are from Macaulay et al., 2016. Age model is from Roud et al., 2021)						
JTP82	990	8,500	-13,8	-7,3	pedogenic	Shamsi
JTP81	972	8,771	-13,5	-7,2	pedogenic	Shamsi
JTP80	941	9,164	-13,0	-8,2	pedogenic	Shamsi
JTP79	916	9,481	-14,1	-7,1	pedogenic	Shamsi
JTP78	885	9,873	-13,7	-7,0	pedogenic	Shamsi
JTP77	834	10,507	-12,1	-6,6	pedogenic	Shamsi
JTP75	760	11,427	-14,2	-7,2	pedogenic	Shamsi
JTP74	730	11,800	-12,7	-6,0	pedogenic	Shamsi
JTP68	569	14,482	-15,3	-6,0	pedogenic	Shamsi
JTP67	544	14,988	-12,5	-6,6	pedogenic	Shamsi
JTP62	449	16,964	-12,5	-6,5	pedogenic	Shamsi
JTP57	245	19,398	-11,4	-6,0	pedogenic	Shamsi
JTP56	224	19,599	-12,3	-7,2	pedogenic	Shamsi
JTP55	186	19,963	-12,5	-5,9	pedogenic	Shamsi
JTP54	144	20,510	-13,4	-5,1	pedogenic	Shamsi
JTP52	58	21,698	-10,4	-5,0	pedogenic	Shamsi
JTP51	37	21,966	-9,3	-3,0	pedogenic	Shamsi
JTP50	2	22,400	-9,0	-5,8	pedogenic	Shamsi
Chon Kyzylsu section (Data are from Macaulay et al., 2016. Age model is from Roud et al., 2021)						
CKP41	947	7,63	-11,7	-7,2	pedogenic	Shamsi
CKP35	916	7,95	-11,5	-8,2	pedogenic	Shamsi
CKP34	855	8,54	-12,5	-8,2	pedogenic	Shamsi
CKP33	806	9,05	-13,7	-6,5	pedogenic	Shamsi
CKP32	769	9,42	-12,7	-6,8	pedogenic	Shamsi
CKP31	744	9,66	-12,6	-6,2	pedogenic	Shamsi
CKP30	707	10,04	-12,5	-8,2	pedogenic	Shamsi
CKP29	703	10,09	-12,8	-8,3	pedogenic	Shamsi
CKP28	657	10,57	-13,5	-8,2	pedogenic	Shamsi
CKP27	628	10,87	-11,3	-7,8	pedogenic	Shamsi
CKP26	613	11,03	-11	-7	pedogenic	Shamsi
CKP25	584	11,35	-12,5	-6,1	pedogenic	Shamsi
CKP24	557	11,65	-11,2	-5,4	pedogenic	Shamsi
CKP23	521	12,05	-13	-8,6	pedogenic	Shamsi
CKP22	468	12,63	-11,1	-7,9	pedogenic	Shamsi
CKP21	440	12,94	-12,7	-7,2	pedogenic	Shamsi
CKP20	427	13,08	-12,4	-6,6	pedogenic	Shamsi
CKP19	414	13,22	-12,4	-6,3	pedogenic	Shamsi
CKP18	385	13,54	-11,8	-6,7	pedogenic	Shamsi
CKP17	375	13,65	-12,9	-6,9	pedogenic	Shamsi
CKP15	346	13,97	-12,8	-6,4	pedogenic	Shamsi
CKP14	331	14,13	-12,7	-6,1	pedogenic	Shamsi
CKP13	325	14,19	-12,6	-5,4	pedogenic	Shamsi
CKP12	316	14,29	-12,2	-6,8	pedogenic	Shamsi
CKP11	293	14,54	-13	-6,8	pedogenic	Shamsi
CKP10	254	14,94	-13	-9,4	pedogenic	Shamsi
CKP09	233	15,13	-13,4	-7,7	pedogenic	Shamsi
CKP08	214	15,30	-11,8	-8,1	pedogenic	Shamsi
CKP06	171	15,70	-12,4	-6,7	pedogenic	Shamsi
CKP07	159	15,81	-12,3	-6	pedogenic	Shamsi
CKP05	128	16,12	-11,6	-5,7	pedogenic	Shamsi
CKP04	96	16,48	-12,7	-7,5	pedogenic	Shamsi
CKP03	36	17,37	-11,9	-4,3	pedogenic	Shamsi
CKP02	18	17,58	-11,6	-4,4	pedogenic	Shamsi
CKP01	8	17,70	-10,8	-4,8	pedogenic	Shamsi

Table S3.2 $^{26}Al/^{10}Be$ data

Locality	Sample ID	Lab ID	ANSTO Be Cathode ID	ANSTO Al Cathode ID	Total Qtz [g]	10Be/9Be (± 1s) [10^-15]	Blank 10Be/9Be (± 1s) [10^-15]	Blank IDs	Cor. 10Be/9Be (± 1s) [10^-15]	9Be Spike [ug]	10Be 07KNSTD (± 1s) [10^3 atoms/g]	26Al/27Al (± 1s) [10^-15]	Blank 26Al/27Al (± 1s) [10^-15]	Blank IDs	Cor. 26Al/27Al (± 1s) [10^-15]	27Al native [ug/g]	26Al (± 1s) KNSTD [10^3 atoms/g]
Ak-Terek	AKT-Q-01	UOW149	Be1053	Al1128	40,020	52.33 (2.01)	0.37 (0.17)	UOW Be 14&15	51.96 (2.01)	288,5	**25.03 (0.99)**	69.8 (5.06)	0.56 (0.4)	UOW Al 08&09	69.24 (5.08)	73,2	**113.15 (9.45)**
lower	AKT-Q-05	UOW579	XBE0733	XAL0182	55,244	98.4 (2.3)	Boron correction*	-	87.14 (2.37)	366,7	**38.65 (1.06)**	64.04 (4.78)	1.41 (1)	UOW Al 33&34	62.63 (4.89)	155,3	**217.02 (19.03)**
Sharpyl Dak	AKT-Q-07	UOW150	Be1054	AL1129	40,012	77.47 (2.14)	0.37 (0.17)	UOW Be 14&16	77.1 (2.14)	288,8	**37.19 (1.08)**	65.08 (5.63)	0.56 (0.4)	UOW Al 08&09	64.52 (5.65)	103,1	**148.52 (14.3)**
42°14'13.30"N	AKT-Q-08	UOW151	Be1055	AL1130/31	100,001	125.7 (3.2)	0.37 (0.17)	UOW Be 14&17	125.33 (3.2)	288,6	**24.17 (0.65)**	50.83 (3.33)	0.56 (0.4)	UOW Al 08&09	50.26 (3.35)	95,8	**107.52 (8.36)**
76°43'39.50"E	AKT-Q-sand	UOW152	Be1056	AL1132	90,010	163.6 (4.57)	0.37 (0.17)	UOW Be 14&19	163.23 (4.57)	287,9	**34.88 (1.02)**	52.89 (4.71)	0.56 (0.4)	UOW Al 08&09	52.32 (4.72)	97,0	**113.28 (11.19)**
Ak-Terek	AKT-U-02	UOW153	Be1057	AL1133/34	70,004	83.59 (3.8)	0.37 (0.17)	UOW Be 14&20	83.22 (3.8)	288,4	**22.91 (1.07)**	10.17 (2.55)	0.56 (0.4)	UOW Al 08&09	9.61 (2.58)	367,1	**78.7 (21.39)**
uppermost Chu	AKT-U-04	UOW154	Be1058	AL1135	40,022	17.51 (0.84)	0.37 (0.17)	UOW Be 14&21	17.14 (0.86)	288,2	**8.25 (0.42)**	44.63 (3.99)	0.56 (0.4)	UOW Al 08&09	44.07 (4.01)	47,3	**46.57 (4.63)**
42°14'19.80"N	AKT-U-06	UOW580	XBE0734	XAL0183	27,761	26.48 (0.95)	Boron correction*	-	16.94 (1.07)	367,3	**14.98 (0.95)**	26.19 (2.7)	1.41 (1)	UOW Al 33&34	24.78 (2.88)	81,1	**44.87 (5.52)**
76°42'39.36"E	AKT-U-07	UOW155	Be1059	AL1136/37	90,010	35.25 (1.31)	0.37 (0.17)	UOW Be 14&22	34.88 (1.32)	289,1	**7.49 (0.29)**	21.66 (3.01)	0.56 (0.4)	UOW Al 08&09	21.1 (3.04)	100,8	**47.46 (7.09)**
	AKT-U-08	UOW581	XBE0735	XAL0184	47,563	138.11 (3.58)	Boron correction*	-	128.73 (3.61)	366,1	**66.21 (1.87)**	34.05 (3.39)	1.41 (1)	UOW Al 33&34	32.64 (3.54)	212,7	**154.94 (17.89)**
	AKT-U-sand	UOW156	Be1060	AL1138/39	40,033	64.36 (2.01)	0.37 (0.17)	UOW Be 14&25	63.99 (2.02)	288,4	**30.8 (1.01)**	19.54 (1.99)	0.56 (0.4)	UOW Al 08&09	18.98 (2.03)	135,4	**57.34 (6.56)**
Kaji Say	PET-QTS-L-01	UOW157	Be1061	AL1140/41	95,014	671.7 (17.48)	0.37 (0.17)	UOW Be 14&26	671.33 (17.48)	289,0	**136.43 (3.75)**	204.61 (8.88)	0.56 (0.4)	UOW Al 08&09	204.04 (8.89)	79,1	**360.36 (21.31)**
uppermost	PET-QTS-L-06	UOW158	Be1062	AL1142/43	80,088	340.9 (8.5)	0.37 (0.17)	UOW Be 14&27	340.53 (8.5)	289,1	**82.13 (2.17)**	99.04 (5.76)	0.56 (0.4)	UOW Al 08&09	98.47 (5.77)	109,2	**240.11 (17.04)**
Sharpyl Dak	PET-QTS-L-07	UOW159	Be1063	AL1144	40,028	48.99 (1.63)	0.37 (0.17)	UOW Be 14&28	48.62 (1.64)	288,8	**23.44 (0.81)**	53.25 (5.35)	0.56 (0.4)	UOW Al 08&09	52.68 (5.37)	76,8	**90.29 (9.89)**
42°10'38.91"N	PET-QTS-L-08	UOW160	Be1064	AL1145/46	100,029	220.5 (5.76)	0.37 (0.17)	UOW Be 14&29	220.13 (5.76)	288,8	**42.47 (1.17)**	63.47 (4.59)	0.56 (0.4)	UOW Al 08&09	62.9 (4.61)	94,3	**132.42 (11.06)**
77°18'3.76"E	PET-QTS-L-sanc	UOW161	Be1065	AL1147/48	85,024	406.4 (10.58)	0.37 (0.17)	UOW Be 14&30	406.03 (10.58)	288,4	**92.04 (2.53)**	159.03 (6.9)	0.56 (0.4)	UOW Al 08&09	158.47 (6.91)	76,9	**272.15 (16.11)**
Kaji Say	PET-QTS-PIT-01	UOW162	Be1066	AL1149/50	60,007	261.5 (6.89)	0.37 (0.17)	UOW Be 14&31	261.13 (6.89)	289,5	**84.19 (2.34)**	51.83 (3.74)	0.56 (0.4)	UOW Al 08&09	51.26 (3.76)	177,2	**202.81 (16.95)**
Chu-Sharpyl Dak	PET-QTS-PIT-03	UOW163	Be1067	AL1151/52	40,041	244.3 (5.83)	0.37 (0.17)	UOW Be 14&32	243.93 (5.83)	288,1	**117.28 (2.99)**	61.79 (3.82)	0.56 (0.4)	UOW Al 08&09	61.22 (3.84)	171,0	**233.65 (17.39)**
transition	PET-QTS-PIT-04	UOW164	Be1068	AL1153/54	35,002	485.1 (12.1)	0.37 (0.17)	UOW Be 14&33	484.73 (12.1)	288,2	**266.75 (7.06)**	152.16 (6.51)	0.56 (0.4)	UOW Al 08&09	151.6 (6.52)	157,1	**531.47 (31.22)**
42°10'26.21"N	PET-QTS-PIT-05	UOW165	Be1069	AL1155/56	40,004	87.79 (2.4)	0.37 (0.17)	UOW Be 14&34	87.42 (2.41)	288,9	**42.19 (1.22)**	29.02 (2.54)	0.56 (0.4)	UOW Al 08&09	28.46 (2.57)	205,0	**130.2 (12.87)**
77°17'9.55"E	PET-QTS-PIT-sa	UOW166	Be1070	Al1157/58	75,010	446.4 (11.62)	0.37 (0.17)	UOW Be 14&35	446.03 (11.62)	288,9	**114.78 (3.16)**	101.46 (6.53)	0.56 (0.4)	UOW Al 08&09	100.89 (6.54)	100,9	**227.15 (17.31)**
Kaji Say	PET-L-17-01	UOW677	XBE0815	XAL0325	61,153	80.22 (1.81)	0.88 (0.22)	UOW Be 66&67	79.35 (1.82)	189,4	**16.43 (0.41)**	36.02 (3.37)	2.03 (1.56)	UOW Al 47&48	33.98 (3.72)	77,2	**58.53 (6.81)**
lower Chu	PET-L-17-03	UOW678	XBE0816	XAL0326	7,155	35.98 (2.89)	0.88 (0.22)	UOW Be 66&68	35.1 (2.9)	130,1	**42.63 (3.54)**	13.99 (2.92)	2.03 (1.56)	UOW Al 47&48	11.96 (3.31)	108,4	**28.94 (8.09)**
42°9'18.69"N	PET-L-17-04	UOW679	XBE0817	XAL0327	3,665	10.14 (1.01)	0.88 (0.22)	UOW Be 66&69	9.26 (1.03)	103,7	**17.52 (1.96)**	3.43 (1.21)	2.03 (1.56)	UOW Al 47&48	1.4 (1.97)	265,2	**8.26 (11.69)**
77°18'36.62"E																	
Kaji Say	PET-U-01	UOW573	XBE0726	XAL0175	99,489	55.26 (1.75)	Boron correction*	-	52.49 (1.79)	365,1	**12.87 (0.44)**	13.41 (1.69)	1.41 (1)	UOW Al 33&34	12 (1.96)	71,8	**19.23 (3.24)**
lower Chu	PET-U-03	UOW574	XBE0728	XAL0280	12,421	24.16 (1.29)	Boron correction*	-	12.16 (1.42)	365,8	**23.94 (2.8)**	20.4 (3.5)	1.41 (1)	UOW Al 33&34	18.99 (3.64)	153,1	**64.89 (12.71)**
42°9'19.31"N	PET-U-06	UOW575	XBE0729	XAL0178	13,520	11.92 (3.32)	Boron correction*	-	2.98 (3.36)	366,6	**5.4 (6.09)**	13.72 (1.82)	1.41 (1)	UOW Al 33&34	12.31 (2.08)	97,9	**26.89 (4.66)**
77°18'36.39"E																	
Jergalan	JGL17-1-01	UOW566	XBE0719	XAL0168	26,400	7.35 (0.64)	Boron correction*	-	3.21 (0.72)	366,2	**2.97 (0.67)**	4.48 (1)	1.41 (1)	UOW Al 33&34	3.07 (1.42)	141,6	**9.71 (4.49)**
Chu-Sharpyl Dak	JGL17-1-03	UOW568	XBE0721	XAL0170	70,775	67.61 (2.16)	Boron correction*	-	63.35 (2.18)	364,9	**21.83 (0.76)**	8.51 (1.64)	1.41 (1)	UOW Al 33&34	7.1 (1.92)	131,0	**20.76 (5.67)**
transition	JGL17-1-06	UOW571	XBE0724	XAL0173	87,871	21.25 (0.95)	Boron correction*	-	19.3 (1.05)	366,5	**5.38 (0.29)**	3.48 (0.97)	1.41 (1)	UOW Al 33&34	2.07 (1.39)	68,6	**3.17 (2.13)**
42°39'53.28"N	JGL17-1-07	UOW572	XBE0725	XAL0174	99,226	27.01 (0.98)	Boron correction*	-	24.44 (1.02)	365,8	**6.02 (0.25)**	3.58 (0.92)	1.41 (1)	UOW Al 33&34	2.17 (1.36)	74,6	**3.62 (2.27)**
78°57'59.35"E																	
Jergalan	JGL-2-02	UOW673	XBE0811	XAL0321	34,866	5.47 (0.52)	0.88 (0.22)	UOW Be 66&69	4.59 (0.56)	190,6	**1.68 (0.21)**	2.33 (0.82)	2.03 (1.56)	UOW Al 47&48	0.3 (1.76)	82,1	**0.54 (3.23)**
Chu	JGL-2-03	UOW674	XBE0812	XAL0322	79,477	32.67 (1.18)	0.88 (0.22)	UOW Be 66&69	31.79 (1.2)	189,8	**5.07 (0.2)**	2.49 (0.83)	2.03 (1.56)	UOW Al 47&48	0.46 (1.77)	107,3	**1.1 (4.23)**
42°39'27.24"N	JGL-2-04	UOW675	XBE0813	XAL0323	92,955	25.02 (1.07)	0.88 (0.22)	UOW Be 66&69	24.14 (1.09)	191,0	**3.32 (0.15)**	2 (1)	2.03 (1.56)	UOW Al 47&48	-0.03 (1.85)	81,1	**-0.06 (-3.35)**
78°57'40.68"E	JGL-2-07	UOW676	XBE0814	XAL0324	53,246	10.68 (0.7)	0.88 (0.22)	UOW Be 66&69	9.8 (0.74)	190,0	**2.34 (0.18)**	1.2 (0.69)	2.03 (1.56)	UOW Al 47&48	-0.84 (1.7)	80,8	**-1.51 (-3.07)**
Cholpon Ata	CA17-1-02	UOW668	XBE0806	XAL0316	4,638	4.48 (0.77)	0.88 (0.22)	UOW Be 66&69	3.6 (0.8)	131,5	**6.82 (1.52)**	8.81 (2.08)	2.03 (1.56)	UOW Al 47&48	6.78 (2.6)	274,1	**41.51 (15.98)**
lower	CA17-1-03	UOW669	XBE0807	XAL0317	43,260	31.08 (1.22)	0.88 (0.22)	UOW Be 66&69	30.2 (1.24)	189,9	**8.86 (0.38)**	33.85 (3.32)	2.03 (1.56)	UOW Al 47&48	31.82 (3.67)	56,3	**40.01 (4.88)**
Sharpyl Dak	CA17-1-05	UOW670	XBE0808	XAL0318	25,363	22.8 (1.09)	0.88 (0.22)	UOW Be 66&69	21.92 (1.11)	155,7	**9 (0.46)**	25.36 (2.78)	2.03 (1.56)	UOW Al 47&48	23.33 (3.19)	88,4	**46.04 (6.56)**
42°43'12.53"N	CA17-1-06	UOW671	XBE0809	XAL0319	81,788	87.52 (2.18)	0.88 (0.22)	UOW Be 66&69	86.64 (2.19)	190,2	**13.47 (0.37)**	47.16 (4.07)	2.03 (1.56)	UOW Al 47&48	45.12 (4.36)	49,9	**50.28 (5.26)**
77°16'41.52"E	CA17-1-07	UOW672	XBE0810	XAL0320	11,672	9.88 (0.75)	0.88 (0.22)	UOW Be 66&69	9 (0.78)	155,6	**8.02 (0.7)**	23.78 (3.18)	2.03 (1.56)	UOW Al 47&48	21.74 (3.54)	89,5	**43.45 (7.28)**
	CA17-2-sand	UOW576	XBE0730	XAL0179	55,731	37.39 (1.65)	Boron correction*	-	21.46 (1.8)	367,3	**9.45 (0.79)**	20.91 (2.23)	1.41 (1)	UOW Al 33&34	19.5 (2.44)	80,5	**35.03 (4.61)**
Cholpon Ata	CA17-6-01	UOW761	XBE0918	XAL0409/10	50,116	25.55 (0.9)	1.38 (0.19)	UOW Be 76	24.17 (0.92)	217,4	**7.01 (0.28)**	29.03 (2.86)	2.61 (1.31)	UOW Al 57	26.42 (3.14)	74,1	**43.68 (5.48)**
upper Chu	CA17-6-02	UOW762	XBE0919	XAL0411/12	50,118	54.76 (1.47)	1.38 (0.19)	UOW Be 76	53.38 (1.48)	217,1	**15.45 (0.46)**	6.91 (1.2)	2.61 (1.31)	UOW Al 57	4.31 (1.78)	489,6	**47.05 (19.49)**
42°42'15.82"N	CA17-6-03	UOW763	XBE0920	XAL0413/14	43,038	34.78 (1.09)	1.38 (0.19)	UOW Be 76	33.4 (1.11)	215,3	**11.16 (0.39)**	22.63 (2.22)	2.61 (1.31)	UOW Al 57	20.02 (2.57)	124,6	**55.67 (7.5)**
77°18'2.79"E	CA17-6-05	UOW765	XBE0922	XAL0417/18	45,994	26.41 (0.94)	1.38 (0.19)	UOW Be 76	25.03 (0.96)	216,2	**7.86 (0.31)**	21.83 (1.73)	2.61 (1.31)	UOW Al 57	19.22 (2.16)	110,6	**47.44 (5.67)**
	CA17-6-06	UOW766	XBE0923	XAL0419/20	65,324	31.75 (1.03)	1.38 (0.19)	UOW Be 76	30.37 (1.04)	214,7	**6.67 (0.24)**	29.81 (2.65)	2.61 (1.31)	UOW Al 57	27.2 (2.95)	81,8	**49.64 (5.74)**
	CA17-6-07	UOW767	XBE0924	XAL0421/22	30,040	17.99 (0.63)	1.38 (0.19)	UOW Be 76	16.61 (0.65)	215,3	**7.96 (0.32)**	31.3 (2.48)	2.61 (1.31)	UOW Al 57	28.69 (2.81)	67,8	**43.39 (4.58)**
	CA17-7-sand	UOW577	XBE0731	XAL0180	55,248	31.61 (1.26)	Boron correction*	-	20.46 (1.38)	366,2	**9.06 (0.61)**	28.19 (2.33)	1.41 (1)	UOW Al 33&34	26.78 (2.53)	83,8	**50.1 (5.15)**

* These samples had elevated boron levels and a boron correction factor was applied to the raw AMS data that also accouted for blank correction. The correction factor ranged between 0.25 and 0.95 with a median of 0.77. Samples were processed as one batch and analysed during the same AMS run. A boron correction factor was determined from the correlation between Be-10 and B-10 count rates for procedural blanks, taking the lowest Be-10 blank values as representative for B-10 leakage into the Be-10

Supplementary paleocurrent and clast count data

Kaji Say

<table>
<tr><th colspan="5">Paleocurrent data</th></tr>
<tr><td>Rose diagram in Fig.3.2</td><td>Stratigraphic position (m)</td><td>Bedding (dip direction and dip angle)</td><td>Cross-beds (dip direction and dip angle)</td><td>Imbricates (dip direction and dip angle)</td></tr>
<tr><td rowspan="4">Lower Chu 0-100 m</td><td>20</td><td>333 19</td><td>345 35
5 31
355 43
5 35
15 40
0 33
345 30
0 30</td><td></td></tr>
<tr><td>72</td><td>355 21</td><td>355 30
5 30
5 28
350 30</td><td></td></tr>
<tr><td>82</td><td>345 21</td><td>310 40
325 40
285 30
260 35
335 42</td><td></td></tr>
<tr><td>95</td><td>345 21</td><td>305 28
315 28
290 25
315 33</td><td></td></tr>
<tr><td>Lower Chu 100-200 m</td><td>144</td><td>345 21</td><td></td><td>125 35
95 20
190 40
110 28
80 55
95 40
110 43
75 40
105 23
130 50
150 18
135 25
100 40
135 20
115 20
160 25
60 35
30 40
90 35
75 30</td></tr>
<tr><td rowspan="2">Lower Chu 200-300 m</td><td>265</td><td>15 64</td><td rowspan="2">355 60
15 85
10 75
15 85
0 87
0 52
5 72
5 67</td><td rowspan="2"></td></tr>
<tr><td>280</td><td>15 64</td></tr>
</table>

<table>
<tr><th colspan="5">Kaji Say</th></tr>
<tr><th colspan="5">Paleocurrent data</th></tr>
<tr><th>Rose diagram in Fig.3.2</th><th>Stratigraphic position (m)</th><th>Bedding (dip direction and dip angle)</th><th>Cross-beds (dip direction and dip angle)</th><th>Imbricates (dip direction and dip angle)</th></tr>
<tr><td rowspan="5">Upper Chu</td><td>457</td><td>10 72</td><td rowspan="4">355 75
65 36
25 38
335 60
335 28
35 22
95 25</td><td rowspan="4"></td></tr>
<tr><td>520</td><td>7 19</td></tr>
<tr><td>570</td><td>50 35</td></tr>
<tr><td>632</td><td>10 16</td></tr>
<tr><td>598</td><td>15 30</td><td></td><td>65 45
205 45
100 50
10 50
35 35
175 30
190 30
225 55
10 45
75 30
120 50
80 55
50 45
70 40
88 50
75 20
190 40
340 20</td></tr>
<tr><td rowspan="2">Sharpyl Dak</td><td>650</td><td>10 16</td><td>315 20
315 22
325 35
120 20</td><td></td></tr>
<tr><td>712</td><td>0 20</td><td></td><td>100 40
105 45
175 25
160 50
75 35
175 35
105 40
125 40
110 28
105 10
145 50
205 35
125 20
145 45
65 50
210 35
175 45
125 42
90 50
195 35</td></tr>
</table>

Kaji Say

Clast count		
Stratigraphic position (m)	**Type of rock**	**Number of clasts**
85	Red granite	35
	Volcanic rocks	20
	Metamorphic sandstone	19
	White granite	14
	Shale	10
	Quartz	3
	Sandstone	3
	Quartzite	2
144	Red granite	69
	White granite	14
	Volcanic rocks	14
	Metamorphic sandstone	13
	Quartzite	1
	Quartz	1
320	Red porphyry with quartz phenocrysts	70
	Red granite	23
	White granite	4
	Volcanic rocks	5
	Sandstone	3
	Quartzite	2
	Quartz	2
411	White granite	55
	Red granite	27
	Red porphyry with quartz phenocrysts	8
	Volcanic rocks	7
	Metamorphic sandstone	5
	Quartzite	1

Ak Terek

Clast count		
Stratigraphic position (m)	**Type of rock**	**Number of clasts**
3	White granite	41
	Red granite	28
	Metamorphic sandstones	22
	Volcanic rocks	10
	Quartzite	2
	Sandstone	2
	Quartz	1

Ak Terek

Paleocurrent data				
Rose diagram in Fig.3.5	**Stratigraphic position** (m)	**Bedding** (dip direction and dip angle)	**Cross-beds** (dip direction and dip angle)	**Imbricates** (dip direction and dip angle)
Chu 0-100 m	36	30 20		210 30 315 23 275 30 45 40 130 30 110 45 345 30 235 25 315 10 350 27 355 29 200 50 285 40 245 20 225 42 245 50 275 25 280 43 280 43 255 55 230 20
	40	25 20	30 60 35 30 75 30	
Chu 100-200 m	140-160	20 10	285 15 225 10 185 85 20 30	
		345 10	30 35 30 25 350 28 10 28 35 20	
Chu 200-300 m	200-260	40 15	15 35	
		5 8	70 30 45 40 55 30 340 30 30 25 75 35 15 45 42 32	
Chu 300-400 m	300-350	5 8	15 25 330 25 10 20 25 35 150 35 10 28 355 20 335 20 330 20 5 28 115 25 340 30 30 20 45 32 30 30	
Chu 400-500 m	450-500	5 8	305 22 95 30 350 40 300 25 285 25	

Jergalan			
Paleocurrent data			
Position	**Bedding** (dip direction and dip angle)	**Cross-beds** (dip direction and dip angle)	**Imbricates** (dip direction and dip angle)
Position of the JGL17 sample 42°39'53.28"N 78°57'59.35"E	330 10		25 42
			30 35
			5 30
			35 55
			5 50
			25 50
			35 55
			35 52
			45 37
			20 50
			35 41
			10 55
			15 48
			55 48
			40 35
			25 30
			50 55
			40 55
			30 48
			10 35

Jergalan		
Clast count		
Position	**Type of rock**	**Number of clasts**
Position of the JGL17 sample 42°39'53.28"N 78°57'59.35"E	Clastic sedimentary rocks	35
	Volcanic rocks	26
	Granite	20
	Quzrtzite	16
	Quartz	8

Toru Aygir			
Paleocurrent data			
Stratigraphic position (m)	**Bedding** (dip direction and dip angle)	**Cross-beds** (dip direction and dip angle)	**Imbricates** (dip direction and dip angle)
1	0 5	60 20 48 30 233 9 210 15 130 45 100 18 95 9	
23	0 5	185 32 80 15 215 20 165 22 15 12 195 30 120 18	

Toru Aygir		
Clast count		
Stratigraphic position (m)	**Type of rock**	**Number of clasts**
23	Subvolcanic rocks with plagioclase phenocrysts Granite Mafic igneous rocks Volcanic rocks	88 11 4 4

Cholpon Ata		
Clast count		
Unit and stratigraphic position (m)	**Type of rock**	**Number of clasts**
Terskey member; 0	Granite Volcanic rocks Phyllite Subvolcanic rocks with plagioclase phenocrysts Clastic sedimentary rocks	55 36 20 15 3

Cholpon Ata				
Paleocurrent data				
Unit	**Stratigraphic position** (m)	**Bedding** (dip direction and dip angle)	**Cross-beds** (dip direction and dip angle)	**Imbricates** (dip direction and dip angle)
Terskey member	0 (just below the section)	45 16		80 25 15 55 35 45 325 25 50 33 345 40 25 42 0 35 35 48 10 52 315 25 300 47 315 40 320 45 300 45 30 60 15 33 95 25 100 48 15 30
Kungey member	10-15	45 16	205 10 245 5 185 28 275 8 310 15 240 20 75 11 250 17 250 22 100 3	
	17	50 7		0 37 5 47 12 40 10 30 25 45 355 27 20 25 15 30 30 35 330 30 355 45 5 17 30 20 5 20 10 20

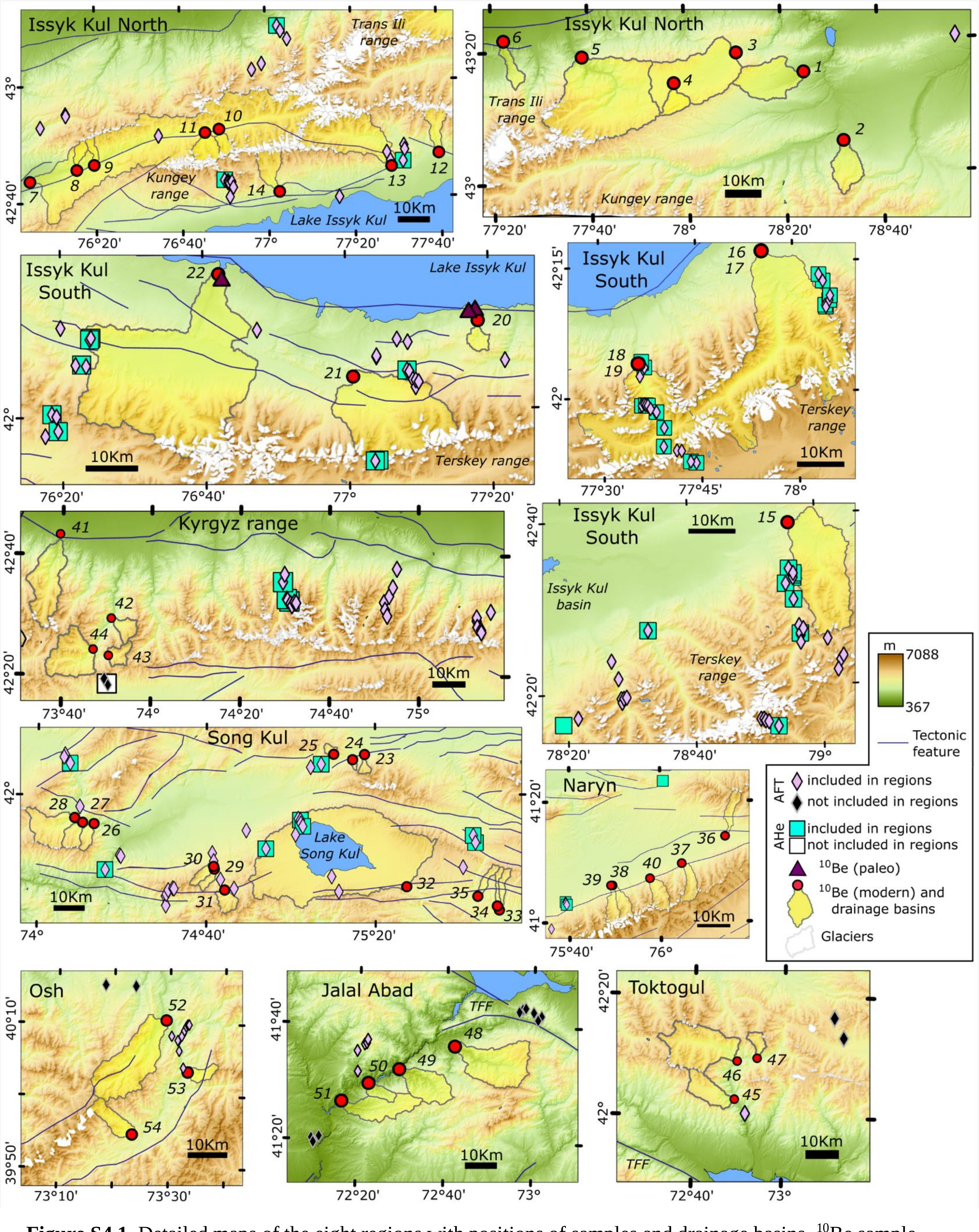

Figure S4.1. Detailed maps of the eight regions with positions of samples and drainage basins. ^{10}Be sample numbers 1-54 correspond to ID numbers of samples in Supplementary Table S5. TFF is Talas-Fergana Fault. Tectonic features are taken from Mohadjer et al. (2016).

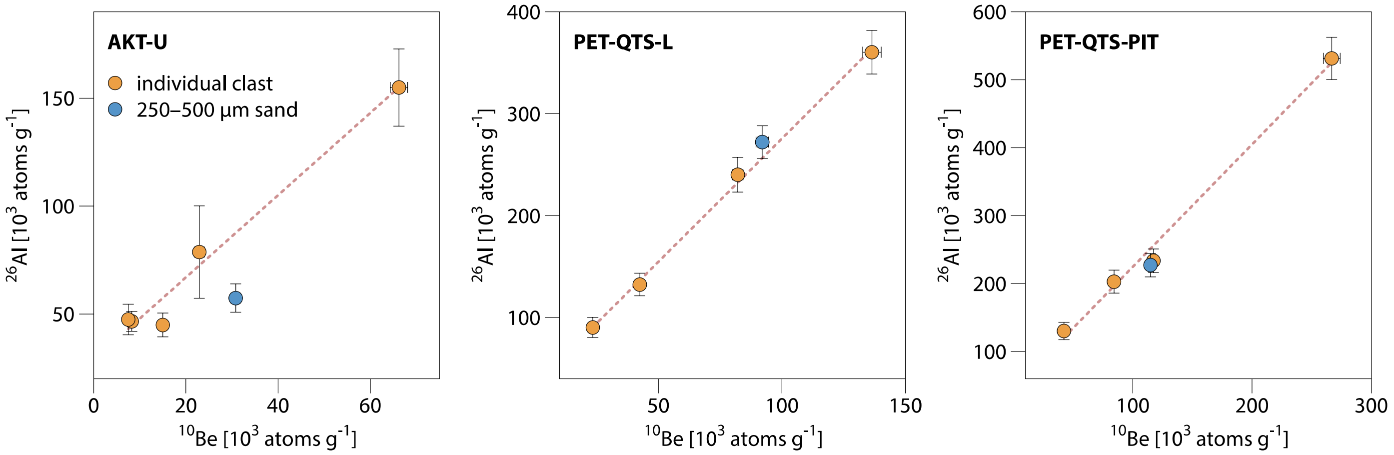

Figure S4.2. ^{26}Al vs. ^{10}Be concentrations in individual clast and amalgamated sand samples collected from Ak Terek (AKT) and Kaji Say (PET-QTS) localities, in the proximity of lake Issyk-Kul (see Chapter 3 for further details).

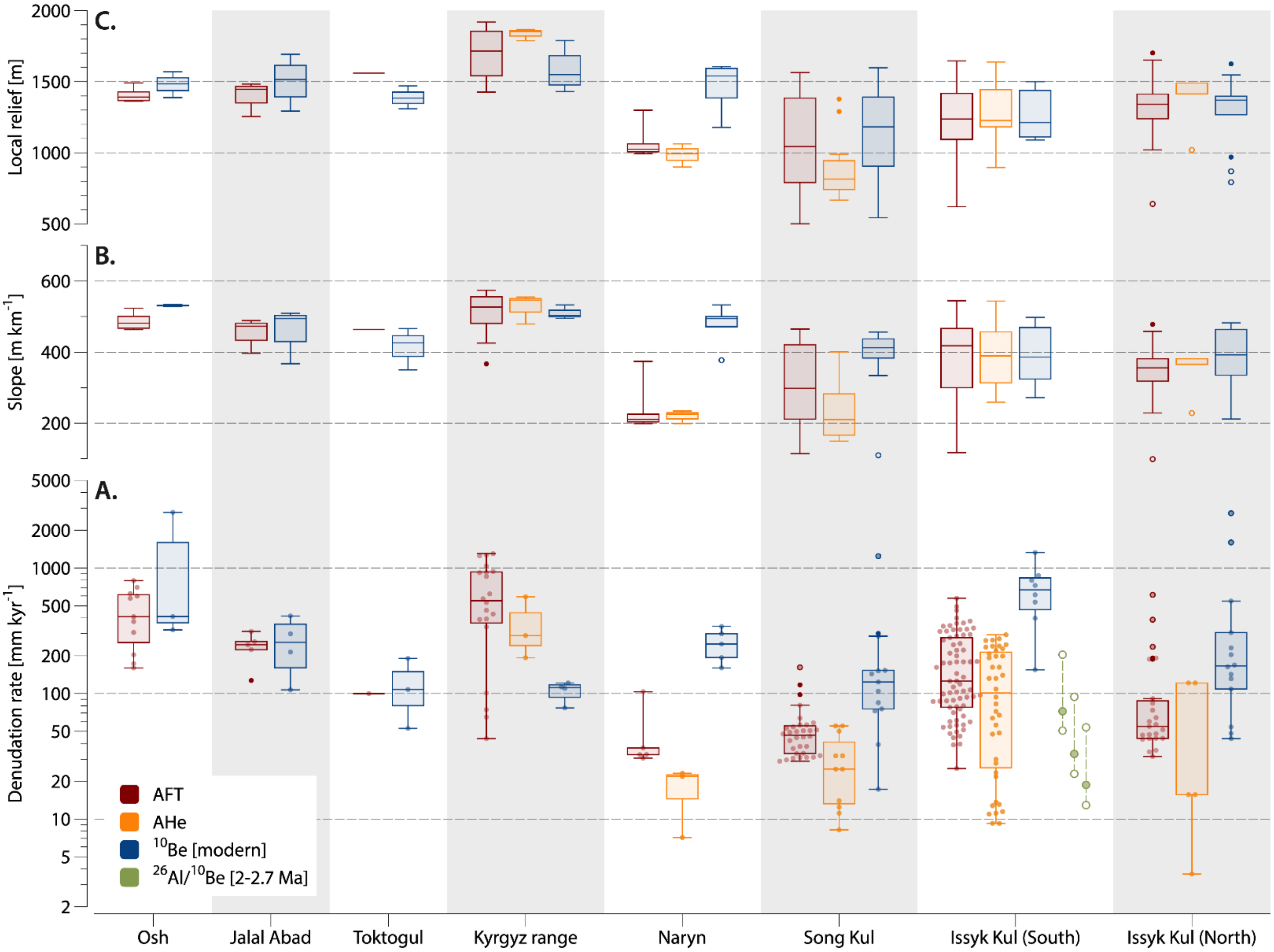

Figure S4.3. ^{10}Be-derived modern and paleo-denudation rates, AFT and AHe exhumation rates, slope, and local relief data distributed by region. Slope and local relief for ^{10}Be data is calculated as average for drainage basins using 90-m SRTM DEM. Slope and local relief for AFT and AHe data is calculated using 90-m SRTM DEM with a 10-km radius buffers created around each AFT and AHe sample location.

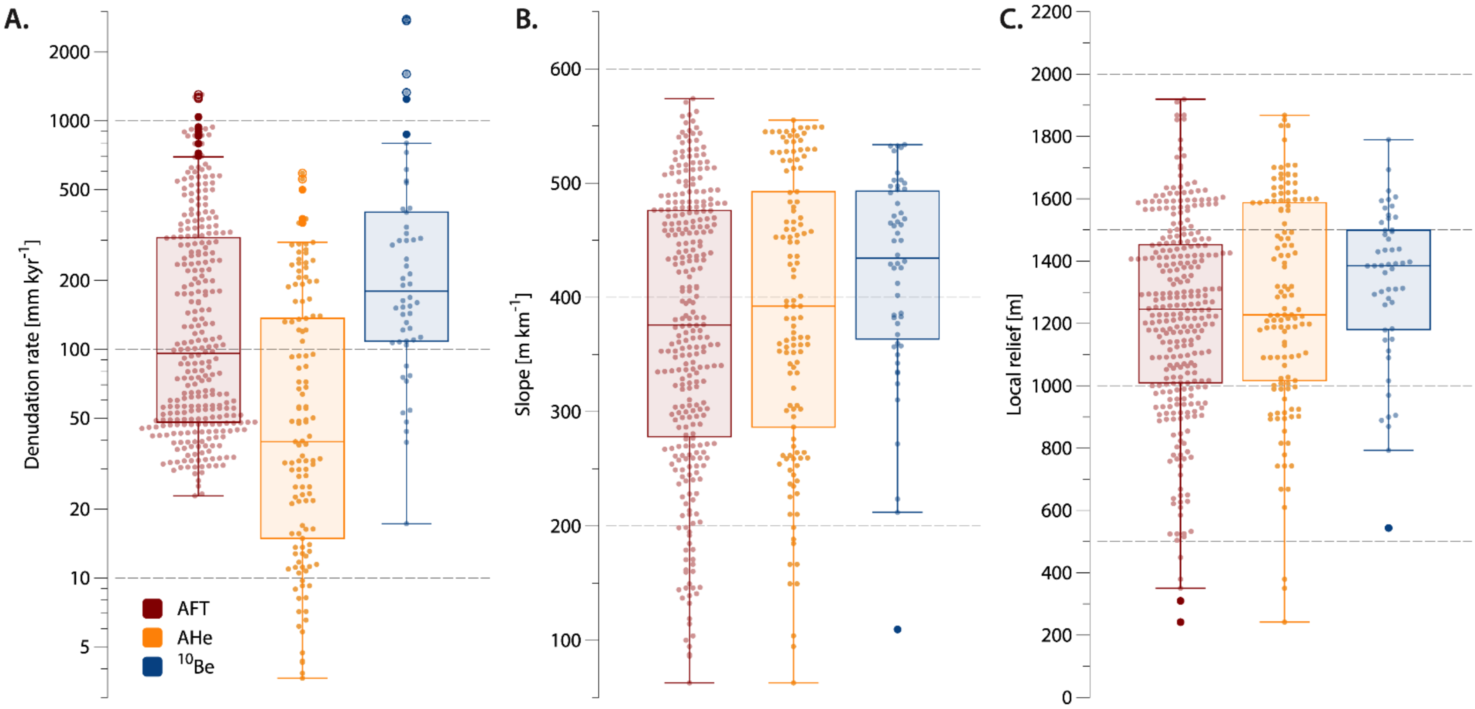

Figure S4.4. Modern ^{10}Be-derived denudation rates, AFT and AHe exhumation rates, slope, and local relief data from across the Kyrgyz Tian Shan plotted together. Slope and local relief for ^{10}Be data is calculated as average for drainage basins using 90-m SRTM DEM. Slope and local relief for AFT and AHe data is calculated using 90-m SRTM DEM with a 10-km radius buffers created around each AFT and AHe sample location.

Additional reference for Supplementary Figure S4.1 (not mentioned in the main text):

Mohadjer, S., Ehlers, T.A., Bendick, R., Stübner, K., & Strube, T.A. (2016). Quaternary fault database for central Asia, *Nat. Hazards Earth Syst. Sci.*, *16*, 529–542, https://doi.org/10.5194/nhess-16-529-2016.

Table S4.1. ^{10}Be data from modern river sand

Sample ID	Lab ID	ANSTO Cathode ID[a]	Latitude[b] WGS84 [deg]	Longitude[b] WGS84 [deg]	Sampled material	Total Qtz [g]	Corr. 10Be/9Be[c,d] [$\times 10^{-15}$]	Blank 10Be/9Be[c] [$\times 10^{-15}$]	9Be Spike [µg]	10Be[c] [$\times 10^{3}$ atoms g^{-1}]	CAIRN Average Scaling	Atm. Pressure[e] [hPa]	10Be Denudation Rate[c,f] [mm kyr^{-1}]	Averaging Timescale [kyr]	Ice shielding corr.[g] [mm kyr^{-1}]
KAZ16-02	UOW347	XBE0772	43,261402	78,406841	sand (250-500 µm)	40,559	644.23 ± 16.23	2.01 ± 1.39 (n = 4)	289,7	**307.51 ± 8.33**	4,99	787,93	**43.72 ± 8.24**	**13,7**	-
KAZ16-03	UOW348	XBE0773	43,084876	78,535171	sand (250-500 µm)	24,073	185.34 ± 4.55	2.01 ± 1.39 (n = 4)	287,9	**148.13 ± 3.92**	5,96	760,44	**108.54 ± 20.15**	**5,5**	-
KAZ16-04	UOW349	XBE0774	43,315848	78,176851	sand (250-500 µm)	40,775	848.79 ± 21.33	2.01 ± 1.39 (n = 4)	288,8	**401.68 ± 10.86**	7,26	734,53	**48.10 ± 8.88**	**12,5**	-
KAZ16-05	UOW350	XBE0775	43,244082	77,959133	sand (250-500 µm)	40,624	889.82 ± 19.54	2.01 ± 1.39 (n = 4)	289,1	**423.11 ± 10.21**	8,64	708,37	**54.16 ± 9.90**	**11,1**	-
KAZ16-06	UOW351	XBE0776	43,316386	77,645298	sand (250-500 µm)	40,158	201.63 ± 5.29	2.01 ± 1.39 (n = 4)	287,8	**96.57 ± 2.71**	8,36	711,58	**231.35 ± 42.26**	**2,6**	**222.77 ± 40.76**
KAZ16-07	UOW352	XBE0777	43,362002	77,376193	sand (250-500 µm)	16,234	54.76 ± 2.09	2.01 ± 1.39 (n = 4)	287,1	**64.72 ± 2.56**	3,96	818,88	**168.67 ± 32.56**	**3,6**	-
KYR14-02	6060	B5991	42,490981	73,850740	sand (250-500 µm)	13,596	175.74 ± 4.53	1.95 ± 0.25 (n = 3)	261,8	**226.17 ± 7.72**	10,36	674,45	**121.52 ± 22.20**	**4,9**	-
KYR14-03	6593	Be268	41,608910	72,699784	sand (250-500 µm)	4,549	10.41 ± 0.62	0.95 ± 0.18 (n = 1)	278,1	**42.52 ± 3.04**	6,54	740,08	**414.92 ± 81.33**	**1,4**	-
KYR14-05	6594	Be272	41,539871	72,489710	sand (250-500 µm)	26,243	53.57 ± 2.09	0.95 ± 0.18 (n = 1)	303,2	**41.36 ± 2.31**	4,51	793,92	**299.00 ± 58.30**	**2,0**	-
KYR14-06	6599	Be277	41,497936	72,373789	sand (250-500 µm)	11,286	28.57 ± 1.25	0.95 ± 0.18 (n = 1)	277,7	**46.98 ± 2.79**	3,62	825,06	**213.82 ± 42.67**	**2,8**	-
KYR14-08	6311	B6315	40,175579	73,488839	sand (250-500 µm)	40,348	18.11 ± 1.72	2.04 ± 0.80 (n = 1)	264,0	**7.92 ± 0.83**	8,22	701,33	**2780.42 ± 581.94**	**0,2**	-
KYR14-10	6312	B6316	40,056496	73,554726	sand (250-500 µm)	40,598	113.38 ± 4.30	2.04 ± 0.80 (n = 1)	264,1	**49.28 ± 2.89**	7,54	714,60	**411.01 ± 78.29**	**1,5**	-
KYR14-12	6598	Be276	39,911627	73,390485	sand (250-500 µm)	13,576	58.47 ± 1.91	0.95 ± 0.18 (n = 1)	277,8	**79.94 ± 4.12**	9,64	677,83	**321.45 ± 60.06**	**1,9**	**316.63 ± 59.19**
KYR14-13	6597	Be275	41,444790	72,272541	sand (250-500 µm)	38,503	249.19 ± 6.59	0.95 ± 0.18 (n = 1)	279,0	**120.66 ± 5.78**	4,74	789,25	**106.97 ± 20.60**	**5,6**	-
KYR14-14	6313	B6317	42,048122	72,820098	sand (250-500 µm)	40,175	1015.60 ± 17.18	2.04 ± 0.80 (n = 1)	264,3	**446.45 ± 21.35**	8,88	699,97	**52.70 ± 9.88**	**11,4**	-
KYR14-16	6314	B6318	42,153606	72,827222	sand (250-500 µm)	40,497	324.67 ± 8.04	2.04 ± 0.80 (n = 1)	265,1	**142.01 ± 7.26**	10,18	678,64	**190.59 ± 35.56**	**3,1**	-
KYR14-17	6315	B6319	42,162628	72,901000	sand (250-500 µm)	40,283	556.79 ± 9.01	2.04 ± 0.80 (n = 1)	264,0	**243.87 ± 11.60**	9,89	682,16	**107.74 ± 20.05**	**5,6**	-
KYR14-18	6595	Be273	42,388008	73,841441	sand (250-500 µm)	13,146	276.44 ± 7.23	0.95 ± 0.18 (n = 1)	278,0	**390.62 ± 18.67**	11,34	661,01	**76.75 ± 14.25**	**7,8**	-
KYR14-19	6596	Be274	42,404503	73,784267	sand (250-500 µm)	9,977	133.70 ± 4.01	0.95 ± 0.18 (n = 1)	278,3	**249.25 ± 12.46**	10,33	675,45	**109.97 ± 20.50**	**5,5**	-
KYR14-20	6061	B5992	42,760601	76,258375	sand (250-500 µm)	39,809	365.81 ± 7.03	1.95 ± 0.25 (n = 3)	262,6	**161.24 ± 4.75**	8,59	704,48	**142.18 ± 26.01**	**4,2**	**141.81 ± 25.94**
KYR14-21	6062	B5993	42,774251	76,327219	sand (250-500 µm)	42,742	374.11 ± 10.35	1.95 ± 0.25 (n = 3)	262,2	**153.36 ± 5.45**	9,41	691,71	**163.35 ± 29.95**	**3,7**	-
KYR14-22	6084	B5995	42,871944	76,813015	sand (250-500 µm)	43,656	48.32 ± 1.94	1.95 ± 0.25 (n = 3)	261,2	**19.32 ± 0.89**	11,64	659,19	**1600.57 ± 294.83**	**0,4**	**1544.32 ± 284.74**
KYR14-23	6063	B5994	42,861841	76,758759	sand (250-500 µm)	40,047	25.23 ± 1.29	1.95 ± 0.25 (n = 3)	263,9	**11.11 ± 0.62**	11,43	662,13	**2735.39 ± 511.57**	**0,2**	**2615.23 ± 489.67**
KYR16-01B	UOW340	XBE0764	42,063803	77,594741	pebbles (~16 mm)	40,811	96.79 ± 2.70	2.01 ± 1.39 (n = 4)	287,4	**45.55 ± 1.35**	12,49	644,78	**727.00 ± 131.25**	**0,8**	**694.61 ± 125.55**
KYR16-01C	UOW341	XBE0765	42,063803	77,594741	pebbles (~32 mm)	40,456	87.28 ± 2.59	2.01 ± 1.39 (n = 4)	287,8	**41.49 ± 1.30**	12,49	644,78	**798.17 ± 144.31**	**0,8**	**762.62 ± 138.05**
KYR16-02A	UOW342	XBE0766	42,272431	77,919767	sand (250-500 µm)	40,710	151.34 ± 4.14	2.01 ± 1.39 (n = 4)	288,5	**71.67 ± 2.09**	10,73	667,83	**398.07 ± 72.14**	**1,5**	**378.02 ± 68.61**
KYR16-02B	UOW343	XBE0767	42,272431	77,919767	pebbles (~32 mm)	40,592	112.41 ± 3.21	2.01 ± 1.39 (n = 4)	288,1	**53.31 ± 1.61**	10,73	667,83	**535.34 ± 97.08**	**1,1**	**508.38 ± 92.34**
KYR16-03	UOW344	XBE0769	42,154270	77,306540	sand (250-500 µm)	40,782	234.67 ± 6.08	2.01 ± 1.39 (n = 4)	288,8	**111.07 ± 3.09**	6,37	747,77	**154.67 ± 28.62**	**3,9**	-
KYR16-04	UOW345	XBE0770	42,650635	78,929829	sand (250-500 µm)	40,880	37.48 ± 1.87	2.01 ± 1.39 (n = 4)	288,8	**17.70 ± 0.90**	8,80	702,17	**1329.50 ± 248.66**	**0,5**	**1324.96 ± 247.84**
KYR16-05	UOW346	XBE0771	42,244247	76,703226	sand (250-500 µm)	40,772	69.90 ± 2.29	2.01 ± 1.39 (n = 4)	288,4	**33.04 ± 1.13**	7,53	723,49	**612.09 ± 112.79**	**1,0**	**578.75 ± 106.92**
KYR16-30	UOW318	XBE0615	42,121579	75,291114	sand (250-500 µm)	27,917	417.58 ± 8.29	2.01 ± 1.39 (n = 4)	288,4	**288.27 ± 6.41**	11,37	661,15	**104.39 ± 18.84**	**5,7**	-
KYR16-31	UOW319	XBE0616	42,106368	75,244224	sand (250-500 µm)	40,648	344.69 ± 6.19	2.01 ± 1.39 (n = 4)	287,7	**163.04 ± 3.35**	9,28	692,54	**151.56 ± 27.46**	**4,0**	-
KYR16-32	UOW354	XBE0778	42,122222	75,169184	sand (250-500 µm)	24,533	419.63 ± 10.64	2.01 ± 1.39 (n = 4)	287,9	**329.07 ± 8.97**	9,35	692,23	**75.39 ± 13.76**	**8,0**	-
KYR16-33	UOW320	XBE0617	41,915455	74,222264	sand (250-500 µm)	40,690	330.92 ± 5.96	2.01 ± 1.39 (n = 4)	288,6	**156.82 ± 3.23**	9,00	695,74	**152.95 ± 27.74**	**3,9**	-
KYR16-34	UOW321	XBE0618	41,919201	74,176656	sand (250-500 µm)	40,053	418.66 ± 7.45	2.01 ± 1.39 (n = 4)	289,6	**202.25 ± 4.13**	9,39	689,58	**123.54 ± 22.38**	**4,9**	**122.16 ± 22.14**
KYR16-35	UOW322	XBE0620	41,932727	74,145678	sand (250-500 µm)	40,077	617.08 ± 12.38	2.01 ± 1.39 (n = 4)	289,2	**297.58 ± 6.67**	9,48	689,21	**84.55 ± 15.35**	**7,1**	-
KYR16-36	UOW323	XBE0621	41,783115	74,698238	sand (250-500 µm)	40,302	367.59 ± 6.59	2.01 ± 1.39 (n = 4)	289,6	**176.5 ± 3.62**	9,52	687,36	**143.53 ± 25.99**	**4,2**	-
KYR16-37	UOW324	XBE0622	41,791160	74,694960	sand (250-500 µm)	40,309	177.74 ± 4.71	2.01 ± 1.39 (n = 4)	288,0	**84.86 ± 2.40**	9,59	685,65	**301.10 ± 54.74**	**2,0**	-
KYR16-38	UOW325	XBE0623	41,721602	74,738549	sand (250-500 µm)	40,865	49.70 ± 2.23	2.01 ± 1.39 (n = 4)	287,2	**23.35 ± 1.07**	10,91	666,08	**1242.84 ± 229.34**	**0,5**	**1241.34 ± 229.07**
KYR16-39	UOW326	XBE0624	41,730721	75,456053	sand (250-500 µm)	40,926	3091.19 ± 53.64	2.01 ± 1.39 (n = 4)	289,3	**1460.12 ± 29.24**	9,69	688,52	**17.26 ± 3.17**	**34,8**	-
KYR16-46	UOW327	XBE0625	41,236140	76,236538	sand (250-500 µm)	40,896	167.57 ± 3.55	2.01 ± 1.39 (n = 4)	288,0	**78.86 ± 1.85**	10,15	676,57	**342.47 ± 61.90**	**1,8**	-
KYR16-48	UOW328	XBE0626	41,161590	76,077442	sand (250-500 µm)	40,423	250.17 ± 5.09	2.01 ± 1.39 (n = 4)	288,7	**119.39 ± 2.71**	11,16	660,30	**248.15 ± 44.72**	**2,4**	**246.73 ± 44.47**
KYR16-49	UOW329	XBE0627	41,102015	75,823582	sand (250-500 µm)	40,722	316.61 ± 6.19	2.01 ± 1.39 (n = 4)	288,7	**150.01 ± 3.30**	10,93	661,74	**193.33 ± 34.86**	**3,1**	**182 ± 32.88**
KYR16-50	UOW330	XBE0628	41,102060	75,818176	sand (250-500 µm)	40,743	202.80 ± 4.26	2.01 ± 1.39 (n = 4)	288,4	**95.94 ± 2.23**	10,81	663,42	**299.33 ± 54.00**	**2,0**	**282.5 ± 51.06**
KYR16-51	UOW331	XBE0629	41,121260	75,959947	sand (250-500 µm)	40,356	382.74 ± 7.09	2.01 ± 1.39 (n = 4)	289,5	**183.46 ± 3.86**	11,07	659,96	**160.06 ± 28.85**	**3,7**	**157.61 ± 28.42**
KYR16-52	UOW332	XBE0630	41,659738	75,819783	sand (250-500 µm)	30,858	921.65 ± 16.11	2.01 ± 1.39 (n = 4)	290,5	**579.82 ± 11.68**	8,60	703,41	**39.20 ± 7.17**	**15,3**	-
KYR16-53	UOW333	XBE0758	41,671970	75,812410	sand (250-500 µm)	40,707	680.43 ± 17.13	2.01 ± 1.39 (n = 4)	288,4	**322.16 ± 8.73**	8,80	699,85	**72.57 ± 13.27**	**8,3**	-
KYR16-54	UOW334	XBE0759	41,700939	75,735962	sand (250-500 µm)	40,970	171.75 ± 4.05	2.01 ± 1.39 (n = 4)	288,9	**80.93 ± 2.07**	8,66	702,83	**286.02 ± 52.07**	**2,1**	-
KYR16-55	UOW335	XBE0760	42,061759	77,012739	sand (250-500 µm)	40,611	67.42 ± 2.21	2.01 ± 1.39 (n = 4)	288,7	**32.03 ± 1.10**	10,49	674,59	**871.91 ± 158.81**	**0,7**	**817.22 ± 149.15**
KYR16-56	UOW336	XBE0761	42,789280	77,662280	sand (250-500 µm)	40,566	411.01 ± 10.45	2.01 ± 1.39 (n = 4)	289,1	**195.72 ± 5.35**	9,64	687,53	**131.03 ± 23.83**	**4,6**	**126.1 ± 22.97**
KYR16-57	UOW337	XBE0762	42,755330	77,478320	sand (250-500 µm)	40,789	202.51 ± 4.93	2.01 ± 1.39 (n = 4)	289,0	**95.87 ± 2.52**	11,04	667,75	**305.78 ± 55.26**	**2,0**	**284.56 ± 51.54**
KYR16-58	UOW338	XBE0763	42,689341	77,042800	sand (250-500 µm)	40,386	316.70 ± 8.09	2.01 ± 1.39 (n = 4)	286,8	**150.28 ± 4.12**	11,57	662,21	**204.09 ± 36.89**	**2,9**	**196.03 ± 35.48**
KYR-DRMS1	280910-4-1	-	42,722351	73,656030	sand (250-500 µm)	31,114	322.77 ± 7.93	3.12 ± 0.56 (n = 1)	304,4	**211.00 ± 5.10**	8,96	696,69	**113.00 ± 20.57**	**5,3**	**112.02 ± 20.39**
KYR-DRMS2	WpChu	-	42,728426	76,076680	sand (250-500 µm)	57,306	142.07 ± 5.53	2.73 ± 0.70 (n = 1)	305,1	**49.58 ± 1.98**	10,16	680,72	**545.60 ± 100.13**	**1,1**	**517.30 ± 95.10**

(a) Cathode IDs starting with 'B' were analysed on the 10 MV ANTARES accelerator at ANSTO and cathode IDs starting with 'Be' and 'XBE' were analysed on the 6 MV SIRIUS accelerator at ANSTO
(b) Sample coordinates indicate basin outlet as extracted from 90 m resolution SRTM data and are not the coordinates recorded in the field
(c) Uncertainties at the 1-sigma level
(d) Normalised to 07KNSTD (Nishiizumi et al., 2007)
(e) Effective atmospheric pressure calculated using CAIRN (Mudd et al., 2016)
(f) Calculated using CAIRN (Mudd et al., 2016) with default values for all parameters
(g) Denudation rates corrected for ice shielding using present day glacier extent from Stroeven et al. (2013)

Table S4.2. ^{10}Be data from buried sediment

Sample ID	Lab ID	ANSTO 10Be Cathode ID(a)	ANSTO 26Al Cathode ID(a)	Latitude(b)	Longitude(b)	Total Qtz	Corr. 10Be/9Be(c,d)	Blank 10Be/9Be(c)	9Be Spike	10Be(c)	Corr. 26Al/27Al(c)	Blank 26Al/27Al(c)	27Al	26Al(c,e)	Burial Age(f)	Palaeo-denud. Rate(g)	Rate Range(h)
				WGS84 [deg]	WGS84 [deg]	[g]	[×10^{-15}]	[×10^{-15}]	[µg]	[×10^{3} atoms g^{-1}]	[×10^{-15}]	[×10^{-15}]	[µg/g]	[×10^{3} atoms g^{-1}]	[Myr]	[mm kyr^{-1}]	[mm kyr^{-1}]
AKT-U-sand	UOW156	Be1060	AL1138/39	42,238833	76,710933	40,033	63.99 ± 2.02	0.37 ± 0.17 (n = 2)	288,4	**30.8 ± 1.01**	18.98 ± 2.03	0.56 ± 0.4 (n = 2)	135,4	**57.34 ± 6.56**	**2.71 ± 0.37**	**72.2 ± 11.7**	**50.6 ± 8.2 — 204.0 ± 32.8**
PET-QTS-L-sand	UOW161	Be1065	AL1147/48	42,177475	77,301044	85,024	406.03 ± 10.58	0.37 ± 0.17 (n = 2)	288,4	**92.04 ± 2.53**	158.47 ± 6.91	0.56 ± 0.4 (n = 2)	76,9	**272.15 ± 16.11**	**2.08 ± 0.14**	**33.0 ± 3.5**	**22.9 ± 2.5 — 94.1 ± 10.0**
PET-QTS-PIT-sand	UOW166	Be1070	Al1157/58	42,173947	77,285986	75,010	446.03 ± 11.62	0.37 ± 0.17 (n = 2)	288,9	**114.78 ± 3.16**	100.89 ± 6.54	0.56 ± 0.4 (n = 2)	100,9	**227.15 ± 17.31**	**2.75 ± 0.15**	**18.7 ± 1.8**	**12.9 ± 1.2 — 53.8 ± 5.1**

(a) Analysed on the 6 MV SIRIUS accelerator at ANSTO

(b) Sample coordinates as determined in the field using a hand-held GPS unit

(c) Uncertainties at the 1-sigma level

(d) Normalised to 07KNSTD (Nishiizumi et al., 2007)

(e) Normalised to KNSTD (Nishiizumi et al., 2004)

(f) Taken from Kudriavtseva et al. (2023) and determined using 26Al/10Be isochron burial dating

(g) Calculated using the isochron burial ages, and assuming continuous and complete burial and a source area average elevation of 1500 m

(h) Palaeo-denudation rate range obtained by assuming ± 500 m uncertainty in source area elevation and allowing for up to 50 % of measured nuclide inventory to be accumulated post deposition and burial (i.e., incomplete burial or lengthy exposure prior to sampling)

Additional reference for Table S4.2 (not mentioned in the main text):

Nishiizumi K. (2004). Preparation of ^{26}Al AMS standards. *Nuclear Instruments and Methods in Physics Research Section B: Beam Interactions with Materials and Atoms, 223* , 388-392.

Table S4.3. AFT data and exhumation rates

ID	Sample ID	Latitude	Longitude	Age (Ma)	Age uncertainty	System	Reference	Elevation (km)	Local relief correction Δh (km)	Exhumation rate high (mm/kyr)	Exhumation rate mid (mm/kyr)	Exhumation rate low (mm/kyr)	Region
0	10CK41	41,4378	71,2268	119,7	6,7	AFT	Bande_etal_2017b	1,369	1,97017	44,45	41,84	39,48	
1	10UM12	42,2331	71,4067	51,5	2,8	AFT	Bande_etal_2017b	3,456	3,27059	137,41	129,83	122,99	
2	10UM14	42,2401	71,4098	27,5	3,2	AFT	Bande_etal_2017b	2,082	3,22857	265,94	235,02	210,41	
3	10UM15	42,2415	71,4133	37,6	3,8	AFT	Bande_etal_2017b	2,945	3,21082	194,93	174,99	158,71	
4	10CK43	41,5843	71,527	51	5,5	AFT	Bande_etal_2017b	1,874	2,0611	118,63	105,47	94,86	
5	10CK44	41,5658	71,5292	64,7	5	AFT	Bande_etal_2017b	1,695	1,95919	87,59	80,53	74,55	
6	10TR17	42,4589	71,5338	25,2	2,8	AFT	Bande_etal_2017b	1,269	1,66663	224,26	199,27	179,10	
7	10TR23	42,1195	71,5466	11	1,6	AFT	Bande_etal_2017b	2,713	2,98523	652,82	563,97	496,07	
8	10TR22	42,1287	71,5576	26,4	2,9	AFT	Bande_etal_2017b	2,458	3,01351	269,95	240,40	216,56	
9	10TR21	42,1837	71,5697	24,5	2,6	AFT	Bande_etal_2017b	2,778	3,16709	297,63	266,34	240,87	
10	10TR20	42,1855	71,5742	27,4	3,5	AFT	Bande_etal_2017b	2,815	3,17137	273,37	238,60	211,51	
11	10TR19	42,1992	71,5856	29,8	2,4	AFT	Bande_etal_2017b	2,978	3,18552	240,02	220,66	204,14	
12	10TR05	42,122	72,0371	25,1	3,1	AFT	Bande_etal_2017b	2,921	3,27493	301,38	264,52	235,51	
13	10TR02	42,1633	72,0405	22	3,1	AFT	Bande_etal_2017b	2,571	3,11526	340,03	292,87	256,95	
14	10TR03	42,1382	72,0405	23	2,3	AFT	Bande_etal_2017b	2,678	3,25691	317,44	286,11	260,27	
15	10TR04	42,1085	72,0426	25,4	2,9	AFT	Bande_etal_2017b	3,12	3,24584	295,11	261,73	234,99	
16	10SU61	41,59	72,3286	16,4	2	AFT	Bande_etal_2017b	1,985	1,6757	354,98	312,86	279,44	Jalal Abad
17	10SU67	41,5306	72,3318	19,2	5,6	AFT	Bande_etal_2017b	0,922	1,35594	344,12	245,15	189,53	Jalal Abad
18	10SU62	41,6092	72,3561	23,9	2,1	AFT	Bande_etal_2017b	2,386	1,82276	244,81	223,46	205,37	Jalal Abad
19	10SU65	41,613	72,3641	20,8	1,9	AFT	Bande_etal_2017b	2,578	1,85857	285,11	259,40	237,83	Jalal Abad
20	10SU64	41,6229	72,3676	43	2,7	AFT	Bande_etal_2017b	2,767	1,94165	135,75	127,02	119,38	Jalal Abad
21	12KA22	40,0047	72,572	21,5	1,8	AFT	Bande_etal_2017a	3,86	3,45047	350,63	321,77	297,44	
22	12KA23	40,0056	72,5765	20,4	1,7	AFT	Bande_etal_2017a	3,66	3,45394	367,42	337,39	312,05	
23	12KA21	40,0033	72,5818	13,6	1,3	AFT	Bande_etal_2017a	3,475	3,49301	549,62	499,53	457,79	
24	12KA24	39,9983	72,6057	11,4	1,1	AFT	Bande_etal_2017a	3,122	3,62573	654,70	595,47	545,86	
25	12KA25	39,9989	72,6081	13	1,2	AFT	Bande_etal_2017a	3,297	3,62951	578,85	528,03	485,41	
26	10FR69	41,7191	72,9562	25,5	2,4	AFT	Bande_etal_2017a	1,844	1,51092	215,96	195,59	178,59	
27	10FR71	41,7104	72,9985	46,5	3,2	AFT	Bande_etal_2017a	2,131	1,64903	117,80	109,47	102,18	
28	10FR73	41,6888	73,0148	10,4	1	AFT	Bande_etal_2017a	1,789	1,87665	546,05	496,95	455,72	
29	10FR72	41,6998	73,0284	22	3	AFT	Bande_etal_2017a	1,939	1,74783	273,48	236,44	208,13	
30	12NU12	40,1286	73,5256	9,8	1,3	AFT	Bande_etal_2017a	1,838	2,46361	654,60	573,86	510,52	Osh
31	12NU17	40,1452	73,5395	7,9	0,9	AFT	Bande_etal_2017a	2,056	2,43928	782,24	701,24	635,18	Osh
32	12NU16	40,1519	73,5429	6,9	1,1	AFT	Bande_etal_2017a	2,21	2,42789	926,31	794,01	694,53	Osh
33	12NU15	40,1615	73,5489	9	0,7	AFT	Bande_etal_2017a	2,5	2,4103	674,13	626,00	584,09	Osh
34	12NU14	40,1658	73,5531	9,5	1,1	AFT	Bande_etal_2017a	2,67	2,40591	668,93	597,48	539,56	Osh
35	12NU13	40,1659	73,5573	36,9	2,7	AFT	Bande_etal_2017a	2,89	2,41432	172,72	159,92	148,84	Osh
36	11TS533	41,2944	73,6358	8,2	1,2	AFT	Bande_etal_2017a	2,911	2,47572	800,75	694,34	612,60	
37	11TS534	41,3383	73,6474	41,6	3,5	AFT	Bande_etal_2017a	2,036	2,3212	148,84	136,11	125,28	
38	11TS532	41,3058	73,655	6,3	0,9	AFT	Bande_etal_2017a	2,758	2,40369	993,59	868,12	770,65	
39	11TS535	41,346	73,6642	51	3,9	AFT	Bande_etal_2017a	2,122	2,2718	119,23	109,86	101,81	
40	12FE30	40,6375	73,7307	48,7	5,3	AFT	Bande_etal_2017a	1,582	1,96518	121,45	107,86	96,91	
41	12NU11	39,6747	73,7777	11,8	1,3	AFT	Bande_etal_2017a	2,939	3,36045	620,48	556,17	503,70	
42	12FE29	40,6586	73,7877	11,4	3,3	AFT	Bande_etal_2017a	1,655	2,24972	660,50	480,45	376,54	
43	12FE28	40,6596	73,7926	38	2,9	AFT	Bande_etal_2017a	1,667	2,26974	158,74	146,38	135,82	
44	12NU02	39,6163	73,8372	10,7	1,3	AFT	Bande_etal_2017a	2,93	3,54285	703,10	623,36	559,59	
45	12FE27	40,6615	73,8711	10,7	2,1	AFT	Bande_etal_2017a	1,765	2,56356	655,70	535,07	451,37	
46	11T75	39,8504	74,4984	6,9	0,9	AFT	Bande_etal_2017a	2,8	2,9498	977,19	863,06	772,64	
47	11T23	39,8382	74,8436	6,7	0,9	AFT	Bande_etal_2017a	3,117	3,16893	1041,96	917,01	818,72	
48	212-16	42,5953	74,4916	15,6	2,3	AFT	Bullen_etal_2003	2,24	2,85227	458,06	392,75	343,53	Kyrgyz range
49	98-33	42,6167	74,498	10,8	2,7	AFT	Bullen_etal_2003	1,8	2,56251	693,25	530,78	429,23	Kyrgyz range
50	212-14	42,5484	74,5065	11,5	1,3	AFT	Bullen_etal_2003	2,69	3,38707	636,38	568,76	513,88	Kyrgyz range
51	98-30	42,5455	74,5091	10,5	2,1	AFT	Bullen_etal_2003	2,8	3,40928	765,34	622,62	524,29	Kyrgyz range
52	212-9	42,5362	74,5203	14,7	1,7	AFT	Bullen_etal_2003	3,2	3,47395	517,41	460,01	413,99	Kyrgyz range
53	212-8	42,5301	74,5259	15,9	2,2	AFT	Bullen_etal_2003	3,4	3,49648	495,62	429,57	378,91	Kyrgyz range
54	212-13	42,5395	74,5347	103,2	11,3	AFT	Bullen_etal_2003	3,63	3,41178	73,24	64,97	58,34	Kyrgyz range
55	212-12	42,5376	74,5412	20,3	5,5	AFT	Bullen_etal_2003	3,97	3,3999	460,56	339,19	268,01	Kyrgyz range
56	KG05-1	42,664	75,5795	68	5	AFT	Chu_etal_2016	2,09	1,89424	83,10	76,72	71,28	
57	KG08-2	41,7872	75,6788	119	7	AFT	Chu_etal_2016	3,126	3,08543	56,38	52,93	49,87	Song Kul
58	KG30-5	42,5785	75,8054	72	5	AFT	Chu_etal_2016	1,495	2,07621	78,63	72,93	67,99	
59	KG06-1B	42,8816	76,119	32	3	AFT	Chu_etal_2016	2,452	2,6092	207,16	187,54	171,28	Issyk Kul North
60	KG28-5	42,3117	76,1308	73	5	AFT	Chu_etal_2016	1,715	1,82944	74,92	69,56	64,89	
61	KG24-5	42,6713	77,2739	88	6	AFT	Chu_etal_2016	1,632	1,79299	61,00	56,64	52,87	Issyk Kul North
62	KG20-5	42,7953	77,4614	63	4	AFT	Chu_etal_2016	2,102	2,47637	97,41	91,00	85,41	Issyk Kul North
63	KG19-6	42,7714	77,4745	85	6	AFT	Chu_etal_2016	1,943	2,26542	69,32	64,21	59,79	Issyk Kul North
64	KG23-5	42,8141	77,528	94	7	AFT	Chu_etal_2016	2,019	2,46368	64,80	59,78	55,45	Issyk Kul North
65	KG25-5	41,9697	77,6364	22	2	AFT	Chu_etal_2016	2,513	3,65189	343,36	312,64	286,83	Issyk Kul South
66	KG26-5	41,871	77,736	58	5	AFT	Chu_etal_2016	3,809	3,93015	137,77	125,66	115,47	Issyk Kul South
67	Al-88	42,3178	76,1275	101	3,5	AFT	DeGrave_etal_2013	1,74	1,81092	51,23	49,36	47,64	
68	TS-04	42,8553	76,5775	132,2	6,7	AFT	DeGrave_etal_2013	2,36	3,12495	49,21	46,60	44,24	Issyk Kul North
69	Al-33	42,1458	76,7908	198	41	AFT	DeGrave_etal_2013	2,22	1,93019	32,24	25,23	20,67	Issyk Kul South
70	TS-06	42,7264	76,8308	137,4	6,8	AFT	DeGrave_etal_2013	3,95	3,25521	50,34	47,76	45,41	Issyk Kul North
71	TS-07	42,7231	76,8436	147	8	AFT	DeGrave_etal_2013	3,7	3,18996	46,45	43,82	41,46	Issyk Kul North
72	TS-08	42,7181	76,8439	147,3	6,2	AFT	DeGrave_etal_2013	3,515	3,13014	45,13	43,13	41,34	Issyk Kul North
73	TS-09	42,7169	76,8497	115,9	3,9	AFT	DeGrave_etal_2013	3,3	3,09884	56,77	54,78	52,93	Issyk Kul North
74	TS-12	42,6778	76,8508	129,7	8	AFT	DeGrave_etal_2013	2,42	2,57005	46,99	43,98	41,30	Issyk Kul North
75	TS-10	42,7206	76,8586	134	5,3	AFT	DeGrave_etal_2013	3,085	3,13373	49,06	47,04	45,17	Issyk Kul North
76	TS-11	42,7047	76,8642	138,2	7,2	AFT	DeGrave_etal_2013	2,86	2,91529	46,41	43,89	41,62	Issyk Kul North
77	ALMA3-01	43,1633	77,0458	22,9	4	AFT	DeGrave_etal_2013	1,64	2,03739	285,05	235,56	200,48	Issyk Kul North
78	ALMA3-02	43,1486	77,0592	29,4	1,4	AFT	DeGrave_etal_2013	1,96	2,27968	201,68	192,02	183,20	Issyk Kul North
79	TS-27	42,0947	77,0681	99,4	5,7	AFT	DeGrave_etal_2013	2,06	2,16322	57,32	53,87	50,81	Issyk Kul South
80	Kyr-33	42,0967	77,0683	115,8	20,8	AFT	DeGrave_etal_2013	2,03	2,14636	56,25	45,73	38,43	Issyk Kul South
81	ALMA3-03	43,125	77,0842	70,9	4	AFT	DeGrave_etal_2013	2,4	2,67053	88,82	83,65	79,02	Issyk Kul North
82	TS-28	42,125	77,1167	85,7	10,7	AFT	DeGrave_etal_2013	1,7	2,05335	70,15	61,02	53,93	Issyk Kul South
83	TS-26	42,0706	77,1386	78,4	6,6	AFT	DeGrave_etal_2013	2,7	2,60154	82,50	75,33	69,26	Issyk Kul South
84	TS-19	42,1197	77,1417	107,5	16,5	AFT	DeGrave_etal_2013	2,02	2,1538	58,92	49,48	42,58	Issyk Kul South
85	Al-09	42,0683	77,1444	68,9	7,9	AFT	DeGrave_etal_2013	2,94	2,65003	99,02	87,33	78,04	Issyk Kul South
86	TS-24	42,0544	77,1519	102,6	8,6	AFT	DeGrave_etal_2013	3,08	2,82456	65,16	59,49	54,70	Issyk Kul South
87	Al-04	42,0411	77,1581	68,2	3,6	AFT	DeGrave_etal_2013	3,35	2,98139	98,84	93,46	88,64	Issyk Kul South
88	TS-23	42,0533	77,1586	72	5	AFT	DeGrave_etal_2013	3,31	2,85844	93,53	86,83	81,05	Issyk Kul South

89	TS-22	42,05	77,1653	69,3	7,2	AFT	DeGrave_etal_2013	3,5	2,91685	102,48	91,55	82,67	Issyk Kul South
90	TS-20	42,0842	77,3678	61,9	3,9	AFT	DeGrave_etal_2013	2,15	2,59996	101,10	94,52	88,76	Issyk Kul South
91	TS-13	42,7692	77,5236	162,8	8,7	AFT	DeGrave_etal_2013	1,85	2,10638	33,41	31,50	29,81	Issyk Kul North
92	TS-14	42,8019	77,5306	153,1	7,9	AFT	DeGrave_etal_2013	2,08	2,34484	37,28	35,25	33,42	Issyk Kul North
93	Kyr-42	42,0394	77,5978	17,6	0,8	AFT	DeGrave_etal_2013	2,255	3,13711	379,63	362,69	347,26	Issyk Kul South
94	Kyr-38	41,8708	77,7361	108,4	5,7	AFT	DeGrave_etal_2013	3,815	3,93139	69,92	66,15	62,73	Issyk Kul South
95	IK-13	42,4519	78,5517	26,3	1,3	AFT	DeGrave_etal_2013	1,97	2,48456	233,00	221,42	210,94	Issyk Kul South
96	IK-12	42,4308	78,9511	38,6	14,4	AFT	DeGrave_etal_2013	2,9	3,4455	279,98	175,36	126,98	Issyk Kul South
97	IK-11	42,4228	79,0208	129,8	9,1	AFT	DeGrave_etal_2013	3,2	3,52534	55,38	51,35	47,87	Issyk Kul South
98	AI-27	42,3811	79,0533	122,6	6,7	AFT	DeGrave_etal_2013	3,765	3,67082	59,73	56,36	53,33	Issyk Kul South
99	AI-40	39,7639	72,5814	8,4	0,3	AFT	DeGrave_etal_2012	4,51	4,15912	889,59	860,83	833,69	
100	AI-42	39,7142	72,6656	22,3	1,1	AFT	DeGrave_etal_2012	3,1	3,59263	326,29	310,47	296,05	
101	KYR-13	40,2567	73,3058	117,8	6,5	AFT	DeGrave_etal_2012	2,34	2,36894	49,90	47,03	44,47	
102	KYR-12	40,2533	73,3975	223	19,3	AFT	DeGrave_etal_2012	1,825	2,18117	25,18	22,86	20,92	
103	AI-37	40,1297	73,5236	18,8	1,6	AFT	DeGrave_etal_2012	1,81	2,46173	334,76	306,66	283,04	Osh
104	AI-38	40,1394	73,5353	14	1,4	AFT	DeGrave_etal_2012	1,99	2,44617	453,15	409,70	373,66	Osh
105	KYR-10	40,0664	73,5411	15,9	1,5	AFT	DeGrave_etal_2012	2	2,68661	412,57	374,73	343,21	Osh
106	AI-93	41,8975	74,8236	152	10,8	AFT	DeGrave_2011	2,29	2,46634	39,41	36,48	33,95	Song Kul
107	AI-97	41,8436	74,9011	201,1	12,3	AFT	DeGrave_2011	3,253	3,03133	32,59	30,52	28,67	Song Kul
108	AI-98	41,885	75,0181	138	5,7	AFT	DeGrave_2011	3,046	3,05034	47,07	45,05	43,18	Song Kul
109	AI-99	41,9322	75,0289	195,6	11	AFT	DeGrave_2011	3,514	2,85865	32,83	30,91	29,19	Song Kul
110	AI-100	41,9281	75,0375	189,3	15,4	AFT	DeGrave_2011	3,364	2,89425	34,96	31,99	29,49	Song Kul
111	AI-101	41,9189	75,0392	194,9	11,6	AFT	DeGrave_2011	3,212	2,94319	33,16	31,10	29,28	Song Kul
112	AI-102	41,91	75,0467	182,5	8,2	AFT	DeGrave_2011	3,066	2,99338	35,04	33,39	31,88	Song Kul
113	AI-92	42,0842	75,0781	154,3	11,3	AFT	DeGrave_2011	2,438	2,79103	41,04	37,90	35,20	Song Kul
114	AI-91	42,0931	75,1197	118,6	5,4	AFT	DeGrave_2011	2,572	2,86634	53,19	50,67	48,37	Song Kul
115	KYR-16	41,7614	75,1606	187,4	12	AFT	DeGrave_2011	3,09	3,14483	35,57	33,20	31,11	Song Kul
116	KYR-17	41,7169	75,1886	206	13,9	AFT	DeGrave_2011	3,72	3,21955	33,30	30,97	28,92	Song Kul
117	KAZ 03	43,2333	74,75	162,2	9,1	AFT	DeGrave_2003	0,76	0,802695	24,83	23,30	21,96	
118	KAZ 01	43,35	74,95	147	7	AFT	DeGrave_2003	1,25	1,13741	30,14	28,58	27,18	
119	TS16	42,4517	75,8564	110,6	6,3	AFT	DeGrave_2003	1,96	2,04279	50,03	47,05	44,38	
120	TS17	42,4536	75,8569	120,2	6,4	AFT	DeGrave_2003	1,83	2,03782	45,40	42,88	40,59	
121	TS02	42,6842	75,8892	128,1	13,4	AFT	DeGrave_2003	1,37	1,76864	42,24	37,58	33,83	
122	TS18	42,4642	76,0144	126	7,5	AFT	DeGrave_2003	1,63	2,06715	43,40	40,69	38,28	
123	_10-20	43,3273	74,8658	109,8	6,6	AFT	DePelsmaeker_etal_2015	0,904	1,06255	40,42	37,83	35,54	
124	SK-32	42,9195	76,2169	120,4	7,7	AFT	DePelsmaeker_etal_2015	3,357	2,9305	55,22	51,56	48,33	Issyk Kul North
125	SK-31	42,915	76,2181	85,1	4,8	AFT	DePelsmaeker_etal_2015	3,076	2,96132	78,15	73,60	69,52	Issyk Kul North
126	_11-28	43,0395	76,9444	16,8	0,8	AFT	DePelsmaeker_etal_2015	3,379	3,09167	406,23	387,39	370,30	Issyk Kul North
127	_11-27	43,056	76,9831	10,1	0,6	AFT	DePelsmaeker_etal_2015	2,51	3,0307	647,50	611,78	579,62	Issyk Kul North
128	SK-05A	43,34	78,9338	128,3	12,4	AFT	DePelsmaeker_etal_2015	1,337	1,30562	38,27	34,35	31,14	Issyk Kul North
129	AI-74	40,5383	75,2937	47,4	2,5	AFT	Glorie_etal_2011	3,591	3,67448	157,41	148,97	141,38	
130	AI-75	40,8275	75,5564	21	1,9	AFT	Glorie_etal_2011	4,005	3,79043	377,15	343,70	315,84	
131	AI-77	40,8273	75,5565	19,5	1,1	AFT	Glorie_etal_2011	3,99	3,79043	390,96	369,38	350,29	
132	AI-62	40,9833	75,5995	62,1	4,4	AFT	Glorie_etal_2011	2,667	3,16414	111,55	103,44	96,44	Naryn
133	AI-73	41,0572	75,6515	153,9	6,7	AFT	Glorie_etal_2011	2,345	2,61414	38,66	36,89	35,27	Naryn
134	AI-72	41,0559	75,6524	173,8	13	AFT	Glorie_etal_2011	2,435	2,62678	35,42	32,64	30,26	Naryn
135	AI-71	41,0535	75,6528	175,1	7,9	AFT	Glorie_etal_2011	2,533	2,64846	34,22	32,59	31,10	Naryn
136	AI-69	41,0497	75,6559	187,8	8,9	AFT	Glorie_etal_2011	2,628	2,68361	32,15	30,53	29,08	Naryn
137	AI-79	40,8088	76,2628	138,2	7,9	AFT	Glorie_etal_2011	3,259	3,33673	50,01	47,02	44,40	
138	Kyr-21	41,2439	76,4072	8,4	0,9	AFT	Glorie_etal_2011	2,615	2,96324	798,87	720,70	656,23	
139	AI-82	40,9857	76,6052	139,5	10	AFT	Glorie_etal_2011	3,086	3,33603	50,07	46,33	43,12	
140	AI-31	41,7367	78,0664	126,1	8,7	AFT	Glorie_etal_2011	4,067	3,83172	60,58	56,28	52,52	
141	AI-29	41,7147	78,1636	56,5	3,9	AFT	Glorie_etal_2011	3,804	3,94708	139,09	129,29	120,78	
142	AI-15	42,1111	79,0686	23	1,3	AFT	Glorie_etal_2011	2,683	3,36632	307,23	290,08	274,68	
143	AI-14	42,0624	79,0841	12,8	0,8	AFT	Glorie_etal_2011	2,619	3,27291	537,95	505,86	477,42	
144	AI-13	42,0643	79,0872	7,9	0,5	AFT	Glorie_etal_2011	2,66	3,27266	842,26	793,87	750,56	
145	AI-11	42,042	79,1027	9,8	1,1	AFT	Glorie_etal_2011	2,663	3,20977	720,88	645,87	584,75	
146	AI-20	42,1998	79,1161	133,5	6	AFT	Glorie_etal_2011	2,781	3,24811	49,85	47,51	45,39	
147	AI-16	42,0198	79,1404	58,9	2,7	AFT	Glorie_etal_2011	3,543	3,09466	116,34	110,89	105,91	
148	Kyr-03	42,3099	73,8379	128,2	12,8	AFT	Glorie_etal_2010	2,77	2,8394	52,26	46,83	42,39	
149	TF-22	42,1192	74,1061	125	9,8	AFT	Glorie_etal_2010	2,49	2,5401	49,68	45,60	42,13	Song Kul
150	TF-21	42,0932	74,1262	114,8	5,5	AFT	Glorie_etal_2010	2,01	2,63196	52,37	49,74	47,35	Song Kul
151	TF-20	41,9657	74,1659	124,7	7,4	AFT	Glorie_etal_2010	1,76	2,52801	47,45	44,52	41,89	Song Kul
152	TF-17	41,7799	74,2676	33,8	2,1	AFT	Glorie_etal_2010	1,775	2,11384	172,51	161,62	151,98	Song Kul
153	TF-19	41,8228	74,3239	97,1	4,6	AFT	Glorie_etal_2010	2,03	2,067	57,11	54,30	51,72	Song Kul
154	TF-18	41,82	74,3289	104,5	4,9	AFT	Glorie_etal_2010	2,2	2,05968	53,11	50,52	48,14	Song Kul
155	IK-06	41,8805	75,7198	157,9	8	AFT	Glorie_etal_2010	2,74	2,88315	39,97	37,87	35,95	Song Kul
156	IK-05	41,8594	75,7281	125	6,5	AFT	Glorie_etal_2010	2,845	2,97439	51,93	49,10	46,59	Song Kul
157	CP1	41,9831	77,6009	38,9	2,5	AFT	Macaulay_etal_2013	3,52	3,54798	191,34	178,88	168,04	Issyk Kul South
158	NP2	42,0624	77,6056	17,9	1,7	AFT	Macaulay_etal_2013	2,447	2,90554	383,37	347,77	318,18	Issyk Kul South
159	CP2	41,9859	77,6074	27,7	2,2	AFT	Macaulay_etal_2013	3,282	3,54559	271,50	250,05	231,67	Issyk Kul South
160	NP1	42,0563	77,61	17,3	1,4	AFT	Macaulay_etal_2013	2,645	2,98534	396,36	365,07	338,36	Issyk Kul South
161	CP3	41,9842	77,6113	23,3	2,6	AFT	Macaulay_etal_2013	3,04	3,55895	332,24	295,71	266,25	Issyk Kul South
162	CP4	41,9832	77,6163	21,2	1,6	AFT	Macaulay_etal_2013	2,839	3,5708	349,41	323,55	301,13	Issyk Kul South
163	CP5	41,9766	77,6229	21,8	2,7	AFT	Macaulay_etal_2013	2,626	3,60495	358,11	314,52	280,18	Issyk Kul South
164	NS	41,9703	77,6377	28,2	3,8	AFT	Macaulay_etal_2013	2,605	3,65059	282,72	244,76	215,62	Issyk Kul South
165	SP4	41,9038	77,6537	26,9	3,4	AFT	Macaulay_etal_2013	3,43	3,81931	305,02	266,83	236,96	Issyk Kul South
166	SS	41,9397	77,6564	58,5	6,6	AFT	Macaulay_etal_2013	2,721	3,7756	134,53	119,00	106,69	Issyk Kul South
167	SP3	41,8956	77,6874	40,2	11,3	AFT	Macaulay_etal_2013	3,641	3,85858	250,77	180,07	140,06	Issyk Kul South
168	SP2	41,8945	77,6993	40,7	29,5	AFT	Macaulay_etal_2013	3,821	3,87113	631,55	178,86	102,69	Issyk Kul South
169	SP1	41,8735	77,7219	92,5	4,9	AFT	Macaulay_etal_2013	3,78	3,90265	82,01	77,55	73,53	Issyk Kul South
170	8TS410	41,9673	76,2935	107,5	9,2	AFT	Macaulay_etal_2014	3,145	3,20696	65,64	59,81	54,95	Issyk Kul South
171	8TS411	42,0054	76,3093	64,7	3,7	AFT	Macaulay_etal_2014	3,835	3,33752	111,19	104,69	98,88	Issyk Kul South
172	8TS413	42,001	76,3199	21	2,3	AFT	Macaulay_etal_2014	3,558	3,34024	361,59	322,72	291,47	Issyk Kul South
173	8TS414	41,9758	76,3235	144,8	10,5	AFT	Macaulay_etal_2014	3,274	3,28044	48,12	44,49	41,37	Issyk Kul South
174	8TS418	42,1548	76,3322	140,3	10,2	AFT	Macaulay_etal_2014	2,122	2,47898	42,78	39,53	36,72	Issyk Kul South
175	8TS421	42,0901	76,3662	111	10,9	AFT	Macaulay_etal_2014	2,853	2,84126	60,76	54,55	49,50	Issyk Kul South
176	8TS419	42,0882	76,3906	87,2	11,8	AFT	Macaulay_etal_2014	3,223	2,79862	81,92	70,47	61,79	Issyk Kul South
177	8TS417	42,1345	76,3999	118,1	6,5	AFT	Macaulay_etal_2014	2,538	2,47401	50,92	47,98	45,36	Issyk Kul South
178	8TS416	42,1371	76,403	144,4	9,1	AFT	Macaulay_etal_2014	2,731	2,45119	41,74	38,99	36,58	Issyk Kul South

179	8TS408	41,8388	76,4693	115,3	6,6	AFT	Macaulay_etal_2014	3,333	3,31286	60,29	56,72	53,53	
180	8TS407	41,8121	76,4973	114,6	5,1	AFT	Macaulay_etal_2014	3,193	3,31835	59,64	56,88	54,37	
181	8TS406	41,7736	76,5406	130,4	6,3	AFT	Macaulay_etal_2014	2,96	3,21754	51,33	48,76	46,41	
182	8TS401	41,6968	76,7163	124,4	9,6	AFT	Macaulay_etal_2014	2,738	2,97651	53,51	49,21	45,53	
183	8TS402	41,7349	76,751	154,9	6,7	AFT	Macaulay_etal_2014	2,999	2,94478	41,16	39,28	37,59	
184	8TS398	41,6648	76,9755	124,1	7,3	AFT	Macaulay_etal_2014	2,988	3,30094	55,32	51,93	48,96	
185	8TS394	41,6722	77,0178	125,8	6,6	AFT	Macaulay_etal_2014	3,522	3,38262	55,59	52,56	49,84	
186	9TS475	41,9141	77,0598	87,6	4,7	AFT	Macaulay_etal_2014	3,918	3,64957	84,52	79,87	75,67	Issyk Kul South
187	8TS368	41,4502	77,3159	107,9	6,7	AFT	Macaulay_etal_2014	3,089	3,56357	66,58	62,31	58,53	
188	8TS372	41,4609	77,3254	121,1	5,8	AFT	Macaulay_etal_2014	3,232	3,53074	58,16	55,27	52,67	
189	8TS371	41,4548	77,3285	122,6	7,3	AFT	Macaulay_etal_2014	3,581	3,55236	58,88	55,26	52,04	
190	8TS369	41,4505	77,3417	122	6,5	AFT	Macaulay_etal_2014	4,061	3,57999	59,75	56,47	53,51	
191	8TS362	41,5108	77,5876	240,7	19,8	AFT	Macaulay_etal_2014	3,142	3,44274	29,15	26,64	24,52	
192	8TS359	41,4986	77,6227	155,9	8,7	AFT	Macaulay_etal_2014	3,797	3,48334	45,59	42,93	40,59	
193	8TS358	41,4968	77,6238	218,3	24,4	AFT	Macaulay_etal_2014	3,95	3,49194	34,42	30,41	27,24	
194	8TS361	41,5036	77,6298	201,2	9,5	AFT	Macaulay_etal_2014	3,482	3,46222	34,24	32,53	31,00	
195	7TS322	42,224	78,0655	30,2	3,6	AFT	Macaulay_etal_2014	2,407	2,64047	226,60	199,44	177,99	Issyk Kul South
196	7TS327	42,2114	78,0757	21,5	2,7	AFT	Macaulay_etal_2014	2,534	2,78559	327,05	286,62	254,87	Issyk Kul South
197	7TS324	42,1649	78,08	64,2	8,4	AFT	Macaulay_etal_2014	3,438	3,20804	118,58	102,72	90,51	Issyk Kul South
198	7TS323	42,1613	78,0818	59,1	8,2	AFT	Macaulay_etal_2014	3,594	3,23828	131,29	112,74	98,66	Issyk Kul South
199	7TS325	42,1739	78,091	51,7	8,7	AFT	Macaulay_etal_2014	3,095	3,13427	151,89	125,88	107,31	Issyk Kul South
200	7TS326	42,1827	78,0931	29,1	2,8	AFT	Macaulay_etal_2014	2,939	3,0629	245,91	222,24	202,65	Issyk Kul South
201	9TS502	42,2864	78,3605	23,9	2,1	AFT	Macaulay_etal_2014	3,445	3,2031	305,18	278,72	256,38	Issyk Kul South
202	7TS321	42,3948	78,4532	105	5,8	AFT	Macaulay_etal_2014	2,188	2,74248	59,23	55,81	52,79	Issyk Kul South
203	7TS320	42,3601	78,4697	39,4	11,8	AFT	Macaulay_etal_2014	2,402	3,08005	231,64	161,74	123,77	Issyk Kul South
204	7TS318	42,3213	78,4749	20,4	1,9	AFT	Macaulay_etal_2014	2,569	3,36092	358,13	325,45	298,07	Issyk Kul South
205	7TS319	42,3139	78,4771	31,9	7,1	AFT	Macaulay_etal_2014	2,551	3,40243	269,53	209,53	171,02	Issyk Kul South
206	7TS317	42,3219	78,482	14,4	2,5	AFT	Macaulay_etal_2014	2,752	3,37052	550,40	458,86	393,14	Issyk Kul South
207	7TS316	42,3238	78,4892	13,4	1,5	AFT	Macaulay_etal_2014	2,866	3,37387	551,95	492,99	445,34	Issyk Kul South
208	9TS467	42,2718	78,8378	72,9	6,5	AFT	Macaulay_etal_2014	4,06	3,85778	109,17	99,22	90,93	Issyk Kul South
209	9TS468	42,2717	78,8452	67,4	12,1	AFT	Macaulay_etal_2014	3,792	3,85436	130,74	106,79	90,13	Issyk Kul South
210	9TS469	42,2681	78,8495	73,3	10,4	AFT	Macaulay_etal_2014	3,616	3,84097	113,96	97,38	85,00	Issyk Kul South
211	9TS470	42,2662	78,858	70	6,8	AFT	Macaulay_etal_2014	3,453	3,82402	112,66	101,46	92,28	Issyk Kul South
212	9TS471	42,2566	78,8828	79,4	4,4	AFT	Macaulay_etal_2014	3,374	3,7614	93,63	88,31	83,54	Issyk Kul South
213	SJTC-6	42,5322	78,9172	10,7	1,3	AFT	Macaulay_etal_2014	2,54	2,96113	648,40	574,79	515,92	Issyk Kul South
214	7TS333	42,5609	78,9268	17,9	1,8	AFT	Macaulay_etal_2014	2,704	2,76777	381,08	343,65	312,87	Issyk Kul South
215	7TS328	42,5012	78,9362	17,2	1,9	AFT	Macaulay_etal_2014	2,719	3,19916	423,49	378,00	341,25	Issyk Kul South
216	7TS331	42,5476	78,9362	19,1	1,4	AFT	Macaulay_etal_2014	3,262	2,89598	358,32	332,57	310,30	Issyk Kul South
217	7TS330	42,5433	78,9368	21,9	2,2	AFT	Macaulay_etal_2014	3,41	2,9285	325,30	293,06	266,74	Issyk Kul South
218	7TS332	42,5517	78,938	15,7	1,7	AFT	Macaulay_etal_2014	3,106	2,86636	445,90	399,29	361,44	Issyk Kul South
219	9TS458	42,4498	78,9476	38,4	5,5	AFT	Macaulay_etal_2014	2,875	3,39033	204,50	174,92	152,77	Issyk Kul South
220	SJTC-5	42,4345	78,9501	46,7	14,9	AFT	Macaulay_etal_2014	2,893	3,43565	212,90	144,29	108,74	Issyk Kul South
221	9TS452	42,4173	78,9504	37,9	6,9	AFT	Macaulay_etal_2014	2,816	3,48342	219,28	179,05	151,17	Issyk Kul South
222	9TS456	42,4436	78,9584	50,2	7,4	AFT	Macaulay_etal_2014	3,264	3,41759	158,87	135,08	117,36	Issyk Kul South
223	SJTC-3	42,3621	79,0455	88	3,4	AFT	Macaulay_etal_2014	3,393	3,68033	81,95	78,68	75,66	Issyk Kul South
224	SJTC-4	42,3888	79,0607	81	3,3	AFT	Macaulay_etal_2014	3,788	3,6601	90,15	86,39	82,91	Issyk Kul South
225	SJTC-1	42,0426	79,0758	6,9	0,7	AFT	Macaulay_etal_2014	2,611	3,24957	983,52	893,96	819,18	
226	9TS465	42,1291	79,08	44,7	7,7	AFT	Macaulay_etal_2014	2,679	3,36466	180,17	148,66	126,44	
227	SJTC-2	42,0695	79,0833	11,3	1,7	AFT	Macaulay_etal_2014	2,612	3,28243	663,56	569,84	498,97	
228	8TS437	42,0542	79,0847	13,7	3,3	AFT	Macaulay_etal_2014	2,698	3,2589	615,15	474,12	385,03	
229	8TS435	42,0545	79,0912	12,4	2,1	AFT	Macaulay_etal_2014	2,857	3,25337	622,34	522,78	450,28	
230	8TS436	42,0545	79,0913	14,6	3,8	AFT	Macaulay_etal_2014	2,857	3,25337	595,36	447,34	357,54	
231	9TS461	42,1212	79,0924	88,3	9,5	AFT	Macaulay_etal_2014	3,292	3,33175	84,18	74,87	67,35	
232	9TS466	42,1743	79,0937	75,2	7,7	AFT	Macaulay_etal_2014	2,657	3,3008	96,62	86,47	78,17	
233	8TS434	42,0548	79,0944	15,3	2,8	AFT	Macaulay_etal_2014	2,992	3,25057	520,26	428,77	364,33	
234	8TS433	42,0545	79,0944	18,7	4,4	AFT	Macaulay_etal_2014	2,992	3,25057	457,64	352,93	286,86	
235	8TS432	42,0535	79,0981	21,5	4,8	AFT	Macaulay_etal_2014	3,204	3,2439	395,66	309,08	253,29	
236	8TS431	42,0541	79,1014	16,6	2,2	AFT	Macaulay_etal_2014	3,43	3,24073	458,43	399,72	354,22	
237	mav658	42,0814	79,2463	105,2	8,6	AFT	Macaulay_etal_2014	2,835	3,39892	67,93	62,20	57,32	
238	8TS427	42,0782	79,275	103,1	15,1	AFT	Macaulay_etal_2014	3,506	3,39205	76,14	64,66	56,11	
239	7TS304	42,3102	79,6467	200,1	11,5	AFT	Macaulay_etal_2014	3,58	3,65491	35,79	33,64	31,73	
240	7TS308	42,3338	79,6848	161,6	16,2	AFT	Macaulay_etal_2014	3,202	3,58738	46,01	41,23	37,32	
241	7TS302	42,2772	79,7506	96,1	7,7	AFT	Macaulay_etal_2014	3,812	3,92617	81,54	74,83	69,10	
242	7TS305	42,2998	79,7627	110,9	12	AFT	Macaulay_etal_2014	3,538	3,89124	71,83	63,82	57,40	
243	KS13-13	41,3376	72,1616	121,8	7,8	AFT	Nachtergaele_etal_2018	0,777	0,851914	34,52	32,14	30,07	
244	KS13-16	41,3281	72,1695	85	16	AFT	Nachtergaele_etal_2018	0,664	0,840304	58,50	46,86	38,98	
245	KS13-17	41,3264	72,1697	91	13	AFT	Nachtergaele_etal_2018	0,648	0,838331	51,30	43,52	37,72	
246	KS13-18	41,3258	72,1697	126	13	AFT	Nachtergaele_etal_2018	0,636	0,838331	34,50	30,68	27,61	
247	KS13-11	41,3428	72,1905	118	11	AFT	Nachtergaele_etal_2018	0,658	0,835865	36,60	32,94	29,93	
248	F11-775	40,3172	72,6317	118,1	6,5	AFT	Nachtergaele_etal_2018	1,2	1,34511	39,90	37,57	35,50	
249	TF-06	42,0092	72,8606	53,2	2,8	AFT	Nachtergaele_etal_2018	1,355	2,10221	105,58	99,82	94,69	Toktogul
250	KYR-04	41,7117	72,9433	73,5	7,4	AFT	Nachtergaele_etal_2018	1,625	1,57887	73,66	65,88	59,59	
251	KYR-05	41,7222	72,9681	97,5	6,7	AFT	Nachtergaele_etal_2018	2,11	1,49441	52,96	49,14	45,82	
252	TF-15	42,2772	73,1858	115,6	6,6	AFT	Nachtergaele_etal_2018	3,3	3,14635	58,76	55,29	52,18	
253	TF-16	42,2219	73,2211	102,2	20,7	AFT	Nachtergaele_etal_2018	2,97	3,10889	78,26	61,90	51,11	
254	KS13-10	40,5323	73,4502	84,1	3,9	AFT	Nachtergaele_etal_2018	2,328	2,04474	66,78	63,53	60,59	
255	KS13-02	40,5252	73,4658	148,4	8,3	AFT	Nachtergaele_etal_2018	1,905	2,08657	36,88	34,71	32,76	
256	KS13-01	40,5246	73,466	144	4,8	AFT	Nachtergaele_etal_2018	1,898	2,09173	37,16	35,83	34,60	
257	KS13-04	40,5266	73,4698	123,8	6,1	AFT	Nachtergaele_etal_2018	1,91	2,07864	44,25	41,97	39,89	
258	KS13-08	40,5312	73,4814	130,4	5,3	AFT	Nachtergaele_etal_2018	1,928	2,03087	41,20	39,44	37,82	
259	KS13-20	40,8335	73,6099	102,2	6,3	AFT	Nachtergaele_etal_2018	1,37	1,66896	50,12	46,86	44,01	
260	KS13-19A	40,8344	73,6117	110	6,1	AFT	Nachtergaele_etal_2018	1,375	1,67574	46,12	43,44	41,02	
261	KYR-15	41,3381	73,6469	110,1	8,2	AFT	Nachtergaele_etal_2018	2,03	2,32391	53,80	49,60	45,99	
262	AI-44	41,3036	73,6494	118,1	5,6	AFT	Nachtergaele_etal_2018	2,817	2,42301	50,58	48,06	45,79	
263	AI-45	41,3467	73,6636	130	5,8	AFT	Nachtergaele_etal_2018	2,125	2,27292	43,50	41,46	39,62	
264	KYR-02	42,3178	73,8281	115,5	7,1	AFT	Nachtergaele_etal_2018	2,92	2,8825	56,37	52,77	49,58	
265	KS13-22	40,8451	74,0999	11,4	0,9	AFT	Nachtergaele_etal_2018	2,501	3,00924	588,08	544,47	506,69	

266	TF-23	42,1117	74,1017	101,5	4,5	AFT	Nachtergaele_etal_2018	2,27	2,55154	59,11	56,37	53,87	Song Kul
267	KS-113	40,3762	74,3414	61,1	2,9	AFT	Nachtergaele_etal_2018	2,651	2,81958	105,50	100,34	95,71	
268	KS-106	40,4002	74,3649	25,1	1,8	AFT	Nachtergaele_etal_2018	2,992	3,02682	276,42	256,74	239,62	
269	KB-135	41,7034	74,5056	53,5	3	AFT	Nachtergaele_etal_2018	2,822	2,92175	124,36	117,24	110,85	Song Kul
270	KS-128	41,6763	74,5072	202,9	20	AFT	Nachtergaele_etal_2018	2,28	2,93634	32,23	28,90	26,17	Song Kul
271	KS-126	41,675	74,5073	198	16	AFT	Nachtergaele_etal_2018	2,2	2,93674	32,31	29,56	27,23	Song Kul
272	KB-134	41,7085	74,5091	64,1	3,1	AFT	Nachtergaele_etal_2018	2,98	2,93508	103,10	97,97	93,36	Song Kul
273	KB-133	41,7205	74,5166	98,6	4,8	AFT	Nachtergaele_etal_2018	3,387	2,9519	67,06	63,67	60,60	Song Kul
274	KB-132	41,7263	74,5344	113,2	5,3	AFT	Nachtergaele_etal_2018	3,802	3,00576	59,13	56,25	53,64	Song Kul
275	KB-131	41,725	74,5392	134,6	6,5	AFT	Nachtergaele_etal_2018	4,143	3,02349	50,10	47,57	45,31	Song Kul
276	KB-124	41,8303	74,6898	111,7	7,5	AFT	Nachtergaele_etal_2018	2,385	2,57045	55,22	51,35	47,97	Song Kul
277	KB-123	41,8067	74,6952	101,3	8,1	AFT	Nachtergaele_etal_2018	2,431	2,74585	63,73	58,44	53,93	Song Kul
278	KB-122	41,7524	74,7222	145,4	9,5	AFT	Nachtergaele_etal_2018	2,578	3,07862	45,30	42,20	39,51	Song Kul
279	KB-121	41,7258	74,7759	80,2	5,6	AFT	Nachtergaele_etal_2018	2,756	3,26516	87,00	80,74	75,29	Song Kul
280	TS158	42,5394	74,8696	4,7	0,7	AFT	Sobel_etal_2006b	2,56	3,34741	1458,56	1269,74	1124,71	Kyrgyz range
281	TS159	42,5185	74,8738	6,9	0,6	AFT	Sobel_etal_2006b	2,85	3,46565	1000,60	922,53	855,59	Kyrgyz range
282	TS161	42,5018	74,8817	7,6	1,9	AFT	Sobel_etal_2006b	3,29	3,51867	1108,84	857,72	699,22	Kyrgyz range
283	TS162	42,5565	74,8892	4,4	0,6	AFT	Sobel_etal_2006b	2,35	3,12738	1474,78	1301,38	1164,94	Kyrgyz range
284	TS163	42,5809	74,9031	5,4	2,8	AFT	Sobel_etal_2006b	2,09	2,82507	1930,98	1040,33	715,52	Kyrgyz range
285	Mav38	42,6319	74,9183	3,9	0,7	AFT	Sobel_etal_2006b	1,84	2,19492	1473,58	1250,36	1086,83	Kyrgyz range
286	TS166	42,4884	75,2162	17	2	AFT	Sobel_etal_2006b	2,87	3,32349	439,90	389,66	349,63	Kyrgyz range
287	TS165	42,4972	75,2166	6,7	1,8	AFT	Sobel_etal_2006b	2,61	3,25527	1210,69	918,59	740,13	Kyrgyz range
288	TS167	42,4706	75,2189	66,6	3,4	AFT	Sobel_etal_2006b	3,16	3,41192	106,32	100,79	95,76	Kyrgyz range
289	TS169	42,4625	75,2324	151,1	7,7	AFT	Sobel_etal_2006b	3,57	3,40649	46,09	43,65	41,45	Kyrgyz range
290	TS170	42,4557	75,2337	91,1	5,6	AFT	Sobel_etal_2006b	3,77	3,42409	79,32	74,31	69,86	Kyrgyz range
291	TS164	42,5123	75,2693	6,3	0,8	AFT	Sobel_etal_2006b	2,25	3,04876	1058,33	938,58	843,05	Kyrgyz range
292	TS84	42,5448	75,8145	150,2	7,6	AFT	Sobel_etal_2006b	1,62	2,05576	35,63	33,70	31,98	
293	TS27	42,6335	75,8427	127,5	10,1	AFT	Sobel_etal_2006b	1,376	1,97337	42,73	39,17	36,14	
294	96TS1	40,1053	73,5282	20,6	1	AFT	Kaessner_etal_2017	1,888	-0,1976704	181,89	172,98	164,85	Osh
295	96TS2	40,1395	73,5053	16,1	0,8	AFT	Kaessner_etal_2017	1,808	-0,5265276	214,26	203,70	194,03	Osh

Site parameters for calculating exhumation rates presented in table S4.3:

T0 = 25; Temperature (deg C) at elevation = 0 km

lapse = 5; Temperature lapse rate (deg C km-1)

Crustal properties:

G_init = 25; initial geotherm, deg C km-1

kappa = 30; thermal diffusivity, km2 My-1

L = 30; model thickness, km

Table S4.4. AHe data and exhumation rates

ID	Sample ID	Latitude	Longitude	Age (Ma)	Age uncertaint y	System	Reference	Elevation (km)	Local relief correction Δh (km)	Exhumation rate high (mm/kyr)	Exhumatio n rate mid (mm/kyr)	Exhumatio n rate low (mm/kyr)	Region
0	KG-13-28	42,0453	79,9622	9	0	AHe	Rolland_etal_2020	5,52	0,551731	356,85	356,96	356,96	
1	KG-13-27	42,0453	79,9622	6,3	0	AHe	Rolland_etal_2020	5,53	0,551731	499,51	499,39	499,39	
2	KG-13-04abe	42,1384	79,9515	41	0,9	AHe	Rolland_etal_2020	3,785	-0,346777	49,64	48,42	47,26	
3	KG-13-0cdf	42,1384	79,9515	15,5	0,1	AHe	Rolland_etal_2020	3,785	-0,346777	140,72	139,81	138,86	
4	KG-13-06c	42,1124	79,9358	67,8	3,4	AHe	Rolland_etal_2020	4,401	-0,0564873	35,17	33,23	31,47	
5	KG-13-06de	42,1124	79,9358	265,7	7,8	AHe	Rolland_etal_2020	4,401	-0,0564873	7,38	7,13	6,90	
6	KG-13-32b	42,1111	79,8908	277,4	20,5	AHe	Rolland_etal_2020	4,625	0,300586	8,87	8,14	7,52	
7	KG-13-32e	42,1111	79,8908	161,2	4,7	AHe	Rolland_etal_2020	4,625	0,300586	15,39	14,89	14,43	
8	KG-13-11ad	42,1067	79,9167	82,6	3	AHe	Rolland_etal_2020	4,75	0,411635	33,98	32,64	31,40	
9	KG-13-11c	42,1067	79,9167	231,5	8,6	AHe	Rolland_etal_2020	4,75	0,411635	10,96	10,51	10,09	
10	KG-13-39ade	41,9958	79,1294	260	1,9	AHe	Rolland_etal_2020	3,566	0,596496	9,00	8,93	8,86	
11	KG-13-39bc	41,9958	79,1294	117,1	1,1	AHe	Rolland_etal_2020	3,566	0,596496	21,85	21,63	21,41	
12	KG-13-48a	42,0205	79,0536	4,6	0,1	AHe	Rolland_etal_2020	2,486	-0,657069	379,98	372,24	364,74	
13	KG-13-48d	42,0205	79,0536	76,2	1	AHe	Rolland_etal_2020	2,486	-0,657069	16,60	16,33	16,07	
14	KG-13-46ac	42,0254	79,0376	21,2	0,2	AHe	Rolland_etal_2020	2,977	-0,290688	96,07	95,06	94,09	
15	KG-13-46bd	42,0254	79,0376	62,9	0,4	AHe	Rolland_etal_2020	2,977	-0,290688	28,21	28,00	27,80	
16	7TS302a	42,2842	79,751	159,9	1,1	AHe	Rolland_etal_2020	3,818	-0,262935	10,81	10,72	10,63	
17	7TS302b	42,2842	79,751	13,6	0,2	AHe	Rolland_etal_2020	3,818	-0,262935	168,72	166,16	163,65	
18	7TS302cd	42,2842	79,751	58	0,3	AHe	Rolland_etal_2020	3,818	-0,262935	34,41	34,20	34,01	
19	7TS305ab	42,3108	79,7712	65,9	0,7	AHe	Rolland_etal_2020	3,54	0,532971	40,17	39,70	39,24	
20	7TS305ce	42,3108	79,7712	30,1	0,3	AHe	Rolland_etal_2020	3,54	0,532971	93,63	92,65	91,67	
21	7TS305d	42,3108	79,7712	110,1	3,6	AHe	Rolland_etal_2020	3,54	0,532971	23,43	22,59	21,80	
22	7TS307ad	42,3341	79,6858	15,3	0,4	AHe	Rolland_etal_2020	3,202	-0,33701	139,18	135,30	131,63	
23	7TS307bc	42,3341	79,6858	55,3	0,7	AHe	Rolland_etal_2020	3,202	-0,33701	33,02	32,53	32,07	
24	8TS416	42,1371	76,403	153,2	6,3	AHe	Macaulay_etal_2014	2,731	0,234574	13,39	12,76	12,19	Issyk Kul South
25	8TS418	42,1345	76,3999	155,8	16	AHe	Macaulay_etal_2014	2,538	0,0462664	12,61	11,12	9,93	Issyk Kul South
26	8TS420	42,0909	76,3803	188,8	27,4	AHe	Macaulay_etal_2014	3,081	0,333992	13,06	10,94	9,38	Issyk Kul South
27	9TS474	41,9154	77,068	87,8	7,5	AHe	Macaulay_etal_2014	4,054	0,302357	30,71	27,81	25,42	Issyk Kul South
28	9TS475	41,9141	77,0598	49,7	5,1	AHe	Macaulay_etal_2014	3,918	0,144629	54,63	48,54	43,60	Issyk Kul South
29	7TS323ab	42,1613	78,0818	80,1	12,7	AHe	Macaulay_etal_2014	3,594	0,32616	36,16	29,88	25,38	Issyk Kul South
30	7TS323c	42,1613	78,0818	28,1	18	AHe	Macaulay_etal_2014	3,594	0,32616	270,61	93,62	54,84	Issyk Kul South
31	7TS324	42,1649	78,08	35,5	4,1	AHe	Macaulay_etal_2014	3,438	0,135386	76,76	67,18	59,61	Issyk Kul South
32	7TS325	42,1739	78,091	42,9	3,8	AHe	Macaulay_etal_2014	3,095	-0,124426	52,67	47,49	43,18	Issyk Kul South
33	7TS326	42,1827	78,0931	11	0,8	AHe	Macaulay_etal_2014	2,939	-0,266073	208,25	192,57	179,12	Issyk Kul South
34	7TS327	42,2114	78,0757	7,6	0,8	AHe	Macaulay_etal_2014	2,534	-0,253997	304,69	272,84	246,70	Issyk Kul South
35	7TS322	42,224	78,0655	8,7	0,5	AHe	Macaulay_etal_2014	2,407	-0,268351	248,70	234,18	221,17	Issyk Kul South
36	9TS496	42,2745	78,3215	95,4	4,4	AHe	Macaulay_etal_2014	2,508	-0,591937	13,88	13,08	12,38	Issyk Kul South
37	7TS330	42,5433	78,9368	11,6	1,2	AHe	Macaulay_etal_2014	3,41	0,413792	266,92	239,24	216,49	Issyk Kul South
38	7TS331	42,5476	78,9362	13,3	2,4	AHe	Macaulay_etal_2014	3,262	0,296193	243,31	198,75	167,42	Issyk Kul South
39	7TS332	42,5517	78,938	9,4	0,2	AHe	Macaulay_etal_2014	3,106	0,125167	270,08	264,42	258,89	Issyk Kul South
40	7TS333	42,5609	78,9268	11,1	0,4	AHe	Macaulay_etal_2014	2,704	-0,121135	205,96	198,34	191,20	Issyk Kul South
41	SJTC-6	42,5322	78,9172	7	1	AHe	Macaulay_etal_2014	2,54	-0,506565	310,15	266,24	232,66	Issyk Kul South
42	7TS328	42,5012	78,9362	7,9	0,1	AHe	Macaulay_etal_2014	2,719	-0,453429	248,39	245,14	242,04	Issyk Kul South
43	SJTC-5	42,4345	78,9501	29,4	3,1	AHe	Macaulay_etal_2014	2,893	-0,356807	72,08	63,65	56,86	Issyk Kul South
44	8TS411ab	42,0054	76,3093	19,9	2,4	AHe	Macaulay_etal_2014	3,835	0,387802	159,88	139,86	124,10	Issyk Kul South
45	8TS411c	42,0054	76,3093	9,6	3,5	AHe	Macaulay_etal_2014	3,835	0,387802	455,05	293,98	215,26	Issyk Kul South
46	8TS414ac	41,9758	76,3235	159,6	25	AHe	Macaulay_etal_2014	3,274	-0,0167319	13,93	11,46	9,69	Issyk Kul South
47	8TS414b	41,9758	76,3235	90,9	35,4	AHe	Macaulay_etal_2014	3,274	-0,0167319	37,99	21,79	14,98	Issyk Kul South
48	9TS471	42,2566	78,8828	32,4	3,5	AHe	Macaulay_etal_2014	3,374	-0,49766	63,78	56,09	49,95	Issyk Kul South
49	8TS369	41,4505	77,3417	68,8	3,4	AHe	Macaulay_etal_2014	4,061	0,535539	41,67	39,44	37,42	
50	8TS370	41,4493	77,3357	59,8	4,8	AHe	Macaulay_etal_2014	3,855	0,29591	45,66	41,66	38,27	
51	8TS371	41,4548	77,3285	86,1	11,7	AHe	Macaulay_etal_2014	3,581	0,0880234	29,48	25,04	21,70	
52	8TS372	41,4609	77,3254	62,4	1,4	AHe	Macaulay_etal_2014	3,232	-0,140448	32,18	31,37	30,59	
53	8TS368	41,4502	77,3159	37	3,8	AHe	Macaulay_etal_2014	3,089	-0,438964	54,44	48,15	43,08	
54	8TS358	41,4968	77,6238	371,1	20,1	AHe	Macaulay_etal_2014	3,95	0,565792	6,54	6,14	5,79	
55	8TS359	41,4986	77,6227	209	21,5	AHe	Macaulay_etal_2014	3,797	0,500968	12,65	11,21	10,05	
56	8TS361ab	41,5036	77,863	108,6	15,5	AHe	Macaulay_etal_2014	3,482	-0,232188	19,53	16,37	14,02	
57	8TS361c	41,5036	77,863	170	21,9	AHe	Macaulay_etal_2014	3,482	-0,232188	11,42	9,73	8,44	
58	9TS463	42,1261	79,0931	22,2	2,3	AHe	Macaulay_etal_2014	3,039	-0,227822	105,28	93,49	83,93	
59	9TS465	42,1291	79,08	40,6	3,7	AHe	Macaulay_etal_2014	2,679	-0,55734	42,97	38,43	34,70	
60	8TS432a	42,0535	79,0981	58,2	8,5	AHe	Macaulay_etal_2014	3,204	0,133874	45,45	38,15	32,77	

61	8TS432b	42,0535	79,0981	28,3	4,1	AHe	Macaulay_etal_2014	3,204	0,133874	99,71	84,22	72,70	
62	SJTC-1	42,0426	79,0758	6,4	0,7	AHe	Macaulay_etal_2014	2,611	-0,534359	324,03	289,23	260,85	
63	SJTC-2ab	42,0695	79,0833	12,9	2,9	AHe	Macaulay_etal_2014	2,612	-0,586743	179,10	136,57	109,49	
64	SJTC-2c	42,0695	79,0833	24,1	4,1	AHe	Macaulay_etal_2014	2,612	-0,586743	84,29	68,28	57,09	
65	8TS428	42,0796	79,2755	435	9,2	AHe	Macaulay_etal_2014	3,367	0,0849629	3,93	3,83	3,74	
66	ALMA3-01	43,1633	77,0458	14,6	0,5	AHe	Macaulay_etal_2014	1,64	-0,34322	126,25	121,49	117,08	Issyk Kul North
67	TS-06	42,7264	76,8308	159,9	4,8	AHe	Macaulay_etal_2014	3,95	0,561368	16,17	15,63	15,13	Issyk Kul North
68	TS-26	42,0706	77,1386	183,5	5,5	AHe	Macaulay_etal_2014	2,7	0,0162651	9,57	9,24	8,92	Issyk Kul South
69	IK-13	42,4519	78,5517	11,4	0,4	AHe	Macaulay_etal_2014	1,97	-0,372563	168,37	162,08	156,22	Issyk Kul South
70	NP1	42,0563	77,61	9,8	0,2	AHe	Macaulay_etal_2014	2,645	-0,318243	211,64	207,12	202,85	Issyk Kul South
71	NP3	42,065	77,6024	7,6	0,1	AHe	Macaulay_etal_2014	2,243	-0,507221	241,64	238,37	235,22	Issyk Kul South
72	NP4	42,0677	77,6026	8	0,3	AHe	Macaulay_etal_2014	2,184	-0,552035	228,99	220,13	211,92	Issyk Kul South
73	CP1	41,9831	77,6009	21,9	0,6	AHe	Macaulay_etal_2014	3,52	0,00426465	111,75	108,49	105,39	Issyk Kul South
74	CP3	41,9842	77,6113	14,7	0,6	AHe	Macaulay_etal_2014	3,04	-0,456169	137,96	132,00	126,44	Issyk Kul South
75	CP4	41,9832	77,6163	13	0,6	AHe	Macaulay_etal_2014	2,839	-0,684889	138,88	131,97	125,67	Issyk Kul South
76	NS	41,9703	77,6377	16,5	0,5	AHe	Macaulay_etal_2014	2,605	-0,97109	85,76	82,74	79,94	Issyk Kul South
77	SS	41,9397	77,6564	19,8	0,7	AHe	Macaulay_etal_2014	2,721	-0,891731	75,04	72,02	69,19	Issyk Kul South
78	SP1	41,8735	77,7219	134,2	4,8	AHe	Macaulay_etal_2014	3,78	-0,187867	14,18	13,60	13,06	Issyk Kul South
79	SP4	41,9038	77,6537	9,3	0,3	AHe	Macaulay_etal_2014	3,43	-0,373966	235,58	227,90	220,67	Issyk Kul South
80	AI-20a	42,1998	79,1161	57	3,4	AHe	Glorie_etal_2011	2,781	-0,34618	31,90	29,70	27,77	
81	AI-20bc	42,1998	79,1161	125,7	7,5	AHe	Glorie_etal_2011	2,781	-0,34618	12,61	11,72	10,94	
82	AI-14ab	42,0624	79,0841	14,9	0,9	AHe	Glorie_etal_2011	2,619	-0,53886	128,13	119,79	112,35	
83	AI-14c	42,0624	79,0841	50,6	3	AHe	Glorie_etal_2011	2,619	-0,53886	31,99	29,78	27,82	
84	AI-13a	42,0643	79,0872	6,6	0,4	AHe	Glorie_etal_2011	2,66	-0,495062	304,95	286,68	270,41	
85	AI-13bc	42,0643	79,0872	33,8	2	AHe	Glorie_etal_2011	2,66	-0,495062	52,72	49,16	46,04	
86	AI-16a	42,0198	79,1404	169	10	AHe	Glorie_etal_2011	3,543	0,451495	14,57	13,62	12,77	
87	AI-16bc	42,0198	79,1404	435	26	AHe	Glorie_etal_2011	3,543	0,451495	5,04	4,70	4,40	
88	AI-31	41,7367	78,0664	107,1	6,4	AHe	Glorie_etal_2011	4,067	0,157056	22,63	21,13	19,81	
89	AI-29	41,7147	78,1636	30	1,8	AHe	Glorie_etal_2011	3,804	-0,233082	77,06	72,02	67,56	
90	AI-73	41,0572	75,6515	73,2	4,4	AHe	Glorie_etal_2011	2,345	-0,175265	24,84	23,12	21,60	Naryn
91	AI-69	41,0497	75,6559	85,1	5,4	AHe	Glorie_etal_2011	2,628	-0,0221321	23,52	21,81	20,32	Naryn
92	AI-77	40,8273	75,5565	10,7	0,6	AHe	Glorie_etal_2011	3,99	0,147801	262,36	247,67	234,46	
93	AI-74	40,3883	75,2937	41,4	2,5	AHe	Glorie_etal_2011	3,591	0,0668047	59,97	56,02	52,52	
94	AI-79	40,8088	76,2628	254,1	15	AHe	Glorie_etal_2011	3,259	-0,0516501	7,03	6,54	6,12	
95	AI-82	40,9857	76,6052	331,9	19	AHe	Glorie_etal_2011	3,086	-0,169425	4,64	4,33	4,05	
96	Kyr-03	42,31	73,8372	57,6	3,5	AHe	Glorie_etal_2010	2,77	-0,149403	34,91	32,50	30,38	
97	TF-17	41,78	74,2669	29,4	1,8	AHe	Glorie_etal_2010	1,775	-0,531511	53,96	50,13	46,74	Song Kul
98	TF-21	42,0933	74,1256	98,6	6,5	AHe	Glorie_etal_2010	2,01	-0,612896	12,16	11,14	10,26	Song Kul
99	IK-05	41,8594	75,7281	119,4	7,2	AHe	Glorie_etal_2010	2,845	-0,171867	15,03	13,98	13,05	Song Kul
100	IK-06	41,8806	75,7192	134,6	8,1	AHe	Glorie_etal_2010	2,74	-0,103474	13,40	12,46	11,64	Song Kul
101	212-10	42,5418	74,5162	10,2	0,8	AHe	Bullen_etal_2003	2,935	-0,448865	209,68	192,74	178,18	Kyrgyz range
102	212-14	42,5484	74,5065	6,4	0,1	AHe	Bullen_etal_2003	2,69	-0,548665	293,97	289,35	284,96	Kyrgyz range
103	212-16	42,5953	74,4916	3	0,2	AHe	Bullen_etal_2003	2,24	-0,446454	626,17	589,96	557,63	Kyrgyz range
104	AI-40	39,7639	72,5814	5	0,3	AHe	DeGrave_etal_2012	4,51	0,329095	587,54	555,58	526,94	
105	AI-41	39,7136	72,6558	12,5	0,8	AHe	DeGrave_etal_2012	3,56	-0,116201	200,92	187,80	176,13	
106	AI-42	39,7142	72,6656	9,7	0,6	AHe	DeGrave_etal_2012	3,1	-0,445541	220,18	206,26	193,89	
107	TS-06	42,7264	76,8308	159,9	9,6	AHe	DeGrave_etal_2013	3,95	0,561368	16,74	15,63	14,66	Issyk Kul North
108	TS-13	42,7692	77,5236	312,3	16,7	AHe	DeGrave_etal_2013	1,85	-0,195455	3,90	3,64	3,41	Issyk Kul North
109	TS-15	42,4492	75,8608	111,6	6,7	AHe	DeGrave_etal_2013	2,15	0,208005	18,19	16,95	15,85	
110	TS-17	42,4536	75,8569	122,5	7,6	AHe	DeGrave_etal_2013	1,83	-0,0352885	13,79	12,78	11,90	
111	TS-26	42,0706	77,1386	183,5	5,1	AHe	DeGrave_etal_2013	2,7	0,0162651	9,55	9,24	8,95	Issyk Kul South
112	KAZ-01	43,35	74,95	296,3	17,8	AHe	DeGrave_etal_2013	1,25	0,061749	4,61	4,27	3,97	
113	KAZ-03	43,2333	74,75	196,6	11,5	AHe	DeGrave_etal_2013	0,76	-0,0635141	6,28	5,81	5,41	
114	IK-03	41,3897	76,0114	186,3	11,2	AHe	DeGrave_etal_2013	2,315	-0,270281	7,68	7,12	6,63	Naryn
115	IK-13	42,4519	78,5517	11,4	0,7	AHe	DeGrave_etal_2013	1,97	-0,372563	173,37	162,09	152,08	Issyk Kul South
116	ALMA3-01	43,1633	77,0458	14,6	0,9	AHe	DeGrave_etal_2013	1,64	-0,34322	130,27	121,50	113,76	Issyk Kul North
117	KYR-38	41,8708	77,7361	85	5,1	AHe	DeGrave_etal_2013	3,815	-0,151585	25,09	23,39	21,89	Issyk Kul South
118	AI-91	42,0931	75,1197	176,5	10,6	AHe	DeGrave_etal_2013	2,57	-0,225584	8,82	8,19	7,63	Song Kul
119	AI-97	41,8436	74,9008	68,8	4,1	AHe	DeGrave_etal_2013	3,25	0,139213	34,11	31,87	29,87	Song Kul
120	AI-100	41,9281	75,0375	45,5	2,7	AHe	DeGrave_etal_2013	3,36	0,357825	59,01	55,20	51,83	Song Kul
121	AI-102	41,91	75,0467	78,3	4,7	AHe	DeGrave_etal_2013	3,065	-0,038656	26,81	24,99	23,39	Song Kul
122	AI-97	41,8436	74,9008	68,8	4,1	AHe	DeGrave_etal_2011	3,25	0,139213	34,11	31,87	29,87	Song Kul
123	AI-100	41,9281	75,0375	45,5	2,7	AHe	DeGrave_etal_2011	3,36	0,357825	59,01	55,20	51,83	Song Kul
124	AI-102	41,91	75,0467	78,3	4,7	AHe	DeGrave_etal_2011	3,065	-0,038656	26,81	24,99	23,39	Song Kul

Site parameters for calculating exhumation rates presented in table S4.4:

T0 = 25; Temperature (deg C) at elevation = 0 km

lapse = 5; Temperature lapse rate (deg C km-1)

Crustal properties:

G_init = 25; initial geotherm, deg C km-1

kappa = 30; thermal diffusivity, km2 My-1

L = 30; model thickness, km

Table S4.5. Modern ^{10}Be denudation rates and basin-wide geomorphic, climatic and tectonic parameters

ID*	Sample	Longitude	Latitude	Region	10Be rate [mm/kyr]	10Be rate uncertainty	Averaging Time [kyr]	Area [km2]	Elevation [m]		
									Mean	Median	St Dev.
1	KAZ16-02	78°24'25"E	43°15'41"N	Issyk Kul North	43,72	8,24	13,7	151,06	2087,25	2013,00	386,50
2	KAZ16-03	78°32'7"E	43°5'6"N		108,54	20,15	5,5	82,04	2333,60	2264,00	483,39
3	KAZ16-04	78°10'37"E	43°18'57"N		48,10	8,88	12,5	330,73	2648,83	2625,00	281,69
4	KAZ16-05	77°57'33"E	43°14'39"N		54,16	9,90	11,1	37,67	2936,06	2936,00	206,94
5	KAZ16-06	77°38'43"E	43°18'59"N		231,35	42,26	2,6	569,75	2828,16	2793,00	613,31
6	KAZ16-07	77°22'34"E	43°21'43"N		168,67	32,56	3,6	36,93	1742,80	1672,00	431,31
7	KYR-DRMS2	76°4'36"E	42°43'42"N		545,60	100,13	1,1	1421,72	3185,98	3292,00	602,61
8	KYR14-20	76°15'30"E	42°45'38"N		142,18	26,01	4,2	22,66	2920,16	2950,50	531,58
9	KYR14-21	76°19'38"E	42°46'27"N		163,35	29,95	3,7	18,03	3046,44	3147,00	550,06
10	KYR14-22	76°48'47"E	42°52'19"N		1600,57	294,83	0,4	29,50	3482,99	3514,00	338,54
11	KYR14-23	76°45'32"E	42°51'43"N		2735,39	511,57	0,2	64,19	3454,55	3487,00	344,29
12	KYR16-56	77°39'44"E	42°47'21"N		131,03	23,83	4,6	58,49	3118,16	3181,00	550,52
13	KYR16-57	77°28'42"E	42°45'19"N		305,78	55,26	2,0	319,93	3351,27	3416,00	554,07
14	KYR16-58	77°2'34"E	42°41'22"N		204,09	36,89	2,9	74,20	3423,73	3509,00	506,63
15	KYR16-04	78°55'47"E	42°39'2"N	Issyk Kul South	1329,50	248,66	0,5	246,82	2994,96	3052,00	476,80
16	KYR16-02A	77°55'11"E	42°16'21"N		398,07	72,14	1,5	607,06	3332,34	3471,00	677,11
17	KYR16-02B	77°55'11"E	42°16'21"N		535,34	97,08	1,1	607,06	3332,34	3471,00	677,11
18	KYR16-01B	77°35'41"E	42°3'50"N		727,00	131,25	0,8	317,05	3654,03	3744,00	482,87
19	KYR16-01C	77°35'41"E	42°3'50"N		798,17	144,31	0,8	317,05	3654,03	3744,00	482,87
20	KYR16-03	77°18'24"E	42°9'15"N		154,67	28,62	3,9	15,55	2515,61	2534,00	268,77
21	KYR16-55	77°0'46"E	42°3'42"N		871,91	158,81	0,7	288,04	3277,18	3339,00	588,02
22	KYR16-05	76°42'12"E	42°14'39"N		612,09	112,79	1,0	705,28	2676,52	2452,00	733,43
23	KYR16-30	75°17'28"E	42°7'18"N	Song Kul	104,39	18,84	5,7	13,14	3462,89	3506,00	338,28
24	KYR16-31	75°14'39"E	42°6'23"N		151,56	27,46	4,0	4,30	3088,29	3040,00	275,32
25	KYR16-32	75°10'9"E	42°7'20"N		75,39	13,76	8,0	10,68	3128,11	3138,00	198,80
26	KYR16-33	74°13'20"E	41°54'56"N		152,95	27,74	3,9	29,31	3038,45	3118,00	504,77
27	KYR16-34	74°10'36"E	41°55'9"N		123,54	22,38	4,9	43,71	3115,46	3223,00	485,61
28	KYR16-35	74°8'44"E	41°55'58"N		84,55	15,35	7,1	128,77	3113,39	3220,00	460,11
29	KYR16-36	74°41'54"E	41°46'59"N		143,53	25,99	4,2	17,82	3170,97	3225,00	319,76
30	KYR16-37	74°41'42"E	41°47'28"N		301,10	54,74	2,0	24,89	3182,08	3198,00	398,47
31	KYR16-38	74°44'19"E	41°43'18"N		1242,84	229,34	0,5	37,83	3417,84	3428,00	315,37
32	KYR16-39	75°27'22"E	41°43'51"N		17,26	3,17	34,8	1350,28	3176,87	3102,00	192,98
33	KYR16-52	75°49'11"E	41°39'35"N		39,20	7,17	15,3	25,80	2992,59	2877,00	308,50
34	KYR16-53	75°48'45"E	41°40'19"N		72,57	13,27	8,3	17,56	3014,60	2856,50	336,89
35	KYR16-54	75°44'9"E	41°42'3"N		286,02	52,07	2,1	24,08	2980,75	2892,00	342,42
36	KYR16-46	76°14'12"E	41°14'10"N	Naryn	342,47	61,90	1,8	31,45	3277,13	3292,00	471,57
37	KYR16-48	76°4'39"E	41°9'42"N		248,15	44,72	2,4	38,07	3465,95	3560,00	462,41
38	KYR16-49	75°49'25"E	41°6'7"N		193,33	34,86	3,1	36,68	3431,15	3497,00	545,84
39	KYR16-50	75°49'5"E	41°6'7"N		299,33	54,00	2,0	33,17	3429,75	3484,00	548,73
40	KYR16-51	75°57'36"E	41°7'17"N		160,06	28,85	3,7	45,57	3500,86	3582,00	462,76
41	KYR-DRMS1	73°39'22"E	42°43'20"N	Kyrgyz range	113,00	20,57	5,3	187,89	2951,35	3126,00	755,92
42	KYR14-02	73°51'3"E	42°29'28"N		121,52	22,20	4,9	37,31	3252,44	3372,00	552,64
43	KYR14-18	73°50'29"E	42°23'17"N		76,75	14,25	7,8	34,55	3464,69	3502,00	299,22
44	KYR14-19	73°47'3"E	42°24'16"N		109,97	20,50	5,5	163,66	3277,78	3341,00	434,95
45	KYR14-14	72°49'12"E	42°2'53"N	Toktogul	52,70	9,88	11,4	86,74	2995,40	3060,00	433,49
46	KYR14-16	72°49'38"E	42°9'13"N		190,59	35,56	3,1	238,52	3239,91	3325,00	409,71
47	KYR14-17	72°54'4"E	42°9'45"N		107,74	20,05	5,6	24,95	3211,57	3264,00	343,77
48	KYR14-03	72°41'59"E	41°36'32"N	Jalal Abad	414,92	81,33	1,4	243,78	2510,15	2528,00	638,36
49	KYR14-05	72°29'23"E	41°32'24"N		299,00	58,30	2,0	129,58	1981,65	2010,00	497,98
50	KYR14-06	72°22'26"E	41°29'53"N		213,82	42,67	2,8	33,63	1689,14	1679,00	390,47
51	KYR14-13	72°16'21"E	41°26'41"N		106,97	20,60	5,6	134,66	2004,09	2125,00	585,18
52	KYR14-08	73°29'20"E	40°10'32"N	Osh	2780,42	581,94	0,2	209,92	2995,35	3045,00	531,70
53	KYR14-10	73°33'17"E	40°3'23"N		411,01	78,29	1,5	21,93	2856,64	2725,00	463,36
54	KYR14-12	73°23'26"E	39°54'42"N		321,45	60,06	1,9	49,11	3283,19	3243,00	451,93

ID*	Topographic gradient [m/km]			Local relief 1km radius [m]			Local relief 2km radius [m]			Local relief 5km radius [m]			Local relief 10km radius [m]		
	Mean	Median	St Dev.	Mean	Median	St Dev.	Mean	Median	St Dev.	Mean	Median	St Dev.	Mean	Median	St Dev.
1	223,59	185,64	139,00	335,28	314,00	144,20	582,77	515,00	209,65	1159,18	1255,00	295,36	1802,19	1811,00	150,95
2	334,85	320,84	163,40	473,70	463,00	154,39	786,99	773,00	233,48	1557,67	1654,00	319,23	2253,33	2288,00	145,81
3	211,93	184,36	134,74	315,91	316,00	135,54	544,98	568,00	181,24	1036,18	1007,00	160,59	1581,36	1521,00	304,99
4	310,35	314,41	122,21	382,37	384,00	72,05	572,47	581,00	67,99	926,79	931,00	50,53	1290,60	1282,00	66,07
5	382,21	355,31	203,98	553,79	539,00	177,27	897,28	896,00	218,30	1613,69	1604,00	297,59	2387,93	2356,00	328,10
6	359,74	346,17	157,28	472,05	439,00	141,79	769,06	776,00	238,12	1592,67	1643,00	458,88	2668,11	2903,00	434,96
7	401,74	393,08	203,50	599,36	597,00	159,77	953,36	954,00	210,91	1604,88	1574,00	275,75	2051,03	2067,00	291,80
8	473,88	499,97	178,46	726,29	759,00	163,92	1204,75	1259,00	195,16	2090,67	2095,50	192,64	2480,94	2479,00	27,38
9	462,60	471,18	167,23	668,42	654,00	137,90	1123,89	1169,50	177,65	1992,49	1986,00	180,70	2407,37	2422,00	39,25
10	482,19	485,41	196,84	691,96	677,00	118,79	1044,87	1027,00	131,98	1613,37	1646,00	80,96	1901,59	1900,00	23,99
11	463,55	467,90	192,45	676,85	669,00	108,20	1026,74	1042,00	100,56	1671,99	1645,00	165,42	2214,62	2230,00	95,39
12	465,07	461,52	190,08	669,04	658,00	114,80	1019,51	1032,00	141,71	1711,99	1795,00	207,54	2342,19	2333,00	139,61
13	425,61	400,70	221,36	633,76	611,00	169,31	1007,59	995,00	204,24	1644,80	1626,00	235,24	2252,47	2300,00	192,75
14	356,80	323,94	178,33	550,08	554,00	99,00	901,66	894,00	105,00	1661,09	1744,00	275,42	2463,29	2511,00	240,76
15	342,54	305,84	192,56	499,01	501,00	154,09	786,10	783,00	179,48	1282,62	1309,00	215,33	1792,91	1810,00	170,48
16	468,78	455,56	271,36	695,98	710,00	257,82	1089,90	1153,00	360,14	1714,36	1787,00	380,77	2255,63	2290,00	257,90
17	468,78	455,56	271,36	695,98	710,00	257,82	1089,90	1153,00	360,14	1714,36	1787,00	380,77	2255,63	2290,00	257,90
18	497,53	501,96	269,14	751,69	716,00	256,42	1179,23	1130,00	367,60	1795,23	1872,50	476,72	2274,77	2318,00	392,13
19	497,53	501,96	269,14	751,69	716,00	256,42	1179,23	1130,00	367,60	1795,23	1872,50	476,72	2274,77	2318,00	392,13
20	429,66	437,21	162,24	566,32	575,00	93,92	881,58	878,00	88,62	1422,32	1440,00	92,89	1718,24	1682,00	158,94
21	324,46	286,33	188,16	506,17	520,00	143,48	833,80	856,00	180,21	1527,13	1491,00	259,05	2253,88	2282,00	271,12
22	271,80	210,98	230,53	420,44	441,00	255,12	698,62	765,00	365,42	1313,07	1350,00	543,50	2016,37	2156,00	573,22
23	386,18	322,35	230,00	581,85	576,00	88,71	1035,67	1055,00	137,80	1826,91	1831,50	112,64	2122,89	2113,00	48,31
24	429,16	434,17	132,05	670,82	678,00	99,09	1177,46	1195,00	113,03	1844,61	1855,00	50,96	2052,45	2057,00	16,03
25	412,31	428,29	132,27	575,92	583,00	67,20	809,66	807,00	45,76	1167,18	1163,00	43,50	1511,93	1493,00	78,22
26	449,48	452,17	190,80	671,26	675,00	112,80	1137,24	1192,00	234,36	2079,78	2139,00	238,93	2502,37	2487,00	44,57
27	431,59	431,31	202,30	626,74	627,50	153,19	1037,91	1079,00	234,54	1939,67	2007,00	276,98	2391,71	2409,00	44,14
28	384,49	367,52	194,85	563,10	538,00	184,83	903,42	859,00	253,80	1576,94	1557,00	259,39	2198,07	2274,00	188,17
29	437,07	412,79	196,47	560,13	549,00	100,26	857,17	863,00	92,07	1437,71	1434,00	87,64	1744,14	1736,00	43,04
30	456,17	480,87	181,43	658,38	679,00	159,79	1001,67	1005,00	203,56	1518,87	1529,00	85,00	1860,84	1861,00	60,65
31	449,88	446,50	188,32	616,95	604,00	87,30	960,09	954,00	132,34	1461,26	1468,00	48,58	1693,42	1688,00	50,89
32	109,52	67,04	125,33	156,09	118,00	146,77	271,07	238,00	227,05	604,55	679,00	360,77	1144,41	1215,00	359,97
33	357,54	338,12	208,95	431,49	460,00	167,77	630,17	680,00	194,99	1056,70	1097,00	170,46	1503,16	1522,00	102,22
34	383,07	375,94	212,07	429,09	483,00	169,22	629,84	640,00	194,90	1036,73	1102,00	204,31	1504,01	1501,00	96,04
35	333,86	307,44	164,89	410,19	389,00	130,56	603,97	547,00	172,64	1075,53	1175,00	199,22	1467,98	1480,00	67,14
36	377,15	391,70	210,45	522,96	583,00	221,06	834,50	957,00	280,50	1413,59	1486,00	231,93	1944,79	1932,00	113,82
37	471,29	487,14	192,65	684,92	683,00	154,93	1019,73	1028,00	193,75	1680,98	1695,00	146,65	2158,80	2154,00	76,13
38	499,96	491,82	242,65	740,93	759,00	167,30	1160,33	1200,00	204,26	1960,32	1967,00	176,21	2562,83	2568,00	94,31
39	494,30	469,21	248,05	726,30	752,00	160,16	1153,74	1190,00	182,53	1928,46	1937,00	145,45	2567,14	2576,00	98,54
40	532,62	531,67	219,48	764,81	768,00	167,81	1162,47	1217,00	227,32	1843,76	1852,00	156,46	2393,38	2399,00	74,26
41	502,60	526,40	215,00	723,50	730,00	168,07	1114,79	1110,00	228,86	1847,40	1938,00	355,19	2621,17	2753,00	434,86
42	532,50	546,67	212,19	777,31	768,00	139,95	1298,12	1330,00	217,74	2317,37	2327,00	233,61	2765,42	2745,00	63,06
43	502,76	519,56	209,47	711,95	697,00	135,76	1090,86	1073,00	173,64	1777,68	1771,00	194,53	2515,33	2558,00	109,42
44	494,86	501,54	211,21	706,24	678,00	176,16	1080,00	1048,00	258,47	1690,25	1706,00	265,18	2245,02	2218,00	236,05
45	349,83	285,79	208,69	529,71	505,00	215,90	888,19	825,00	280,56	1665,23	1698,00	291,10	2457,62	2483,00	177,14
46	425,90	433,57	185,11	632,17	614,00	154,19	972,38	937,00	220,53	1522,35	1547,00	287,27	2112,09	2112,00	261,80
47	466,16	492,20	196,16	708,90	695,00	166,29	1094,47	1073,00	217,52	1838,11	1894,00	184,55	2241,27	2232,00	49,23
48	497,31	489,09	235,63	743,24	747,00	222,29	1204,98	1234,00	286,16	2054,62	2036,00	315,22	2771,52	2774,00	177,09
49	508,98	517,75	186,63	715,77	695,00	169,29	1136,17	1147,00	213,03	1871,81	1844,00	181,74	2424,60	2463,00	81,21
50	491,61	498,94	165,78	693,63	688,00	119,42	1108,97	1109,00	133,81	1847,83	1814,00	178,64	2329,80	2305,00	126,89
51	367,51	359,42	151,85	505,37	495,00	119,36	829,40	812,00	189,12	1575,88	1611,00	236,44	2263,75	2234,00	147,26
52	531,09	537,50	245,51	766,42	755,00	178,54	1172,17	1170,00	215,90	1773,95	1763,00	200,93	2229,13	2262,00	127,80
53	533,66	556,25	171,19	754,09	747,00	157,88	1183,59	1162,00	271,05	1927,13	1970,00	190,66	2417,60	2439,00	77,14
54	528,27	560,63	180,76	726,54	743,00	160,86	1075,00	1115,00	185,02	1628,82	1620,00	92,94	2126,84	2146,00	101,67

ID*	Local relief average of radii [m]			Ksn [stream threshold = 10^6]			Strain rate [10^-9 yr^-1]			BIO12 Annual precipitation			BIO13 Precipitation of wettest month			Aridity index		
	Mean	Median	St Dev.	Mean	Median	St Dev.	Mean	Median	St Dev.	Mean	Median	St Dev.	Mean	Median	St Dev.	Mean	Median	St Dev.
1	969,48	985,00	154,60	194,77	187,90	81,34	56,91	56,91	0,80	673,64	681,50	32,08	90,73	90,00	5,38	6076,36	6014,50	781,35
2	1267,54	1303,00	182,22	293,38	306,97	80,46	36,02	54,33	25,45	671,74	684,00	45,00	92,84	95,00	6,78	6463,21	6676,00	797,17
3	869,23	846,00	141,93	148,02	147,24	61,60	27,66	29,27	3,91	638,26	643,00	26,60	90,78	91,00	2,62	6912,79	6862,00	295,20
4	792,69	799,00	37,33	183,69	193,24	45,45	34,98	34,14	8,89	612,17	614,50	12,19	91,57	92,00	1,25	7261,45	7286,50	241,14
5	1362,80	1380,00	205,97	377,72	295,24	260,05	21,67	20,04	5,43	576,18	579,00	17,10	85,84	86,00	6,12	6803,26	6662,00	1067,59
6	1375,10	1475,00	292,58	276,45	275,27	71,10	23,56	23,74	3,92	511,66	504,00	17,19	72,69	72,00	2,40	4641,81	4526,00	600,02
7	1301,78	1299,00	174,17	346,98	322,78	177,74	35,74	34,81	16,79	456,48	481,00	75,27	79,77	84,00	13,79	6184,33	6395,00	1860,53
8	1625,29	1656,00	118,03	440,34	391,31	89,37	31,99	28,14	7,40	437,00	453,00	83,09	75,92	79,50	15,36	4881,95	4902,00	1425,58
9	1547,68	1547,00	117,19	465,75	443,72	149,19	31,57	28,14	8,61	465,62	491,00	79,78	80,59	86,00	14,85	5476,00	5559,00	1481,35
10	1312,57	1311,00	70,41	362,81	367,27	97,65	29,06	28,73	4,76	483,39	486,50	19,92	85,35	86,00	5,22	6879,80	6939,00	865,09
11	1397,18	1407,00	81,05	341,15	330,01	108,17	28,58	29,70	4,42	484,43	489,00	21,40	85,80	87,00	5,12	7042,49	7105,00	925,02
12	1435,31	1444,00	117,23	420,92	370,57	207,54	46,33	48,90	12,08	544,14	546,50	12,22	83,68	85,50	6,38	6850,10	6927,00	1149,95
13	1384,28	1358,00	149,24	358,54	309,09	185,70	43,47	43,58	0,42	511,42	510,00	23,69	84,53	86,00	7,51	6974,19	6958,00	1223,45
14	1393,65	1422,00	147,07	426,47	311,04	262,16	50,22	44,52	6,26	515,82	526,00	31,77	86,04	88,50	8,36	7017,81	7112,50	1374,36
15	1089,79	1080,00	140,72	260,76	240,04	154,18	86,03	101,32	23,49	513,15	474,00	90,12	83,46	80,00	7,49	5825,62	5709,00	325,73
16	1438,60	1492,00	274,47	372,41	338,86	242,98	24,71	22,10	6,18	357,41	356,00	23,62	60,38	60,00	3,28	4463,93	4373,00	676,88
17	1438,60	1492,00	274,47	372,41	338,86	242,98	24,71	22,10	6,18	357,41	356,00	23,62	60,38	60,00	3,28	4463,93	4373,00	676,88
18	1499,86	1518,00	344,57	418,97	367,23	312,63	25,33	26,12	2,90	345,41	344,00	18,32	61,85	62,00	4,33	4648,02	4697,50	727,26
19	1499,86	1518,00	344,57	418,97	367,23	312,63	25,33	26,12	2,90	345,41	344,00	18,32	61,85	62,00	4,33	4648,02	4697,50	727,26
20	1146,74	1148,00	42,99	272,38	262,42	63,27	58,55	53,83	14,33	319,50	320,00	16,61	55,46	56,00	3,84	3038,15	3046,50	282,72
21	1279,87	1296,00	141,25	315,15	259,05	199,88	66,63	63,15	6,42	350,19	357,00	35,91	63,53	65,00	7,09	4258,40	4212,00	1079,66
22	1111,75	1173,00	389,95	209,14	156,98	221,12	99,78	97,69	21,84	311,29	292,50	76,72	57,93	55,50	14,78	3338,82	2695,00	1505,41
23	1391,47	1395,00	58,08	370,55	432,37	150,13	41,01	38,85	4,58	441,24	451,00	43,78	76,24	78,00	6,06	5447,10	5613,00	938,52
24	1435,95	1452,00	56,73	302,43	293,73	11,90	38,74	38,79	0,07	391,17	389,50	33,38	68,50	69,00	5,35	4389,67	4333,50	634,84
25	1015,80	1014,00	31,39	239,76	252,97	39,86	35,54	35,54	0,00	441,67	444,00	22,20	73,27	74,00	3,23	4994,07	5007,00	393,19
26	1597,29	1640,00	127,85	514,90	466,36	274,89	33,19	33,96	3,37	501,26	514,50	66,44	76,96	79,00	10,60	5593,83	5615,00	1198,05
27	1498,63	1523,00	161,50	455,43	448,83	268,86	31,35	31,35	0,33	522,73	543,00	63,29	80,03	83,00	10,02	6078,08	6263,00	1233,04
28	1310,01	1309,00	198,64	361,90	281,72	247,34	29,81	31,28	5,61	544,73	568,50	65,04	82,41	87,00	10,42	6461,37	6753,00	1269,80
29	1149,40	1145,00	58,92	288,88	225,85	112,17	17,26	13,36	5,81	468,78	486,00	39,72	76,15	77,00	5,58	5405,44	5688,00	758,93
30	1259,57	1268,00	96,59	290,88	332,13	115,50	17,66	19,36	2,40	479,32	481,00	51,01	77,24	77,00	6,75	5506,39	5482,00	1007,81
31	1182,56	1177,00	50,28	318,26	265,22	117,43	13,07	11,88	3,07	469,38	471,50	31,58	75,05	75,00	4,47	5804,64	5846,50	628,26
32	543,65	568,00	255,20	42,43	0,00	148,21	19,92	20,45	7,70	408,54	404,00	28,62	70,27	69,00	4,04	4736,07	4600,00	503,55
33	905,00	903,00	93,23	202,55	200,38	108,20	55,89	71,68	30,56	364,61	353,00	43,19	68,76	67,00	8,31	3843,63	3603,00	742,17
34	899,54	882,00	99,29	211,85	188,50	106,38	58,60	71,68	29,25	364,40	351,00	47,48	68,36	66,00	8,81	3844,76	3559,00	810,75
35	889,05	904,00	108,15	207,91	213,34	40,37	27,84	45,51	44,33	360,89	352,00	38,20	68,05	67,00	7,43	3778,46	3559,00	672,90
36	1178,58	1274,00	189,49	265,74	228,34	123,56	57,51	53,80	15,44	319,22	325,00	37,98	58,20	59,00	7,30	3662,90	3616,50	902,51
37	1385,74	1395,00	130,28	391,22	382,05	157,74	17,30	17,19	8,12	297,47	308,00	27,61	53,49	55,00	4,81	3570,88	3782,00	677,68
38	1605,73	1633,00	134,80	452,99	442,80	159,69	21,61	21,63	2,74	296,89	306,00	34,46	53,50	56,00	6,16	3542,24	3650,00	791,06
39	1593,54	1633,00	124,37	478,15	443,20	111,12	21,74	23,28	3,22	299,60	310,00	38,98	53,83	56,00	6,75	3616,79	3728,00	887,96
40	1540,73	1581,00	132,38	447,20	433,01	200,50	14,99	17,63	5,22	301,43	307,00	28,89	54,06	55,00	4,83	3652,71	3726,50	684,78
41	1576,34	1616,00	258,56	461,47	372,65	284,70	26,71	26,52	20,41	617,24	662,00	90,36	90,97	96,00	11,52	7429,85	7909,00	2058,46
42	1789,18	1800,00	135,37	552,49	588,19	289,09	26,63	25,48	5,86	621,81	653,00	77,43	90,15	94,00	10,11	7485,76	7852,00	1545,93
43	1523,58	1520,00	133,02	386,72	380,27	168,44	35,51	35,52	9,67	672,87	672,00	25,00	95,43	96,50	4,81	8498,20	8446,50	744,14
44	1430,00	1416,00	203,30	399,37	345,15	209,95	75,35	75,35	10,31	649,65	666,00	57,55	92,60	95,00	8,56	8289,32	8550,00	1336,79
45	1384,81	1332,00	201,02	355,27	240,90	373,20	16,53	14,80	5,74	654,37	654,00	25,29	100,08	101,00	5,07	7530,02	7522,50	857,69
46	1309,37	1309,00	200,81	361,91	315,72	216,66	13,15	13,15	3,36	656,95	656,00	33,42	97,79	99,00	5,78	8067,44	8205,00	953,89
47	1470,32	1471,50	132,98	430,86	288,61	329,53	6,84	6,13	3,87	669,37	673,00	25,08	101,89	104,00	5,08	7949,34	7976,50	669,14
48	1693,22	1714,00	188,67	455,08	412,75	262,72	38,84	38,90	2,03	666,95	667,00	43,84	101,46	102,00	7,85	6742,38	6858,00	852,15
49	1536,71	1517,00	114,49	356,22	360,44	108,76	32,42	31,78	4,07	652,39	676,50	81,04	95,59	100,50	13,66	5793,59	6253,00	1027,33
50	1494,68	1489,00	92,69	329,93	301,40	105,08	24,23	23,96	0,80	600,11	637,00	92,73	86,18	90,00	15,25	4993,84	5177,00	1052,91
51	1293,23	1312,00	128,76	322,07	241,55	229,70	25,60	25,60	2,39	614,25	665,00	105,50	90,50	100,00	17,59	5404,43	6033,00	1329,98
52	1485,04	1482,00	127,96	345,30	301,86	390,88	25,98	25,98	11,89	429,28	431,00	16,97	73,13	73,00	3,37	4286,94	4210,00	447,67
53	1570,23	1610,00	141,69	374,53	366,94	97,95	35,18	35,75	8,15	364,50	360,50	13,29	63,63	62,50	2,75	3393,44	3319,50	187,21
54	1388,92	1409,00	105,90	310,23	325,33	116,29	44,04	47,07	6,97	405,82	407,00	26,19	66,71	67,00	2,00	4213,60	4149,00	703,21

* ID numbers correspond to sample numbers in the Supplementary Figure S4.1

Table S4.6. Mean and median ^{10}Be, AFT and AHe values

Region	AFT Mean			AFT Median			AHe Mean			AHe Median			10Be Mean (modern)	10Be Median (modern)
	High	Mid	Low	High	Mid	Low	High	Mid	Low	High	Mid	Low		
All	**244,6**	**212,0**	**189,6**	**102,8**	**95,9**	**88,7**	**102,9**	**94,1**	**88,2**	**43,0**	**39,4**	**37,4**	**393,8**	**179,6**
IK North	120,1	111,6	104,5	56,8	54,8	52,9	58,7	55,6	52,8	16,7	15,6	15,1	463,0	166,0
IK South	205,9	176,0	157,3	137,8	125,7	106,7	138,8	121,5	111,5	124,9	101,1	92,7	678,3	669,5
Kyrgyz range	774,4	625,8	535,8	664,8	549,8	471,6	376,6	357,4	340,3	294,0	289,4	285,0	105,3	111,5
Song Kul	55,5	52,1	49,1	49,9	46,6	44,2	31,2	29,1	27,2	26,8	25,0	23,4	215,0	123,5
Naryn	50,4	47,2	44,4	35,4	32,6	31,1	18,7	17,3	16,2	23,5	21,8	20,3	248,7	248,2
Toktogul	105,6	99,8	94,7	105,6	99,8	94,7	no data	no data	no data	no data	no data	no data	117,0	107,7
Jalal Abad	273,0	233,6	206,3	285,1	245,2	205,4	no data	no data	no data	no data	no data	no data	258,7	256,4
Osh	497,8	447,3	406,5	453,2	409,7	373,7	no data	no data	no data	no data	no data	no data	1171,0	411,0